Linear-Variable Optical Filters for microspectrometer application

Arvin Emadi

8G0597 5059804

Linear-Variable Optical Filters for microspectrometer application

Proefschrift

ter verkrijging van de graad van doctor
aan de Technische Universiteit Delft,
op gezag van de Rector Magnificus prof. ir. K.C.A.M. Luyben,
voorzitter van het College voor Promoties,

in het openbaar te verdedigen

op woensdag 8 december 2010 om 10.00 uur

door
Arvin EMADI
Master of Science in Engineering,
Chalmers University of Technology, Sweden
geboren te Tehran, Iran

TU Delft Library
Prometheusplein 1
2628 ZC Delft

Dit proefschrift is goedgekeurd door de promotor:

Prof. dr. ir. G.C.M. Meijer

Copromotor: Dr. ir. R.F. Wolffenbuttel

Samenstelling promotiecommissie:

Rector Magnificus	voorzitter
Prof. dr. ir. G.C.M. Meijer,	Technische Universiteit Delft, promotor
Dr. ir. R.F. Wolffenbuttel,	Technische Universiteit Delft, copromotor
Prof. dr. J.H.G. Correia,	University of Minho, Portugal
Prof. dr. P. Enoksson,	Chalmers University of Technology, Sweden
Prof. dr. ir. A.J.P. Theuwissen	Technische Universiteit Delft
Prof. dr. ir. P.P.L. Regtien	Universiteit Twente
Prof. dr. B. Dam	Technische Universiteit Delft
Prof. dr. K. Makinwa	Technische Universiteit Delft, reservelid

Printed by Ipskamp Drukkers B.V.

ISBN: 978-90-813316-8-5

Copyright © 2010 by A. Emadi

All rights reserved. No part of this publication may be reproduced or distributed in any form or by any means, or stored in a database or retrieval system, without the prior written permission of the author.

Printed in The Netherlands

To my parents, brother and sister

Dit proefschrift is goedgekeurd door de promotor:

Prof. dr. ir. G.C.M. Meijer

Toegevoegd promotor: Dr. ir. R.F. Wolffenbuttel

Samenstelling promotiecommissie:

Rector Magnificus	voorzitter
Prof. dr. ir. G.C.M. Meijer	Technische Universiteit Delft, promotor
Dr. ir. R.F. Wolffenbuttel	Technische Universiteit Delft, toegevoegd promotor
Prof. dr. J.H.G. Correia	University of Minho, Portugal
Prof. dr. P. Enoksson	Chalmers University of Technology, Sweden
Prof. dr. ir. A.J.P. Theuwissen	Technische Universiteit Delft
Prof. dr. ir. P.P.L. Regtien	Universiteit Twente
Prof. dr. [illegible] Dam	Technische Universiteit Delft
Prof. dr. K. Makinwa	Technische Universiteit Delft, reservelid

Printed by [illegible]
ISBN: 978-90-[illegible]

Copyright © [illegible]
All rights reserved. No part of this publication may be reproduced or distributed in any form or by any means, or stored in a database or retrieval system, without the prior written permission of the authors.

Printed in The Netherlands

Contents

1 **Introduction** **1**

1.1 The purpose of microspectrometers 1
1.2 Grating-based microspectrometers 4
1.2.1 Fixed grating and a detector array 4
1.2.2 Moving grating microspectrometer 8
1.3 Optical Filter based microspectrometers 8
1.3.1 Tunable Fabry-Perot interferometer 9
1.3.2 Microspectrometer based on an array of discrete filters 10
1.3.3 Microspectrometer based on a Linear Variable Optical Filter 11
1.4 Organization of thesis 13
1.5 References 14

2 **Optical Design** **16**

2.1 Introduction 16
2.2 Ellipsometry 16
2.3 Interference optical filter design 21
2.3.1 Bragg Reflector 21
2.3.2 Edge filters 23
2.3.3 Fabry-Perot filter 27
2.3.4 Practical issues for designing multilayered Fabry-Perot 31
2.4 LVOF microspectrometer 36
2.5 References 41

3 **Fabrication and characterization of interference filter banks** **43**

3.1 Introduction 43
3.2 Interference filters for Infra-red 44
3.2.1 Materials characterization 44
3.2.2 Infra-red filters for 2 µm to 3 µm 50
3.2.3 Infra-red filters for 1.4 µm to 2.0 µm 57
3.2.4 Infra-red filters for 3 µm to 4.5 µm 58
3.3 Interference filters for visible spectral range 60
3.4 Interference filters for UV (300 nm – 400 nm) 65
3.5 References 69

4 **Fabrication of tapered layers using reflow** **70**

4.1 Introduction 70
4.2 Modeling of the reflow process 72

4.2.1 Analytical modeling 73
4.2.2 Finite element Simulation 76
4.3 Mask design and lithography 78
4.4 Resist reflow process 83
4.4.1 Thermal reflow 83
4.4.2 Chemical (solvent) reflow 85
4.4.3 Chemical-Thermal reflow 85
4.5 Experimental results 87
4.6 Topography transfer by plasma etching 89
4.7 References 93

5 LVOF spectrometer for visible spectrum 95

5.1 Introduction 95
5.2 Design of the LVOF for 570 nm – 740 nm 96
5.3 Fabrication of the LVOFs 98
5.4 Characterization of LVOFs 99
5.5 Signal processing and spectral measurements with LVOF microspectrometer 102
5.6 Narrowband LVOF 106
5.7 Wideband visible LVOF 116
5.8 Visible LVOF with Silver as metallic mirrors 126
5.9 References 132

6 LVOF microspectrometer for the UV spectral range 134

6.1 Introduction 134
6.2 Design and fabrication of UV LVOF 135
6.3 Characterization and calibration of UV LVOF 139
6.4 Spectral measurement 142
6.5 References 147

7 CMOS photodiode array and LVOF integration 148

7.1 Introduction 148
7.2 Smart CTIA-APS 150
7.2.1 Detector array 150
7.2.2 Active pixel sensor with CTIA 150
7.2.3 In-pixel CDS 152
7.2.4 Variable integration time 153
7.2.5 Circuit diagram 154
7.3 Device performance 155
7.3.1 Photodetectors: Spectral Response and Leakage Current 156
7.3.2 Basic APS operation 157
7.3.3 Temporal noise 157
7.3.4 CTIA-APS operation: Fixed Integration Time Control 159
7.3.5 CTIA-APS operation: Fixed Voltage Difference 159

7.4 System configuration with LVOF 160
7.5 Post-processing of a LVOF on CMOS chip at die-level 161
7.6 References 165

8 **Conclusions** **167**

8.1 UV to IR Linear Variable Optical Filter microspectrometers 167
8.2 Suggestions for future work 171
8.3 References 172

Summary **173**

Samenvatting **177**

Acknowledgements **181**

List of Publications **183**

About the Author **188**

1 Introduction

1.1 The purpose of microspectrometers

Spectroscopy is the science of studying light interaction with matter as a function of wavelength (λ). The interaction between light and matter can change the state of electrons in atoms and molecules and hence exchanging energy between them will cause either scattering of light, emission of light or absorption of light.

When light is absorbed by the electrons in an atom or molecule, they are excited to higher quantized energy levels in the atomic structure. The absorption spectrum of an atom or molecule depends on its energy level structure and is a useful tool to identify different materials.

The excited electrons in atoms or molecules can subsequently travel down to lower energy levels, and this process involves releasing energy in the form of photons and results in emission of light. Assuming that the energy level difference between normal and excited states is ΔE, the frequency of absorbed or emitted photon, ν, is described by Planck's equation: $\Delta E = h\nu$. Where ν is

the frequency of absorbed or emitted photon and h represents the Planck's constant; $h = 6.626 \cdot 10^{-34}\ J \cdot s$.

Light can also be redirected when hitting matter. The light that is redirected at the same wavelength as the incoming light is called Rayleigh scattering. Rayleigh scattering happens due to non-uniformities in the medium through which light passes. Following the reflection law at all the non-uniformity regions, the light is redirected in many different angles. A small part of the scattered light can have a wavelength shift from the incident light. This happens when incident light changes vibrational, rotational or electronic energy of molecules. This phenomenon is called Raman scattering and detection of the wavelength shifted part of the light is a non-destructive tool for material analysis.

The emission spectrum of a material is referred to the fingerprint of this material. The specific peaks in the spectra identify the presence of the atomic states and hence prove the existence of a specific material. This technique, emission spectroscopy, is widely used in astronomy to identify the gas compounds and determining temperature of a star. Absorption spectroscopy on the other hand, compares the light spectrum before and after interaction with a material. As mentioned earlier, absorption at specific wavelengths happens when the photons energy matches the energy differences of atomic states of the material. By analyzing the recorded spectra, the presence and the amount or concentration of compounds can be calculated. This technique is called spectrometry and the device which performs this task is a spectrometer.

In this thesis, and many books and articles, a spectrometer is referred to an instrument that can record the spectrum of light in a specific spectral region. A more proper term could be a spectrograph, however to comply with other references the term spectrometer is used in this thesis.

Microspectrometers can be used for color measurement for quality inspection in industry and agriculture. Another application is in body fluid analysis in point-of-care diagnostics, [1.1]-[1.2]. They read the chromatography results by measuring UV to the infrared (IR) absorption of the chemical constituent between the light source and a dispersion element. Micromachining can be implemented for fabrication of the dispersion and detection elements in a silicon microspectrometer, so that it can analyze the spectrum of incident light, [1.3]. Single-chip optical microspectrometers have huge potential in many applications, such as identification of bio-molecules and in chemical analysis, because of their properties such as low-cost and low sample volumes. There are

many applications where cost and size are much more important than possible spectral resolution.

There are many different kinds of spectrometers which are usually classified according to their fundamental operating mechanism. The implementation is typically application dependent. Spectrometers with very high spectral resolutions are used in astronomy and are very bulky. Spectrometers used for material identifications used in laboratories are also big and expensive. However, for many applications such huge, bulky and expensive instruments are not required. It is possible to detect spectral lines of many liquids and gases with smaller versions of spectrometers which have lower spectral resolutions. A highly interesting approach is to strive for the maximum theoretically possible spectral resolution within the constraint of a very small (1 – 1000 cm^3) volume determined by the optical path travelled in the spectrometer. These types of spectrometers are called microspectrometer.

Similar to its macroscopic counterpart, microspectrometer operation may be based on either an array of detectors, each with a unique spectral response, or a scanning dispersion element using a single calibrated detector. The dispersive element can also be either grating or optical filters. Therefore we can name four different approaches:

1- Moving grating as dispersive element plus one calibrated detector.

2- Fixed grating as dispersive element plus an array of detectors.

3- Tunable optical filter plus one calibrated detector.

4- Array of detectors each with a unique optical filter

Compared to bulky macroscopic devices, microspectrometers have inferior spectral resolution, but their small size and low cost more than compensate for this limitation in many applications.

Classifying based on dispersive element, the two major types of microspectrometers are grating-based microspectrometers (options 1 and 2) and optical-filter based microspectrometers (options 3 and 4). The grating-based microspectrometers have the advantage of higher operating bandwidth and the optical-filter based microspectrometers have the advantage of higher spectral resolution in a narrow bandwidth and easier integration with electronics.

1.2 Grating-based microspectrometers

1.2.1 Fixed grating and a detector array

The structure of this type of microspectrometers includes a slit, grating(s) and reflective surfaces. The shape of the grating and reflective surface can be planar or concave. The light goes through the optical path of microspectrometer and is refracted and reflected from the surfaces and eventually makes an image of the spectrum on a photodetector array. The final image recorded on the detector array represents the spectrum of the incident light. The optical system in principle makes an image of the slit on the detector array. The position of the slit images is different for each wavelength in the spectrum of the incident light.

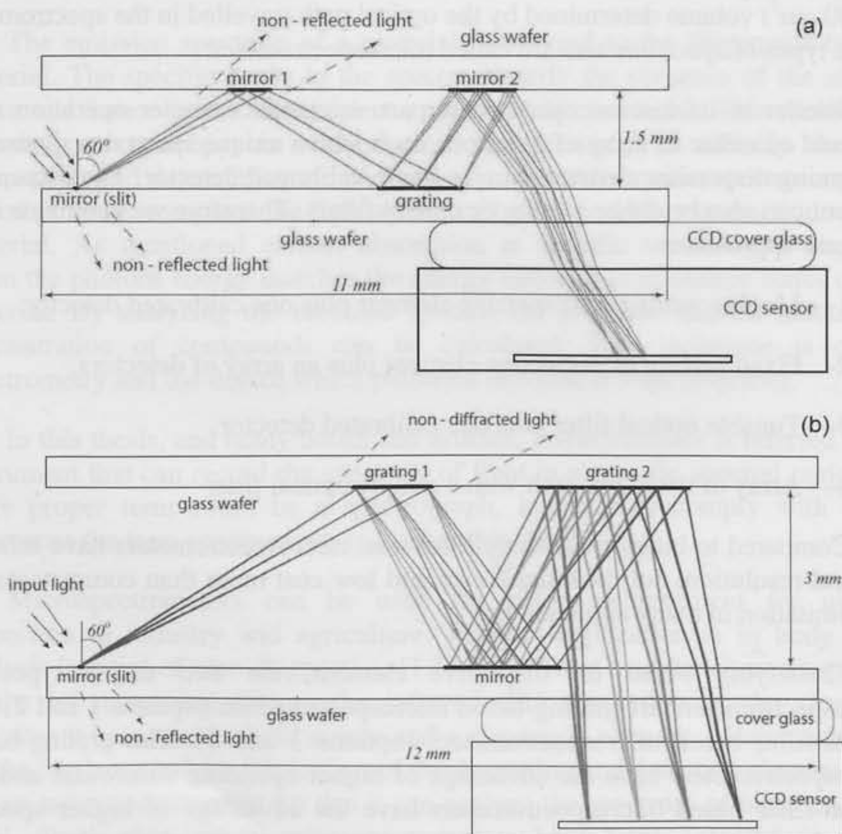

Figure 1.1. *Schematic of a) one grating and b) two grating microspectrometer.*

Maximum resolving power can be achieved in a careful design using ray tracing optical simulation tools. Figure 1.1 shows the schematic of two different grating based microspectrometers [1.4]-[1.6]. One is with a single grating and the other with two gratings. Light which is projected on the slit from an optical fiber is reflected to gratings and eventually imaged on the CCD detector array. Figure 1.2 shows the implementation and experimental setup of the microspectrometer. Most of the volume in the spectrometer is due to the size of the commercial CCD detector with readout circuitry and electronics required for interfacing to computer software. Using a customized detector substantially decreases the volume of the setup.

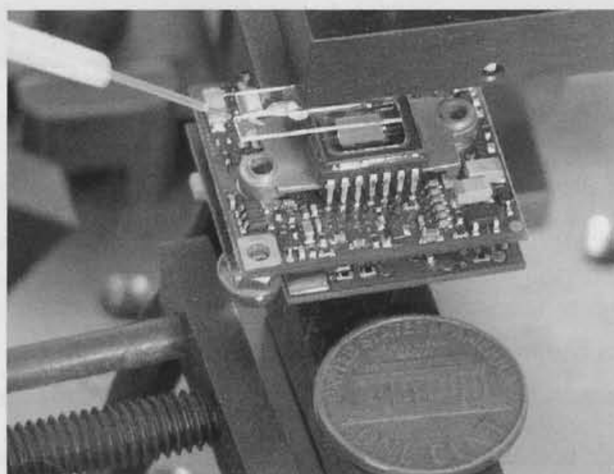

Figure 1.2. *Double grating microspectrometer mounted on a CCD detector.*

A spectral resolution of 7 nm has been achieved from the single grating microspectrometer and 3 nm from the double grating microspectrometer.

To get even higher spectral resolution, curved surfaces need to be used in the optical path of a microspectrometer. This can be implemented by using concaved grating or concave mirror.

Figure 1.3 shows the schematic of a microspectrometer using an external spherical mirror, [1.7]. The advantage of this microspectrometer is high improvement in spectral resolution. However, alignment can be costly and time consuming. Figure 1.4 shows photograph of the glass substrate which includes

the slit and grating mounted on a commercial CCD and an external spherical mirror aligned with them as shown schematically in Figure 1.3.

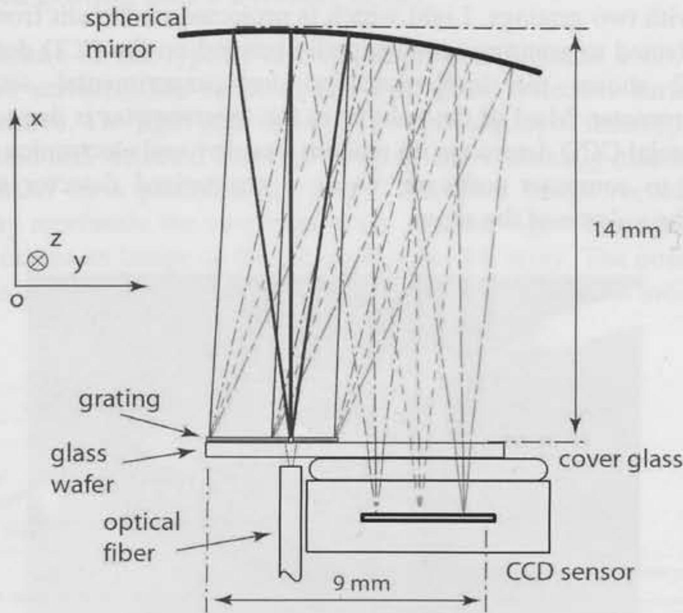

Figure 1.3. *Schematic of a microspectrometer using external spherical mirror.*

A spectral resolution of 0.7 nm has been demonstrated with this microspectrometer. An important characteristic of these types of microspectrometers is the inverse proportionality of spectral resolution with numerical aperture. To achieve a spectral resolution better than 1 nm, optical systems have to be designed with very low value numerical aperture which results in low levels of light intensity inside the system. One way to improve light efficiency is to use blazed type of gratings to compensate for the limited amount of light entering the optical system. Using very sensitive photodetectors or long integration time can also compensate for the limited light intensity, provided that the application allows.

The grating based microspectrometer can also be realized in a waveguide platform. Figure 1.5 shows such a waveguide grating-based microspectrometer [1.8].

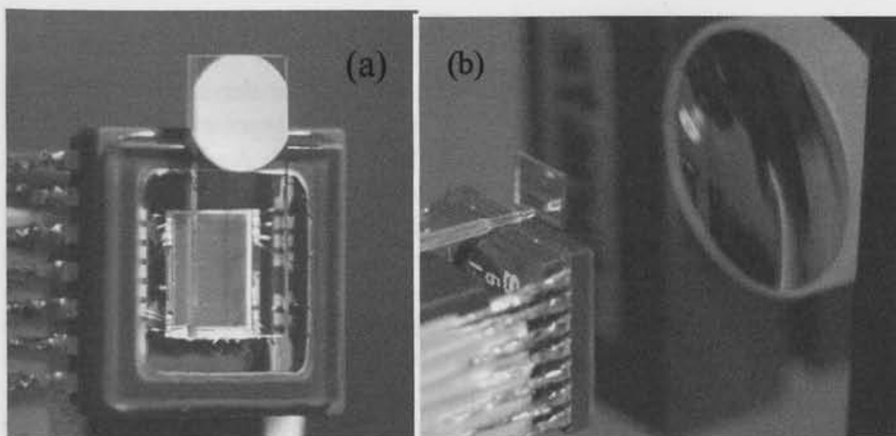

Figure 1.4. *Photograph of a) glass substrate with grating mounted on the CCD detector and b) external spherical mirror aligned with the CCD and glass substrate.*

The light to be analyzed is introduced into the polymer waveguide through an optical fiber, is dispersed in a self-focusing (imaging) reflection grating that has been fabricated using deep reactive ion etching of the polymer and projected onto an array of fibers that guide the spectral components to an photodetector array. Device area is 18 × 6.4 mm^2 and the resolution obtained is R = 10 over a spectral range extending between 720 and 900 nm.

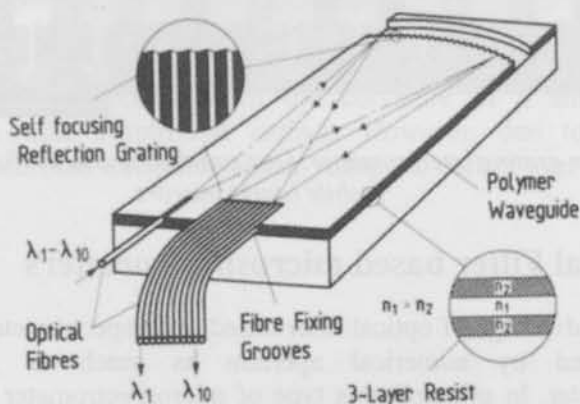

Figure 1.5. *Principal layout of a grating spectrograph with a self-focusing reflection grating fabricated by deep-etch.*

1.2.2 Moving grating microspectrometer

A binary grating with a variable depth operating in the zero order of the diffraction pattern is called a lamellar grating. This type of apparatus was invented by Strong and Vanasse in 1960, [1.9]. A lamellar grating interferometer is used as a Fourier spectrometer, but, in contrast with a Michelson interferometer, which splits wave amplitudes at the beam splitter, a lamellar grating interferometer divides the wave front. At the grating the wave front is separated such that one half of the beam is reflected by the front facets (fixed mirrors) and one half by the back facets (mobile mirrors), Figure 1.6 from [1.10] shows a SEM photo of such a device. The distance between the two series of mirrors determines the optical path difference (OPD) between the two parts of the wave. The mobile mirrors are actuated by an electrostatic comb drive actuator and the motion is linear.

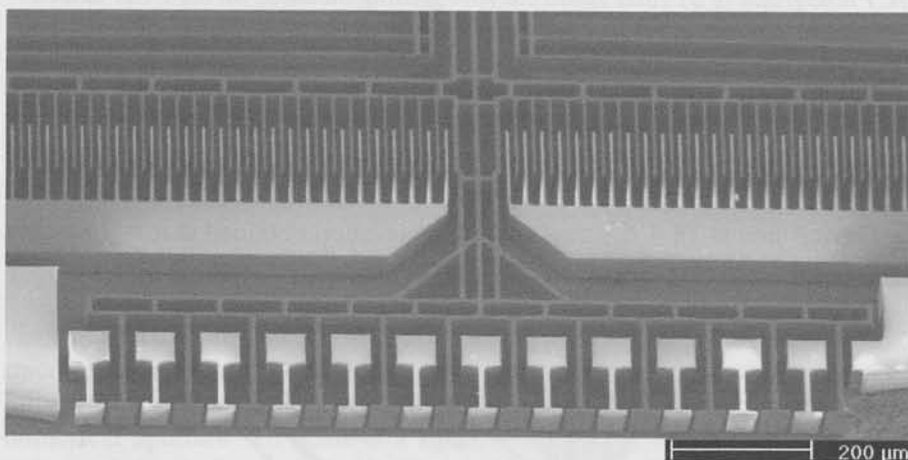

Figure 1.6. *Lamellar grating interferometer. One can distinguish the fixed (light) and mobile (dark) mirrors.*

1.3 Optical Filter based microspectrometers

The main advantage of optical filter based microspectrometers is that these are not limited by numerical aperture as much as grating based microspectrometer. In principle this type of microspectrometer is more useful than grating based one when a high spectral resolution is required over a narrow spectral range. Since filter-based microspectrometer can be fabricated chip-size using IC-compatible process, these are the best option for large volume

production of microspectrometers. Thus, the associated unit-cost, which is the main driver in microspectrometer industry, can therefore be reduced in such an optical micro-instrument. There can be three main microspectrometers based on optical filters. Vast majority of the devices are based on Fabry-Perot resonator. A Fabry-Perot resonator is made of a transparent medium with two parallel highly reflective mirrors on either side. The wavelength which is allowed to be transmitted through the filter is determined by the medium thickness. Theoretical and mathematical issues are addressed in 2.3.3 .

1.3.1 Tunable Fabry-Perot interferometer

The simplest realization of the Fabry-Perot interferometer uses bulk micromachining of the two wafers followed by wafer-to-wafer bonding, [1.11]. Figure 1.7 shows the basic device structure. The wafer-level processing is the same for both wafers. A special spacer prevents the aluminum electrodes from touching after bonding. Applying a voltage tunes the resonance cavity to the desired wavelength. A silicon frame ensures a flat membrane at the mirror area.

The main design challenges of this Fabry-Perot interferometer are:

1- Tuning the movable mirror over a sufficiently large spectrum with acceptable voltage levels.

2- Fabrication of mirror surfaces of sufficient reflectivity and flatness and achieving parallelism between the two mirrors.

Electrostatic force acting on the membrane to change the cavity length also deforms the area outside the frame. This frame prevents reduced optical performance that results from the curvature of a simple suspended membrane with a mirrored surface. However, due to the increased structural stiffness it requires higher voltage to deflect over the same spacer distance.

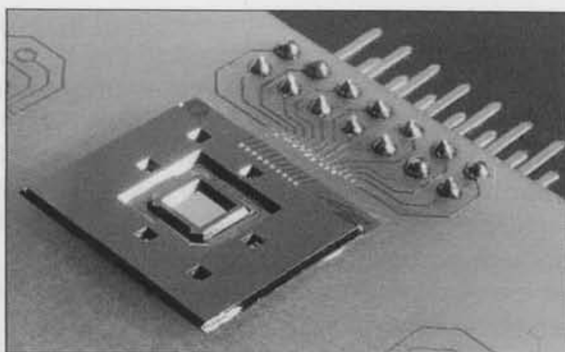

Figure 1.7. *Photograph of the two-wafer bulk-micromachined Fabry-Perot interferometer. A frame is used to keep the membrane flat.*

1.3.2 Microspectrometer based on an array of discrete filters

An alternative approach that circumvents these problems uses 16 fixed Fabry-Perot resonators with different spacing between cavities, [1.12]. Oxide layers space the mirrors to keep them parallel. Four subsequent masked oxide-etch steps fabricate cavities of 16 different thicknesses. The 16 channels cover the entire visible spectrum.

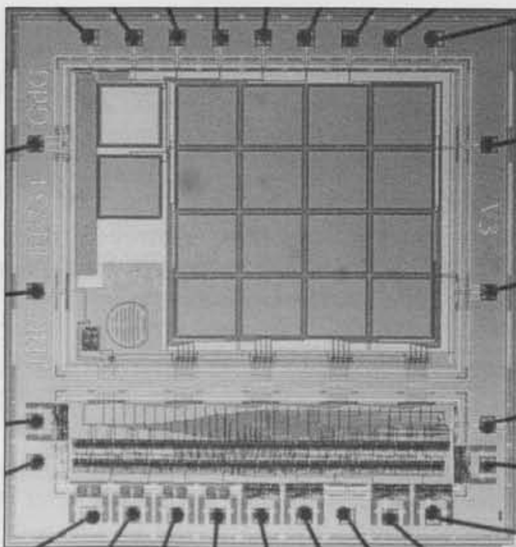

Figure 1.8. *Photograph of the 16-channel CMOS integrated microspectrometer.*

The fabrication of each of these Fabry-Perot resonators is compatible with a standard complimentary metal-oxide-semiconductor (CMOS) process which enables the integration of circuits on-chip for selection and readout of the array photodiodes covered by the different resonators. Figure 1.8 shows the resulting device.

Although it is a very interesting device, designing a system based on array of discrete filters becomes unpractical when high spectral resolution is required for an application. The reason is that the number of lithography steps needs to be increased and alignment of such lithography steps can become challenging. The other reason is tolerances in processes like etching does not allow having all the necessary filters.

These problems are circumvented in a third option for using optical filters which is Linear Variable Optical Filter (LVOF).

1.3.3 Microspectrometer based on a Linear Variable Optical Filter

The Linear Variable Optical Filter (LVOF) is basically a one-dimensional array of many Fabry-Perot (FP)-type of optical resonators. Rather than a huge number of discrete devices, the LVOF has a center layer (the resonator cavity) in the shape of a strip and a thickness that changes over its length. Highly reflective mirrors are on either side. The spectral resolution of a FP resonator is determined by: surface flatness, mirror parallelism and mirror reflectivity.

The spectral range of FP-type of LVOF is determined by the thickness variation of the cavity layer over the length of it and has to be in order of quarter of the wavelength and very well-controlled, which makes fabrication of miniature LVOFs a technological challenge. The possibility to have many channels results in high spectral resolution. A small Linear Variable Optical Filter (LVOF) integrated with an array of optical detectors is a very suitable candidate for a high-resolution microspectrometer.

Piegari et al. [1.13]-[1.15] have demonstrated fabrication of Linear Variable Optical Filters based on a moving mask method shown in Figure 1.9. The masks optimized based on desired thickness slope of the layers are mounted on the substrate and during the deposition are moving back and forth on the substrate. The slope is realized since each part of the substrate is exposed to deposited material for different durations.

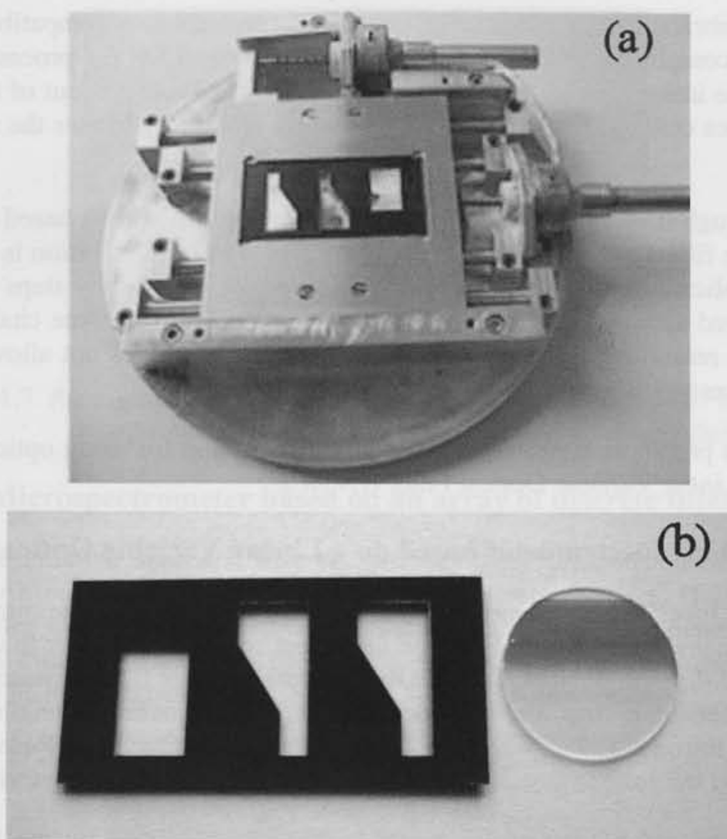

Figure 1.9. *(a)Picture of the shaped mask apparatus (b) masks for obtaining tapered layers and sample with a graded multilayer coating that shows a transmission variation along the vertical direction.*

Very high quality LVOFs have been realized with this technique. However, the process is very time consuming and expensive for microspectrometer applications. The deposition for each LVOF can take several weeks to complete. These LVOFs have been specially designed and fabricated for a space application where launching cost and reliability issues are very critical. Hence, IC-compatible technique for fabrication and low cost realizations were not considered.

In this thesis, an IC-compatible process for fabrication of Linear Variable Optical Filters is introduced. The process allows wafer-level fabrication of LVOFs which is very suitable for large-volume production of LVOF-based

microspectrometers. IC-Compatible fabrication enables the fabrication of LVOFs as a post-process in CMOS. Having the detector array and electronic circuits realized in CMOS prior to application of the post-process offers opportunities for low unit costs in case of a high production volume. The IC-Compatible fabrication technique provides the possibility to directly deposit LVOFs on standard CCD or CMOS imagers and transforming these into microspectrometers.

The operating principle of the LVOF, the fabrication procedure, the basic measurements and the required signal processing for enhanced spectral measurements are discussed in the following chapters.

1.4 Organization of thesis

This thesis presents research on theoretical issues of LVOF operation, reflow and IC-compatible LVOF fabrication, measurements and required signal processing for Linear-Variable Optical Filter microspectrometers. Linear-Variable Filters have been designed, fabricated and measured for the UV (300 nm – 400 nm), Visible (570 nm – 740 nm) and Visible (400 nm - 700 nm) spectral bands. The thesis outline is as follows:

This introduction chapter for introducing microspectrometers, which provides examples and presents the basic classification of microspectrometers.

Chapter two reviews the basic and necessary optical theories required for understanding the operations of optical filters. Later in the chapter Linear-Variable Optical Filters are introduced and explained.

Chapter three discusses the design, simulation, and measurements for filter arrays fabricated for five different spectral bands. Understanding the design and differences between simulation and measurements helps in the final goal of designing LVOFs for those spectral bands.

Chapter four explains in details the IC-compatible process developed for fabrication of tapered optical layers. The basic idea, which is based on resist reflow and involves only one mask lithography, is described. The tapered shape of the resist layer needs to be transferred into the oxide to obtain a useful optical layer. This process involves optimizing for a minimum roughness etching process. The necessary parameters for transferring resist layers into oxide by plasma etching are discussed in the final part of this chapter.

Chapter five presents all the design and measurements and signal processing implemented in LVOFs in the spectral band of (580 nm – 740 nm). The spectrum of Neon lamp has been measured using the LVOF microspectrometer.

Chapter six presents design, measurements and signal processing for a UV (300 nm – 400 nm) LVOF microspectrometer. The spectrum of a Mercury lamp in this spectral range has been measured and presented.

Chapter eight presents design and measurements of a customized CMOS chip containing an array of 128 photodiode pixels with readout circuitry in a 0.35 µm multiuser CMOS process. A LVOF has been integrated with the CMOS chips at the die level and presented at the end of this chapter.

And finally the last chapter gives conclusions for this work and presents some suggestions for possible future works.

1.5 References

[1.1] G. Minas, R.F. Wolffenbuttel, J.H. Correia, An array of highly selective Fabry–Perot optical channels for biological fluid analysis by optical absorption using a white light source for illumination, *J. Opt. A: Pure Appl. Opt.*, Volume **8**, (2006), pp. 272–278.

[1.2] G. Minas, R.F. Wolffenbuttel, J.H. Correia, A lab-on-a-chip for spectrophotometric analysis of biological fluids, *RSC Lab Chip*, Volume **5**, Issue 11, (2005), pp. 1303–1309.

[1.3] R F Wolffenbuttel, MEMS-based optical mini- and microspectrometers for the visible and infrared spectral range, *J. Micromech. Microeng.*, Volume **15**, (2005), pp. 145-152.

[1.4] Semen Grabarnik, Reinoud Wolffenbuttel, Arwin Emadi, Mikhail Loktev, Elena Sokolova, and Gleb Vdovin, Planar double-grating microspectrometer, *Opt. Express*, Volume **15**, (2007), pp. 3581-3588.

[1.5] S. Grabarnik, A. Emadi, H. Wu, G. de Graaf, G. Vdovin, and R. F. Wolffenbuttel, IC-compatible microspectrometer using a planar imaging diffraction grating, *Proc. SPIE*, Volume **6992**, (2008), pp. 699215.

[1.6] Semen Grabarnik, Arvin Emadi, Elena Sokolova, Gleb Vdovin, and Reinoud F. Wolffenbuttel, Optimal implementation of a

microspectrometer based on a single flat diffraction grating, *Appl. Opt.*, Volume **47**, (2008), pp. 2082-2090.

[1.7] Semen Grabarnik, Arvin Emadi, Huaiwen Wu, Ger de Graaf, and Reinoud F. Wolffenbuttel, High-resolution microspectrometer with an aberration-correcting planar grating, *Appl. Opt.*, Volume **47**, (2008), pp. 6442-6447.

[1.8] J. Mohr, B. Anderer, W. Ehrfeld, Fabrication of a planar grating spectrograph by deep-etch lithography with synchrotron radiation, *Sensors and Actuators A: Physical*, Volume **27**, Issues 1-3, (1991), pp. 571-575.

[1.9] J. Strong and G. A. Vanasse, Lamellar grating far-infrared interferomer, *J. Opt. Soc. Am.,* Volume **50**, Issue 2, (1960), pp. 113-118.

[1.10] O. Manzardo, R. Michaely, F. Schädelin, W. Noell, T. Overstolz, N. De Rooij, and H. P. Herzig, "Miniature lamellar grating interferometer based on silicon technology", *Opt. Lett*, Volume **29**, Issue 13, (2004), pp. 1437-1439.

[1.11] J. H. Correia, M. Bartek, R. F. Wolffenbuttel, Bulk-micromachined tunable Fabry-Perot microinterferometer for the visible spectral range, *Sensors and Actuators A: Physical*, Volume **76**, Issues 1-3, 30 August, (1999), pp. 191-196.

[1.12] J. H. Correia, G. de Graaf, S. H. Kong, M. Bartek, R. F. Wolffenbuttel, Single-chip CMOS optical microspectrometer, *Sensors and Actuators A*, Volume **82**, (2000), pp. 191-197.

[1.13] A. M. Piegari, E. Masetti, and J. Bulir, Variable transmission filters with wide rejection band for space applications, *Optical Interference Coatings*, OSA Technical Digest Series, (2004), paper ThB4.

[1.14] Angela Piegari and Jiri Bulir, Variable narrowband transmission filters with a wide rejection band for spectrometry, *Appl. Opt.*, Volume **45**, (2006), pp. 3768-3773.

[1.15] A. Krasilnikova, A. Piegari, M. Dami, L. Abel-Tiberini, F. Lemarquis, and M. Lequime, Spatially resolved spectroscopy for non-uniform thin film coatings: comparison of two dedicated set-ups, *Proc. SPIE*, Volume **5965**, (2005), pp. 59651V/1-8.

2 *Optical Design*

2.1 Introduction

In this chapter the issues that are essential in the optical design of a LVOF microspectrometer are discussed. The chapter starts by introducing ellipsometry which is widely used for the characterization of the optical properties of thin films. In the subsequent section the design principle of interference optical filters is explained. Fabry-Perot, reflective mirrors, high-pass and low-pass filter structures are designed and simulated and the effect of process variations is discussed. The final section of this chapter contains design principles and simulation for Linear Variable Optical Filter (LVOF) spectrometers.

2.2 Ellipsometry

An interference based optical filter consists of a multilayer of dielectric thin films with different optical constant. As light travels through the stack of dielectrics, light waves are reflected and transmitted at each of the boundaries in the stack. Interference of all the light waves transmitted and reflected results in the spectral response of the filter. Reflection and transmission at the boundaries

depends on the optical properties of the dielectrics, therefore for a reliable design of an interference filter it is vital to know the exact optical properties of the materials.

Ellipsometry is based on the measurement of a change in polarization as light is reflected at or transmitted into another material, [2.1]-[2.4]. The measured response depends on the optical properties of the two materials and the thickness of individual layers. In the usual setup the incident medium of light is air.

Ellipsometry is primarily used to determine film thickness and optical constants. It can also be applied to characterization of the composition, crystallinity, roughness, doping concentration and other material properties associated with a change in optical properties.

The mathematical theory behind ellipsometry is based on Fresnel reflection and transmission equations for polarized light. Ellipsometric measurement is normally expressed in terms of Psi (Ψ) and Delta (Δ):

$$\tan(\Psi)e^{i\Delta} = \rho = \frac{r_p}{r_s} \quad (2.1)$$

In which r_p and r_s are the complex Fresnel reflection coefficients for the p-polarized (in the plane of incidence) and s-polarized (perpendicular to the plane of incidence) light. Figure 2.1 shows a diagram of a ray of light interaction with an interface of two materials.

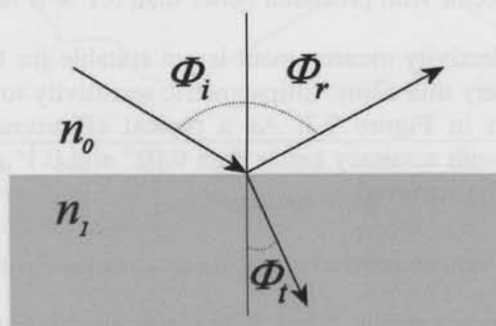

Figure 2.1. *Reflection from a surface boundary.*

Fresnel showed that p-polarized and s-polarized reflection can be calculated separately by solving the Maxwell equations at the boundary and described these as follows:

$$r_s = \frac{n_0\cos(\Phi_i) - n_1\cos(\Phi_t)}{n_0\cos(\Phi_i) + n_1\cos(\Phi_t)} = \frac{n_0\cos(\Phi_i) - n_1\sqrt{1-\left(\frac{n_0}{n_1}\sin(\Phi_i)\right)^2}}{n_0\cos(\Phi_i) + n_1\sqrt{1-\left(\frac{n_0}{n_1}\sin(\Phi_i)\right)^2}} \tag{2.2}$$

$$r_p = \frac{n_0\cos(\Phi_t) - n_1\cos(\Phi_i)}{n_0\cos(\Phi_t) + n_1\cos(\Phi_i)} = \frac{n_0\sqrt{1-\left(\frac{n_0}{n_1}\sin(\Phi_i)\right)^2} - n_1\cos(\Phi_i)}{n_0\sqrt{1-\left(\frac{n_0}{n_1}\sin(\Phi_i)\right)^2} + n_1\cos(\Phi_i)} \tag{2.3}$$

Spectroscopic ellipsometry measures Psi (Ψ) and Delta (Δ) as a function of wavelength. In Variable Angle Spectroscopic Ellipsometry (VASE), Ψ and Δ are measured as a function of both wavelength and angle of incidence.

Since the ratio between two reflected light is measured in ellipsometry, the absolute value of incident and reflected light is in principle not important. To show the advantage of ellipsometry over reflectivity measurement we can consider Figure 2.2. It shows the calculated change in reflectivity caused by a change of 0.1 nm in a 10 nm SiO_2 deposited on a Silicon wafer. In an absolute measurement a detector with precision better than 0.1 % is required [2.1]-[2.4].

Therefore, reflectivity measurement is not suitable for the measurement of small changes in very thin films. Ellipsometric sensitivity to the same thickness variation is shown in Figure 2.3. As a typical ellipsometer can accurately measure Ψ and Δ with accuracy better than 0.02° and 0.1° respectively, a very high precision can be achieved.

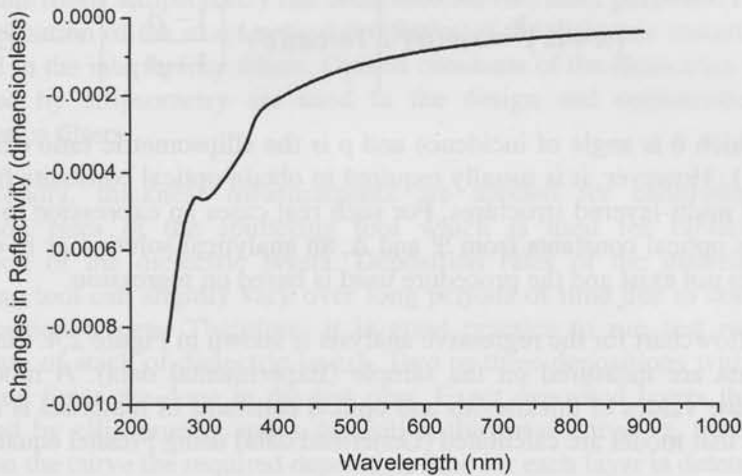

Figure 2.2. *Change in reflectivity in a 10 nm SiO_2 layer caused by a 0.1 nm thickness change.*

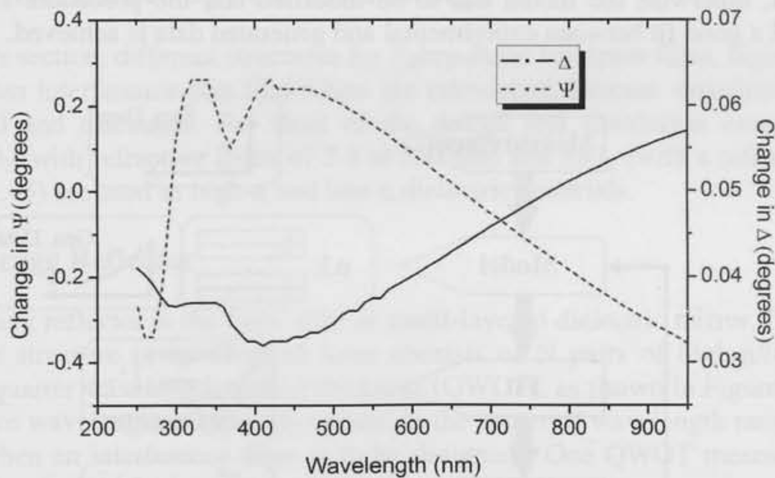

Figure 2.3. *Ellipsometric sensitivity to a 0.1 nm thickness change in a 10 nm SiO_2.*

The ellipsometric data in terms of Ψ and Δ which is measured from a bulk material can be directly converted to optical constants of the material with the following equation:

$$(n+ik)^2 = \sin(\theta)^2.\left[1+\tan(\theta)^2.\left(\frac{1-\rho}{1+\rho}\right)^2\right] \quad (2.4)$$

In which θ is angle of incidence and ρ is the ellipsometric ratio defined by equation 1. However, it is usually required to obtain optical constants from thin films and multi-layered structures. For such real cases an expression to directly derive the optical constants from Ψ and Δ, an analytical solution as in equation (2.4), does not exist and the procedure used is based on regression.

The flowchart for the regressive analysis is shown in Figure 2.4. Initially, Ψ and Δ data are measured on the sample (Experimental data). A model with approximate values of thicknesses and optical constants of materials is made. Ψ and Δ for that model are calculated (Generated data) using Fresnel equations.

Generated and experimental data are subsequently compared to make an error function which is used in an optimization algorithm to fine tune the parameters, such as thicknesses and optical constants, in the model. If the final error of the algorithm is small enough, it proves that a proper model has been used, otherwise the model has to be modified and the procedure starts again until a good fit between experimental and generated data is achieved.

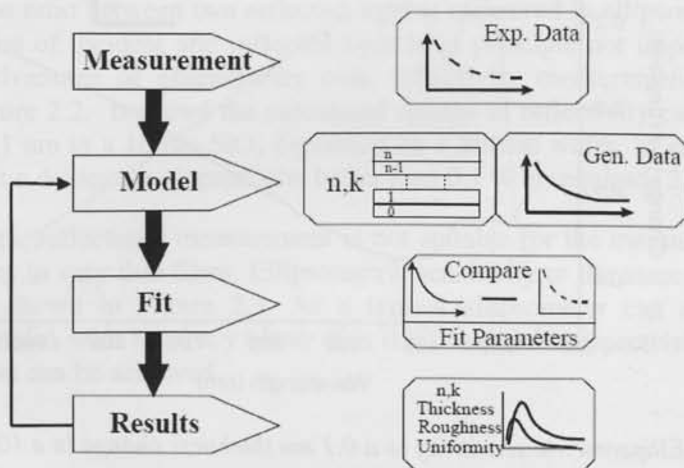

Figure 2.4. *Flowchart of regressive algorithm to calculate n, k from measured Ψ and Δ*

In this thesis, ellipsometry has been used for two main purposes. Firstly, for characterization of the exact optical properties of the dielectric materials which are used in the interference filters. Optical constants of the dielectrics which are measured by ellipsometry are used in the design and optimization of the interference filters.

Secondly, thickness measurements are applied for calibration of the deposition rates of the sputtering tool which is used for fabrication and deposition of the dielectric layers. Deposition rates of the materials in the sputtering tool can slightly vary over long periods of time due to consumption of deposition targets. Therefore, it is good practice to run test runs before deposition of stack of dielectric layers. Two or three depositions with different deposition times are done in the test runs. Exact deposited layers thickness is measured by ellipsometry and a deposition thickness curve vs. time is made. Based on the curve the required deposition time for each layer is determined.

Throughout this thesis ellipsometry data analysis tool WVASE32® has been used and examples will be given in the next chapter.

2.3 Interference optical filter design

In this section, different structures for Fabry-Perot bandpass filter, highpass and lowpass interference thin film filters are introduced. Process variations are considered and discussed. For most of the design and simulation examples given TiO_2 (with refractive index of 2.4 at 550 nm) and SiO_2 (with a refractive index of 1.45) are used as high-n and low-n dielectric materials.

2.3.1 Bragg Reflector

A Bragg reflector is the basic type of multi-layered dielectric mirror, [2.5]-[2.6]. The structure in its simplest form consists of N pairs of high-n/low-n layers of quarter wavelength optical thickness (QWOT), as shown in Figure 2.5. A reference wavelength is typically chosen in the center of wavelength range of interest when an interference filter is to be designed. One QWOT means one quarter of optical thickness at the reference wavelength:

$\text{QWOT} = \frac{\lambda_0}{4n}$, in which λ_0 is the reference wavelength and n is refractive index at the reference wavelength.

Adding one high-n layer at the substrate will increase the reflectivity. The structure is described as Medium/(**HL**)^N**H**/Substrate in which each **H** and **L** represent a QWOT layer of high-n and low-n dielectric.

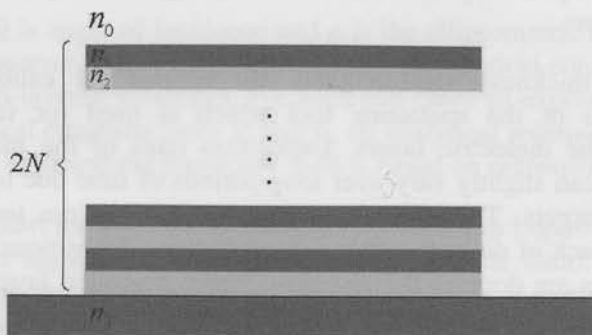

Figure 2.5. *The Structure of a Bragg reflector.*

Figure 2.6 shows the simulated spectral response of the Bragg reflector with Air/(**HL**)^N**H**/Glass configuration for λ_0=550 nm and N=3, 4, 5 and 8. It should be noted the reflectivity of the mirror in the stopband region of $\Delta\lambda$ is increased by adding more layers (larger value N). The reflectivity and the stopband of the mirror can be expressed analytically by the following equations, [2.7]:

$$r = \frac{n_0 n_2^{2N} - n_3 n_1^{2N}}{n_0 n_2^{2N} + n_3 n_1^{2N}} \qquad (2.5)$$

$$\frac{\Delta\lambda}{\lambda_0} = \frac{4}{\pi} Arc\sin\left(\frac{n_2 - n_1}{n_2 + n_1}\right) \qquad (2.6)$$

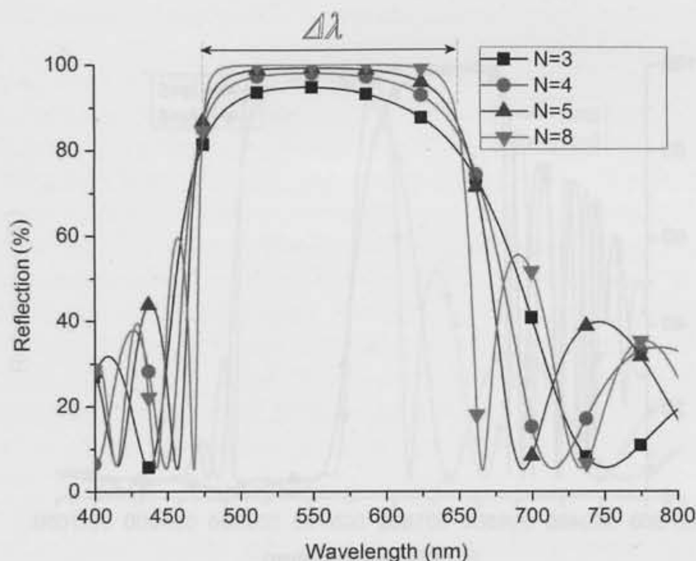

Figure 2.6. *Simulated spectral response of Bragg reflector for different N values.*

The above equations reveal the benefit of using materials with refractive index as far as possible apart. Higher difference between the refractive index of the two dielectric layers results in larger stopband region of the mirror. Moreover, fewer layers are required to achieve a specific level of reflectivity.

2.3.2 Edge filters

An edge filter is a multilayered interference coating with a passband on either side of the stopband. The basic core is the same as Bragg reflector. As it can be seen from Figure 2.6, there are big ripples in the wavelength response on both side of the stopband region. Using two **0.5 H** layers, instead of **H** as the first and last layer of the stack, removes the ripples on the high wavelength region after the stopband and consequently results a high wavelength pass edge filter. The structure would be Medium/**0.5H** $\mathbf{(LH)}^{N-1}$ **L0.5H**/Substrate which is also conventionally expressed as Medium/$\mathbf{(0.5HL0.5H)}^{N}$/Substrate. Figure 2.7 shows the simulation result for N=5 and N=8 cases.

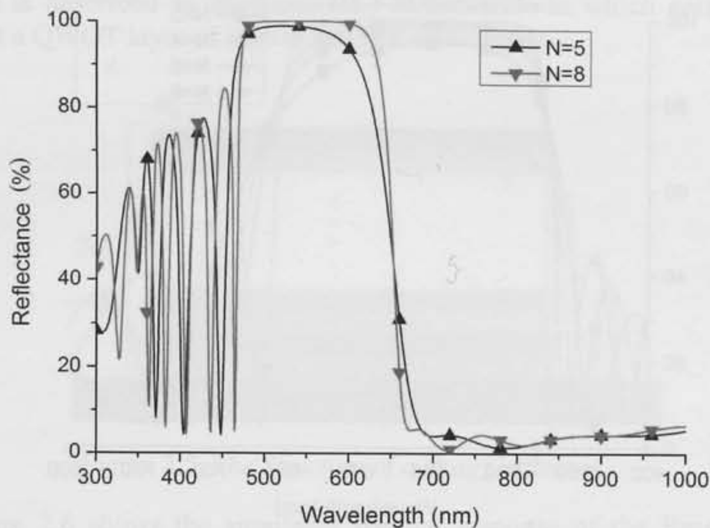

Figure 2.7. *Simulated spectral response of high-λ pass filter.*

In a similar way, if the structure starts and ends with **0.5L** layers, the result is a low ripple of the lower wavelength end of the pass filter. The structure is expressed as Medium/(**0.5LH0.5L**)^N/Substrate. Figure 2.8 shows the result for N=5 and N=8 cases. It can be directly understood that the stopband of such filters is limited by equation (2.6).

When a wider stopband is required two or more filters should be combined to provide the sufficient stopband bandwidth. The reference (center) wavelength of the two filters should be shifted in the spectrum so that their combination gives the widest possible rejection bandwidth with no leakage. A particular filter design can be shifted over the spectrum by simply changing the reference wavelength under the condition that the refractive indices are not significantly wavelength dependent. Figure 2.9 shows the concept for achieving wider stopband region. Two filters with Medium/(**0.5LH0.5L**)^8/Substrate structures have been simulated for λ_0=550 nm and λ_0=715 nm. The total transmission through both stacks has a wide stopband of 470 nm to 835 nm.

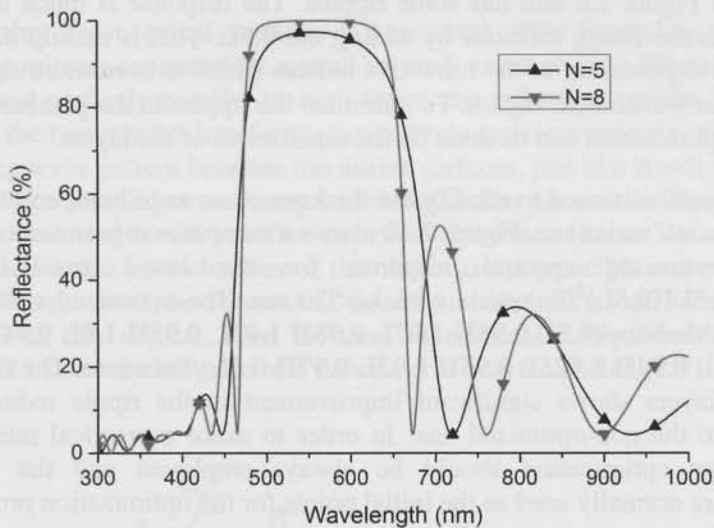

Figure 2.8. *Simulated spectral response of low-λ pass filter.*

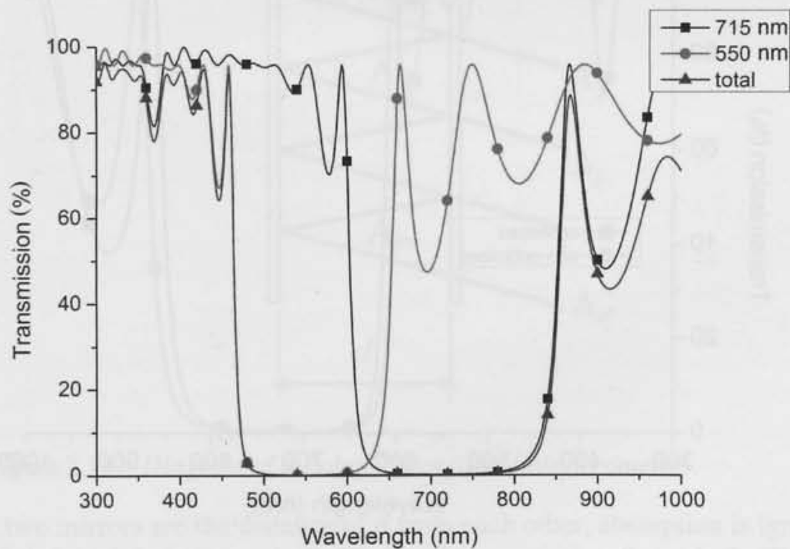

Figure 2.9. *Increasing the stopband by combining two filters*

In a filter design there is always room for a final optimization. The spectral response of Figure 2.8 still has some ripples. The response is much improved compared to the Bragg reflector by adding the **0.5L**. This is mainly due to the wavelength dependency of the refractive indices which is even more significant at the shorter wavelength region. To minimize the ripples in the passband region the filter, optimization can be done on the thicknesses of the layers.

Optimization is used to modify the thicknesses so as to compensate for the refractive index variations. Figure 2.10 shows a comparison between optimized and non-optimized spectral response for the low-λ pass filter of Medium/(**0.5LH0.5L**)^8/Substrate with λ_0=550 nm. The optimized structure for the filter is Medium/(**0.5L 0.98H 1.07L 0.98H 1.03L 0.93H 1.0L 0.94H 1.01L 0.93H 1.01L 0.94H 1.025L 0.95H 1.03L 0.97H 0.5L**)/Substrate. The filter with optimized layers shows significant improvement in the ripple reduction, as compared to the non-optimized one. In order to make a practical interference optical filter optimization should be always employed and the standard structures are normally used as the initial points for the optimization procedure.

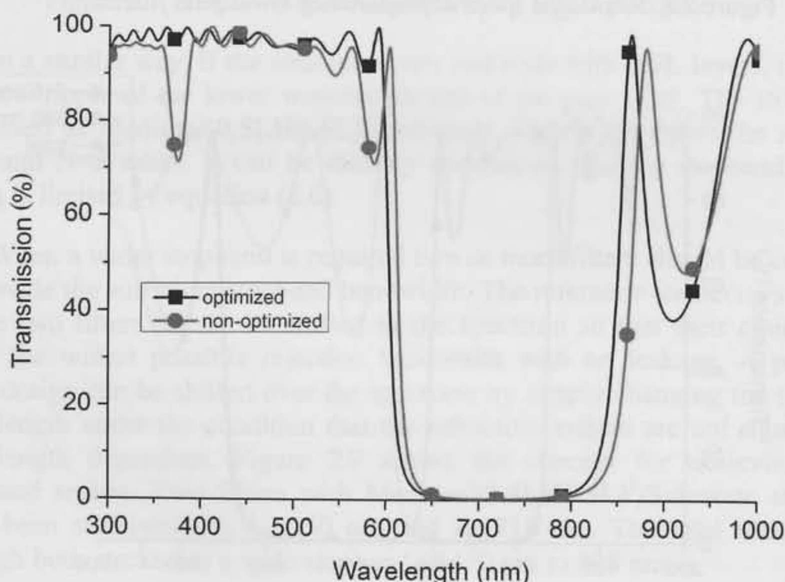

Figure 2.10. *Optimized low-λ pass filter compared with normal filter.*

2.3.3 Fabry-Perot filter

A Fabry-Perot optical resonator is a resonant cavity formed by two parallel reflecting mirrors separated by a medium such as air or gas. When the mirrors are aligned perfectly parallel to each other, the reflections of the light waves between the two mirrors interfere constructively and destructively, giving rise to a standing wave pattern between the mirror surfaces, just like standing waves on a string. For standing waves, any wavelengths that are not an integer multiple of half a wavelength will interfere destructively. Since Linear Variable Optical Filters used in the next chapters of this thesis are in principle a special version of the FP structures, the theoretical details and limitations of Fabry-Perot are presented in this section. First the case of an ideal Fabry-Perot is assumed. Figure 2.11 show the diagram of a Fabry-Perot interferometer, [2.8].

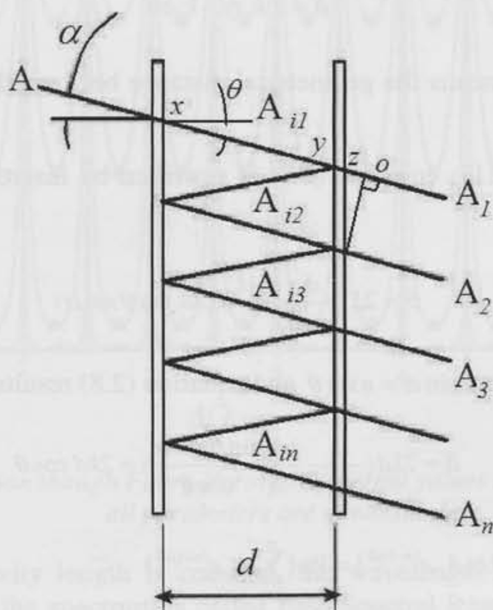

Figure 2.11. *Diagram of a Fabry-Perot filter (interferometer).*

The two mirrors are the distance of d from each other, absorption is ignored and reflectivity of the mirrors is R. The total transmission through the Fabry-Perot can be calculated by superposition of each transmitted trace of light wave.

For the amplitude of each reflected wave:

$A_{i1} = \sqrt{1-R}.A_0$

$A_{in} = A_{i(n-1)}.R \rightarrow A_{in} = \sqrt{1-R}.R^{n-1}.A_0$

Also,

$A_n = \sqrt{1-R}.A_{in} \rightarrow A_n = (1-R).R^{n-1}.A_0$

Considering the phase shift difference at each travel between the two reflective surfaces, the pathlength difference for adjacent rays is $2\overline{xy} - \overline{zo}$ therefore the phase difference for adjacent rays can be written as:

$$\delta = 2.k.\overline{xy} - k_0\overline{zo} \tag{2.7}$$

In which $\overline{AB}$ means the geometrical distance between the two points of A and B.

Using Figure 2.11, equation (2.7) is rewritten by inserting the expression for $\overline{xy}$, $\overline{zo}$ and k:

$$\delta = 2k.\frac{d}{\cos\theta} - (\frac{k}{n}).(2d\tan\theta\sin\alpha) \tag{2.8}$$

Snell's law gives: $\sin\alpha = n\sin\theta$ and equation (2.8) results:

$$\delta = 2kd(\frac{1}{\cos\theta} - \frac{1}{n}\frac{\sin\theta\sin\alpha}{\cos\theta}) = 2kd\cos\theta \tag{2.9}$$

$$E = \sum_{n=1}^{\infty} E_n = \sum_{n=1}^{\infty} \mathrm{Re}\{A_n.e^{(n-1)i\delta}\} = \mathrm{Re}\{\sum_{n=1}^{\infty} A_n.e^{(n-1)i\delta}\}$$

Intensity of the transmitted light is given by $I = E.E^*$, therefore:

$$I = I_0.\frac{(1-R)^2}{(1-R.e^{i\delta}).(1-R.e^{-i\delta})} = \frac{(1-R)^2}{(1-R)^2 + 4.R.\sin^2(\delta/2)} \tag{2.10}$$

Or

$$\frac{I}{I_0} = \frac{1}{1 + F\sin^2(2\pi d\cos\theta/\lambda)} \tag{2.11}$$

Where $F = \frac{4R}{(1-R)^2}$ is called coefficient of finesse. Coefficient of finesse is an optical parameter of the mirrors.

Figure 2.12 shows the transmission through Fabry-Perot interferometer for different values of mirror reflectivity R. The transmission is periodic with a periodicity of $d/\lambda = 0.5$.

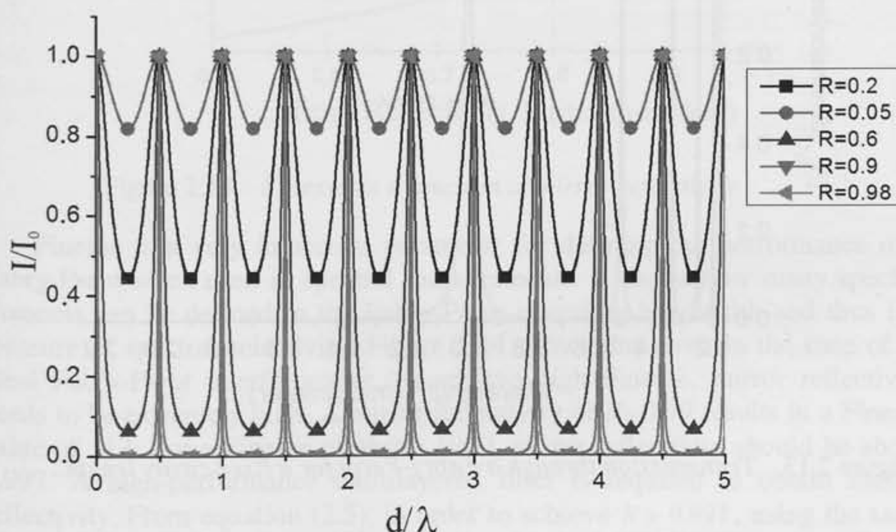

Figure 2.12. *Transmission though Fabry-Perot for different values of mirror reflectivity, all parameters are dimensionless.*

When the cavity length is constant, the wavelength range between two adjacent peaks in the spectrum is called Free Spectral Range (FSR). Thus, the FSR is dependent of the wavelength at which the Fabry-Perot is operating and can be calculated as, Figure 2.13:

$$\frac{2\pi d\cos\theta}{\lambda_1} - \frac{2\pi d\cos\theta}{\lambda_2} = \pi \rightarrow \frac{\lambda_2 - \lambda_1}{\lambda_2\lambda_1} = \frac{1}{2d\cos\theta}$$

And thus:

$$\text{FSR} = \frac{\lambda_2^{\,2}}{\lambda_2 + 2nd\cos\theta} \tag{2.12}$$

Figure 2.13 shows the FSR and FWHM for a Fabry-Perot with $d = 0.5\mu m$ and $n = 1$.

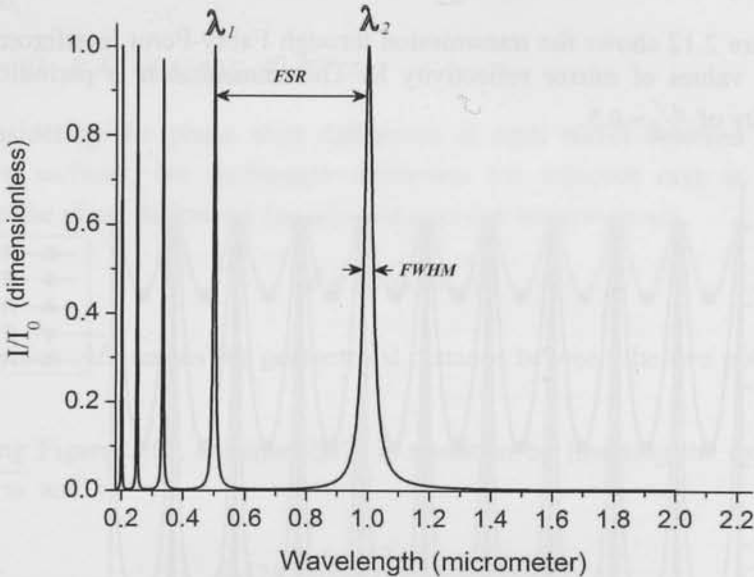

Figure 2.13. *Transmission through a Fabry-Perot for a fixed cavity length..*

From equation (2.11) it can be concluded that when $\delta = 2\arcsin(\frac{1}{\sqrt{F}})$ the transmission through the Fabry-Perot is at its half maximum value. Noting the fact that for each FSR, δ is changed for 2π, we can write:

$$f = \frac{\Delta\lambda}{\text{FWHM}} = \frac{\pi}{2\arcsin(\frac{1}{\sqrt{F}})} \tag{2.13}$$

This ratio is called the finesse of the Fabry-Perot. In contrary to coefficient of finesse used in (2.11), finesse of the FP is a structural quality factor of the filter. Figure 2.14 shows the plot of Finesse as a function of mirror reflectivity.

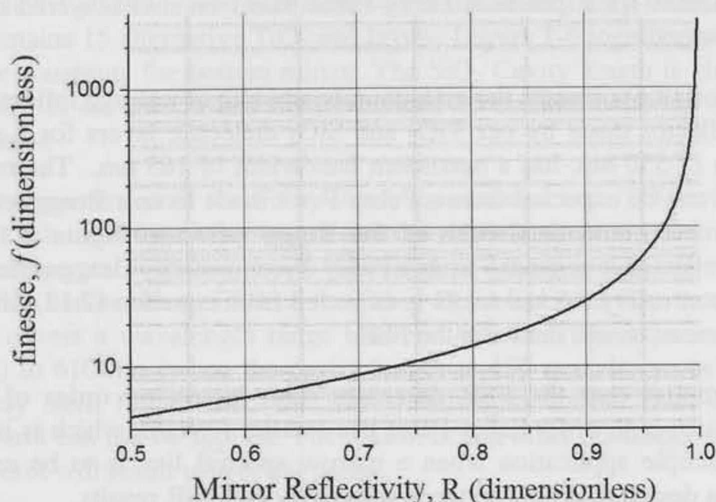

Figure 2.14. *Finesse as a function of mirror reflectivity.*

Finesse is a very important parameter for defining the performance of a Fabry-Perot when used in spectral measurements. It shows how many spectral channels can be defined in the Fabry-Perot operating bandwidth and thus is a measure of spectral selectivity. Figure 2.14 shows that even in the case of an ideal Fabry-Perot interferometer, to achieve high Finesse, mirror reflectivity needs to be extremely high. A mirror reflectivity of R=0.99 results in a Finesse value of 312. For a Finesse of above 1000, mirror reflectivity should be above 0.997. A high-performance multilayered filter is required to obtain such a reflectivity. From equation (2.5), in order to achieve $R \succ 0.997$, using the same optical data for TiO_2 and SiO_2 as in section 2.3, N need to be 8. This implies 16 dielectric layers for each reflective mirror and a total of 32 layers for the Fabry-Perot structure.

2.3.4 Practical issues for designing multilayered Fabry-Perot

As it was explained in the previous section for a Fabry-Perot to have high spectral resolution, highly reflective mirrors are required. Bragg reflector, section 2.3.1 , and metallic reflectors are two options. Realizing both of such mirrors however includes complications. Fabry-Perot based on metallic reflector are discussed in section 5.8 and in this section we will discuss

important issues for a practical Fabry-Perot based on multi-layered dielectric Bragg reflectors.

Equation (2.6) presents the maximum bandwidth of a Bragg reflector. Thus, a Bragg reflector made by our TiO_2 and SiO_2 dielectric layers for a reference wavelength of 550 nm, has a maximum bandwidth of 165 nm. The maximum FSR which can be expected from a Fabry-Perot made from a Bragg reflector is half of the maximum bandwidth of the Bragg reflector. Figure 2.15 shows simulated reflectance response from a Fabry-Perot made by Bragg reflectors for three different cavity thickness. As is expected from equation (2.12), increasing cavity thickness, *d*, will decrease the FSR.

This implies that the FSR decreases with increasing order of the FP. However, such high order Fabry-Perot has smaller FWHM, which is important for spectroscopic application when a narrow spectral line is to be measured. Therefore, a design trade-off between selectivity and FSR results.

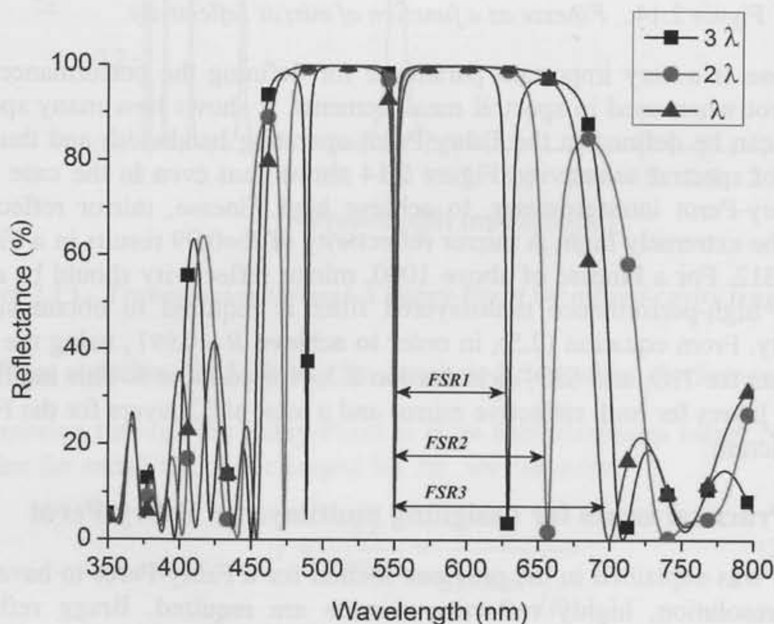

Figure 2.15. *Simulated Reflectance from a Fabry-Perot with dielectric mirrors for different cavity thicknesses.*

Table 2.1 shows layers thicknesses for a dielectric Fabry-Perot. The Fabry-Perot contains 15 alternative TiO_2 and layers. Layers 1-6 together with the glass substrate constitute the bottom mirror. The SiO_2 Cavity length is changed from 3.2 QWOT to 4.8 QWOT and finally layers 9-15 constitute the top mirror of the Fabry-Perot.

The transmission of the Fabry-Perot is simulated with TFCalc®, [2.9], for different values of the cavity length and the result is shown in Figure 2.16. The simulated spectral response shows a FWHM of 2.8 nm at 550 nm central peak. The usable bandwidth or FSB of the Fabry-Perot has been illustrated in Figure 2.16. It covers a wavelength range between 490 nm (when the cavity SiO_2 is 300 nm) to 610 nm (when the cavity length is 450 nm). It can be understood intuitively from Figure 2.16 that for wavelengths shorter than 490 nm the Fabry-Perot can not be applied. The reason is that other resonance orders of the Fabry-Perot will result in spectral peaks.

Table 2.1. *Layers thickness for a dielectric Fabry-Perot*

Layer #	Material	Thickness (QWOT)	Thickness (nm)
Substrate	Glass	-	-
1	TiO_2	1	57
2	SiO_2	1	94
3	TiO_2	1	57
4	SiO_2	1	94
5	TiO_2	1	57
6	SiO_2	1	94
7	TiO_2	1	57
8	SiO_2	3.2 - 4.8	300 - 450
9	TiO_2	1	57
10	SiO_2	1	94
11	TiO_2	1	57
12	SiO_2	1	94
13	TiO_2	1	57
14	SiO_2	1	94
15	TiO_2	1	57

It can be seen that for a cavity length of 450 nm there are two peaks in the spectral response, one at 610 nm wavelength and the other at 482 nm wavelength.

Therefore, for a Fabry-Perot interferometer it is important to limit the wavelength range of operation. This can be done using two edge filters. For this example, one high-λ pass filter at 485 nm and one short-λ pass filter at 615 nm

will remove the unwanted parts of the spectrum. Alternatively, one can state that the FP interferometer is only useful in relatively narrowband applications.

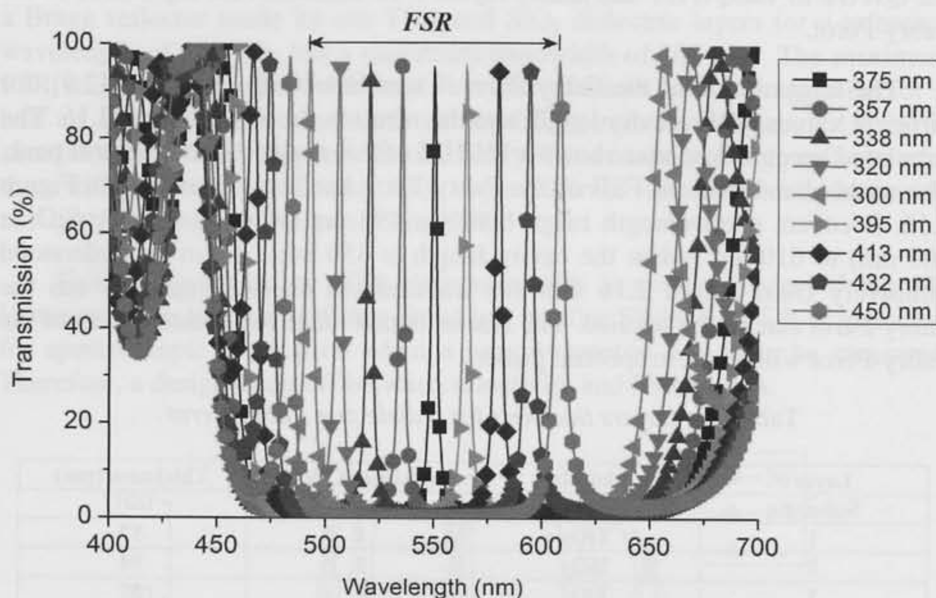

Figure 2.16. *Transmission spectral of a Fabry-Perot for different cavity length.*

The other important issue that should be taken into account when designing Fabry-Perot filters (or any other type of interference multilayered optical filter) is thickness control tolerance during fabrication. For sample or prototype fabrications using *in-situ* ellipsometry it is possible to control the thickness of a sputtered dielectric layer better than ±1 %. However, in full-scale production such specifications are often beyond reach.

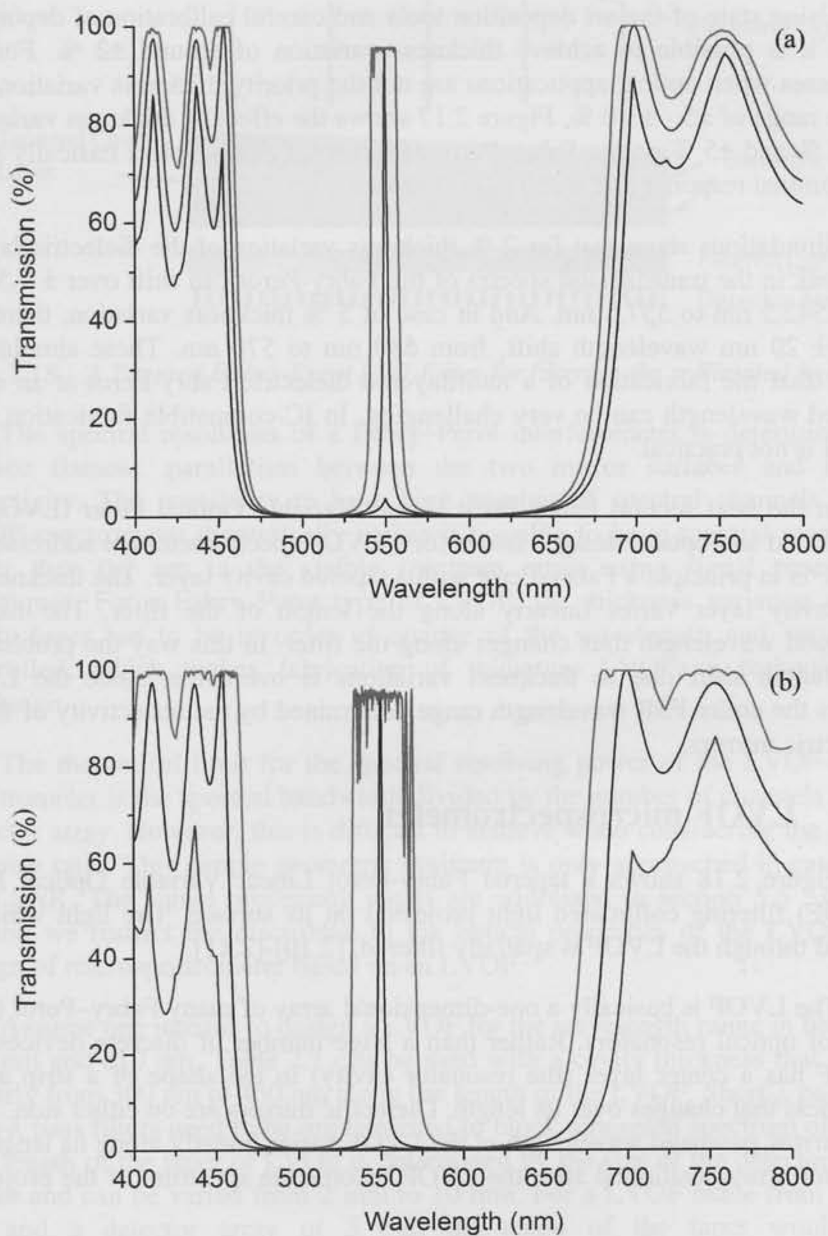

Figure 2.17. *The effect of a) ±2 % and b) ±5 % thickness tolerances.*

Using state-of-the-art deposition tools and careful calibration of deposition rates, it is possible to achieve thickness variation of around ±2 %. For IC-processes when optical applications are not the priority thickness variations are in the range of ±5 - ± 10 %. Figure 2.17 shows the effect of thickness variations of ±2 % and ±5 % on the Fabry-Perot of Table 2.1. These plots basically show the nominal response and worst case contours.

Simulations show that for 2 % thickness variation of the dielectric layers, the peak in the transmission spectra of the Fabry-Perot can shift over ± 7.5 nm, from 542.5 nm to 557.5 nm. And in case of 5 % thickness variation, there can be a ± 20 nm wavelength shift, from 530 nm to 570 nm. These simulations imply that the fabrication of a multilayered dielectric Fabry-Perot at an exact desired wavelength can be very challenging. In IC-compatible fabrication such a goal is not practical.

In the next section Fabry-Perot Linear Variable Optical Filter (LVOF) is introduced and optical designs issues for a LVOF spectrometer are addressed. A LVOF is in principle a Fabry-Perot with a tapered cavity layer. The thickness of the cavity layer varies linearly along the length of the filter. The narrow passband wavelength thus changes along the filter. In this way the problem of wavelength shift due to thickness variations is overcome, since the LVOF covers the entire FSR wavelength range determined by the reflectivity of the its dielectric mirrors.

2.4 LVOF microspectrometer

Figure 2.18 shows a tapered Fabry-Perot Linear Variable Optical Filter (LVOF) filtering collimated light projected on its surface. The light which is passed through the LVOF is spatially filtered, [2.10]-[2.11].

The LVOF is basically a one-dimensional array of many Fabry–Perot (FP)-type of optical resonators. Rather than a huge number of discrete devices, the LVOF has a center layer (the resonator cavity) in the shape of a strip and a thickness that changes over its length. Dielectric mirrors are on either side. Thus the narrow passband wavelength of the LVOF varies linearly along its length. A detector array positioned after the LVOF records the spectrum of the projected light.

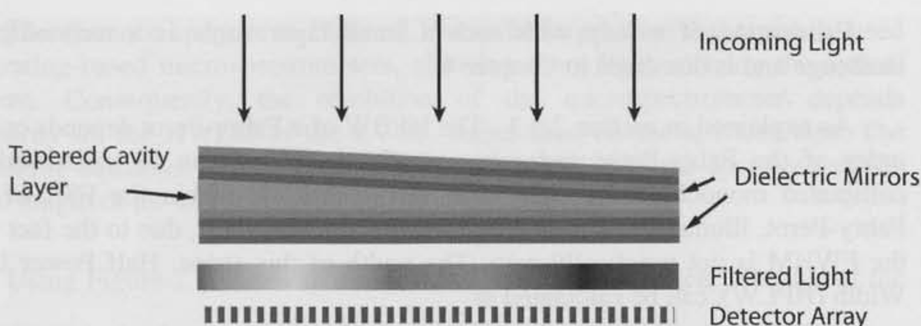

Figure 2.18. *A Tapered Fabry-Perot LVO Filter for filtering the collimated light.*

The spectral resolution of a Fabry–Perot interferometer is determined by surface flatness, parallelism between the two mirror surfaces and mirror reflectivity. The possibility to have high number of spectral channels in an LVOF spectrometer theoretically makes it possible to have spectral resolution better than 0.2 nm in the visible spectrum range using signal processing techniques. For a Fabry–Perot type of LVOF, the thickness variation of the cavity layer has to be in order of quarter of the wavelength and very well controlled, which makes fabrication of miniature LVOFs a technological challenge.

The theoretical limit for the spectral resolving power of the LVOF-based spectrometer is the spectral bandwidth divided by the number of channels in the detector array. However, this is difficult to achieve when considering the signal to noise ratio. This simple geometric optimum is only approached in case of a high SNR. The signal processing issues are addressed in section 5.5 . In this section we restrict the discussion to the optical properties of the LVOF and design of microspectrometer based on an LVOF.

Assume one intends to design a LVOF for the wavelength range in between 490 nm and 610 nm. Table 2.1 can be used with a cavity thickness that varies linearly from 300 nm to 450 nm along the length of the LVOF. Short-λ pass and high-λ pass filters need to be implemented to block unwanted spectrum of light. The length of the taper of LVOF is determined by the size of the detector array in use and can be varied from 2 mm to 10 mm. For a LVOF made from Table 2.1 and a detector array of 5 mm the angle of the taper would be: $\theta = \frac{150\text{nm}}{5\text{mm}} = 30\mu\text{rad} = 0.00172^\circ$.

Fabrication of a strip with such a small taper angle is a technological challenge and is discussed in Chapter 4.

As explained in section 2.3.3 , The HPBW of a Fabry-Perot depends on the order of the Fabry-Perot and mirrors reflectivity and can be calculated. A collimated monochromatic light with wavelength λ_0, within the FSR of the Fabry-Perot, illuminates a region on the detector beneath it, due to the fact that the FWHM is not practically zero. The width of this stripe, Half Power Line Width (HPLW), can be calculated as:

$$\Delta x = \frac{FWHM}{\theta} \quad (2.14)$$

Where θ denotes the slope of the tapered cavity layer of Fabry-Perot. When the LVOF made from Table 2.1 and the length of LVOF is 5 mm: $\Delta x = \frac{2.8mm}{30\mu rad} \approx 93\mu m$. Thus, a collimated monochromatic light illuminates a region after passing a LVOF and not just a single photodetector. In our example, if the detector array has a pixel pitch of 5 µm, consequently around 20 pixels are illuminated on the detector array.

The structure of an LVOF-based microspectrometer is shown in Figure 2.19. Light passes an aperture and collimating optics before being projected onto the LVOF, which is placed or deposited on the top of the detector.

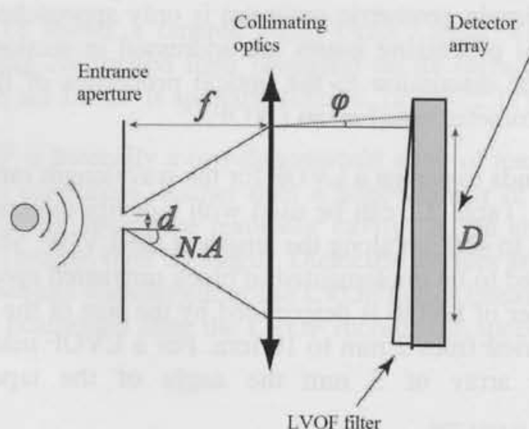

Figure 2.19. *Structure of a LVOF microspectrometer.*

The entrance aperture in Figure 2.19 can be larger than that typically used in grating-based microspectrometers, allowing more light entering the optical system. Consequently, the resolution of the microspectrometer depends primarily on the HWFM of the LVOF, rather than on the aperture size. The following equations can be used to determine the size of the aperture and the focal length of the collimating lens.

Using Figure 2.19 one can easily find: $f = \frac{D}{2\text{NA}}$, in which D is size of the LVOF, f is the focal length of the lens and NA is entrance numerical aperture. The Smith–Helmholtz invariant theorem, [2.12], results in $d \times \text{NA} = D \times \varphi$, which can be rewritten as:

$$d = \frac{D\varphi}{\text{NA}} \tag{2.15}$$

In which, d is the diameter of the aperture and φ is maximum acceptable angle of incidence on the LVOF. Since these equations depend on φ, transmission through the multilayered Fabry–Perot filter (which can be at any position along the length of the LVOF) is simulated at different angles. Figure 2.20 shows the result.

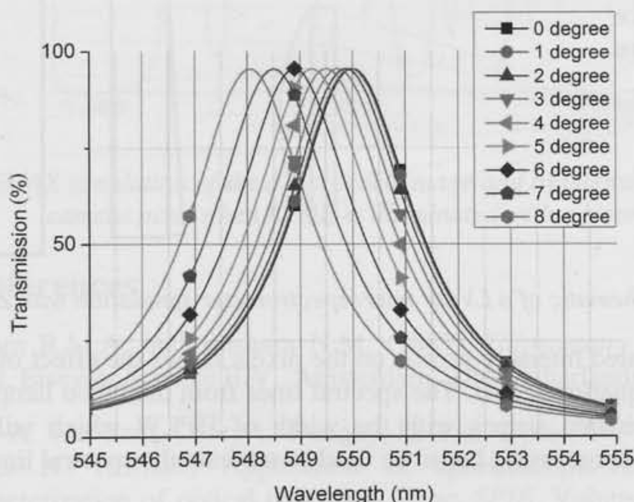

Figure 2.20. *Transmission through Fabry-Perot at different angles.*

It can be seen that at 4° angle of incident there is 0.5 nm wavelength shift in the spectral response. A 6° angle of incident this wavelength shift has increased to 1 nm. Based on these simulations φ can be selected. For spectral accuracy better than 2 nm, $\varphi = 6°$ is an acceptable choice.

In summary, to determine the parameters for a LVOF microspectrometer, first the size of the detector and thus the length of LVOF are selected. Subsequently, transmission through the Fabry-Perot is simulated at different angles to determine maximum acceptable divergence of the light on LVOF, φ. An acceptable value for NA is chosen and from equation (2.15), the size of aperture is determined. Finally, $f = \frac{D}{2\mathrm{NA}}$, results in the focal length of the lens.

Eventually, Optical ray tracing simulation can be carried out using ZEMAX® software to calculate the image on the camera when illuminated with different light sources, e.g. a Neon lamp. Figure 2.21 shows the schematics of simulation. Simulated recorded image on the camera and the corresponding intensity profile of the pixels when the LVOF of Table 2.1 is illuminated with a Neon lamp are shown in Figure 2.22.

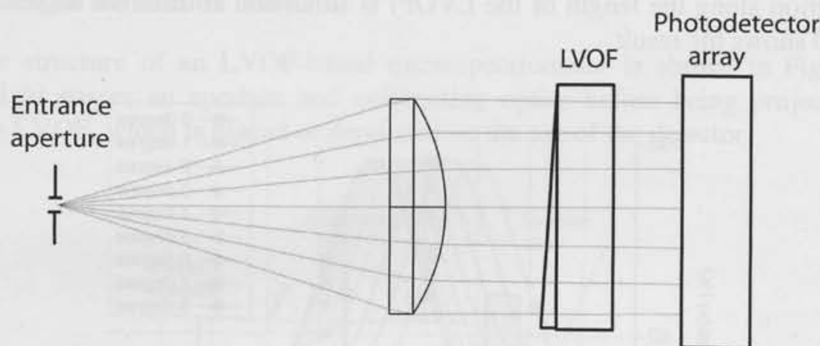

Figure 2.21. *Schematic of a LVOF microspectrometer simulation with ZEMAX.*

The simulated intensity profile on the pixels shows the effect of the HPLW expressed in equation (2.14). The spectral lines from the Neon lamp widen and result in illuminated stripes with the width of HPLW which will be added together. Signal processing has to be used to separate the spectral lines.

The concept and implementation of a signal processing algorithm to extract the spectrum from recoded image on the camera will be discussed in the chapter 5.

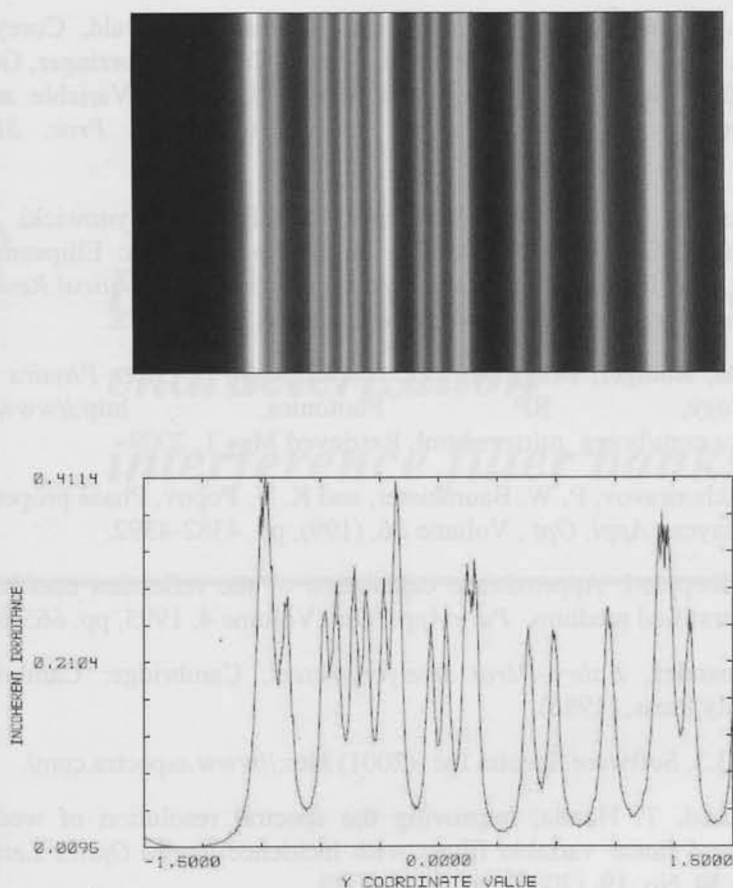

Figure 2.22. *ZEMAX simulation of the a) recorded image and b) intensity profile of the camera pixel when LVOF is illuminated with a Neon lamp.*

2.5 References

[2.1] Azzam R.M.A. and Bashara N.M. (1987). *Ellipsometry and Polarized Light*, Elsevier Science B.V., Amsterdam, The Netherlands.

[2.2] John A. Woollam, Corey L. Bungay, Li Yan, Daniel W. Thompson, and James N. Hilfiker, Application of spectroscopic ellipsometry to characterization of optical thin films, *Proc. SPIE,* Volume **4932**, (2003), pp. 393-404.

[2.3] John A. Woollam, James N. Hilfiker, Thomas E. Tiwald, Corey L. Bungay, Ron A. Synowicki, Duane E. Meyer, Craig M. Herzinger, Galen L. Pfeiffer, Gerald T. Cooney, and Steven E. Green, Variable angle spectroscopic ellipsometry in the vacuum ultraviolet, *Proc. SPIE,* Volume **4099**, (2000), pp. 197-205.

[2.4] J.A.Woollam, B.Johs, C.M.Herzinger, J.Hilfiker, R.Synowicki and C.L.Bungay, Overview of Variable Angle Spectroscopic Ellipsometer (VASE), Part I: Basic Theory and Typical Applications, *Critical Reviews of Optical Science and Technology*, Volume **CR72**, pp. 1-28.

[2.5] Paschotta, Rüdiger, Bragg Mirrors, *Encyclopedia of Laser Physics and Technology*, RP Photonics, http://www.rp-photonics.com/bragg_mirrors.html, Retrieved May 1, 2009.

[2.6] A. V. Tikhonravov, P. W. Baumeister, and K. V. Popov, Phase properties of multilayers, *Appl. Opt.*, Volume **36**, (199), pp. 4382-4392.

[2.7] C J R Sheppard, Approximate calculation of the reflection coefficient from a stratified medium, *Pure Appl. Opt.,*Volume **4**, 1995, pp. 665-669.

[2.8] G. Hernandez, *Fabry–Pérot Interferometers*, Cambridge: Cambridge University Press, (1986).

[2.9] TFCalc 3.3, Software Spectra Inc. (2001) http://www.sspectra.com/.

[2.10] R. McLeod, T. Honda, Improving the spectral resolution of wedged etalons and linear variable filters with incidence angle, *Optics Letters*, Volume **30**, No. 19, (2005), pp. 2647-2649.

[2.11] S.F. Pellicori, *US Patent* 4957371, Wedge-filter spectrometer.

[2.12] M. Born, E. Wolf, Principles of Optics: Electromagnetic Theory of Propagation, Interference and Diffraction of Light, 7th ed., (1999), pp. 176–178.

3 *Fabrication and characterization of interference filter banks*

3.1 Introduction

In this chapter fabrication procedure and characterization of dielectric interference filter banks for UV to infra-red (300 nm – 5 μm) are described. The characterization data are compared with simulated responses of the filters and differences are discussed. This is a good starting point toward the fabrication of Linear Variable Optical Filters which are based on them. Moreover, filter banks can potentially be applied in various absorbance measurement spectroscopy techniques like NDIR (non-Dispersive Infra-red absorbance) system.

3.2 Interference filters for Infra-red

3.2.1 Materials characterization

Since the filter is intended for use in an integrated system, it is important that the materials used are IC-compatible. For this filters we have used Poly-Silicon as the high-***n*** and SiO_2 as a low-***n*** material. Silicon has an extinction coefficient (k) smaller than 10^{-3} at wavelengths beyond 1.2 μm and further reduced to below 10^{-5} at 1.5 μm. SiO_2, however, is transparent in the visible range and its extinction coefficient increases sharply beyond 3 μm wavelengths, as shown in Figure 3.1.

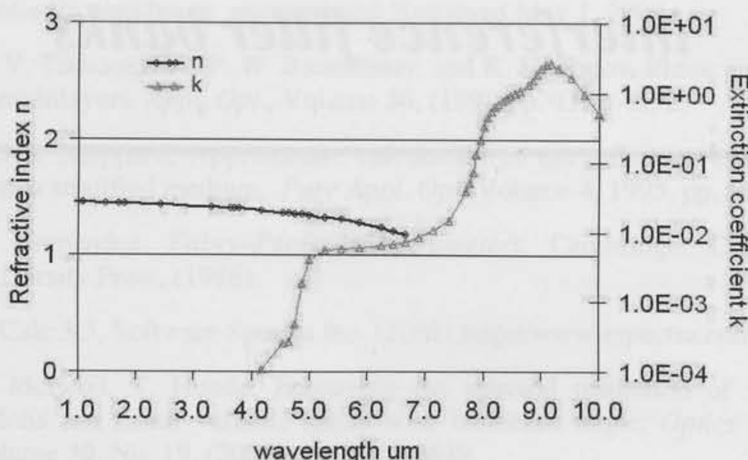

Figure 3.1. *Refractive index and extinction coefficient of SiO_2 in the infra-red.*

Absorption is proportional to ***k*** and SiO_2 is not usually considered to be a good material in IR applications. However, we will show here that, because of the small thickness of layers in IR interference filters, it can still be used with acceptable loss of transmission at resonance. According to Lambert's law of absorption:

$$P(x) = P_0 \exp(-\alpha x) \qquad (3.1)$$

Where α denotes the absorption coefficient, is expressed in terms of extinction coefficient as:

$$\alpha = \frac{4\pi k}{\lambda} \quad (3.2)$$

Assuming the central wavelength at 3 µm and total thickness of all SiO_2 layers to be 500 nm, and assuming that we accept a loss in transmission of 20% it can be found that:

$$\exp\left(-\frac{-4\pi k}{3000} \times 500\right) > 0.8 \rightarrow k < 0.1 \quad (3.3)$$

Therefore, from Figure 3.1 it can be concluded that the use of SiO_2 in optical filters up to 8 µm is acceptable when considering the total thickness of the SiO_2 layers and tolerable loss.

Ellipsometry has been used to characterize sputtered Silicon. Two tests have been carried out for the characterization of sputtered Silicon. In the first one, Silicon is sputtered for 3 minutes on a wafer with 400 nm thermal oxide. In the second test, Silicon is sputtered on a bare Silicon substrate for 394 sec. The assumed deposition rate of 0.71 nm/sec results in an assumed thickness of 282 nm. It is important that the test depositions thickness be in the same range of thickness required for the interference filter as the deposition rate could be slightly nonlinear. Figure 3.2 shows the experimental (measured) and generated (modeled) Ψ and Δ values in the first test. The model in WVase® software used for the fitting is shown in Table 3.1 and the parameters of the model optimized are shown in Table 3.2. Apart from the thickness values, other parameters are dimensionless.

Table 3.1.*Model used for sputtered Silicon characterization in test 1*

3 srough	0.669 nm
2 fhe_a-si_p	128.169 nm
1 SiO_2	413.834 nm
0 si_jaw	1 mm

Table 3.2.*Parameters fitted in the ellipsometry for test 1*

MSE=8.098			Thick.1	413.834±0.143	nm
Thick.2	128.169±0.121	nm	Thick.3	0.669±0.0304	nm
Disc1.2	0.677±0.0304		En1.2	2.947±0.0121	
Br1.2	751.3±6.99		Am1.2	29.549±0.368	

A small value for Mean Square Error (MSE) in the ellipsometry analysis means the model is a good approximation of the actual situation and that the resulting thickness values and optical properties are reliable.

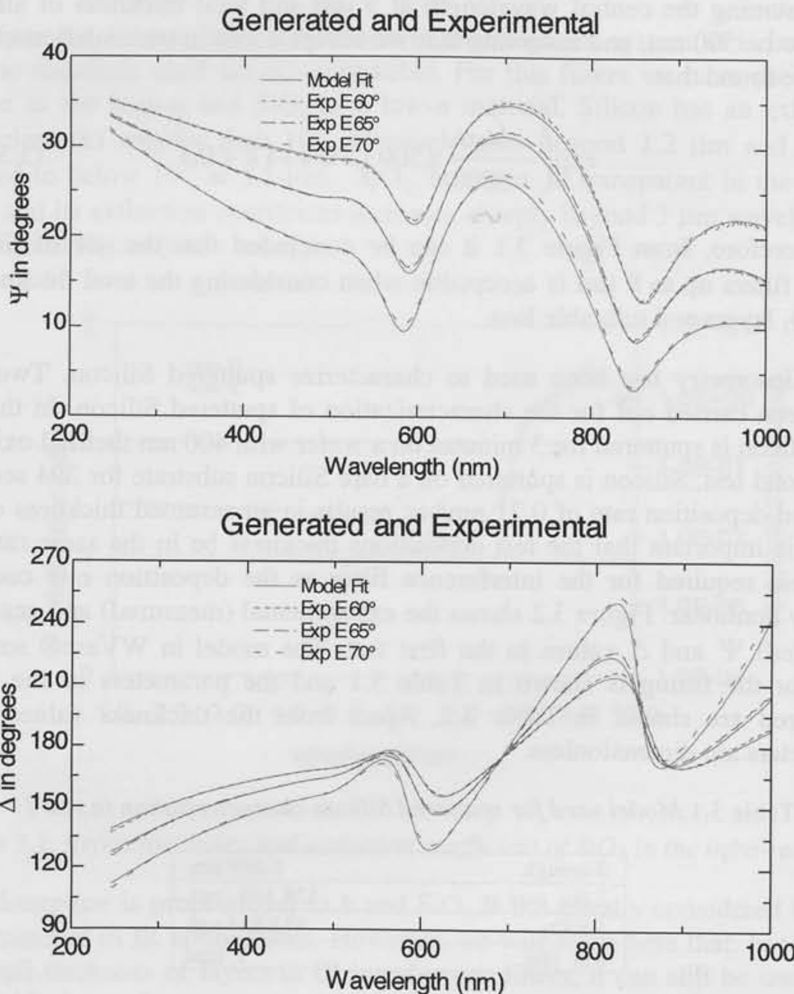

Figure 3.2. *Generated and measured* Ψ *and* Δ *values of a stack composed of 128 nm sputtered Si deposited on 400 nm* SiO_2 *on a Si substrate.*

From the ellipsometry result, deposition rate is calculated to be 0.71 nm/sec and optical properties of sputtered Silicon are plotted in Figure 3.3.

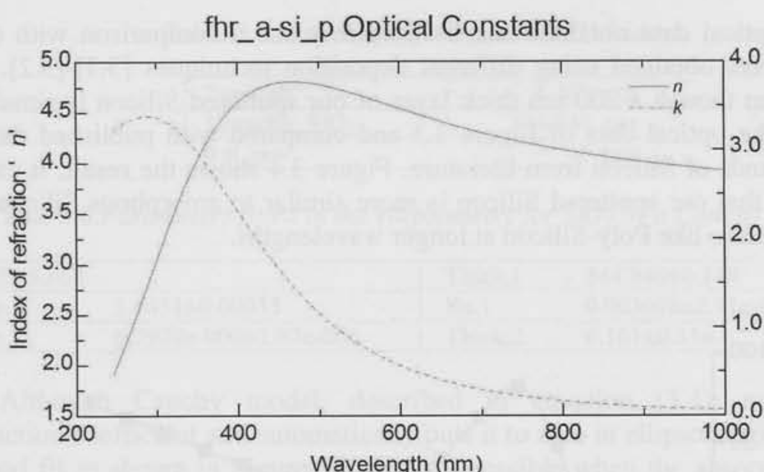

Figure 3.3. *Optical properties of sputtered Si measured by ellipsometry.*

The WVase® model and ellipsometric parameters for the second deposition test are also shown in Table 3.3 and Table 3.4. Apart from thickness values, other parameters are dimensionless. The second test also results in the same deposition rate, 0.71nm/sec, as in test 1, while optical properties are identical. The necessity of doing two separate tests originates from two facts. First, there are two different thicknesses in the desired interference filter for the Silicon layer. Secondly, it was not certain in the start of the experiment if the result would have a small MSE for a sputtered Silicon layer on bare Silicon, as the two materials have close optical properties.

Table 3.3.*Model used for sputtered Silicon characterization of test 2*

3 SiO_2	2.702 nm
2 fhe_a-si_p	307.714 nm
1 SiO_2	5.894 nm
0 si_jaw	1 mm

Table 3.4.*Parameters fitted in the ellipsometry for test 2*

MSE=2.89			Thick.1	5.894±0.0762	nm
Thick.2	307.714±0.32	nm	Thick.3	2.702±0.0277	nm
En1.2	3.3533±0.00956		Br1.2	724.66±2.54	
Am1.2	36.256±0.207		Disc1.2	0.21516±0.0135	

The optical data obtained can be used to make a comparison with other Silicon layers obtained using different deposition techniques [3.1]-[3.2]. The transmission though a 200 nm thick layer of our sputtered Silicon is simulated based on the optical data of Figure 3.3 and compared with published data of different kinds of Silicon from literature. Figure 3.4 shows the result. It can be concluded that our sputtered Silicon is more similar to amorphous Silicon and tend to be more like Poly-Silicon at longer wavelengths.

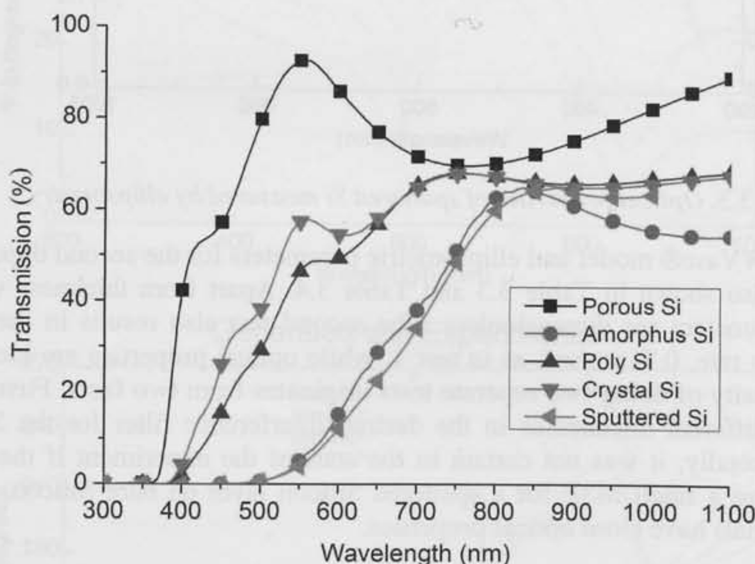

Figure 3.4. *Transmission through a 200 nm layer of our sputtered Silicon as compared to data on other Silicon types.*

Also, the optical properties of our sputtered SiO_2 should be compared with oxides obtained using different techniques. To check the deposition test and ellipsometric modeling has been done for the available SiO_2 thin film. SiO_2 has been modeled by a Cauchy model in the ellipsometry software. The good Ψ and Δ fitting (very small MSE) proves that the k value (extinction coefficient) of the film is negligible in the spectral range of ellipsometry. The deposition rate has been calculated as 0.23 nm/sec or 14 nm/min. Table 3.5 and Table 3.6 show the WVase® model used and parameters optimized in the model. Apart from thickness values, other parameters are dimensionless.

Table 3.5. *Model used for sputtered Dioxide*

2 srough	6.161 nm
1 cauchy_SiO_2	344.840 nm
0 si_jaw	1 mm

Table 3.6. *Parameters fitted in the ellipsometry for SiO_2 by a Cauchy model*

MSE=3.664		Thick.1	344.840±0.149	nm
An.1	1.4451±0.00035	Bn.1	0.003698±2.91e-005	
Cn.1	6.7979e-006±1.67e-006	Thick.2	6.161±0.116	nm

Although Cauchy model, described in equation (3.4), neglects the extinction coefficient and automatically puts it to zero in ellipsometric modeling, a good fit as shown in Figure 3.5, is only possible when the absorption in the film is indeed negligible. As can be noted from Table 3.5, three terms of the expression (An.1, Bn.1 and Cn.1) have been used. The roughness on the sputtered SiO_2 has also been modeled by ellipsometry and is measured to be 6.2 nm.

$$n(\lambda) = A + \frac{B}{\lambda^2} + \frac{C}{\lambda^4} + ... \qquad (3.4)$$

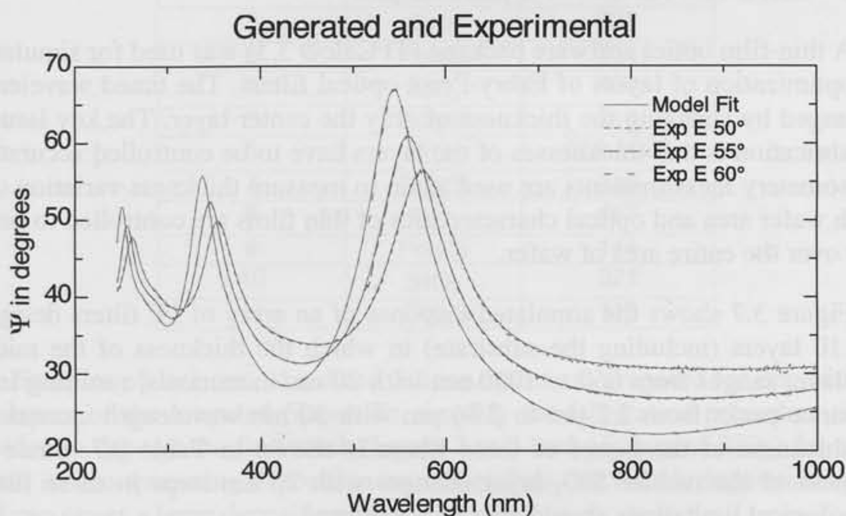

Figure 3.5. *Generated and measured Ψ and Δ values of 344 nm sputtered SiO_2 on a Si substrate.*

Refractive index of the sputtered SiO2 is shown in Figure 3.6, based on the Cauchy model. Extinction coefficient is calculated to be zero in the entire wavelength range.

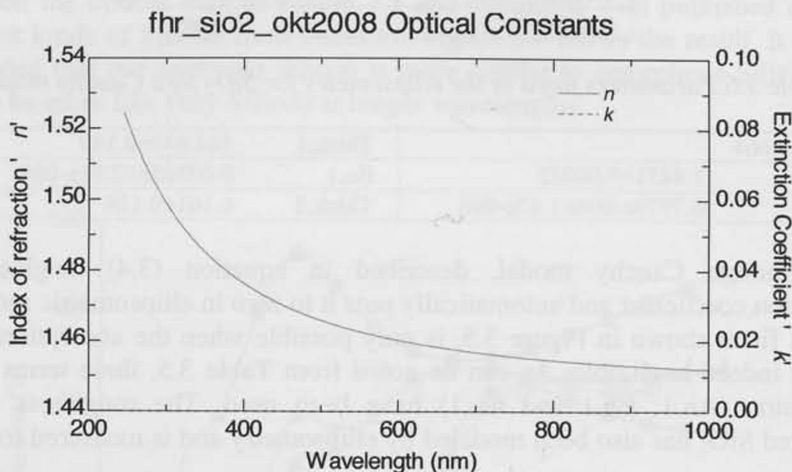

Figure 3.6. *Refractive index (n) of sputtered* SiO_2 *measured by ellipsometry.*

3.2.2 Infra-red filters for 2 μm to 3 μm

A thin-film optics software package (TFCalc® 3.3) was used for simulation and optimization of layers of Fabry-Perot optical filters. The tuned wavelength is changed by changing the thickness of only the center layer. The key issue in the fabrication is that thicknesses of the layers have to be controlled accurately. Ellipsometery measurements are used again to measure thickness variation over 6 inch wafer area and optical characteristics of thin films are controlled to be the same over the entire area of wafer.

Figure 3.7 shows the simulated response of an array of FP filters designed with 10 layers (including the substrate) in which the thickness of the middle SiO_2 layer ranges from 660 to 1020 nm with 20 nm increments, resulting in 20 resonance peaks from 2.2 μm to 2.86 μm with 30 nm wavelength increments. The thickness of the layers of these filters is shown in Table 3.7. Since the thickness of the middle SiO_2 layer changes with 20 nm steps in these filters, technological limitations should also be considered.

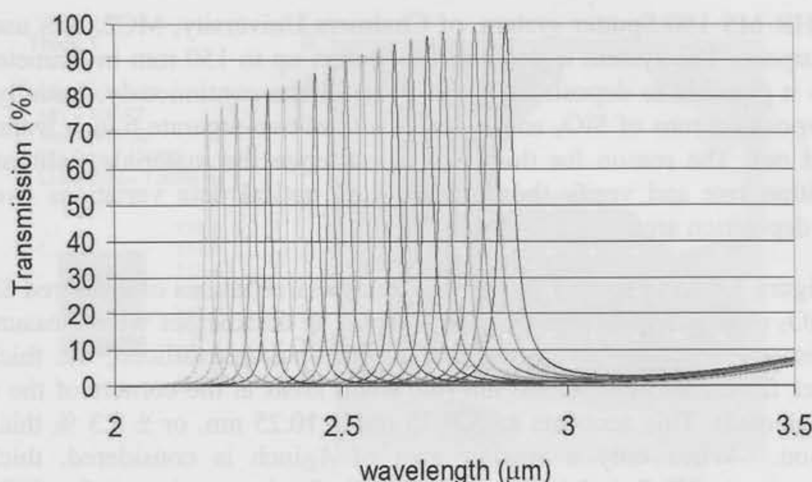

Figure 3.7. *Simulated spectral response of the 20 channel FP filters.*

Table 3.7.*Designed values of thicknesses for the FP filters*

Layer number	Material	Thickness (nm)
1	Si(Substrate)	-
2	SiO_2	321
3	PolySi	144
4	SiO_2	463
5	PolySi	216
6	SiO_2	660-1020
7	PolySi	216
8	SiO_2	463
9	PolySi	144
10	SiO_2	321
11	PolySi	116

Samples of 1×1 cm^2 of a diced Silicon wafer are prepared for deposition of the layers of the intended filters. To simplify the fabrication procedure, it was decided to deposit the first stack (layers 2 to 5 and 660 nm of SiO_2) for all the layers in one sputtering deposition run. Therefore, we need a deposition system that can cover a large deposition area.

FHR MS 150 Sputter system, of Chalmers University, MC2, was used for this purpose. The system is dedicated to wafers up to 150 mm in diameter and makes it possible to deposit SiO_2 and Poly-Silicon continuously. Initially, two test deposition runs of SiO_2 and Poly-Silicon on two separate 6 inch wafers are carried out. The reason for this is to characterize the materials, calibrate the deposition rate and verify the thickness and optical data variations over the entire deposition area.

Figure 3.8 and Figure 3.9 show the thickness variations of sputtered Silicon and SiO_2 over 149 points on a 6 inch wafer. The thicknesses were measured by ellipsometry at 69 points on the wafer. For sputtered Silicon, the thickness changes from 299.5 nm to 320 nm (the small areas at the corners of the wafer are neglected). This accounts to 309.75 nm ± 10.25 nm, or ± 3.3 % thickness variation. When only a smaller area of 4 inch is considered, thickness variations are 309.7 ± 5.1 nm or ± 1.6 %. In the same way for SiO_2, the thickness variation over a 6 inch wafer area is 113.05 ± 2.55 nm or ± 2.2 % thickness variation. When only the smaller 4 inch inner area is considered, it would result in 112.5 nm to 115.6 nm thickness values or 114.05 nm ± 1.55 nm which implies a ± 1.36 % thickness variation.

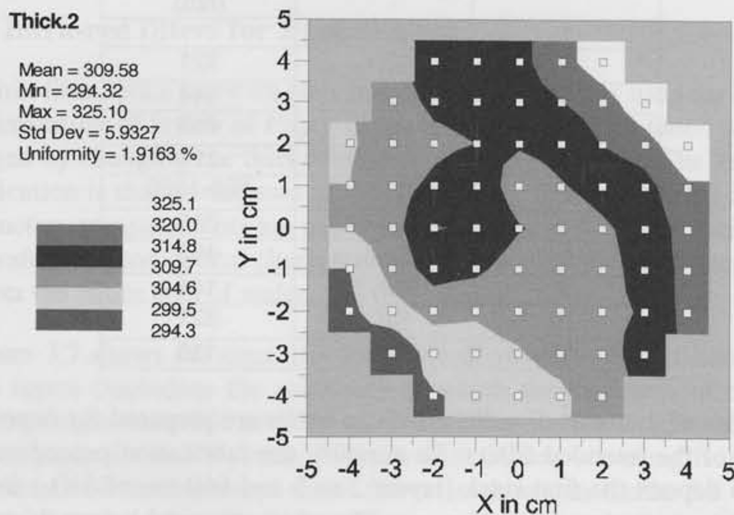

Figure 3.8. *Thickness variation of Sputtered Silicon over a 6" wafer, all values in nm.*

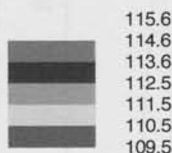

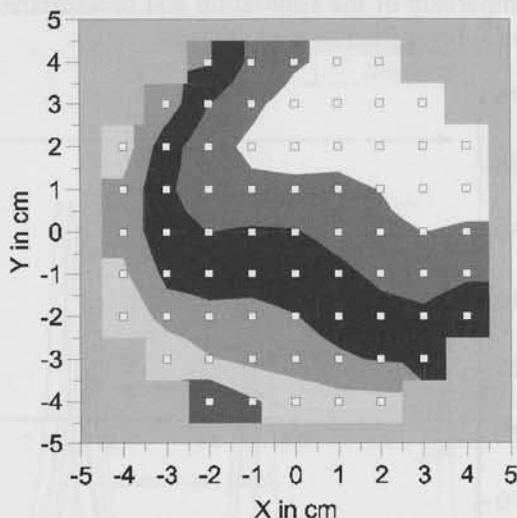

Figure 3.9. *Thickness variation of Sputtered SiO_2 over a 6" wafer, all values in nm.*

Considering thickness profiles of both materials over the wafer, a sample holder was created for the sputtering machine which allows keeping the 1×1 cm^2 sized samples on a circle with radius of 3.5 cm. Over the area between circles of radius 3.5 cm and 4.cm from the center of wafer the thickness variation for SiO_2 is around 1.5 % and for sputtered Silicon is 2.8%. In the first deposition run layers 2 to 5 and 660 nm of SiO_2 are deposited on all the samples. Afterwards, middle SiO_2 is deposited individually on samples. Layers 7 to 11 are also deposited on all the samples in one deposition run at the end.

Filters are measured with a Fourier Transform Spectrometer which provides a 2 nm spectral resolution. Figure 3.10 shows the measured response of the filters. One filter with peak at the shorter wavelength part of the band, three filters in the middle and five filters with peaks at the end of the band of interest are chosen and shown.

Comparison between measured and designed response of filters show some wavelength shift in the peaks and also a change in the throughput of the filters. The simulated filters in Figure 3.7 have a throughput between 75 and 100 percent while measured filters show 45 to 62 percent throughput. The wavelength shift in the filters originates most probably from the fact that the thicknesses of the layers slightly differ from the designed values. Figure 3.11

shows comparison of the simulation and measurement of one of the filters with a center SiO_2 layer thickness of 850 nm.

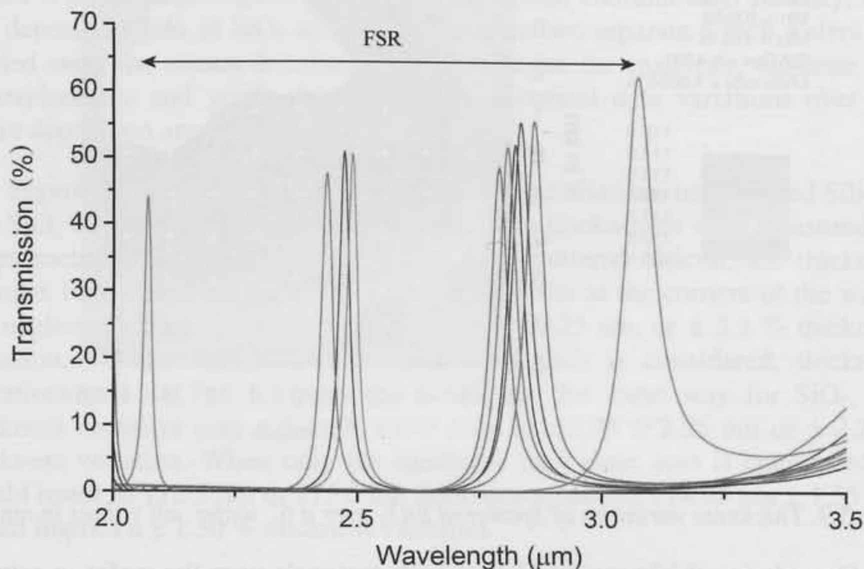

Figure 3.10. *Measurement spectral response of FP filters with FTS.*

The fabricated filter in Figure 3.11 has a HPBW of 35 nm and the peak wavelength is shifted around 100 nm away from its designed target of 2.7 μm. There is also about 10 % difference in the throughput of the fabricated and designed filter. To find the reason for these differences in the performance of the filter from its designed target, ellipsometry measurements are done on the multi-layered filters.

Ellipsometry measurements were done at three stages on the samples; after deposition of the first stack of layers, after depositing the middle SiO_2 layer and after deposition of the final layers. Ellipsometric data analysis software of WVASE32 is used to find actual thicknesses of the layers. Data analysis is also carried out in three stages according to three sets of ellipsometric data. The purpose of the ellipsometric data analysis is to find a multilayered model in which by changing the parameters (in this case layers thicknesses) calculated Ψ and Δ values of the model would make a better fit to the measured Ψ and Δ values of the sample.

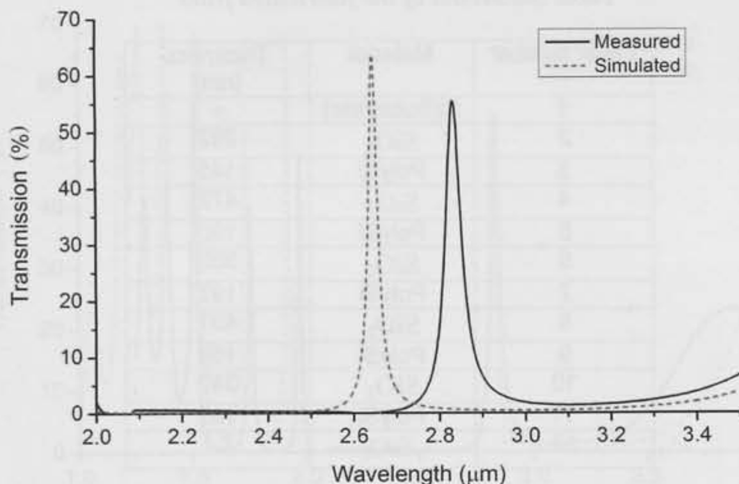

Figure 3.11. *Comparison of the designed and the fabricated filters.*

A mean square error optimization procedure is used by the software to minimize the error between measured and calculated Ψ and Δ values by changing the layers thicknesses. Figure 3.12 shows the fitting of Ψ values of one of the filters and Table 3.8 shows its corresponding model.

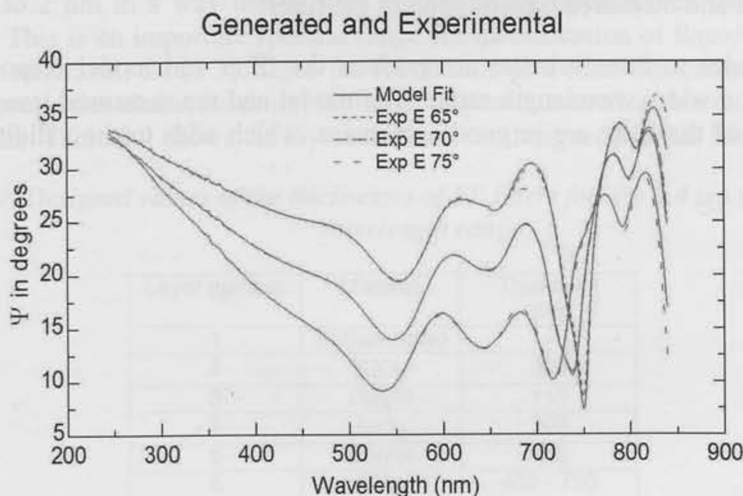

Figure 3.12. *Fitting of* Ψ *values of the filter model with measured values with WVase32.*

Table 3.8.*Model of the fabricated filter*

Layer number	Material	Thickness (nm)
1	Si(Substrate)	-
2	SiO_2	292
3	PolySi	145
4	SiO_2	472
5	PolySi	190
6	SiO_2	985
7	PolySi	197
8	SiO_2	491
9	PolySi	159
10	SiO_2	343
11	PolySi	130
12	SiO_2	7.1

It can be seen from the values extracted by the model in Table 3.8 that the maximum deviation from target thickness is in the middle SiO_2 layer. The error is about 14 % for this layer and is the major reason for 100 nm shift of the filter as was observed in Figure 3.11. For Silicon layers the error is about 3 %.

The model parameters extracted by ellipsometry in Table 3.8 is fed into TFCalc 3.3 to simulate the transmission. Figure 3.13 compares the response of the model and measured transmission of the filter.

In order to have a better comparison the filter and model responses are shown in a wider wavelength range. The model and the measured transmission response of the filter are in good agreement, which adds to the validity of the model.

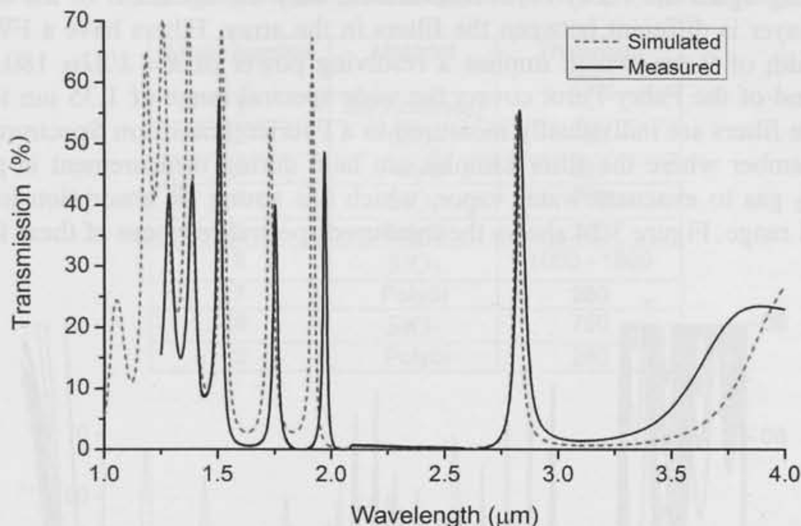

Figure 3.13. *Comparison of the simulated model and the fabricated filter.*

3.2.3 Infra-red filters for 1.4 μm to 2.0 μm

Filter array has been design, fabricated and measured for spectral range of 1.4 μm to 2 μm in a way that is very similar to the approach in the previous section. This is an important spectral range for identification of liquids, such as alcohol, water, oil, etc [3.3]. Since the fabrication procedure for calibration and optical properties characterization is similar to previous section, we only present the results. Table 3.9 shows the layers thicknesses designed for this filter array.

Table 3.9. *Designed values of the thicknesses of FP filters for the 1.4 μm to 2.0 μm wavelength range*

Layer number	Material	Thickness (nm)
1	Si(Substrate)	-
2	SiO_2	300
3	PolySi	115
4	SiO_2	300
5	PolySi	115
6	SiO_2	450 - 750
7	PolySi	115
8	SiO_2	300
9	PolySi	115

Using again the Fabry-Perot mechanism, only the thickness of the center cavity layer is different between the filters in the array. Filters have a FWHM bandwidth of 9 nm, which implies a resolving power of $R= \lambda/\Delta\lambda= 180$. The stop-band of the Fabry-Perot covers the wide spectral range of 1.35 μm to 2.5 μm. The filters are individually measured in a Fourier Transform Spectrometer. The chamber where the filter samples are held during measurement is purge with N_2 gas to evacuate water vapor, which has strong IR absorption in that spectral range. Figure 3.14 shows the measured spectral response of these filters.

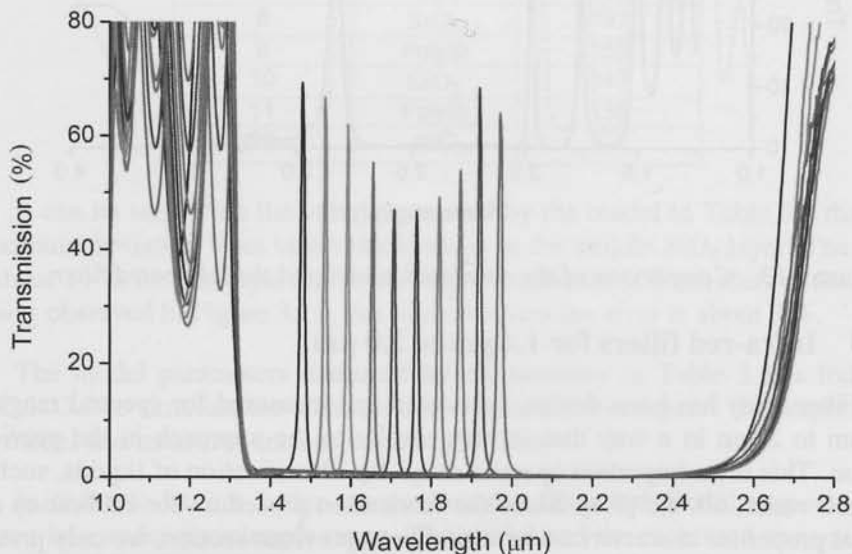

Figure 3.14. *Measured spectral response of a 10 channel Fabry-Perot array.*

3.2.4 Infra-red filters for 3 μm to 4.5 μm

The final IR Fabry-Perot filter bank that has been designed and fabricated is for operation in the spectral range of 3 μm to 4.5 μm. This spectral range has application for sensing and detection of gases, like CO, CO_2, NO_2, etc [3.4]. Table 3.10 shows designed and fabricated layers thickness for this Fabry-Perot filter array. Measured spectral response of the filter array is shown in Figure 3.15.

Table 3.10. *Designed thickness values for FP filters of 3.0 μm to 4.5 μm*

Layer number	Material	Thickness (nm)
1	Si(Substrate)	-
2	SiO_2	760
3	PolySi	281
4	SiO_2	760
5	PolySi	280
6	SiO_2	1000 - 1800
7	PolySi	280
8	SiO_2	760
9	PolySi	280

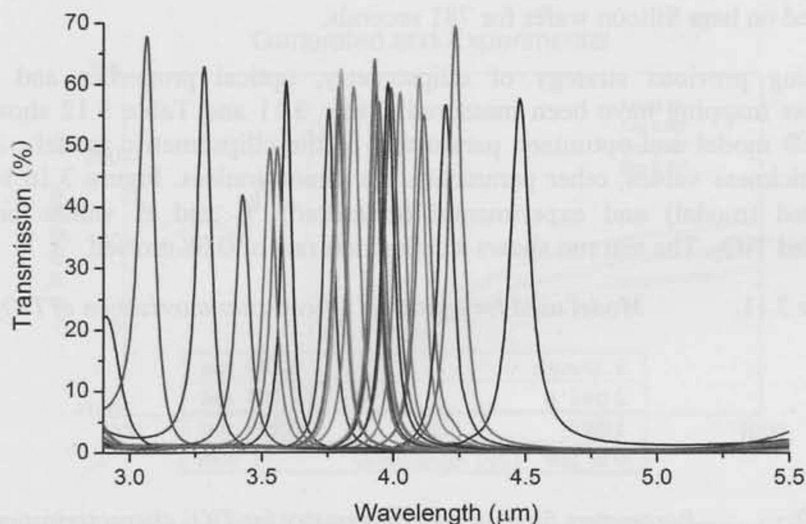

Figure 3.15. *Measured spectral response of the Fabry-Perot array for operation in the 3-5.5 μm spectral range.*

Filters have FWHM bandwidth of 50 - 60 nm, which implies a resolving power $R= \lambda/\Delta\lambda \approx 70 - 80$. The stop-band of the Fabry-Perot covers the wide spectral range of 3.0 μm to 5.5 μm.

3.3 Interference filters for visible spectral range

A set of Fabry-Perot filters has also been realized for visible spectral range of 600 nm – 700 nm. The importance of making filter array for this spectral range was that the Linear Variable Optical Filters intended for visible spectroscopy of plant fluorescence and H-α spectroscopy are in the same spectral range. Fabrication of the filter array in the same range proves the operation principle of the later LVOF filters. The dielectric materials used for these filter are TiO_2 and SiO_2.

Initially, deposition rate and optical properties of available TiO_2 has to be characterized. Fabrication of these filters has also been carried out in a MS 150 FHR sputter machine. Using this sputtering tool TiO_2 has been reactively DC-sputtered on bare Silicon wafer for 781 seconds.

Using previous strategy of ellipsometry, optical properties and TiO_2 thickness mapping have been measured. Table 3.11 and Table 3.12 show the WVase® model and optimized parameters of the ellipsometric model. Apart from thickness values, other parameters are dimensionless. Figure 3.16 shows generated (model) and experimental (measured) Ψ and Δ values on the deposited TiO_2. The test run shows a deposition rate of 0.08 nm/sec.

Table 3.11. *Model used for sputtered Silicon characterization of TiO_2*

Layer	Thickness
3 srough	6.589 nm
2 tio2_p	62.104 nm
1 SiO_2	0.000 nm
0 si_jaw	1 mm

Table 3.12. *Parameters fitted in the ellipsometry for TiO_2 characterization*

MSE=17.48			Thick.2	62.104±0.0698	nm
PolePos.2	11.352±0.764		PoleMag.2	345.34±46.1	
En1.2	3.6835±0.00477		Am1.2	0.78591±0.0106	
Thick.3	6.589±0.0936	nm			

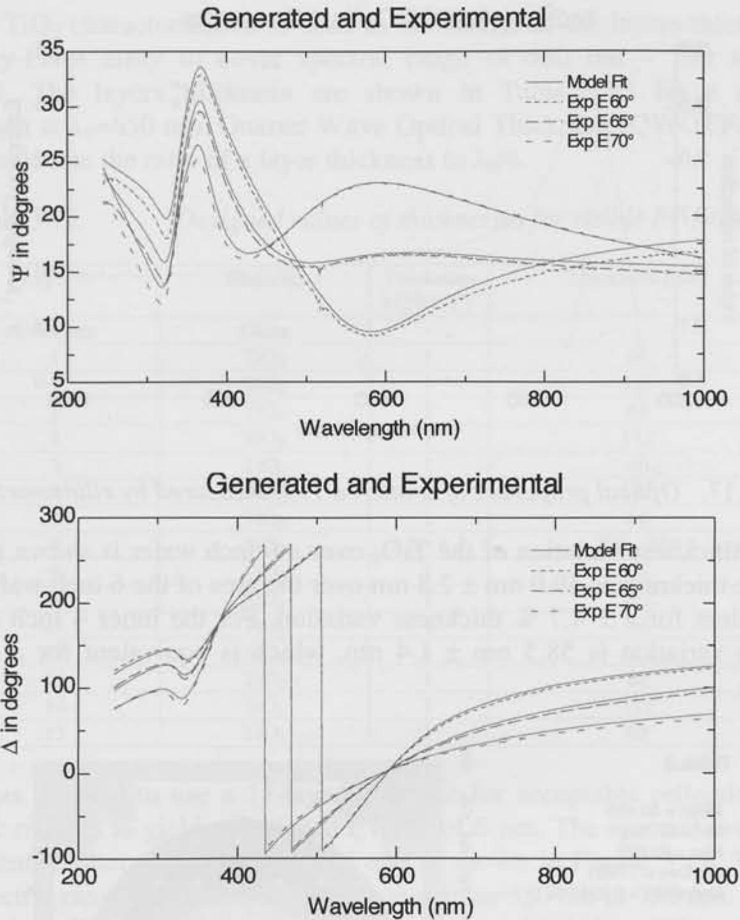

Figure 3.16. *Generated and measured Ψ and Δ values of 62 nm sputtered TiO_2 on Si substrate.*

The optical properties of sputtered TiO_2, based on this measurement, are shown in Figure 3.17. The extinction coefficient of our sputtered TiO_2 is essentially zero for wavelength down to 385 nm. According to literature, it is expected that optimization the deposition process can result in a transparent film at wavelengths down to 350 nm [3.5].

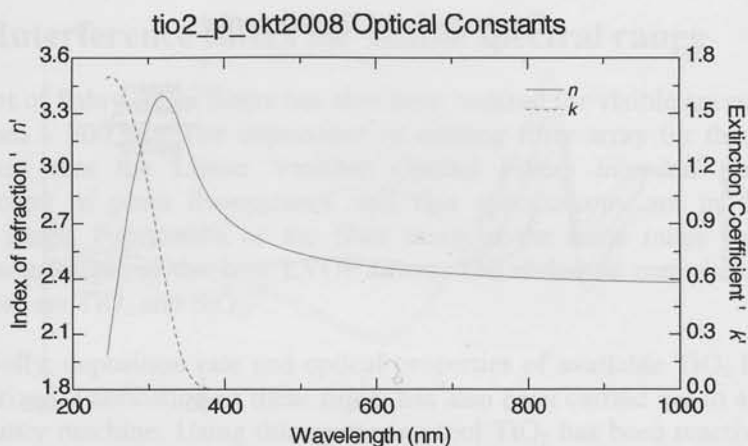

Figure 3.17. *Optical properties of sputtered TiO_2 measured by ellipsometry.*

The thickness variation of the TiO_2 over a 6 inch wafer is shown in Figure 3.18. The thickness is 59.9 nm ± 2.8 nm over the area of the 6 inch wafer which is equivalent for a ± 4.7 % thickness variation. For the inner 4 inch area, the thickness variation is 58.5 nm ± 1.4 nm, which is equivalent for a ± 2.4 % variation.

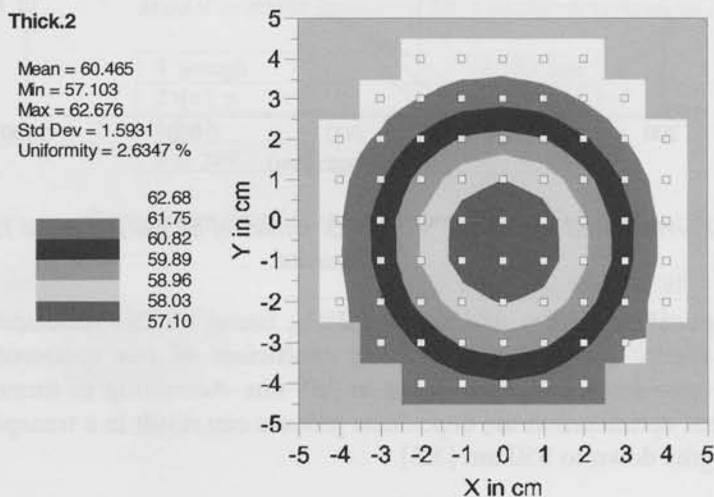

Figure 3.18. *Thickness variation of Sputtered TiO_2 over a 6" wafer, values in nm.*

The TiO_2 characterization is used in the design of the layers thickness for the Fabry-Perot array to cover spectral range of 580 nm – 720 nm using TFCalc®. The layers thickness are shown in Table 3.13 for a reference wavelength at λ_0=650 nm. Quarter Wave Optical Thickness (QWOT) shown in the tables denote the ratio of a layer thickness to $\lambda_0/4$.

Table 3.13. *Designed values of thicknesses for visible FP filters*

Layer #	Material	Thickness (QWOT)	Thickness (nm)
Substrate	Glass	-	-
1	TiO_2	1	66
2	SiO_2	1	112
3	TiO_2	1	66
4	SiO_2	1	112
5	TiO_2	1	66
6	SiO_2	1	112
7	TiO_2	1	66
8	SiO_2	3.5 - 4.5	390 - 500
9	TiO_2	1	66
10	SiO_2	1	112
11	TiO_2	1	66
12	SiO_2	1	112
13	TiO_2	1	66
14	SiO_2	1	112
15	TiO_2	1	66

It was decided to use a 15-layered device for acceptable reflection of the dielectric mirrors to yield a designed FWHP of 6 nm. The spectral response of the fabricated filter array is measured and is shown in Figure 3.19. The stop-band spectral range of the dielectric mirror is from 580 nm to 780 nm. It should be noted from Figure 3.19 that the two peaks appearing below 580 nm are from another resonance order and the desired order peaks are appearing in the spectral range of the Fabry-Perot at 730 nm and 740 nm. Considering the thickness variations, there is a good agreement between simulated spectral response using TFCalc and measured response of the Fabry-Perot filters.

One important performance parameter to be used in optical filters for spectroscopic applications is out of band rejection. To define the out of band rejection, assume λ_{MIN} and λ_{MAX} as the wavelength where the transmission through the Fabry-Perot falls to 0.5 % of its peak. The Out-of-band-rejection is defined by:

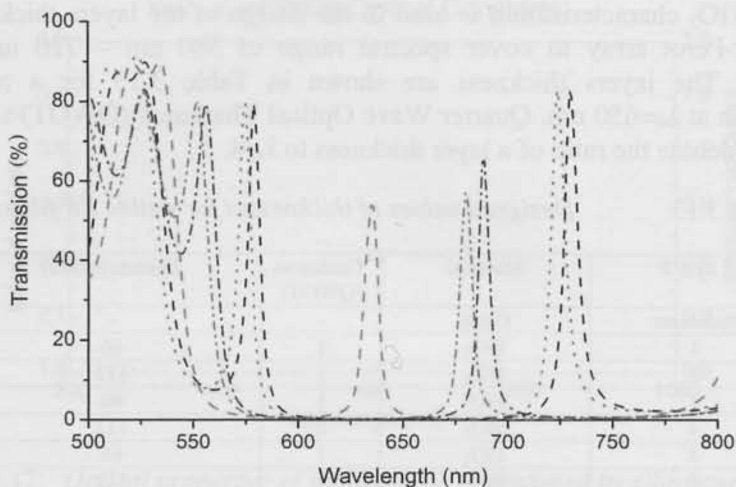

Figure 3.19. *Measured spectral response of visible Fabry-Perot array.*

$$\text{Out-of-Band-rejection} = \frac{\int F(\lambda)d\lambda - \int_{\lambda_{MIN}}^{\lambda_{MAX}} F(\lambda)d\lambda}{\int F(\lambda)d\lambda} \qquad (3.5)$$

For the fabricated visible filters, $\lambda_{MAX} - \lambda_{MIN} = 30$ nm.

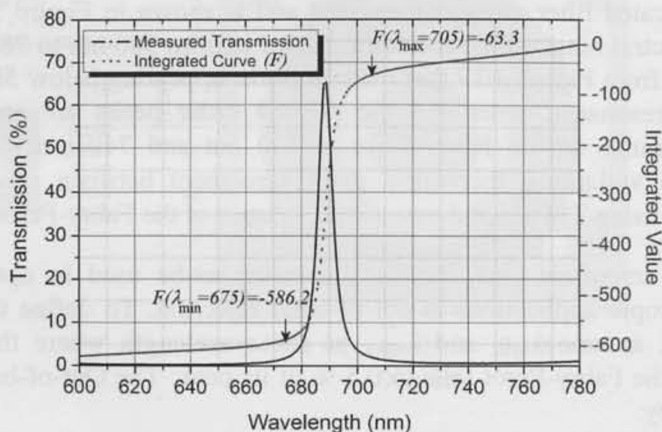

Figure 3.20. *Calculating the out-of-Band-Rejection by integration.*

The spectral response of one of the Fabry-Perot filters of the array is integrated and plotted in Figure 3.20. For the bandwidth of 600 nm to 780 nm:

$$\int F(\lambda)d\lambda = 621.1$$

Therefore from Figure 3.20 and equation (3.5):

$$\text{Out-of-Band-Rejection} = \frac{621-(586.2-63.3)}{621} \approx 15\%$$

When a smaller bandwidth of 160 nm is considered, the Out-of-Band-Rejection is calculated to be 12 %.

3.4 Interference filters for UV (300 nm – 400 nm)

The final design of an array of Fabry-Perot filters presented here is intended for the UV spectral range of 300 nm – 400 nm. Many biological molecules are fluorescent. The excitation wavelengths are usually in the UV part of the optical spectrum [3.6]. Since TiO_2 is absorbing in this spectral range as noted from Figure 3.17, HfO_2 is selected and used as the high-n material. The same sputter tool in the previous filter arrays provides the possibility of reactively depositing HfO_2 thin films. Also, HfO_2 has to be characterized using the approach presented before and the deposition rate needs to be calibrated.

HfO_2 has been sputtered on a bare silicon wafer for 300 seconds. The HfO_2 has been modeled by a Cauchy model in the ellipsometry software similar to SiO_2 modeling. The good Ψ and Δ fitting of Figure 3.21 proves that the k value (extinction coefficient) of the film is negligible in the spectral range of ellipsometry. Table 3.14 and Table 3.15 show WVase® model used and optimized parameters in the model. Apart from thickness value, other parameters are dimensionless.

Table 3.14. *Model used for sputtered HfO_2*

1 hfo2_fhr	41.747 nm
0 si_jaw	1 mm

Table 3.15. *Cauchy parameters optimized for HfO_2*

MSE=7.648		Thick.1	41.747±0.0197	nm
An.1	2.0039±0.00125	Bn.1	0.023355±0.000135	

As it can be noted from Table 3.15, only two terms of Cauchy model expression have been used in the optimization. The deposition rate has been calculated as 0.14 nm / sec.

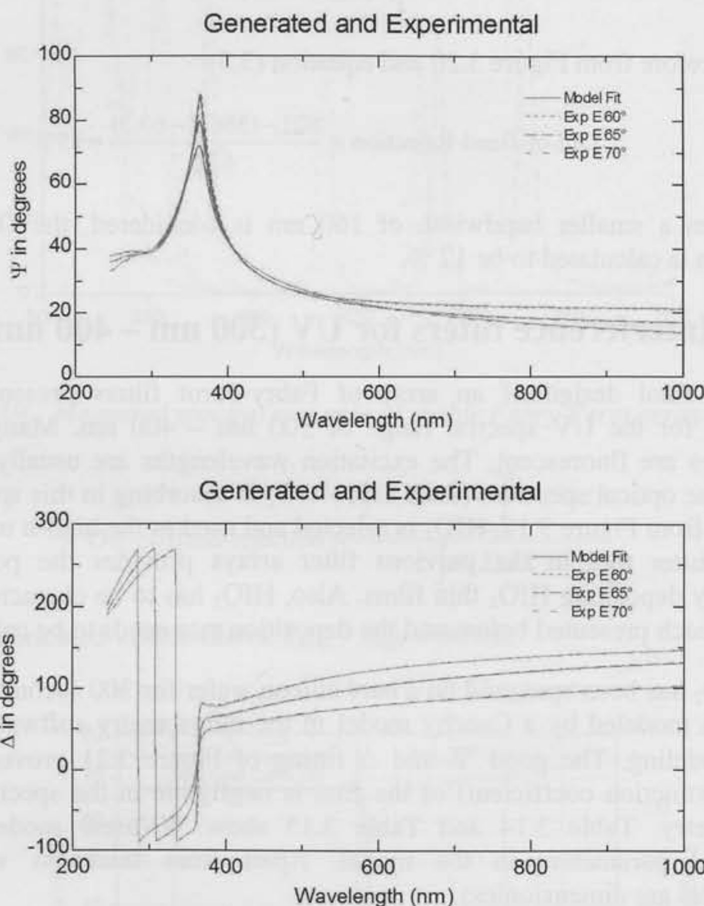

Figure 3.21. *Generated and measured Ψ and Δ values of 41.7 nm sputtered HfO_2 /Si substrate.*

The refractive index of the HfO_2 thin film is shown in Figure 3.22. The figure indicates that the refractive index changes from 2.25 to 2.15 in the 300 nm – 400 nm spectral range which is slightly higher than that reported in [3.7]. The Extinction coefficient is calculated to be zero for the entire wavelength

range. Using $n_2 = 2.2$ and $n_1 = 1$ (Figure 3.6) and equation (2.6) results: $\frac{\Delta\lambda}{\lambda_0} = 0.24$. For $\lambda_0 = 350$ nm, $\Delta\lambda = 84$ nm.

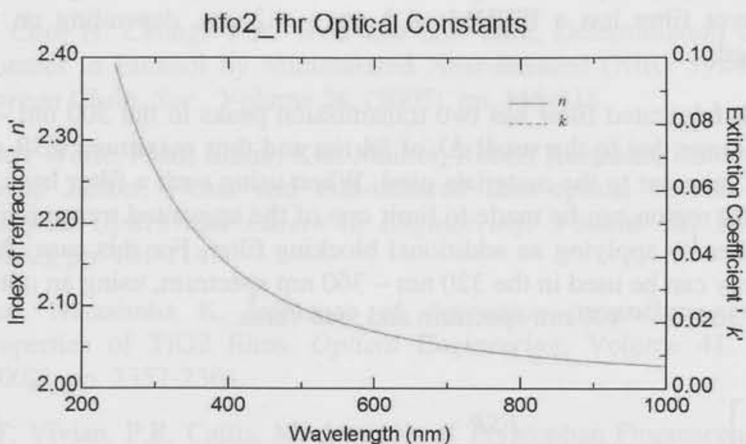

Figure 3.22. *Optical properties of sputtered HfO_2 measured by ellipsometry.*

Table 3.16. *Designed values of thicknesses for UV FP filters*

Layer number	Material	Thickness (nm)
-	Glass	-
1	HfO_2	40
2	SiO_2	59
3	HfO_2	40
4	SiO_2	59
5	HfO_2	40
6	SiO_2	59
7	HfO_2	40
8	SiO_2	59
9	HfO_2	40
10	SiO_2	440 nm – 600 nm
11	HfO_2	40
12	SiO_2	59
13	HfO_2	40
14	SiO_2	59
15	HfO_2	40
16	SiO_2	59
17	HfO_2	40
18	SiO_2	59
19	HfO_2	40

Table 3.16 shows the designed and implemented layers thicknesses for the UV Fabry-Perot filter array. The cavity layer thickness changes from 440 nm to 600 nm between different filters in the array to cover spectral range of interest.

The measured spectral response of the filters is shown in Figure 3.23. Each Fabry-Perot filter has a FWHM of 3 nm – 4.2 nm, depending on the peak wavelength.

Each fabricated filter has two transmission peaks in the 300 nm – 400 nm spectral range due to the small $\Delta\lambda$ of 84 nm and thus maximum FSR of 42 nm which is inherent to the materials used. When using such a filter bank a choice of spectral region can be made to limit one of the unwanted transmission peaks of the filter by applying an additional blocking filter. For this case, the Fabry-Perot array can be used in the 320 nm – 360 nm spectrum, using an optical filter to block 360 nm – 400 nm spectrum and vice versa.

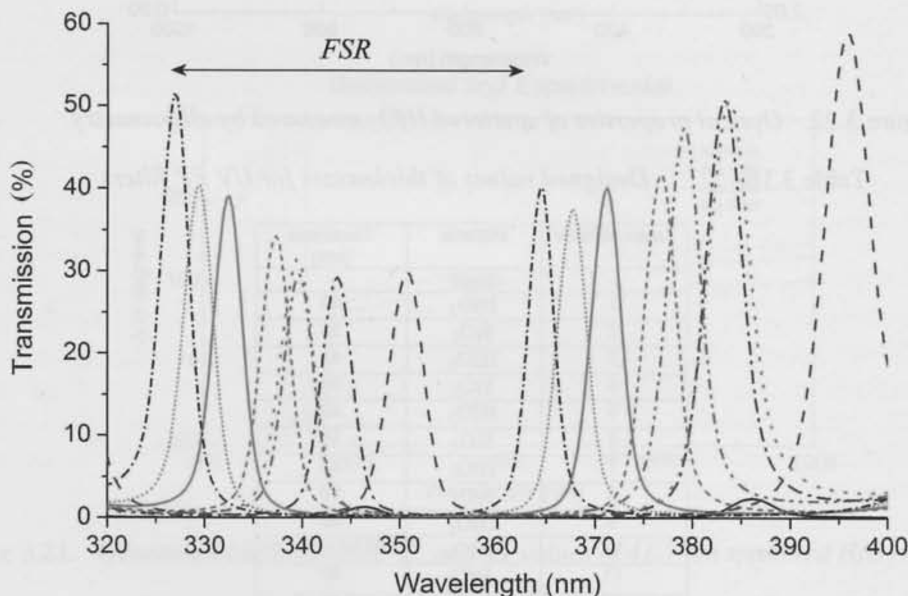

Figure 3.23. *Measured spectral response of UV Fabry-Perot array.*

3.5 References

[3.1] Handbook of Optics, 3rd edition, Vol. 4. McGraw-Hill, 2009.

[3.2] SOPRA N&K Database, *http://www.sopra-sa.com/*.

[3.3] S. Cho, H. Chung, Y.A. Woo and H.J. Kim, Determination of Water Content in Ethanol by Miniaturized Near-Infrared (NIR) System, *Bull. Korean Chem. Soc.*, Volume **26**, (2005), pp. 115-118.

[3.4] Peter Werle, Franz Slemr, Karl Maurer, Robert Kormann, Robert Mucke, Bernd Janker, Near- and mid-infrared laser-optical sensors for gas analysis, *Optics and Lasers in Engineering*, Volume **37**, Issues 2-3, (2002), pp. 101-114.

[3.5] Rao, Narasimha K, Influence of deposition parameters on optical properties of TiO2 films, *Optical Engineering*, Volume **41**, Issue 9, (2002), pp. 2357-2364.

[3.6] J.T. Vivian, P.R. Callis, Mechanisms of Tryptophan Fluorescence Shifts in Proteins, *Biophysical journal*, Volume **80**, issue 5, (2001), pp. 2093 – 2109.

[3.7] M. Fadel, O.A. Azim M., O.A. Omer and R.R. Basily, A study of some optical properties of hafnium dioxide (HfO2) thin films and their applications, *Applied Physics A: Materials Science & Processing*, Volume **66**, Number 3, pp. 335-343.

4 *Fabrication of tapered layers using reflow*

4.1 Introduction

This chapter reports on the IC-compatible fabrication of tapered optical layers for use in LVOFs. Conventional approaches for fabrication of tapered optical layers are based on gray tone lithography [4.1], shadow masking [4.2], moving mask [4.3] and polishing. However, these techniques are either not IC-compatible (moving mask) or can not result in required angle slopes for LVOF application.

In our reflow based fabrication process, the taper angle is fully defined by mask design. Only one masked lithography step is required for defining both strips of photoresist and the local trench density therein, as shown schematically in Figure 4.1. The trench density defines the local amount of material removed (Figure 4.1a) and is followed by a reflow of this patterned photoresist to locally planarize the remaining strip of material (Figure 4.1b). The result is an effective

reduction of the resist layer thickness by a value defined by localized trench density. Hence a taper can be flexibly programmed by mask design to be from 0.001° to 0.1°, which enables the simultaneous fabrication of tapered layers of different taper angle.

The sloped taper is in the resist which can not be used in a practical device. Thus, the structure can be subsequently transferred into Si or SiO_2 by appropriate etching and be used as the cavity layer of a Fabry-Perot LVOF. An LVOF results in case the taper is fabricated in a layer that is deposited on top of a dielectric mirror and another dielectric mirror is deposited on top of the tapered layer. Flexibility in the slopes achieved by this technique makes it possible to use such tapered also for coupling of optical fibers into optical planar waveguides.

Since the process is mainly controlled by reflow of resist material, the reflow process needs to be analyzed in details which is the subject of this chapter. Analytical calculation, numerical simulation and experimental verification of the surface profile of reflowed structures in photoresist are used to gain a better insight. A simple analytical model, which assumes a fixed contact angle between resist and substrate and constant volume, is used to provide an indication of the expected profile. Finite Element Method (FEM) simulations are also used to simulate the profile of the resist after reflow in more detail. The information from these simulations has been used in the lithography mask design.

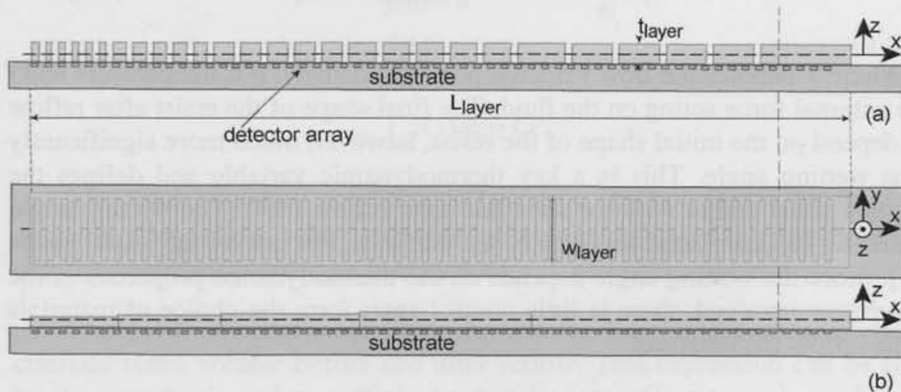

Figure 4.1. *a) Trench density variation in the resist after lithography b) tapered profile of resist after reflow of the pattern.*

Photoresist reflows when heated above its glass-transition temperature. Resist reflow is mainly used for surface planarization and as a low-cost IC-compatible technique for fabrication of micro-lenses [4.4]-[4.6]. Resist reflow techniques are also used in fabrication of sub-micron contact holes [4.7]-[4.8]. Recently, resist reflow has also been investigated for IC-compatible fabrication of tapered structures with a relatively large taper (Δz / L = 10 μm / 1 mm) for optical coupling [4.9]. The actual surface profile of the reflowed layer is not critical in the fabrication of sub-micron contact holes. Moreover, the "droplet" shape used in lenses fabricated using reflow is a direct result of the reflow mechanism. However, the shape of a tapered layer should be highly linear and needs a more detailed investigation of the mechanisms involved in the reflow process. A more detailed understanding of this mechanism is crucial for assessing the possible angles of the taper and minimizing the surface roughness. Moreover, accurate prediction of the resist profile after reflow avoids test runs, decreases processing time and reduces cost.

4.2 Modeling of the reflow process

The viscosity of the resist decreases rapidly at temperatures above the glass transition temperature and the material flows because of surface tension, while remaining coherent [4.10]. The flow of such a low-viscosity material across a substrate is described by the Navier-Stokes equations [4.11].

$$\rho(\frac{\partial V}{\partial t} + V.\nabla V) = -\nabla p + \mu\nabla^2 V + f \qquad (4.1)$$

Where V denotes the flow velocity, ρ is fluid density, p is the pressure and f is the external force acting on the fluid. The final shape of the resist after reflow does depend on the initial shape of the resist, however, much more significantly on the wetting angle. This is a key thermodynamic variable and defines the angle that resist makes with the substrate after reflow [4.4]. The wetting angle depends on the interfacial tensions of the surfaces, but not on the initial shape [4.12]. Since the wetting angle depends on the thermodynamic properties of the two surfaces involved, there is little control apart form the choice of materials and the reflow temperature.

The result is adequate for fabrication of high-density arrays of micro-lenses. However, more control is required in case of application for the fabrication of layers of high planar aspect ratio, small taper angle and highly linear taper required for a structure of a Linear Variable Optical Filter, which is typically

0.5-5 μm thick, several mm long and 100 μm wide. The taper angle is smaller than 1°. Control of the profile of the tapered layers is possible by patterning of the photoresist to define both the outer contour of the rectangular initial layer to be reflowed, but also for fine-definition of the inner area to ensure highly localized reflow only. A detailed analysis of the reflow process in such a structure is required for predicting the final profile, which can subsequently be used for designing the mask that is to be used for the definition of the fine-patterning of the layer.

4.2.1 Analytical modeling

The simple analytical expression for prediction of the resist profile after reflow of a resist assumes an initial structure of length 2L and thickness T. Since the shape of the resist structure after reflow is non-linear, the 6th order polynomial expression in (4.2), is used for approximation of the resist profile. Therefore, the center of the 2L-long initial structure is taken as the origin of the system. due to symmetry only even orders are available.

$$y(x) = A + bx^2 + cx^4 + dx^6 \tag{4.2}$$

The four unknowns can be calculated from the applicable boundary conditions.

$$\begin{aligned} & y(L) = 0 \\ & y(0) = h \\ & \frac{dy(x)}{dx}(x = L) = -\tan(\theta) \\ & \int_0^L y(x)dx = LT \end{aligned} \tag{4.3}$$

The third boundary condition is based on the knowledge on the critical angle, θ, after reflow, which depends on the wettability of the particular resist-substrate combination shown in Figure 4.2.

The forth boundary condition formulates the logical assumption of a constant resist volume before and after reflow. This expression can be refined by the introduction of a coefficient η to take into account any loss of material due to e.g. evaporation during thermal reflow.

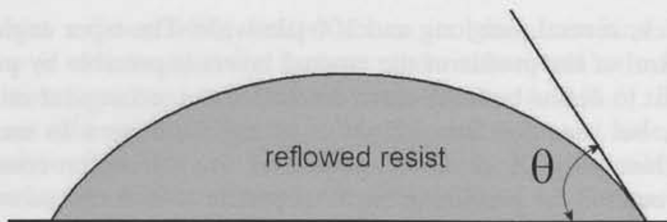

Figure 4.2. *Definition of the critical angle, θ.*

Figure 4.3 shows the measured profile of a 1300 µm long structure after reflow. The resist used is AZ 4562 and is reflowed on a hotplate at 150º C for 60 minutes. The initial thickness of the resist before reflow is 5.7 µm. From the measurement the critical angle is found as θ = 19.2º. When reflow is done by heating, there is a slight decrease in the volume of the resist due to evaporation of the resist solvent.

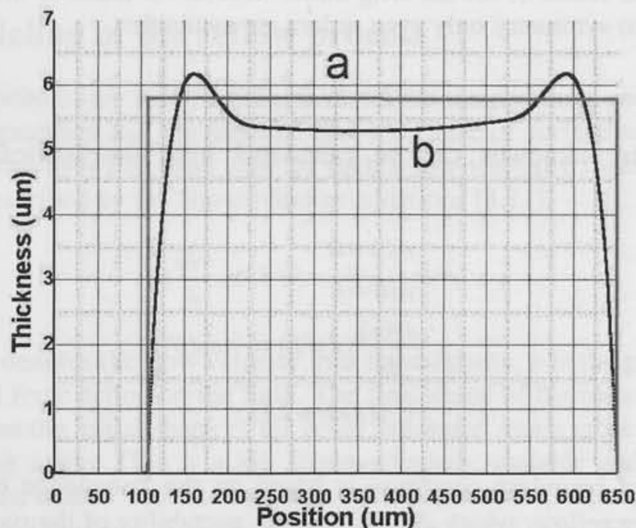

Figure 4.3. *(a) Initial profile and (b) measured profile of the resist after reflow.*

Solving Equation (4.2) for the boundary conditions expressed in equation (4.3), results in a profile as shown in Fig. 2. Figure 4.4a shows the profiles in case the wettability angle changes from 20° to 2° in steps of 2°. This result has been obtained using the same analytical approach. The higher the wettability angle, the angle at the edge of the resist increases. However, the ripple on the

profile also increases with wettability. The analytical approach used assumes small non-linearity in the profile.

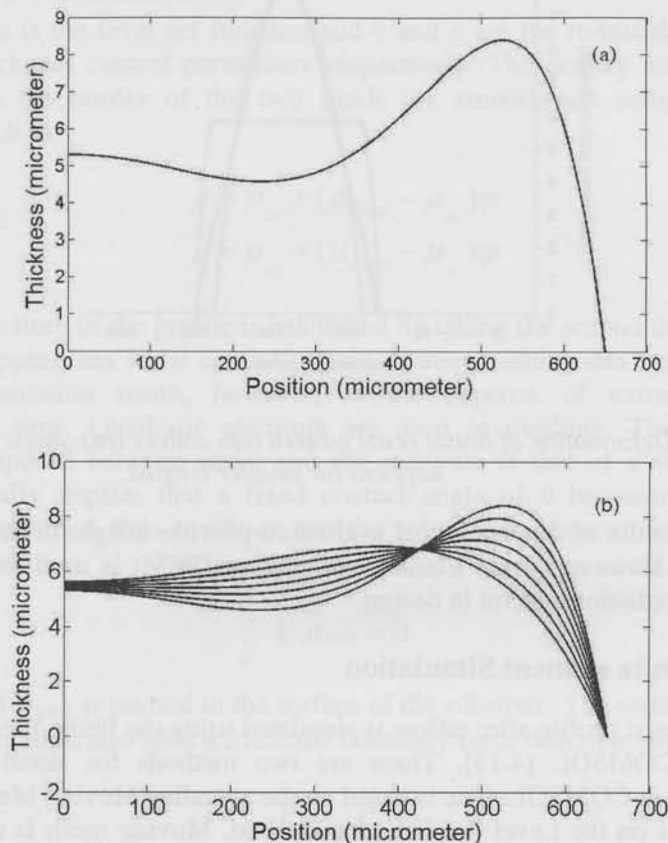

Figure 4.4. *Predicted profile of the resist after reflow with a) wettability from measurement b) different wettability angles.*

Relatively short resist structures result in a convex lens-like shape after reflow. The lower the contact angle the longer the column of photoresist can be to make a lens. Figure 4.5 shows such a structure. The initial length of the resist pattern is 125 μm with initial thickness of 5.5 μm which results in a bump shape resist structure with peak of 10 μm and length of 100 μm, with the same reflow conditions as mentioned before.

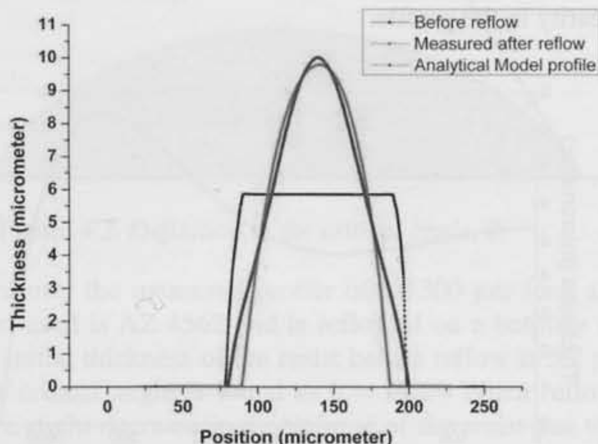

Figure 4.5. *Deformation of initial resist pattern into convex lens-shape by reflow happens for smaller lengths.*

The results of this analytical evaluation provide insight in the mechanism of reflow. However Finite Element Simulation (FEM) is used to obtain more accurate predictions useful in design.

4.2.2 Finite element Simulation

The resist profile after reflow is simulated using the Finite Element Method software COMSOL [4.13]. There are two methods for simulating objects movement in COMSOL. One is based on the so-called Moving Mesh [4.14] and the other is on the Level Set Function method. Moving mesh is more suitable for small motions of an object.

Considering the surface tension requires calculation of curvature of deformation, which is mathematically more difficult. To include surface tension forces in the Navier-Stokes equations, the curvature of the profile has to be calculated at each time step. A border is assumed between the resist (as fluid 1) and air (as fluid 2) in the level set method, by defining a level set function φ. The value of φ is 0 in the reflowing resist area and 1 in the air. The value of the level set function, φ, changes from 0 to 1 between the two fluids. The border is thus represented as the 0.5 contour of the level set function. The transport of the border is given by [4.13]:

$$\frac{\partial \varphi}{\partial t} + \nabla.(\varphi\vec{V}) + \gamma[(\nabla.(\varphi(1-\varphi)\frac{\nabla\varphi}{|\nabla\varphi|})) - \varepsilon\nabla.\nabla\varphi] = 0 \quad (4.4)$$

Where φ is the level set function and γ and ε are the re-initialization and interface thickness control parameters respectively. The density and viscosity jump across the border of the two fluids are smoothened using level set functions such as:

$$\begin{aligned} \rho &= \rho_{air} + (\rho_{water} - \rho_{air})\varphi \\ \mu &= \mu_{air} + (\mu_{water} - \mu_{air})\varphi \end{aligned} \quad (4.5)$$

The curvature of the profile is calculated by taking the second derivative of φ. Mesh mapping has to be carefully done. Dense meshing can result in very accurate simulation result, however, at the expense of extremely long computation time. Quadratic elements are used in meshing. The boundary condition imposed between resist and the substrate is that of a wetted wall, which basically implies that a fixed contact angle of θ between resist and substrate is assumed, thus condition sets the velocity component normal to the substrate to zero:

$$\vec{V}.\vec{n}_{wall} = 0 \quad (4.6)$$

In which $\vec{n}_{wall}$ is normal to the surface of the substrate. The wetted wall boundary condition also adds a frictional boundary force described by:

$$\vec{F} = -\frac{\mu}{\beta}\vec{V} \quad (4.7)$$

In which, μ is viscosity and β is slip length. Slip length is set equal to mesh element size. Silicon has been used as the substrate in experiments, which has a contact angle of 19° with the resist. The critical surface tension coefficient of the resist is set to 19 mN/m, according to the datasheet.

Figure 4.6 and Figure 4.7 show the simulation results obtained using COMSOL for both long and short structures. An animation-type of simulation is done with time steps of 0.1 msec. The border contour obtained from simulation is also compared with the measured profile in for a 120 µm wide

resist structure and a 540 µm wide one. It can be seen that FEM simulation gives a good prediction of the profile.

The most important information derived from the simulation is the movement of the contact line. However, the resolution to find this value is limited to the mesh size. Inserting measurement results on contact angle of into the FEM simulation results in the expected shape of the resist after reflow and its contact line movement.

Figure 4.6. *Final time step of FEM simulation, the value of level set function changes from 1 to zero from resist to air.*

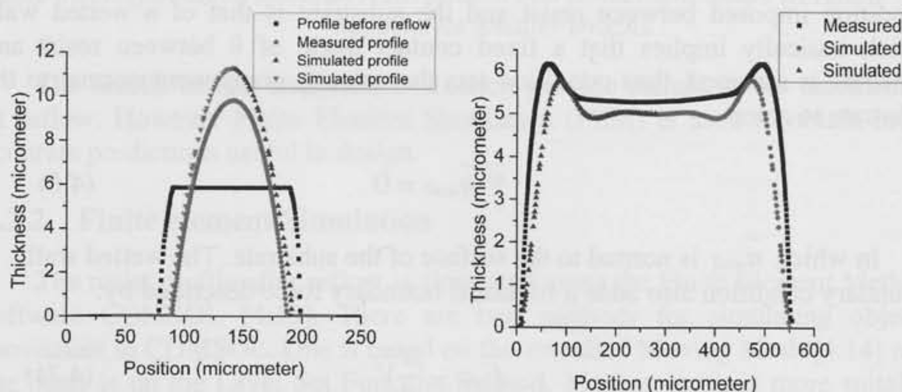

Figure 4.7. *comparison between measured and simulated profile.*

4.3 Mask design and lithography

A mask is designed composed of an array of holes or trenches with a density based on the amount of photoresist that has to be locally removed. Using the mask to photolithographically define the pattern into the LVOF layer and a subsequent reflow, transforms the original flat surface into a tapered shape. Figure 4.8 shows the model used for calculation of the position of trenches in the resist layer as a function of strip dimensions and required taper angle, ψ.

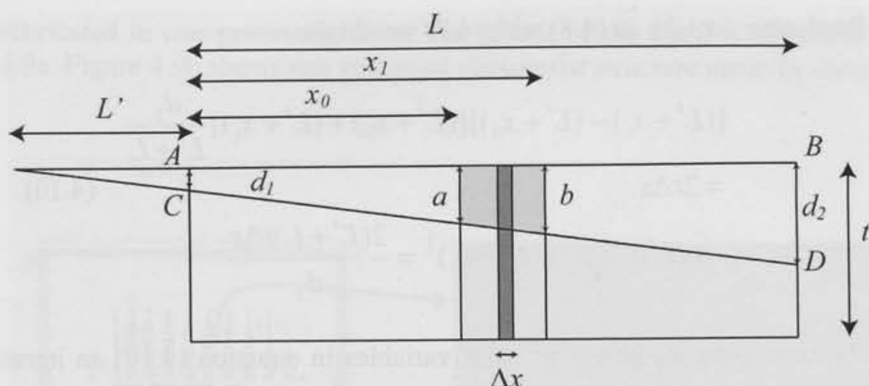

Figure 4.8. *Principle of the lithography mask design. The Areas of the two filled sections are equal.*

The initial layer is of uniform thickness t and the length of the strip is L. Assume an application, which calls for a taper of thickness t-d_1 at the long wavelength limit and t-d_2 at the short wavelength limit. The AB line is the top of photoresist before any pattern and line CD is the surface of the photoresist after patterning and reflow. The pattern in principle consists of many thin trench lines of width Δx which are made by lithography in the photoresist layer. Δx is the thinnest line we can achieve by the available lithography system.

The idea used in the design is to start from point A and to move toward point B (the length of tapered structure depends on the application), the objective is to make a trench with width of Δx in the middle of an area in which the volume removed by the trench is the volume that should be removed if we want to have the desired slope of CD at that area. The volume removed is expressed by equation (4.8).

$$\frac{(x_1 - x_0)(a+b)}{2} = t \cdot \Delta x \qquad (4.8)$$

From Figure 4.8 we have:

$$\frac{a}{L'+x_0} = \frac{b}{L'+x_1} = \frac{d_2}{L'+L} = \frac{a+b}{[(L'+x_0)+(L'+x_1)]}$$
$$\rightarrow (a+b) = [(L'+x_0)+(L'+x_1)]\frac{d_2}{L'+L} \qquad (4.9)$$

Replacing $(a+b)$ in (4.8) with (4.9) we obtain:

$$[(L'+x_1)-(L'+x_0)][(L'+x_0)+(L'+x_1)]\frac{d_2}{L'+L}$$
$$=2t\Delta x \tag{4.10}$$
$$\rightarrow (L'+x_1)^2-(L'+x_0)^2=\frac{2(L'+L)t\Delta x}{d_2}$$

By expressing x_1 based on other variables in equation (4.10) an iterative procedure is derived.

$$x_1=\sqrt{2\Delta x\alpha_2 L\frac{\alpha_1}{\alpha_1-\alpha_2}+(x_0+L\frac{\alpha_2}{\alpha_1-\alpha_2})^2}-L\frac{\alpha_2}{\alpha_1-\alpha_2} \tag{4.11}$$

In which $\alpha_1=\frac{t}{d_1},\alpha_2=\frac{t}{d_2}$. In the iterative procedure, x_0 is the length until which the necessary trenches are drawn and x_1 is calculated by (4.11) in a way that the next trench be made in the middle of x_0 and x_1. Initial value for x_0 is zero and the procedure stops when $x_1-x_0<2\Delta x$. The slope of the taper can be calculated in degrees with the equation below:

$$\psi=\text{Arc}\tan\left(\frac{d_2-d_1}{L}\right)=\text{Arc}\tan\left(\frac{t}{L}\times\frac{\alpha_1-\alpha_2}{\alpha_1\alpha_2}\right) \tag{4.12}$$

Based on the above equations several patterns with different values for α_1 and α_2 are made on a full wafer 4 inch mask.

The patterns are divided into two parts. For the first part L = 2 mm and there are 10 different values for $1/\alpha_1=\frac{d_1}{t}$ and 9 values for the slope. The purpose is to have 10 different slopes with 9 different heights in 90 patterns.

For the second part L = 5 mm and there are 25 patterns with different slopes. The benefit is that several different kinds of tapered structures can be

fabricated in one processing time. The layout of the mask is shown in Figure 4.9a. Figure 4.9b shows one patterned photoresist structure made by the mask.

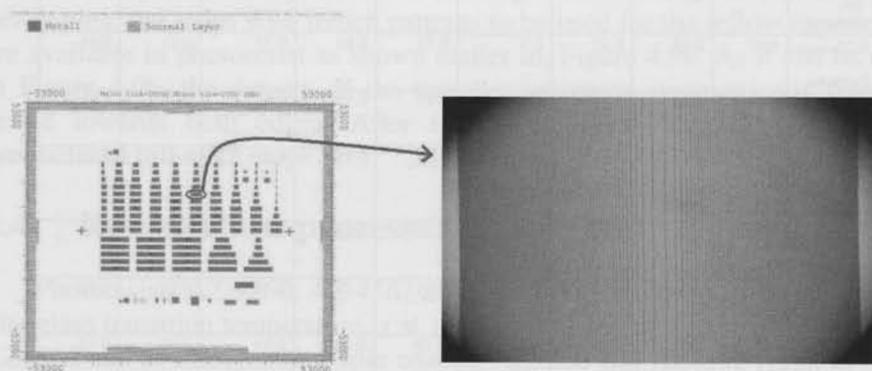

Figure 4.9. *a) Layout of the mask with 115 structures. b) photoresist pattern in one of the structures.*

Table 4.1 presents the values if the parameters for the designed structures of the lithography mask. Expected slope angle of each structure is presented on the table. For the 90 patterns, $L = 2$ mm, on the top part of the mask the slope angle changes from 0.86 mdeg to 43 mdeg. The slope is constant between the structures on the same row and for the structures on the same column the initial thickness of the slopes, d_1, is kept constant. For the 25 structures on the lower part of the lithography mask with $L = 5$ mm, initial thickness of the slopes, d_1, constant and the slope angle of the structures increase from left to right on the mask. The slope for $L = 5$ mm varies from 0.46 mdeg to 16 mdeg.

Table 4.1.*Taper parameters for a) L= 2 mm and b) L= 5 mm structures*

	$1/\alpha_1 = 0$	$1/\alpha_1 = 0.02$	$1/\alpha_1 = 0.05$	$1/\alpha_1 = 0.08$	$1/\alpha_1 = 0.13$	$1/\alpha_1 = 0.2$	$1/\alpha_1 = 0.28$	$1/\alpha_1 = 0.37$	$1/\alpha_1 = 0.47$
$\frac{\alpha_1-\alpha_2}{\alpha_1\alpha_2} = 1$ $\theta = 43m$ deg	0.5	0.52	0.55	0.58	0.63	0.7	0.78	0.87	0.97
$\frac{\alpha_1-\alpha_2}{\alpha_1\alpha_2} = 0.83$ $\theta = 36m$ deg	0.42	0.44	0.47	0.5	0.55	0.64	0.72	0.81	0.91
$\frac{\alpha_1-\alpha_2}{\alpha_1\alpha_2} = 0.67$ $\theta = 29m$ deg	0.34	0.36	0.39	0.42	0.47	0.54	0.62	0.71	0.81
$\frac{\alpha_1-\alpha_2}{\alpha_1\alpha_2} = 0.50$ $\theta = 21.5m$ deg	0.25	0.27	0.3	0.33	0.38	0.45	0.53	0.62	0.72
$\frac{\alpha_1-\alpha_2}{\alpha_1\alpha_2} = 0.33$ $\theta = 14m$ deg	0.16	0.18	0.21	0.24	0.29	0.36	0.44	0.53	0.63
$\frac{\alpha_1-\alpha_2}{\alpha_1\alpha_2} = 0.26$ $\theta = 11m$ deg	0.18	0.2	0.23	0.26	0.31	0.38	0.46	0.55	0.65
$\frac{\alpha_1-\alpha_2}{\alpha_1\alpha_2} = 0.13$ $\theta = 5.5m$ deg	0.06	0.08	0.11	0.14	0.19	0.26	0.34	0.43	0.53
$\frac{\alpha_1-\alpha_2}{\alpha_1\alpha_2} = 0.07$ $\theta = 3m$ deg	0.03	0.05	0.08	0.11	0.16	0.23	0.31	0.4	0.5
$\frac{\alpha_1-\alpha_2}{\alpha_1\alpha_2} = 0.03$ $\theta = 1.3m$ deg	0.015	0.035	0.065	0.095	0.145	0.215	0.295	0.385	0.485
$\frac{\alpha_1-\alpha_2}{\alpha_1\alpha_2} = 0.02$ $\theta = 0.86m$ deg	0.01	0.03	0.06	0.09	0.14	0.21	0.29	0.38	0.48

$1/\alpha_1 = 0.02$ $\theta = 1.3m$ deg $\frac{1}{\alpha_2} = 0.12$ 0.07	$1/\alpha_1 = 0.05$ $\theta = 3.2m$ deg $\frac{1}{\alpha_2} = 0.28$ 0.17	$1/\alpha_1 = 0.08$ $\theta = 5m$ deg $\frac{1}{\alpha_2} = 0.45$ 0.26	$1/\alpha_1 = 0.17$ $\theta = 9.6m$ deg $\frac{1}{\alpha_2} = 0.87$ 0.52	$1/\alpha_1 = 0.28$ $\theta = 16m$ deg $\frac{1}{\alpha_2} = 1.45$ 0.86
$1/\alpha_1 = 0.02$ $\theta = 1.1m$ deg $\frac{1}{\alpha_2} = 0.1$ 0.06	$1/\alpha_1 = 0.05$ $\theta = 2.5m$ deg $\frac{1}{\alpha_2} = 0.23$ 0.14	$1/\alpha_1 = 0.08$ $\theta = 3.9m$ deg $\frac{1}{\alpha_2} = 0.37$ 0.275	$1/\alpha_1 = 0.17$ $\theta = 7.3m$ deg $\frac{1}{\alpha_2} = 0.7$ 0.435	$1/\alpha_1 = 0.28$ $\theta = 12.1m$ deg $\frac{1}{\alpha_2} = 1.17$ 0.725
$1/\alpha_1 = 0.02$ $\theta = 0.92m$ deg $\frac{1}{\alpha_2} = 0.08$ 0.05	$1/\alpha_1 = 0.05$ $\theta = 1.8m$ deg $\frac{1}{\alpha_2} = 0.18$ 0.115	$1/\alpha_1 = 0.08$ $\theta = 2.7m$ deg $\frac{1}{\alpha_2} = 0.28$ 0.18	$1/\alpha_1 = 0.17$ $\theta = 5m$ deg $\frac{1}{\alpha_2} = 0.53$ 0.35	$1/\alpha_1 = 0.28$ $\theta = 8.2m$ deg $\frac{1}{\alpha_2} = 0.88$ 0.55
$1/\alpha_1 = 0.02$ $\theta = 0.69m$ deg $\frac{1}{\alpha_2} = 0.07$ 0.045	$1/\alpha_1 = 0.05$ $\theta = 1.1m$ deg $\frac{1}{\alpha_2} = 0.13$ 0.09	$1/\alpha_1 = 0.08$ $\theta = 1.6m$ deg $\frac{1}{\alpha_2} = 0.2$ 0.14	$1/\alpha_1 = 0.17$ $\theta = 2.7m$ deg $\frac{1}{\alpha_2} = 0.37$ 0.27	$1/\alpha_1 = 0.28$ $\theta = 4.3m$ deg $\frac{1}{\alpha_2} = 0.6$ 0.44
$1/\alpha_1 = 0.02$ $\theta = 0.46m$ deg $\frac{1}{\alpha_2} = 0.05$ 0.0375	$1/\alpha_1 = 0.05$ $\theta = 0.46m$ deg $\frac{1}{\alpha_2} = 0.08$ 0.065	$1/\alpha_1 = 0.08$ $\theta = 0.46m$ deg $\frac{1}{\alpha_2} = 0.12$ 0.1	$1/\alpha_1 = 0.17$ $\theta = 0.46m$ deg $\frac{1}{\alpha_2} = 0.2$ 0.185	$1/\alpha_1 = 0.28$ $\theta = 0.46m$ deg $\frac{1}{\alpha_2} = 0.32$ 0.3

To do the lithography of the patterns, the wafers are exposed to HMDS vapour for 10 minutes prior to resist coating to enhance adhesion between resist and substrate. Resist is subsequently spin coated and soft baked using the standard recipe. After exposure to UV using a contact aligner and subsequent developing, the strips with trench patterns to be used for the reflow experiments are available in photoresist as shown earlier in, Figure 4.9b. As it can be noted in Figure 4.9b, the density of the trenches increases symmetrically from the centre towards both edges. After reflow the result should appear like a symmetrical hill-alike slope.

4.4 Resist reflow process

Photoresists AZ 9260, AZ 4562 and SPR3012 have been used in this work. The glass transition temperature is at 140 °C for AZ9260 and at 120 °C for both AZ4562 and SPR3012. After spin coating AZ9260 and AZ4562 result in layers of about 5 μm thickness and SPR 3012 in about 1 μm thickness. Reflow of the photoresist takes place when its viscosity drops, due to at temperatures beyond the glass transition temperature or when exposed to a solvent.

Cross-linking of the resist is avoided when carrying out the reflow in a chamber saturated with the solvent vapour. This approach for reflow is referred to as *chemical reflow*.

4.4.1 Thermal reflow

Reflow of the photoresist takes place at temperatures beyond the glass transition temperature, at which the resist becomes soft and starts to flow on the substrate due to surface tension. This approach for reflow is referred to as *thermal reflow*. The lateral flow of the resist depends on the contact (wetting) angle between the substrate and the resist. A smaller contact angle implies a higher degree of wettability and more flow of the resist on the substrate. Although glass transition temperature of resist is relatively low value, the resist does not flow well over the substrate due to its high viscosity. Therefore, the resist has to be kept at elevated temperatures for a long period of time to ensure sufficient flow over the substrate for a smooth surface. However, the elevated temperature also starts cross-linking of the resist, resulting in a hardened material, which does not flow.

Figure 4.10 shows the shapes of resist stripes with different width before and after thermal reflow. The width of stripes varies from 60 μm to 300 μm.

The gap between the stripes is 20 µm to ensure that the reflowed stripes would not join. The contact angle θ between patterned resist and substrate is 48° before reflow and 17.2º after reflow in all the structures.

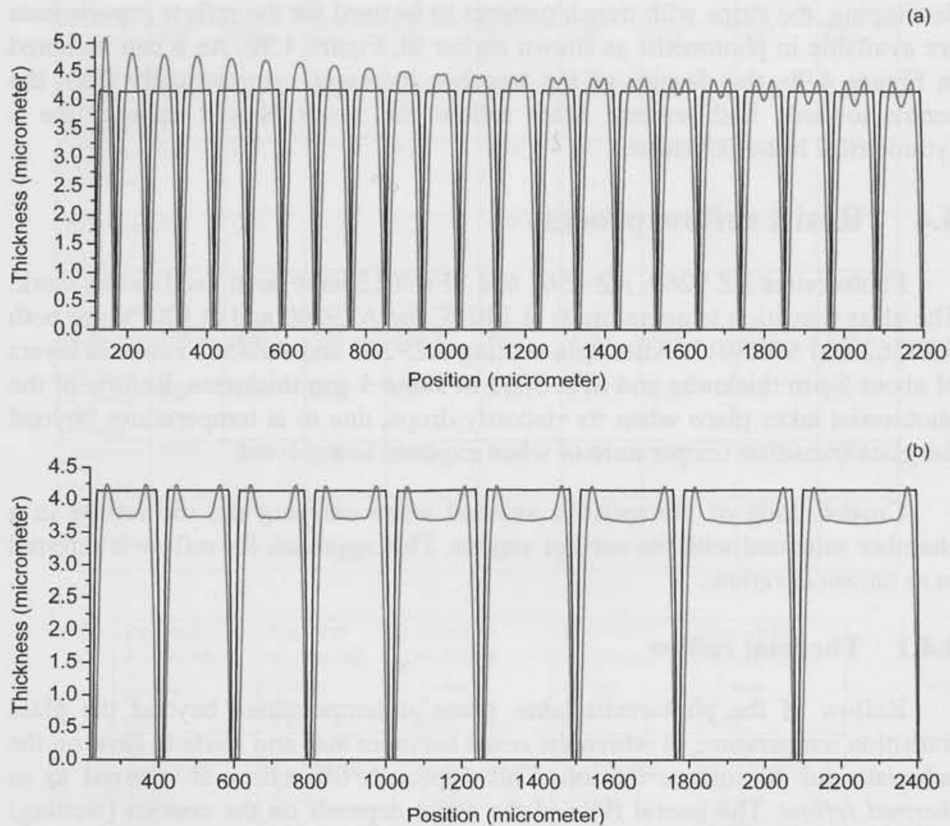

Figure 4.10. *Profile of resist stripes of different width after thermal reflow. a) the stripes width changes from 60 µm to 100 µm. b) the stripes width changes from 160 µm to 300 µm.*

This initial experiment demonstrates an edge effect which is limited to about 50 µm from the circumference and is not affected by the width of the strip. The edge effect occurs in stripes wider than 72 µm. This property determines the maximum width of the strips that can planarize gaps.

4.4.2 Chemical (solvent) reflow

Cross-linking of the resist is avoided when carrying out the reflow in a chamber saturated with the solvent vapour. This approach for reflow is referred to as *chemical reflow*. The wafers are put inside a beaker of solvent (in the case of the resists used, in PGMEA) with a cover on top. The beaker is heated up to 40-60 °C and the vapour of the solvent is absorbed by the patterned resist. The result is a very soft substance, which flows easily over the substrate. Chemical (solvent) reflow is a very fast reflow technology. However, the main problem in this technique is the uncontrollability of condensation of the solvent vapour on the substrate. When this takes place all structures are flushed away. Nevertheless, this technique is suitable for resist with high viscosity, especially if the resist cross-links easily at the glass transition temperature (like AZ4562). The probability of condensation is significantly reduced when the substrate is kept at a higher temperature than the vapour inside the beaker.

4.4.3 Chemical-Thermal reflow

In the combined approach the wafer is alternatively exposed for short time to solvent, so that the resist absorbs some of the solvent vapour and is subsequently exposed to a temperature above glass transition temperature until most of the solvent is removed. Cross-linking of the resist is avoided and a better control on the quality of the surface is obtained. A process has been designed with a limited number of solvent exposure/baking cycles and optimized towards minimum surface roughness for the desired range of taper angles.

Figure 4.11 shows the same structure as shown in Figure 4.10 after a chemical-thermal reflow process. The sample is exposed to PGMEA vapour at 40 °C for 5 min and subsequently heated on hotplate at 120 °C for 15 minutes. Comparison between Figure 4.10 and Figure 4.11 shows that the wettability is much higher in chemical-thermal reflow. The contact angle between resist and the substrate is 8º and resist structures small than 60 µm start to spread considerably over the substrate. Considering this fact most structures in the mask are designed with stripes not more than 60 µm. This gives a requirement for the minimum trench density.

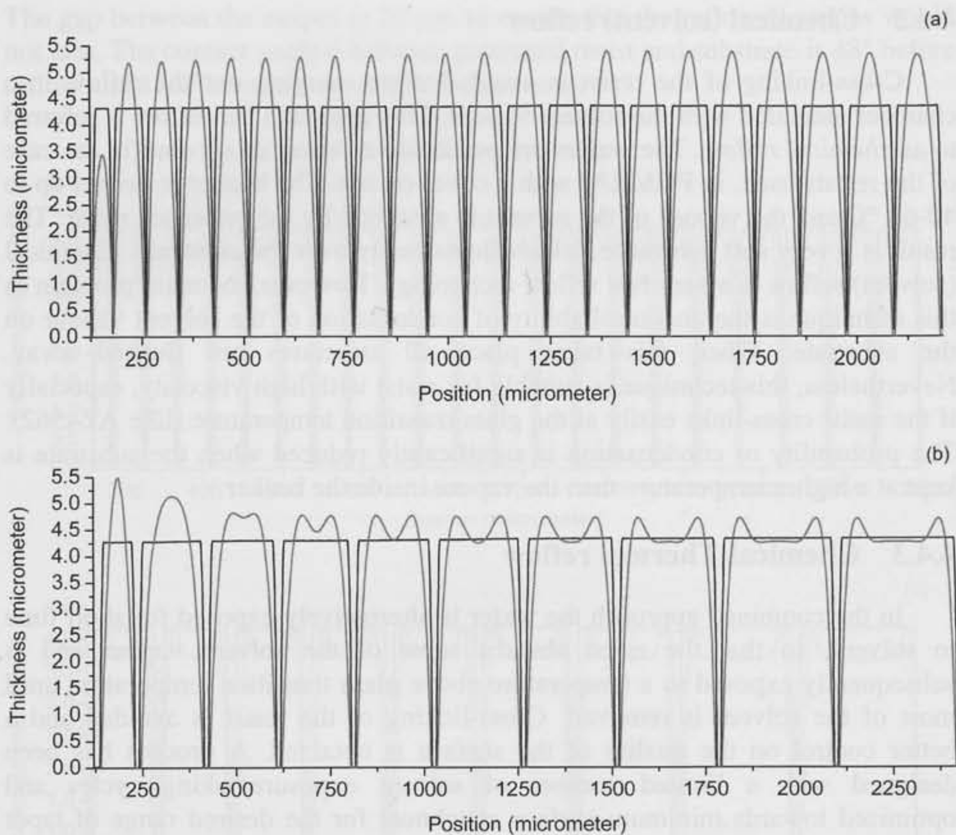

Figure 4.11. *Profile of resist stripes of different widths after chemical-thermal reflow. a) the stripes width changes from 60 μm to 100 μm. b) the stripes width changes from 160 μm to 300 μm.*

The edge effect happens in stripes wider than 162 μm compared to 72 μm in case of thermal reflow. This means that wider resist stripe can planarize patterns with lower trench density and therefore smaller taper angles can be fabricated. Figure 4.12 also shows the comparison between thermal and chemical thermal reflow for a 50 μm wide resist strip. It can be noted that the resist has smeared beyond the initial contact line with the substrate, which is very important for planarization to fill up the gaps between the stripes.

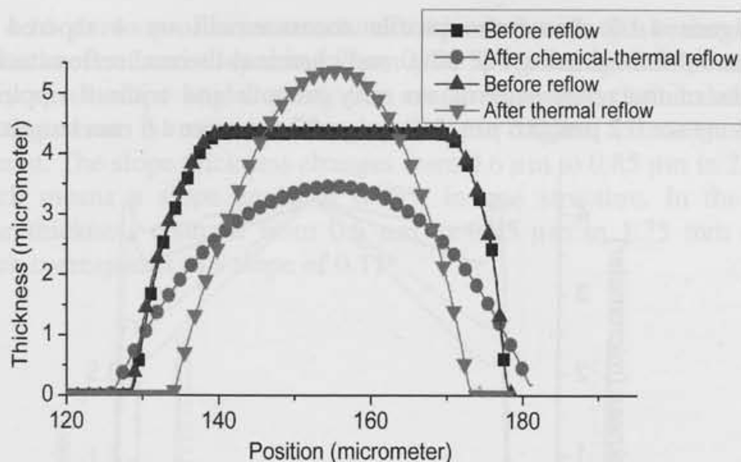

Figure 4.12. *Comparison between thermal reflow and chemical-thermal reflow on a 50 µm stripe.*

4.5 Experimental results

Figure 4.13 shows the profile of a structure fabricated in AZ 4562 resist. The resist was thermally reflowed at 180 °C for 24 hours. The figure confirms the large surface roughness characteristic to thermal reflow. Moreover, there are ripples on the profile of the surface.

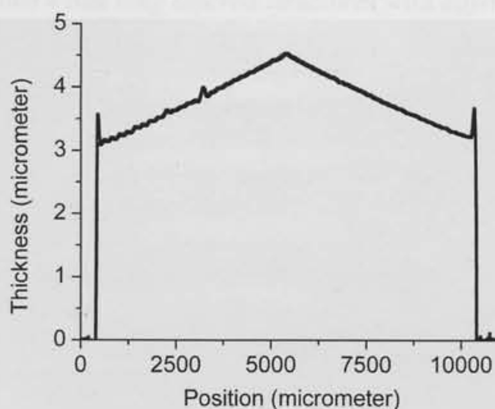

Figure 4.13. *Profile of a pattern on AZ4562 resist. Reflowed only thermally.*

Figure 4.14 shows the profile measurement on 4 tapered photoresist patterns fabricated using AZ 9260 and chemical-thermal reflow technique. The surfaces of the resist patterns are very smooth and without ripple. Thickness variations are 0.2 µm, 0.6 µm, 1.5 µm and 2 µm over a 5 mm length.

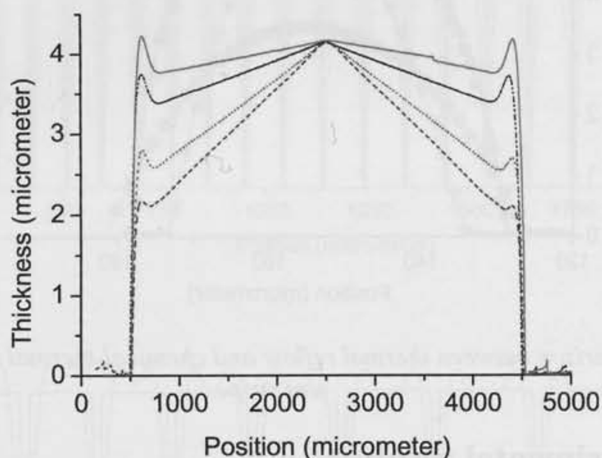

Figure 4.14. *Measured profile of four 10 mm long tapered structures with different slopes and same thickness in AZ 9260.*

Figure 4.15 shows a photograph of 4 tapered structures fabricated using the combined thermal-chemical reflow of AZ 9260 also. The colour profile along the structure due to interference demonstrates the sloped layer thickness.

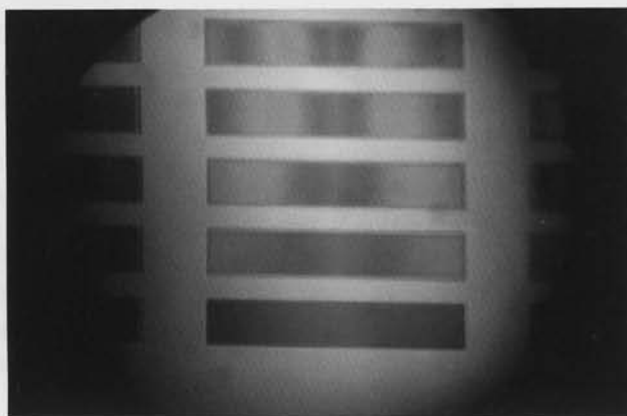

Figure 4.15. *Colour change along the resist layer proves the thickness slope. The slope increase from bottom to the top.*

Figure 4.16 shows profile on structures fabricated with thin resist of SPR 3012. The thickness of resist layer is 1.2 µm after spin coating. It is possible to achieve very small slope angles using thin resist. However chemical-thermal process optimization is more challenging due to higher viscosity of the patterned resist. The slope thickness changes from 0.6 µm to 0.85 µm in 2.0 mm length which means a slope angle of 0.005º in one structure. In the other structure the thickness changes from 0.5 µm to 0.85 µm in 1.75 mm of the length, which corresponds to a slope of 0.11º.

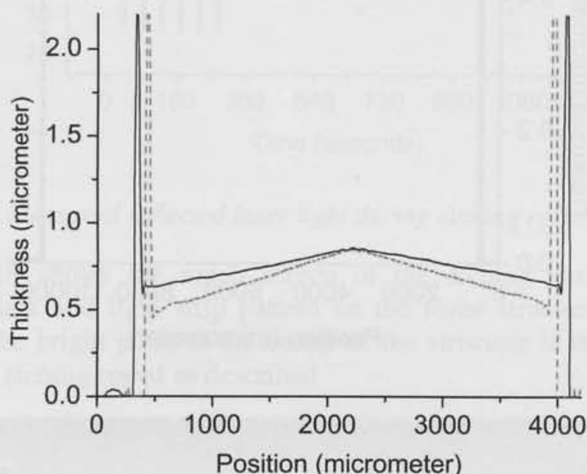

Figure 4.16. *Profile of two 4 mm long tapered structures with different slopes and same thickness in SPR3012.*

4.6 Topography transfer by plasma etching

The resist topography can be subsequently transferred into silicon or silicon-dioxide if required by the application. The benefit is that such materials are more stable and more reliable for different devices. Another benefit is better optical properties of these materials than resist. Moreover, by increasing the resist/oxide or resist/silicon etch-rate ratio the slope angle can be further decreased.

Plasma etching in a CF_4, SF_6 and O_2 mixture has been used to transfer the resist slopes into silicon. Figure 4.17 shows the results of profile measurement on the etched structure in silicon. Although a number of imperfections can be identified in the replicated structure, which can be significantly reduced in an

improved etching process, the result shows a structure that can be used as a LVOF in the Infra-Red (IR) spectral range. The thickness of the silicon structure changes 150 nm in 5 mm length which gives a slope of 0.0017º.

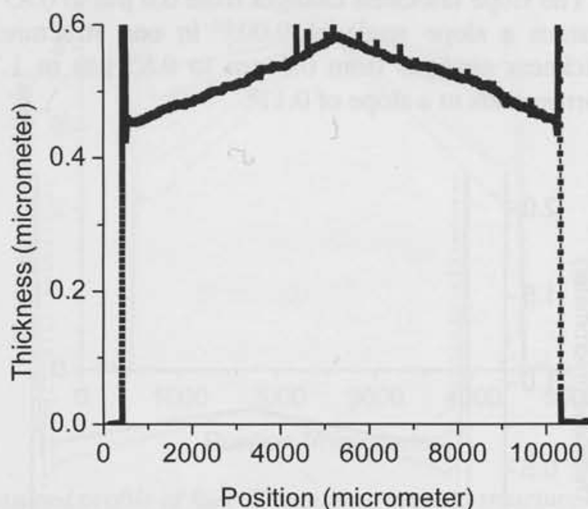

Figure 4.17. *Slope in Silicon by transferring resist topography using plasma etching.*

The process for transferring the resist structure into SiO_2 is optimized to get an optically smooth surface. The process uses a mixture of NF_3 5 sccm, Ar 50 sccm and O_2 30 sccm at 20 mTorr with 100 Watt. For optimization purposes a test resist is patterned on 500 nm of SiO_2. The chamber pressure should be set to the minimum possible value (typically around 2 – 3 mbarr) to avoid the effect of nano-masking, which results in a rough surface after the plasma etching, as described in [4.15]. A laser spot is put on the surface of the resist and reflected light is measured and plotted versus time. The plot is shown in figure 13 for the optimized mixture of gases. Considering the change in optical thickness and interference, etched rates of the resist and SiO_2 can be derived from the graph. The frequency of the plot changes in the interface between resist and SiO_2. The strong signal of reflected light from SiO_2 in the plot shows that the oxide surface is not getting rough. For this process a resist/SiO_2 etch ratio of 6.2 is achieved. It is possible to increase the etch-rate ratio by increasing the O_2 flow. However, the penalty is a rougher surface on SiO_2. Increasing Ar flow results in a smoother surface by sputtering away the small roughness.

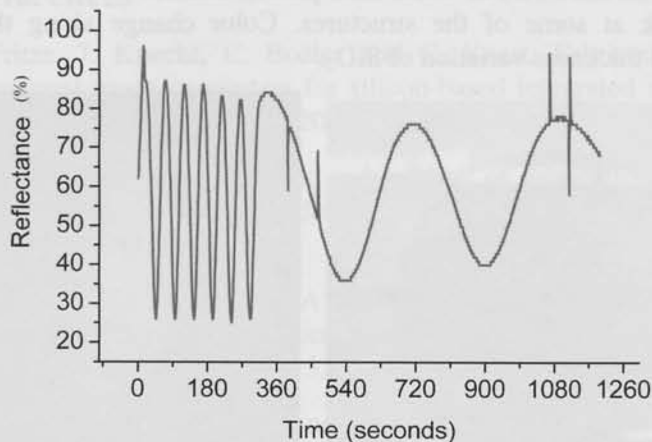

Figure 4.18. *Measured reflected laser light during etching resist on SiO_2.*

Figure 4.19 shows the video screen of the etching system during the etching. The dark and light strip pattern on the resist structure illustrates the slope shape. The bright point at the center of the structure is the laser spot for controlling the etching speed as described.

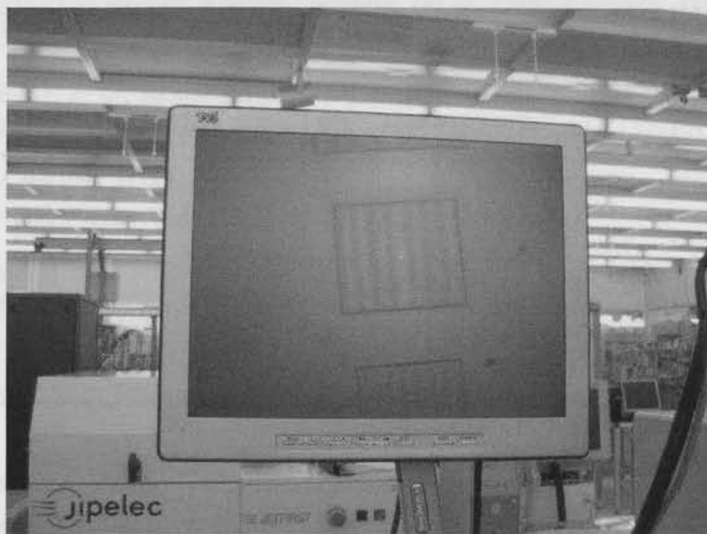

Figure 4.19. *Patterns, due to interference, illustrate the sloped shape of the structures.*

Figure 4.20 shows a full wafer after pattern transfer into SiO_2 together with a closer look at some of the structures. Color change along the structure illustrates the thickness variation of SiO_2.

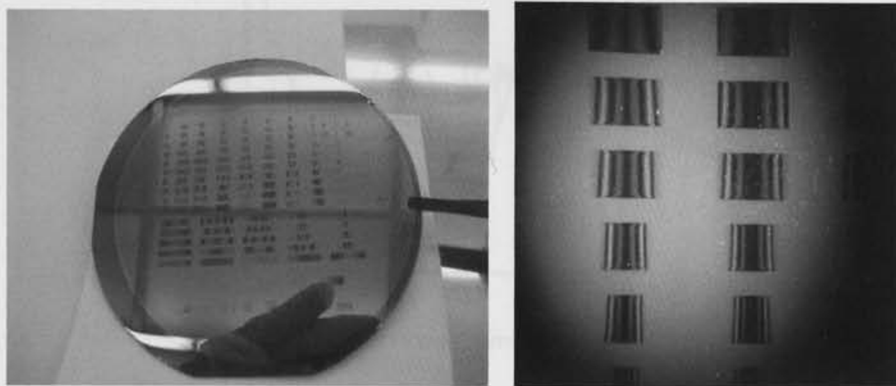

Figure 4.20. *left) A full wafer with different tapered SiO_2 structures. right) several tapered SiO_2 structures.*

Figure 4.21 shows some profile measurement on tapered SiO_2 structures. The center of the structure in Figure 4.21b shows 3 bumps. The center of trenches in the patterned resist was very low at the center position. Therefore, the width of the three center resist strips is large and, as discussed in section 4.4 , no complete reflow has taken place at that location.

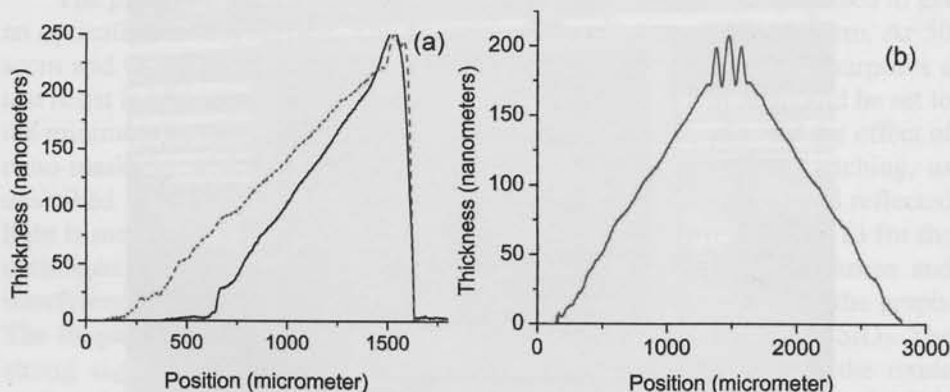

Figure 4.21. *a) Tapered SiO_2 with 0.008º and 0.011º angles. b) Hill-like 0.0065º tapered SiO_2.*

4.7 References

[4.1] M. Fritze, J. Knecht, C. Bozler and C. Keast, Fabrication of three-dimensional mode converters for silicon-based integrated optics *J. Vac. Sci.. Technol.* B, Volume **21**, (2003), pp. 2897-902.

[4.2] Duk-Jong Choi, Shadow mask and method of fabrication of vertically tapered structure using shadow mask, *US Patent application* US 20060032832-A1.

[4.3] A. Piegari, J. Bulir and A. Krasilnikova, Variable narrow-band transmission filters for spectrometry from space. 2. Fabrication process *Appl. Opt.*, Volume **47**, Issue 13, (2008), pp. C151-C156.

[4.4] Che-Ping Lin, Hsiharng Yang and Ching-Kong Chao, Hexagonal microlens array modeling and fabrication using a thermal reflow process, *J. Micromech. Microeng.*, Volume **13** , Number 5, (2003), pp. 775-781.

[4.5] F.T. O'Neill and J.T. Sheridan, Photoresist reflow method of microlens production Part I: Background and experiments *Int. J. Light Electron Opt.*, Volume **113**, Issue 9, (2002), pp. 391-404.

[4.6] F.T. O'Neill and J.T. Sheridan, Photoresist reflow method of microlens production Part II: Analytic models, *Int. J. Light Electron. Opt.*, Volume **113**, (2002), Issue 9, pp. 405-420.

[4.7] Lee J-E *et al*, Resist reflow modeling including surface tension and bulk effect, *Japan. J. Appl. Phys.*, Volume **46**, (2007), pp. 1757-1762.

[4.8] J.M Park *et al*, Photoresist adhesion effect of resist reflow process, *Japan J. Appl. Phys.*, Volume **46**, (2007), pp. 5738-5741.

[4.9] Method and apparatus for compactly coupling an optical fiber and a optical planar waveguide, *European patent application*, EP1555551A1.

[4.10] T. A. Osswald , L.S. Turng and P.J Gramann, *Injection Molding Handbook* , Munich: Hanser, (2007), ISBN:978-1569904206.

[4.11] D. J. Acheson, Elementary Fluid Dynamics, Oxford Applied Mathematics and Computing Science Series, (1990).

[4.12] T. S. Chow, Wetting of rough surfaces *J. Phys.: Condens. Matter*, Volume **10**, Number 27, (1998), pp. L445-L451.

[4.13] COMSOL Multiphysics 3.4, (2008), COMSOL Inc., *www.comsol.com.*

[4.14] S. Rabier and M. Medale, Computation of free surface flows with a projection FEM in a moving mesh framework, *Comput. Methods Appl. Mech. Eng*, Volume **192**, Issues 41-42, (2003), pp. 4703-4721.

[4.15] K. Mohamed, M.M. Alkaisi, Three-dimensional pattern transfer on quartz substrates, Microelectronic Engineering, Volume **87**, Issues 5-8, *The 35th International Conference on Micro- and Nano-Engineering (MNE)*, (2010), pp. 1463-1466.

5 *LVOF spectrometer for visible spectrum*

5.1 Introduction

In this chapter design, fabrication and measurement results of the LVOF for the visible spectral band are presented. Two main different designs are presented; the first for the spectral band of 570 nm – 740 nm and the other for the narrower spectral band of 610 nm to 680 nm. The signal processing algorithm to improve spectral resolution which was introduced in 2.4 is explained in details and actually used for the first time in this chapter. The signal processing algorithm is also used in the designs presented in the coming chapters.

The theory and main fabrication steps to make LVOFs have already been discussed in the previous chapters. However, in this chapter we briefly revisit the design parameters and analyze their impact in this particular band. Characterization and measurements are presented.

5.2 Design of the LVOF for 570 nm – 740 nm

The multilayered filtered used for the LVOF in this range is shown in Table 5.1. The LVOF is intended to operate in the band between 570 nm and 720 nm. This wavelength range contains the essential information in applications such as fluorescence spectroscopy of plants and H-α spectroscopy [5.1]-[5.2]. The performance characterization of the LVOF and the resulting microspectrometer in this wavelength range can be tested using a Neon lamp, which has most of its major peaks in this wavelength range. The LVOF is based on the design presented in Table 5.1. The LVOF operates at higher order compared to the visible Fabry-Perot filters presented in section 3.3 . The operating order of a Fabry-Perot can be expressed as: $N=2nd/\lambda_0$ or N=d/(2QWOT). Thus, this LVOF operates at the 4th order for the central (reference) wavelength. The transmission spectrum of the LVOF for three different values of the cavity thickness is plotted in Figure 5.1.

Table 5.1.*Designed values of thicknesses for visible LVOF*

Layer #	Material	Thickness (QWOT)	Thickness (nm)
Substrate	Glass	-	-
1	TiO_2	1	68.5
2	SiO_2	1	112
3	TiO_2	1	68.5
4	SiO_2	1	112
5	TiO_2	1	68.5
6	SiO_2	1	112
7	TiO_2	1	68.5
8	SiO_2	7.1 – 9.3	800 - 1050
9	TiO_2	1	68.5
10	SiO_2	1	112
11	TiO_2	1	68.5
12	SiO_2	1	112
13	TiO_2	1	68.5
14	SiO_2	1	112
15	TiO_2	1	68.5

Applying the theories mentioned in chapter 2 to Figure 5.1 results in $\Delta\lambda$ = 720 nm – 470 nm = 250 nm. This is the rejection bandwidth of the Fabry-Perot mirrors which is inherent to the dielectric materials. The maximum operating wavelength is 720 nm and the minimum operating wavelength is 470 nm. Based on the value of $\Delta\lambda$, we know from chapter 2 that the maximum possible Free-Spectral-Range (FSR) is $\Delta\lambda/2$ = 125 nm. However, the Fabry-Perot structure of

the LVOF is intended to be used at a higher order. From Figure 5.1 we can observe FSR = 100 nm. For each thickness of the cavity we can note from Figure 5.1 that the filter has two or three transmission peaks in the $\Delta\lambda$ wavelength range.

In other words, if we limit the operating spectral range of the LVOF to the FSR, at position along the LVOF (for each cavity thickness), the LVOF allows only one wavelength. When the entire spectral range is considered for measurements, at each position along the LVOF (for each cavity thickness) the LVOF passes through two or three wavelengths.

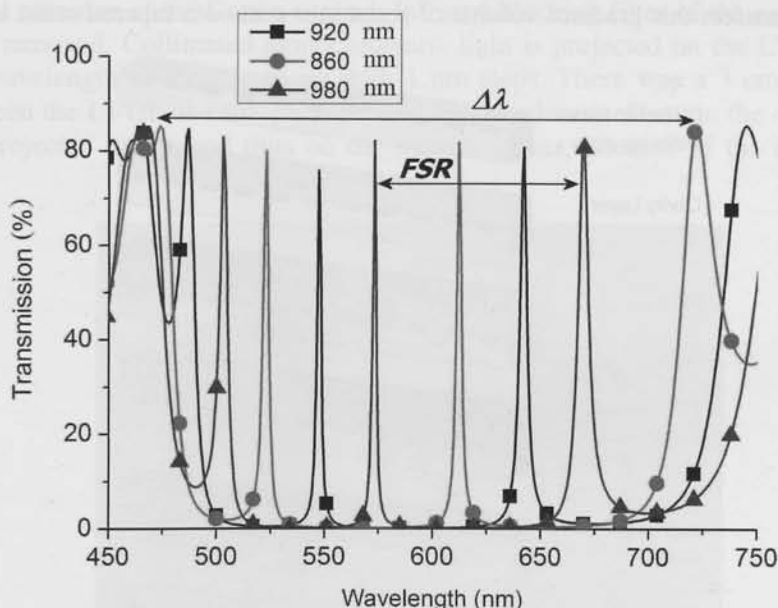

Figure 5.1. *Simulated spectra of LVOF for three values of the cavity thickness.*

Considering this, two different types of LVOF have been fabricated and measured. The first type only covers a small spectral range of 80 nm, and the second type covers the entire $\Delta\lambda$ range. It will be shown that signal processing makes it possible to differentiate between the different transmission peaks that occur at each location of LVOF when the entire $\Delta\lambda$ range is used.

5.3 Fabrication of the LVOFs

LVOF fabrication is based on reflow of a specially patterned layer of resist. Figure 5.2 shows the process steps for the fabrication of an IC-Compatible LVOF. The process starts by deposition of the lower dielectric mirror stack and the oxide layer that results in the cavity layer (as in section 3.3). Photoresist is spin coated as the next step and lithography is applied to define the strip-like structure in the resist layer to be reflowed (As explained in details in chapter 4). A series of trenches of constant width and with variable spatial frequency or trenches of variable width and constant pitch are etched over the length of the strip of resist to vary the effective amount of resist per unit area. The subsequent reflow transfers this gradient volume of resist into a smooth tapered resist layer.

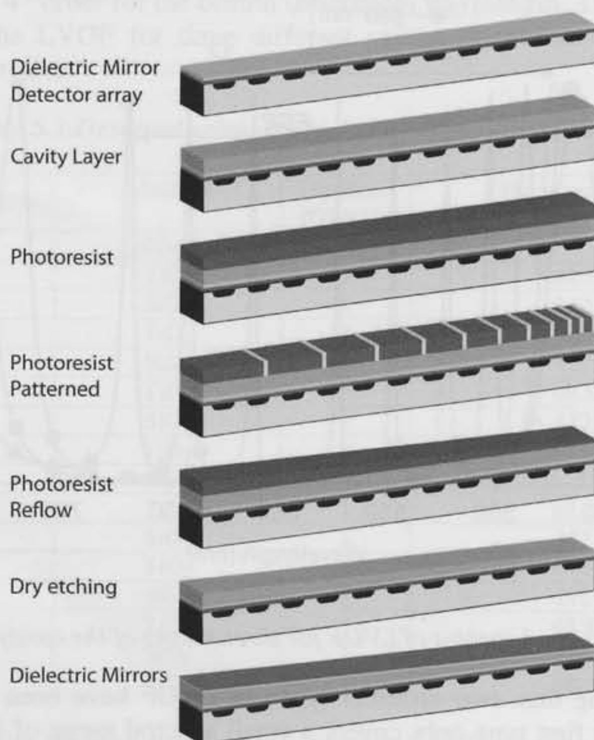

Figure 5.2. *Process flow for fabrication of Linear Variable Optical Filters.*

The topography of the tapered resist layer is transformed into the thick oxide cavity layer by an appropriate plasma etching process (as described in section 4.6). The process is completed by deposition of the top dielectric mirror

stack. This LVOF is fabricated on a glass substrate. However, fabrication directly on a CMOS detector chip as a compatible post-process is well possible and will be shown in section 7.5 .

5.4 Characterization of LVOFs

Characterization involves illumination of the LVOF with monochromatic light and recording the image due to transmission through the LVOF using a CCD. The wavelength of the monochromatic light is swept over the wavelength range of the LVOF. For an initial test a Canon EOS 10D camera has been used for the characterization of the LVOF filter. Figure 5.3 shows the LVOF placed on the entrance of the Canon camera. Infrared blocking filter of the camera has been removed. Collimated monochromatic light is projected on the LVOF and the wavelength of light is swept with 1 nm steps. There was a 3 cm distance between the LVOF and the camera. This has an adverse effect on the quality of the projected image and thus on the measurements, because of the diverging light.

Figure 5.3. *LVOF deposited on the glass mounted at the entrance of the Camera. The glass contains five different LVOF filters.*

Figure 5.4 shows the projected image on the camera at several wavelengths. The illuminated part moves along the detector as the wavelength is swept. The illuminated strip is around 1 mm, which is a much larger spot size than the calculated 75 μm strip size. This is directly due to the distance between the

LVOF and the detector. It can be easily calculated that a 1° diverging angle causes a 1mm area spot size in case of a 3cm distance.

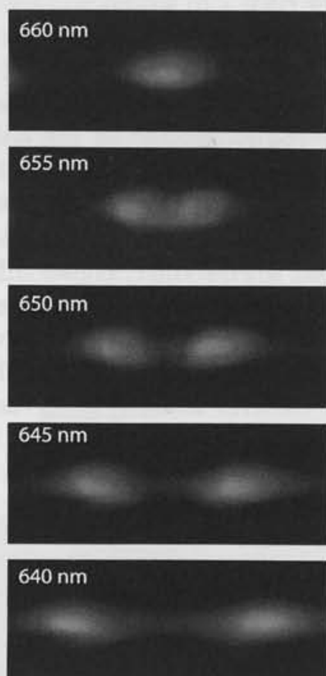

Figure 5.4. *Image recorded on the CCD at several wavelengths.*

To better characterize the LVOFs, these need to be placed as close as possible to the detector. LVOFs are mounted on a commercial CMOS camera. Figure 5.5 shows the LVOF deposited on a glass substrate mounted on a CMOS camera. When the LVOF is as close as possible to the detector widening of the spot on the recorded image is avoided and better characterization is done.

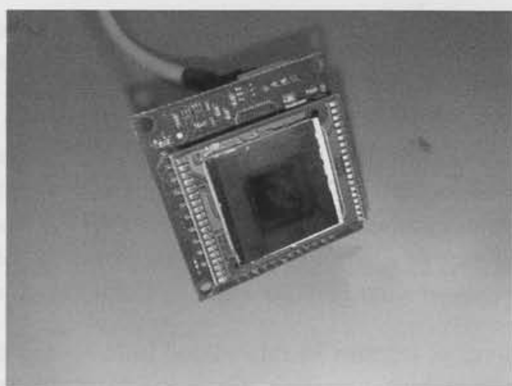

Figure 5.5. *LVOF deposited on the glass mounted on the CMOS camera.*

Figure 5.6 illustrates the schematics for characterization of the LVOFs. In simple case we avoid imaging optics by directly putting the LVOF filter right on the top of the detector. Similar to the previous mentioned procedure the camera with the LVOF on the top is placed in front of a monochromator and the wavelength of the light projected on the camera is swept with minimum possible step size in the entire operating wavelength range of the LVOF. The minimum wavelength step size in our case is 0.5 nm.

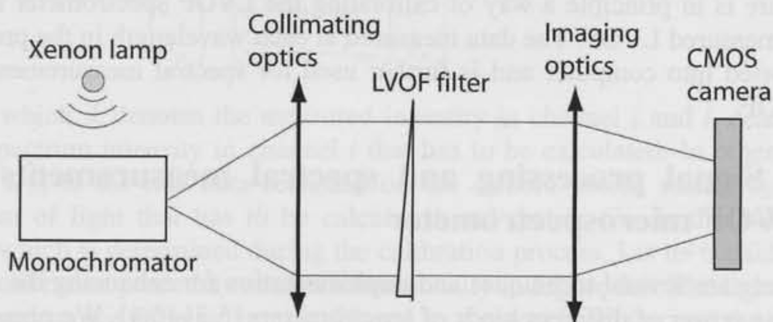

Figure 5.6. *Schematic for characterization of Linear Variable Optical Filters.*

Figure 5.7 shows recorded image on the camera when LVOF is mounted on the top. Comparison with Figure 5.4 shows much smaller width of the lines, due to less divergence of the light.

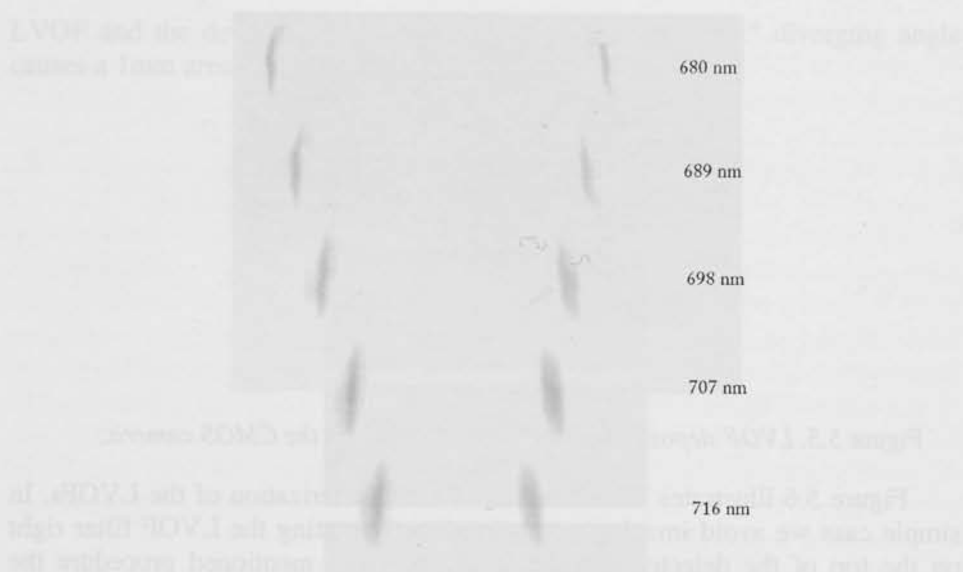

Figure 5.7. *Inverted recorded image when LVOF is on top of the camera.*

The measurement results are presented in more detail in the following sections for the two different LVOFs mentioned earlier. The characterization procedure is in principle a way of calibrating the LVOF spectrometer resulted by the measured LVOF. The data measured at each wavelength in the procedure is imported into computer and is further used for spectral measurements with the LVOF.

5.5 Signal processing and spectral measurements with LVOF microspectrometer

There are several techniques and implementation for enhancing the spectral resolving power of different kinds of spectrometers [5.3]-[5.4]. We present here an algorithm based on Least Mean Square (LMS) and discuss the necessity and importance of its application for LVOF measurements.

A LVOF operating within its FSR with a certain HPBW at each position, in its simplest application can provide FSR/HPBW spectral channels. For the LVOF with layers defined in Table 5.1 and transmission spectra shown in Figure 5.1, this equals to 40 channels each 2.5 nm wide. Although this is already a significant advantage compared to discrete number of Fabry-Perot filters, we can show that using some numerical analysis and signal processing it

is possible to further improve the number of available spectral channels and thus the resolving power of the microspectrometer.

The LVOF is placed on top of a detector array or camera with a small pixel size. From the characterization of the LVOF it is observed that the illuminated region on the detector shifts over around 5 – 10 pixels (depending on the specifics camera and LVOF) for each 1 nm of wavelength shift of the projected light. The basic idea is to use this fact by finding a simple mathematical model which allows us to detect small changes on the pixels intensity.

Let us assume the spectral bandwidth of interest is divided into N spectral channels and there exists N spectrally different (independent) detectors. The element C_{ij} in matrix C is defined as the intensity of channel i of the detector to component j in the spectrum (i, j = 1...N). The matrix C can be directly constructed from the data of a calibration measurement process. The maximum value of N is the number of the pixels on the camera, but can be limited by the spectral capability of the calibrating instrument (a monochromator). Hence, the measured intensity on the detector channels can be described as:

$$\begin{bmatrix} d_1 \\ d_2 \\ \ldots \\ d_N \end{bmatrix} = \begin{bmatrix} c_{11} & c_{12} \ldots c_{1N} \\ c_{21} & c_{22} \ldots c_{21} \\ \ldots & \ldots \ldots\ldots \\ c_{N1} & c_{N2} \ldots c_{NN} \end{bmatrix} \begin{bmatrix} I_1 \\ I_2 \\ \ldots \\ I_N \end{bmatrix} \text{ or } D_{IN} = C_{NN} * I_{IN} \qquad (5.1)$$

In which d_i denotes the measured intensity in channel i and I_i denotes the input spectrum intensity in channel i that has to be calculated. In other words, Matrix D_{IN} is the raw data recorded on the camera pixels, matrix I_{IN} is the spectrum of light that has to be calculated and matrix C_{NN} is the calibration matrix which is determined during the calibration process. Let us consider once again calibration procedure shown schematically in Figure 5.6. The light from a broadband source (Xenon lamp) is filtered by a monochromator and the selected wavelength is varied in the spectral range of interest for all the N spectral channels. For each spectral channel from the above equations, calibration is equivalent to deliberately having: $I = [0, 0, \ldots 0, I_m = 1, 0, \ldots 0]$ when channel m is selected from the monochromator. In this case the recorded intensities on the pixels give the values of column m of the C matrix:

$$\begin{bmatrix} d_1 \\ d_2 \\ \ldots \\ \ldots \\ \ldots \\ d_N \end{bmatrix} = \begin{bmatrix} c_{11} & c_{12} \ldots c_{1N} \\ c_{21} & c_{22} \ldots c_{21} \\ \ldots & \ldots \ldots\ldots \\ \ldots & \ldots \ldots\ldots \\ \ldots & \ldots \ldots\ldots \\ c_{N1} & c_{N2} \ldots c_{NN} \end{bmatrix} \begin{bmatrix} 0 \\ 0 \\ \ldots \\ I_m \\ \ldots \\ 0 \end{bmatrix} \rightarrow \begin{bmatrix} d_1 \\ d_2 \\ \ldots \\ d_N \end{bmatrix} = \begin{bmatrix} c_{1m} \\ c_{2m} \\ \ldots \\ I_{Nm} \end{bmatrix} \tag{5.2}$$

Repeating the procedure for all the N spectral channels results in determination of C_{NN} matrix. Plotting the rows and columns of the C matrix, Figure 5.8, gives good information about the spectral response of the LVOF.

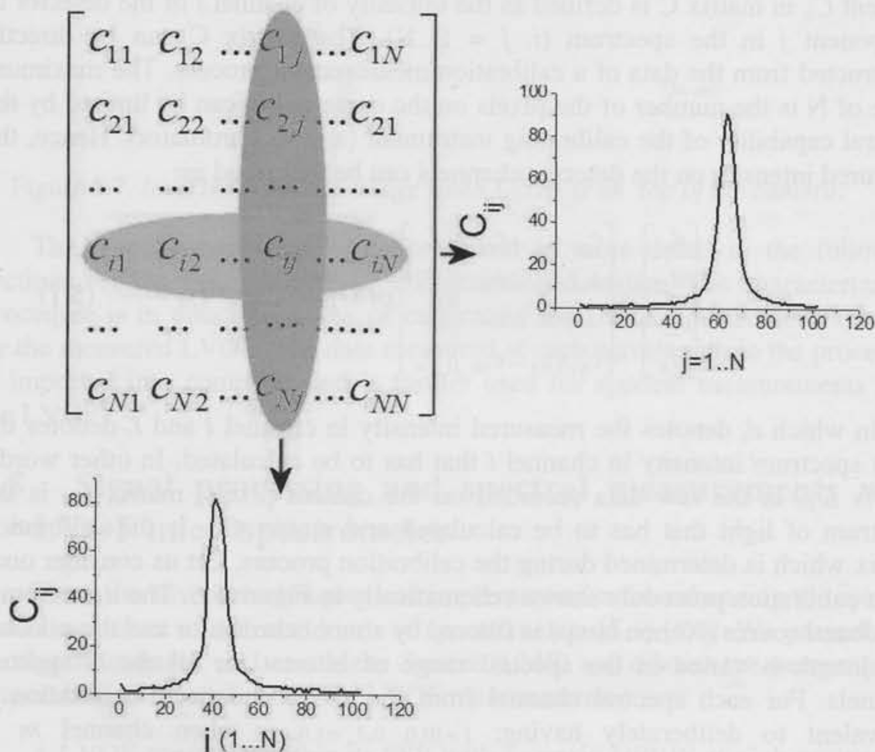

Figure 5.8. *Plotting rows and columns of the calibration matrix.*

The plot of the i-th row of the C matrix, demonstrates the spectral response of the i-th channel in the detector array and the plot of the j-th row of the C matrix shows the recorded response on the detector array with for the monochromatic wavelength of channel j-th.

For a properly designed and fabricated LVOF, Matrix C has no singularity and it is possible to take the inverse transform of the matrix. Therefore, matrix I can be calculated as:

$$\begin{bmatrix} I_1 \\ I_2 \\ \dots \\ I_N \end{bmatrix} = \begin{bmatrix} c_{11} & c_{12} \dots c_{1N} \\ c_{21} & c_{22} \dots c_{21} \\ \dots & \dots \dots\dots \\ c_{N1} & c_{N2} \dots c_{NN} \end{bmatrix}^{-1} \begin{bmatrix} d_1 \\ d_2 \\ \dots \\ d_N \end{bmatrix} \quad \text{or } I_{1N} = C_{NN}^{-1} * D_{1N} \qquad (5.3)$$

However, since the measured matrix D is added with noise the above solution does not give the best answer. The sources of the disturbance (or noise) in the measure raw data include primarily insufficient collimation and out of the band signal. If the disturbance in the system is not negligible as compared to the signal (low SNR) the above approach would result in negative values in some spectral channels which are not physically acceptable. An iterative procedure needs to be implemented to calculate the matrix I by minimizing matrix E:

$$E = \begin{bmatrix} d_1 \\ d_2 \\ \dots \\ d_N \end{bmatrix} - \begin{bmatrix} c_{11} & c_{12} \dots c_{1N} \\ c_{21} & c_{22} \dots c_{21} \\ \dots & \dots \dots\dots \\ c_{N1} & c_{N2} \dots c_{NN} \end{bmatrix} \begin{bmatrix} \widehat{I_1} \\ \widehat{I_2} \\ \dots \\ \widehat{I_N} \end{bmatrix} \qquad (5.4)$$

In which matrix $\hat{I}$ is the estimate of I. The Least Mean Square (LMS) algorithm is implemented based on the following equations:

$$\begin{aligned} E_n &= d - C\hat{I}_n \\ \hat{I}_{n+1} &= \hat{I}_n + \mu C E_n \end{aligned} \qquad (5.5)$$

E_n denotes the error and $\widehat{I_n}$ denotes the estimate of the spectrum at each recursive step. μ is the convergence coefficient. A higher value for μ results in faster convergence of the algorithm. However, it can also result in completely diverging (instability) of the algorithm. The goal of the algorithm is to decrease

the mean square of E_n at each step. This results in the best possible estimate for the spectrum vector $\hat{I}$. The value of E_n does not go to zero due to noise and disturbances in the measurements. The Matlab® code for implementation of the algorithm is presented in an appendix at the end of the thesis.

5.6 Narrowband LVOF

A LVOF based on Table 5.1 has been characterized. The cavity length of this LVOF varies from 850 nm to 980 nm. Therefore the transmission spectral peak goes from 600 nm to 685 nm and is operating in its FSR.

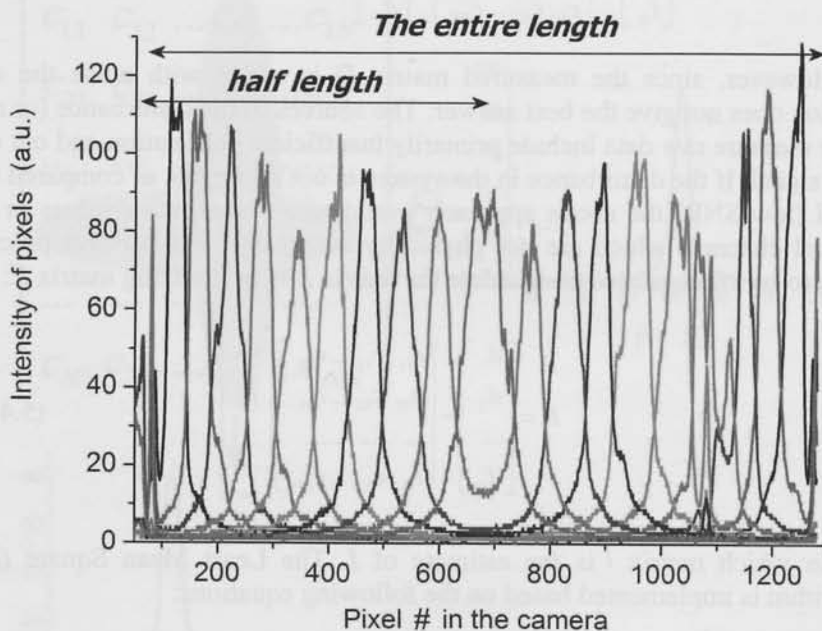

Figure 5.9. *Recorder intensity profile of pixels at 615 nm – 670 nm with 5 nm steps.*

The LVOF is mounted on CMOS camera and the characterization (calibration) procedure is applied with 0.5 nm wavelength steps. Figure 5.9 shows the intensity profile on pixels for the spectral range in between 610 nm and 665 nm with 5 nm steps.

The peak transmission on the camera shifts by 12 pixels / nm. The Half Power Line Width (HPLW) is 40 pixels, which equals to 240 μm in length. As discussed in section 4.3 the structures of LVOF are in principle the result of photolithography and reflow step and have been designed to have hill-shape structures. The thickness increases linearly from the sides to the center which is the thickest part of the LVOF. Therefore each structure includes two identical LVOFs at each side. The transmission peaks can be observed for both of the LVOFs from Figure 5.9. Increasing the wavelength, the transmission peaks at each LVOF side of structure move closer to each other towards the center of the filter structure.

Based on optical designs discussed in section 2.4 , suitable collimating optics has been designed and implemented in a C-mount holder to be put on the top of the CMOS camera, shown in Figure 5.10. Although C-mount holder is relatively bulky, it is a convenient solution when parameters of collimating optics need to be changed for different experiments. In a final microspectrometer the C-mount holder has to be replaced with a miniaturized version.

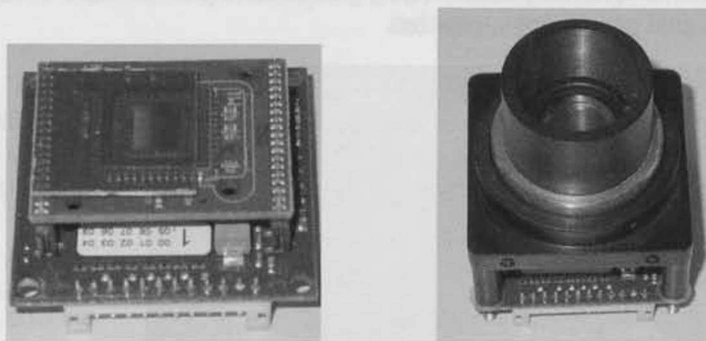

Figure 5.10. *LVOF mounted on the CMOS camera together with the C-mount holder for the collimating optics.*

Figure 5.11 shows a 2D plot of the value of the 121×121 Calibration matrix formed for the LVOF. The x-axis on the plot presents different wavelength channels and the y-axis presents the channels or pixels on the detector array. The plot demonstrates linear movement of illuminated regions on the detector as the wavelength is linearly increased. We can note that there is a one to one relation between the spectral channels and the detector channels. This proves that for each spectral band there is only one of the detector channels which will be excited.

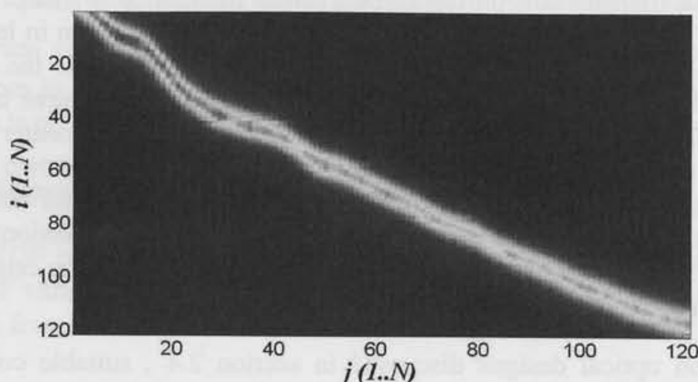

Figure 5.11. *Surface plot for calibration matrix.*

Figure 5.12 shows the image recorded on the camera when LVOF microspectrometer is illuminated by a Neon lamp. The Out-of-band spectra of the Neon lamp, $\lambda < 610$ nm and $\lambda > 670$ nm, have been eliminated by two commercial optical filters. The pixel intensity profile from the recorded image is imported to the signal processing algorithm.

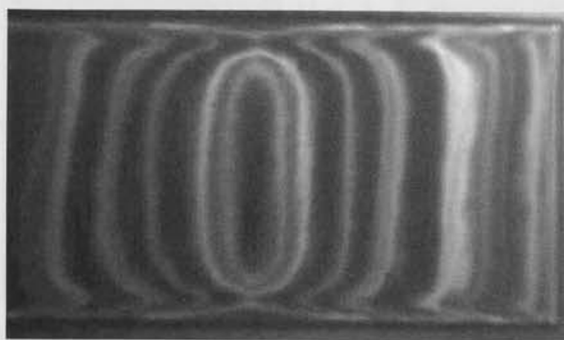

Figure 5.12. *Image recorded by the camera with narrowband LVOF.*

By applying the LMS algorithm the spectrum of the Neon lamp is calculated and plotted in Figure 5.13.

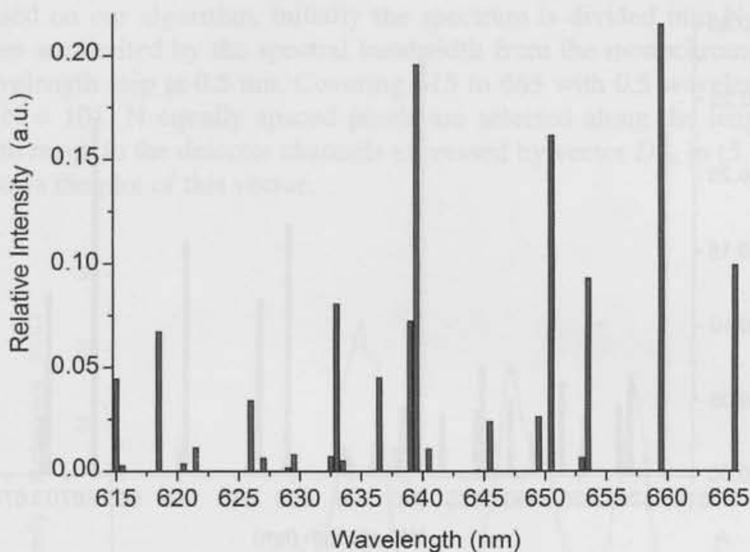

Figure 5.13. *Calculated spectrum from LVOF measurement of Neon lamp in 615 nm - 665 nm range.*

To validate the calculation and also possibility for further comparison another LVOF has also been measured which, cover a slightly wider spectrum, 615 nm – 675 nm. The intension is to resolve the two strong peaks in Neon lamp spectrum at about 670 nm. Figure 5.14 shows the result.

We can see from both calculated spectrum peaks at 640 nm, 650.5 nm, 653 nm, 659 nm. Additionally from Figure 5.14 we can note two peaks at 667.5 nm and 672 nm.

To better understand the purpose of the signal processing and the extraction of the spectrum from recorded image, we can first refer to Figure 5.15 which plots the recorded intensity of the pixels from Figure 5.12. We can intuitively understand that this plot does not directly give us the information about the spectrum of light. Analyzing this data is carried out using the calibration data and LMS algorithm discussed in the previous section.

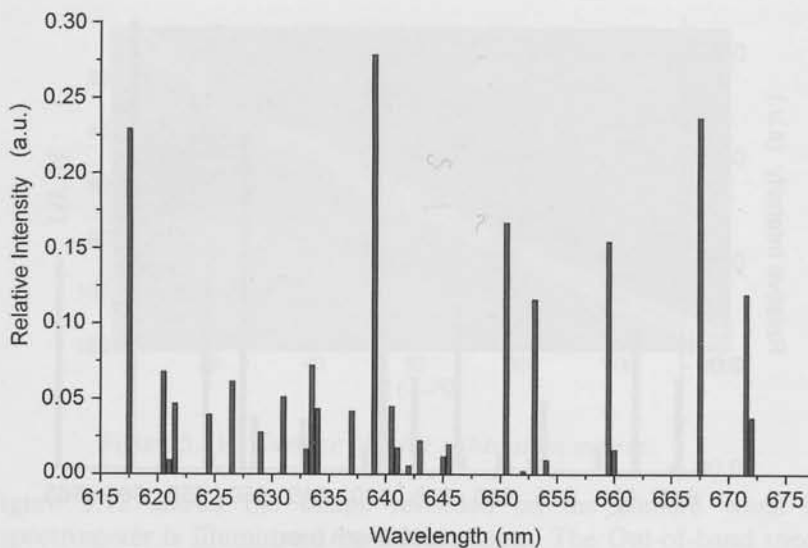

Figure 5.14. *Calculated spectrum from LVOF measurement of Neon lamp in 610 nm - 675 nm range.*

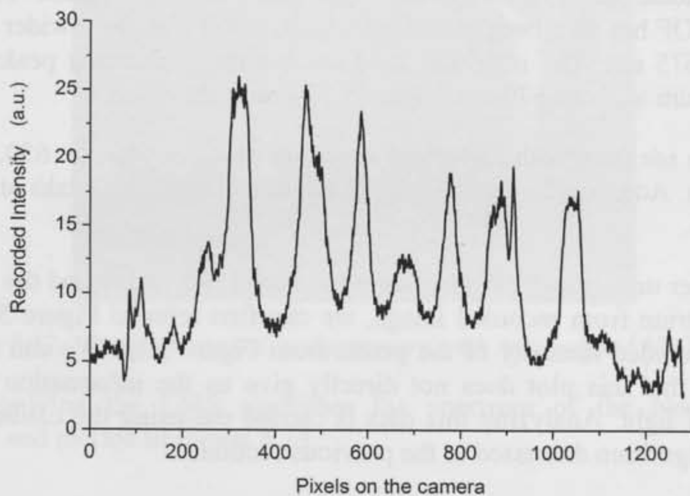

Figure 5.15. *Recorded intensity of pixels on the camera.*

Based on our algorithm, initially the spectrum is divided into N channels. Since we are limited by the spectral bandwidth from the monochromator used, our wavelength step is 0.5 nm. Covering 615 to 665 with 0.5 wavelength steps means N = 101. N equally spaced pixels are selected along the length of the LVOF to result in the detector channels expressed by vector D_{IN} in (5.1). Figure 5.16 shows the plot of this vector.

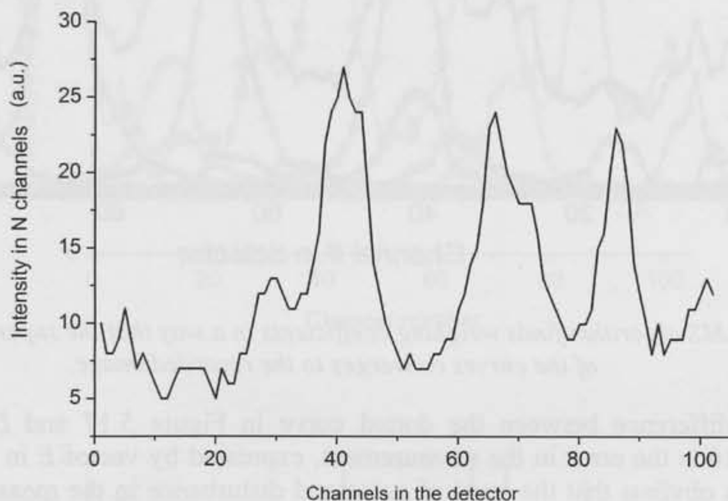

Figure 5.16. *Recorded intensity in detector channels (Vector D_{IN}).*

Extracting the spectrum from this data, or calculating I_{IN}, means finding weighing coefficient for measured intensity profiles in calibration in a way that the resulted superposition will converge to Figure 5.16. This is illustrated in Figure 5.17. The curve, with dot markers on the top, is the result of superposition of other smaller curves. And the smaller curves are the intensity profile curves measured in calibration process multiplied by their weighing coefficient in the LMS algorithm. Mathematically, the dot marked curve is expressed by:

$$\begin{bmatrix} c_{11} & c_{12} \dots c_{1N} \\ c_{21} & c_{22} \dots c_{21} \\ \dots & \dots \dots\dots \\ c_{N1} & c_{N2} \dots c_{NN} \end{bmatrix} \begin{bmatrix} \widehat{I_1} \\ \widehat{I_2} \\ \dots \\ \widehat{I_N} \end{bmatrix}$$

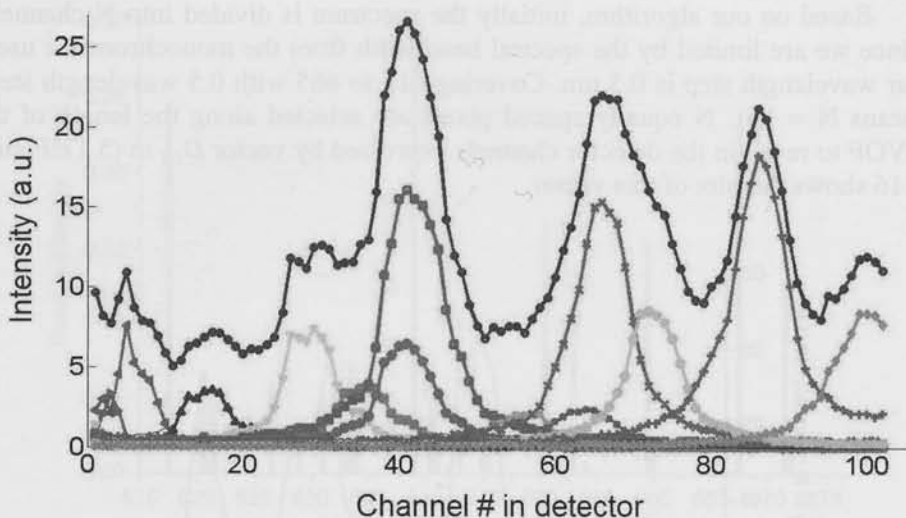

Figure 5.17. *LMS algorithm finds weighing coefficients in a way that the superposition of the curves converges to the recorded image.*

The difference between the dotted curve in Figure 5.17 and D_{IN} from Figure 5.16 is the error in the measurement, expressed by vector E in equation (5.4). It is obvious that the level of noise and disturbance in the measurement, determines the minimum achievable error. Figure 5.18a compared the blue curve in Figure 5.17 and Figure 5.16. The mathematical difference between these two is plotted in Figure 5.18b.

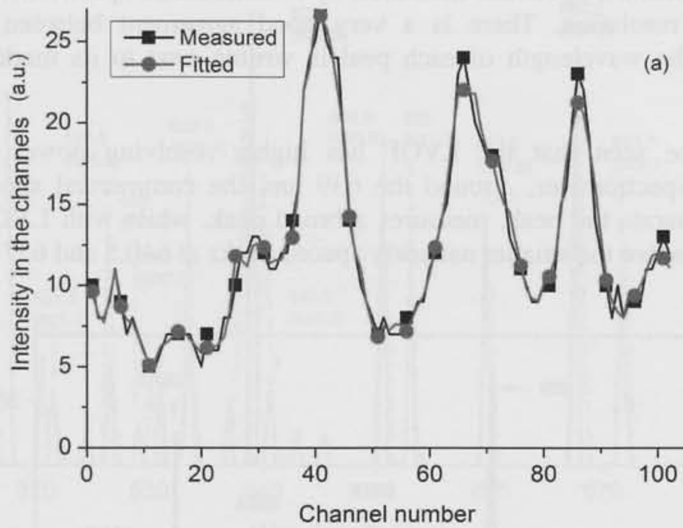

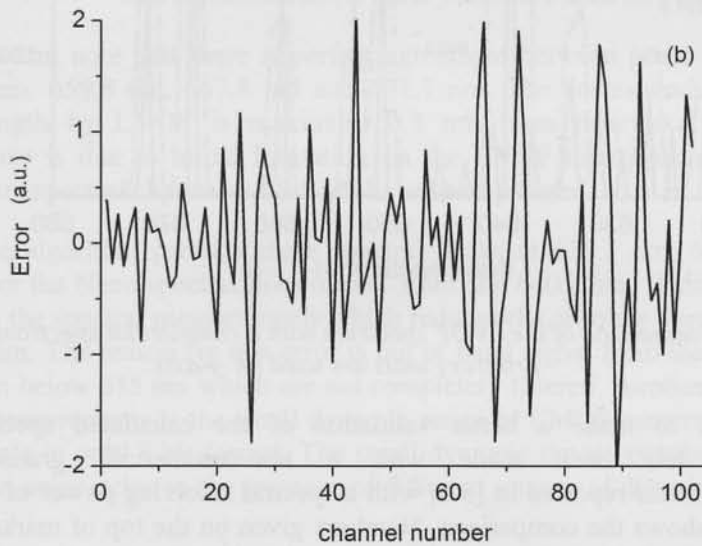

Figure 5.18. *a) Comparison between fitted and measured intensity in the channels b) Plot of the final error.*

Figure 5.19 shows a comparison between the calculated spectrum from the LVOF data with the spectrum measured by a commercial spectrometer with 2 nm spectral resolution. There is a very good agreement between the two spectrums. The wavelength of each peal is written next to its marker in the figure in nm.

It can be seen that the LVOF has higher resolving power than the commercial spectrometer. Around the 639 nm, the commercial spectrometer unable to separate the peak, measures a broad peak, while with LVOF it was possible to resolve the smaller narrowly spaced peaks at 640.5 and 637 nm.

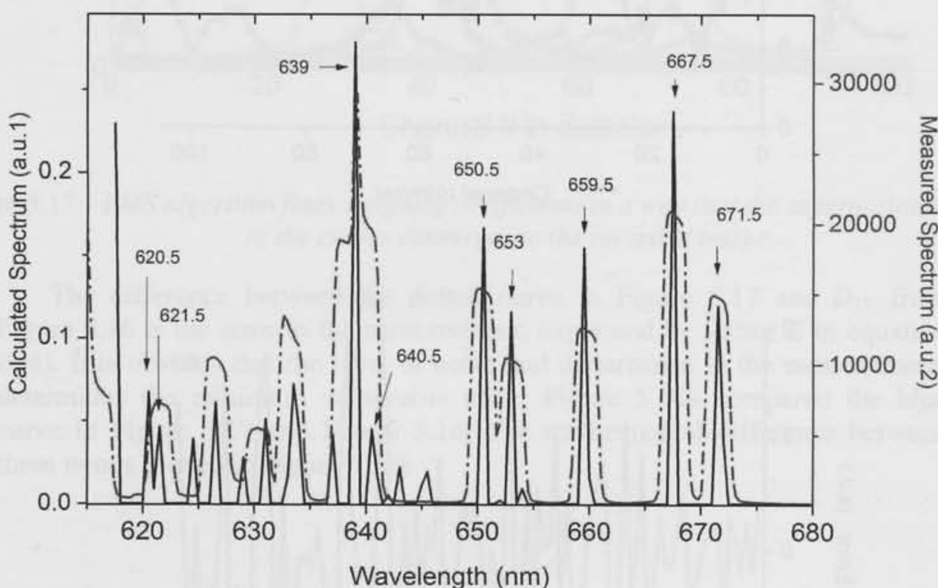

Figure 5.19. *Comparison of the LVOF spectrum with a commercial spectrometer, arbitrary units are used on y-axis.*

In order to make a better validation of the calculated spectrum, a comparison has been made with a non-commercial grating-based microspectrometer reported in [5.5] with a spectral resolving power of 0.7 nm. Figure 5.20 shows the comparison. Numbers given on the top of marker show the wavelength of the peak as calculated from the algorithm and the numbers in parenthesis show the wavelength from the reference [5.6].

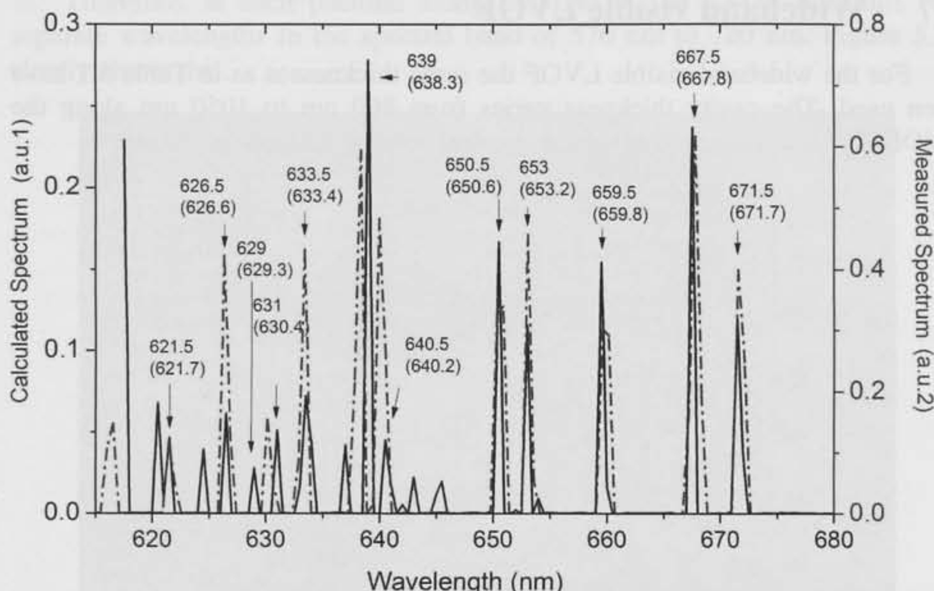

Figure 5.20. *Comparison between LVOF spectrum with a high resolution grating-based microspectrometer, arbitrary units are used on y-axis.*

We can note that there is perfect agreement between peaks at 650.6 nm, 653.2 nm, 659.8 nm, 667.8 nm and 671.7 nm. The corresponding calculated wavelength by LVOF is maximum 0.3 nm from their exact value. The difference is due to initial limitation on the LVOF microspectrometer when minimum spectral channels of 0.5 nm have been selected.

The algorithm predicts three spectral peaks at 637.1 nm, 638.3 nm and 640.5 for the Neon spectral lines of 638.3 nm and 640.2 nm. This is the largest error in the spectral measurements which reduces the absolute spectral accuracy to 0.7 nm. The reason for this error is out of band signal from the strong peaks of Neon below 615 nm which are not completely filtered. Another limitation in these measurements is the small dynamic range of CMOS camera. The camera gives data in only 8-bit format. The small dynamic range contributes to higher signal to noise ration in the presence of different sources of disturbance.

5.7 Wideband visible LVOF

For the wideband visible LVOF the same thicknesses as in Table 5.1 have been used. The cavity thickness varies from 800 nm to 1050 nm along the LVOF. The intention is to cover the spectral band of 570 nm to 720 nm.

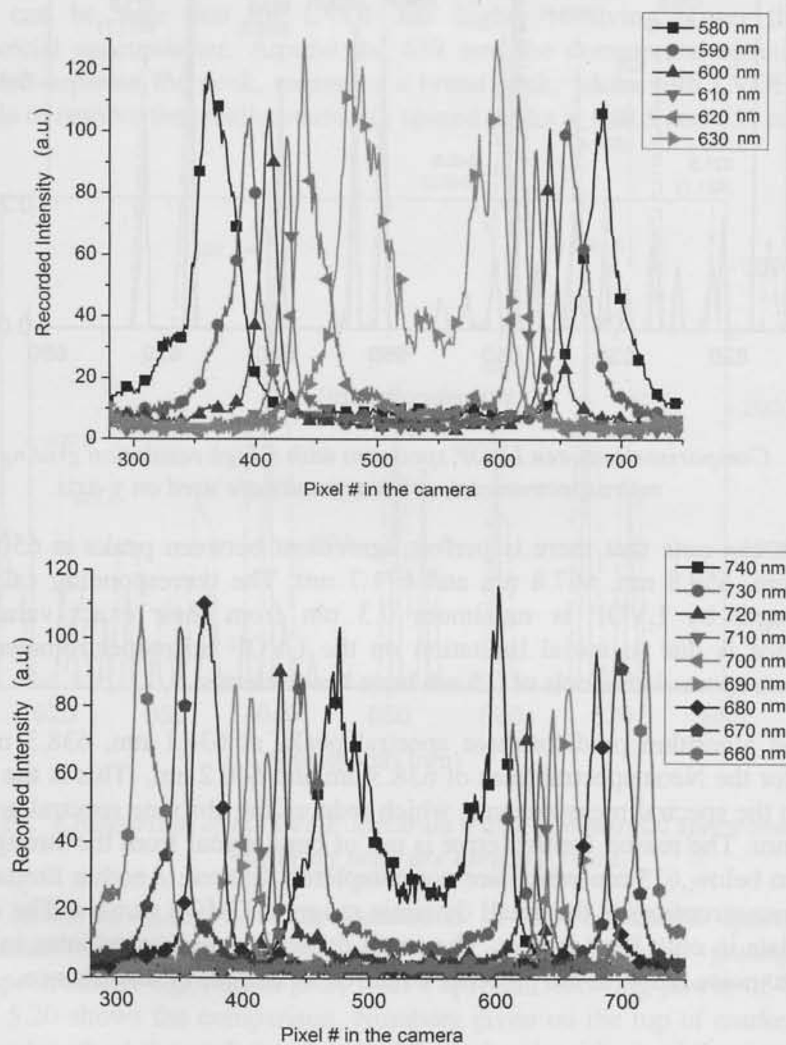

Figure 5.21. *Recorded intensity profile of the camera pixels with monochromatic light from 580 nm to 740 nm.*

Therefore, at each position along the LVOF, the LVOF transmits two separate wavelengths in the spectral band of 570 nm to 720 nm. Figure 5.21 clearly shows this.

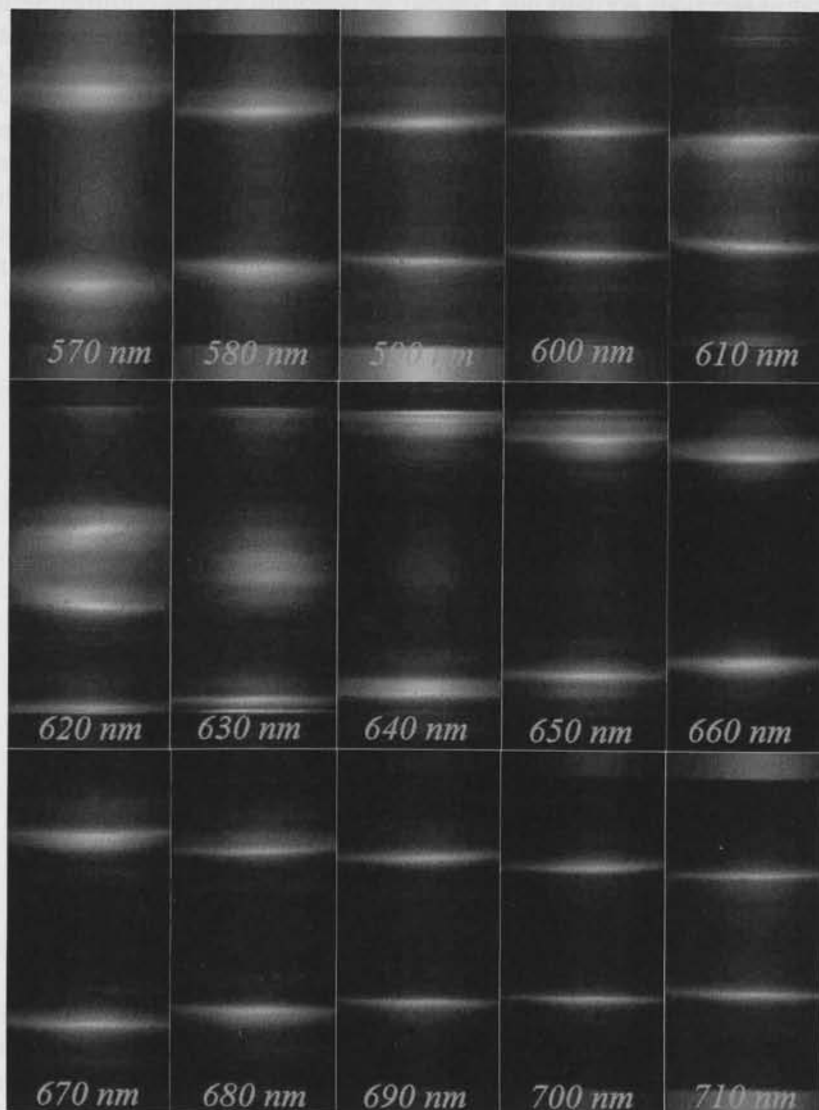

Figure 5.22. *Image recorded on the camera for LVOF to cover 570 nm – 740 nm for several monochromatic light.*

Image recorded on the camera at different wavelengths is shown in Figure 5.22. It can be seen that the illuminated part of the LVOF is at the two sides of the structure for 570 nm and moves toward the center until 630 nm when it will reappear at the sides for 640 nm. Similar to previous section collimating optics are applied using a C-mount. An aperture of 1 mm is used together with an aspherical lens with focal length of 15 mm. The theory is previously explained in 2.4 .

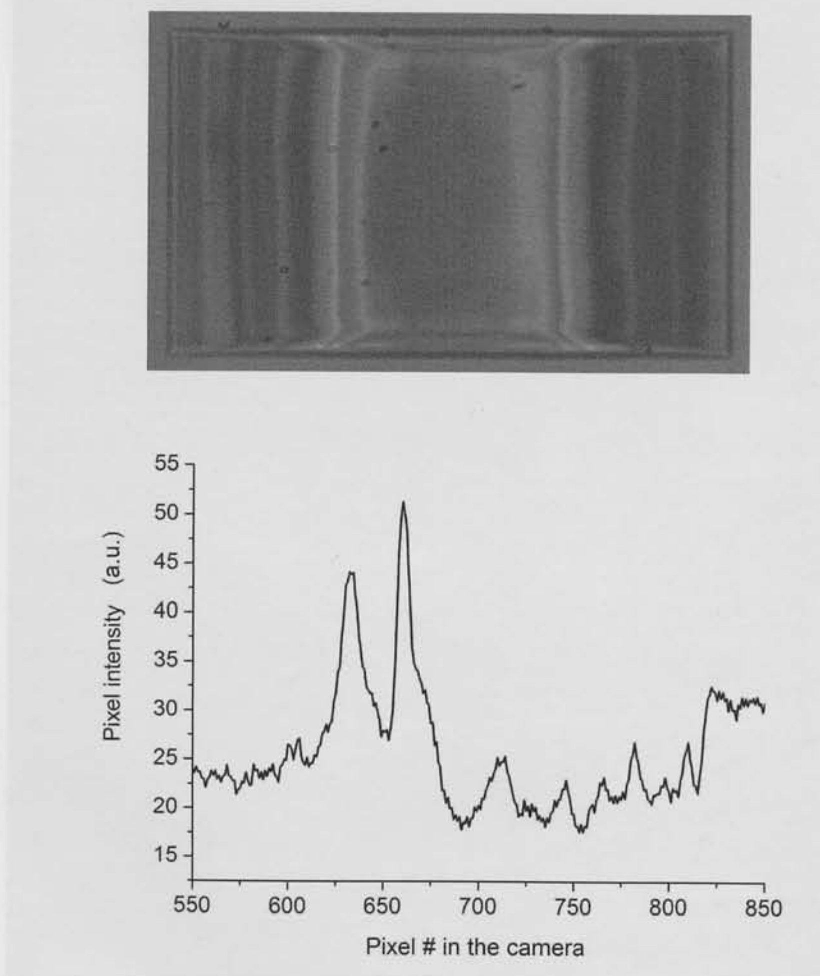

Figure 5.23. *Recorded image together with recorded intensity on the pixels.*

An Infra-red blocking filter has been placed on the aperture of collimating optics to remove the Infra-red part of the Neon lamp spectrum and long-λ pass filter is used to block the spectrum below 570 nm. Figure 5.23 shows image recorded by the camera. The intensity profile recorded on the pixels is the raw data fed to the signal processing algorithm.

Out-of-band light is main source of disturbance or noise in the LVOF system which can substantially limit the performance. Using IR block is essential. The effect of IR block is shown in Figure 5.24. The IR block filter removes the IR light that would otherwise be transmitted through the LVOF and detected on the camera. The separation between different peaks is more obvious when IR has been applied.

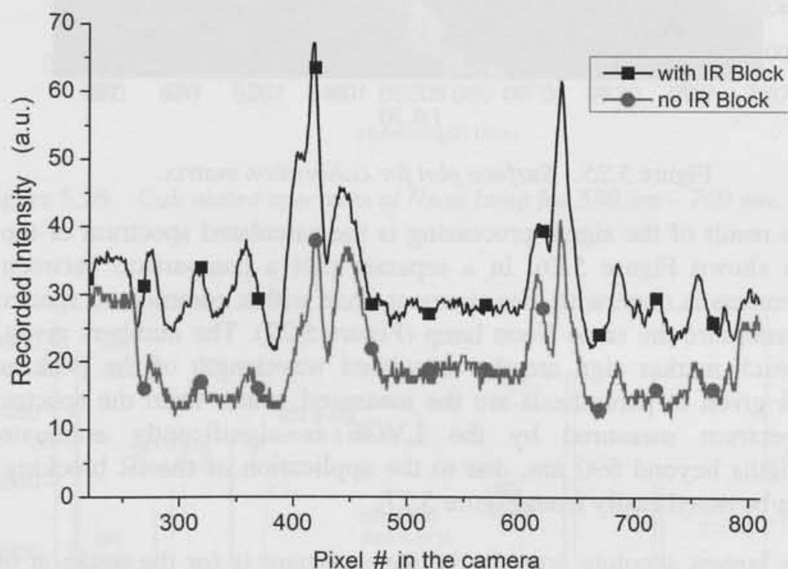

Figure 5.24. *Comparison between recorded image with and without IR block.*

Similar to Figure 5.11 in this case 2D plot of the value of the 171×171 Calibration matrix is plotted in Figure 5.25. The x-axis on the plot presents different wavelength channels and the y-axis presents the channels or pixels on the detector array. The plot demonstrates the movement of illuminated regions on the detector as the wavelength is linearly increased. We can note that there is not a one to one relation between the spectral channels and the detector

channels. This illustration of the calibration matrix shows that each detector channel is illuminated by two separate spectral wavelengths.

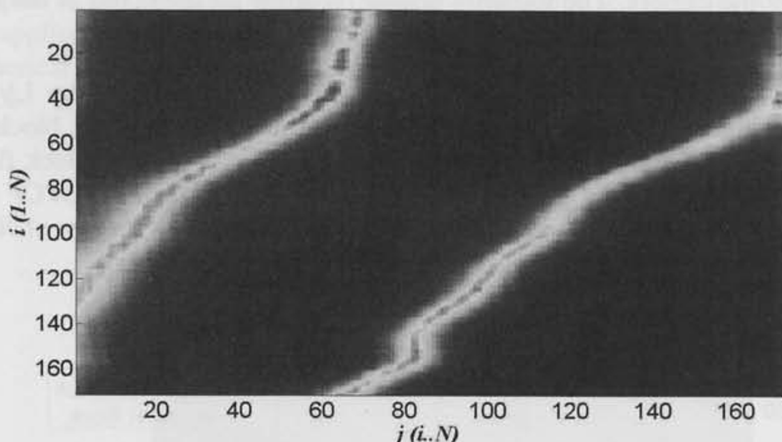

Figure 5.25. *Surface plot for calibration matrix.*

The result of the signal processing is the calculated spectrum of the Neon lamp as shown Figure 5.26. In a separate plot a comparison between these measurements is done with measurement done with a commercial spectrometer used to measure the same Neon lamp (Figure 5.27). The numbers given at the top of each marker sign are the calculated wavelength of the peak and the numbers given in parenthesis are the measured values from the spectrometer. The spectrum measured by the LVOF is significantly attenuated for wavelengths beyond 690 nm, due to the application of the IR blocking filter. This can be noted easily from Figure 5.27.

The largest absolute error in the measurement is for the peaks at 668 nm and 671 nm which are calculated to be at 673 nm and 680 nm. A spectral resolving power of around 3 nm has been achieved by this LVOF filter.

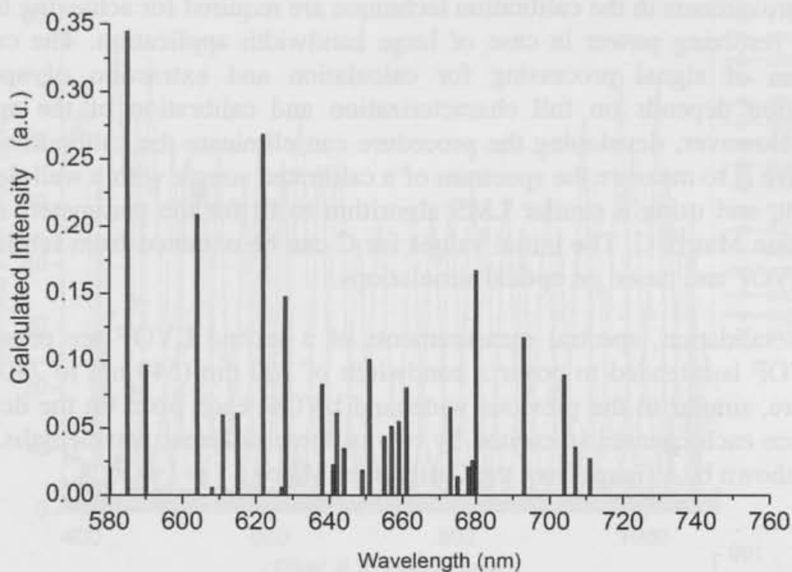

Figure 5.26. *Calculated spectrum of Neon lamp for 580 nm – 760 nm.*

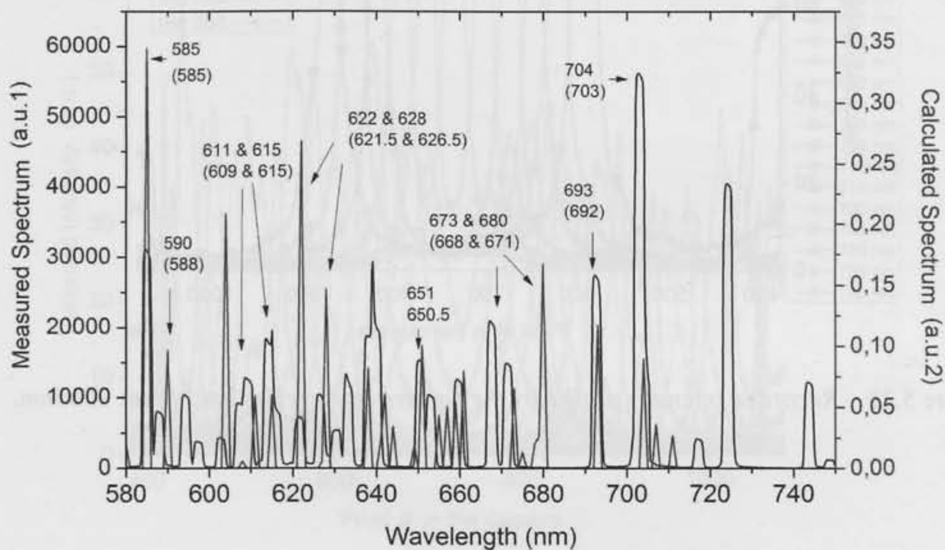

Figure 5.27. *Comparison between LVOF spectrum and a commercial spectrometer.*

Improvements in the calibration technique are required for achieving higher spectral resolving power in case of large bandwidth application. The current procedure of signal processing for calculation and extraction of spectral information depends on full characterization and calibration of the applied LVOF. However, developing the procedure can eliminate the calibration. One alternative is to measure the spectrum of a calibrated source with a well-defined spectrum, and using a similar LMS algorithm to fit for the parameters of the Calibration Matrix C. The initial values for C can be obtained from fabrication of the LVOF and based on optical simulations.

For validation, spectral measurements of a second LVOF are presented. The LVOF is intended to cover a bandwidth of 200 nm (540 nm to 740 nm). Therefore, similar to the previous wideband LVOF, each pixel on the detector and hence each channel is excited by two or three different wavelengths. This will be shown by a figure from the Calibration Matrix.

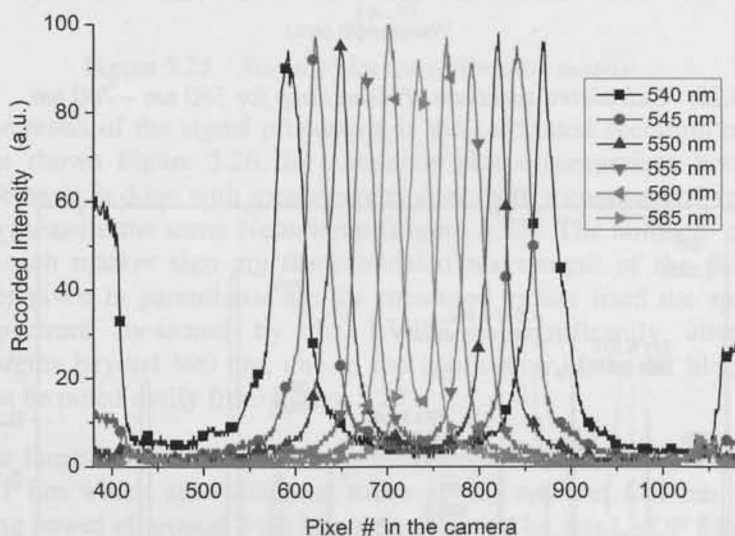

Figure 5.28. *Recorded intensity profile by the camera at wavelengths 540nm - 565nm.*

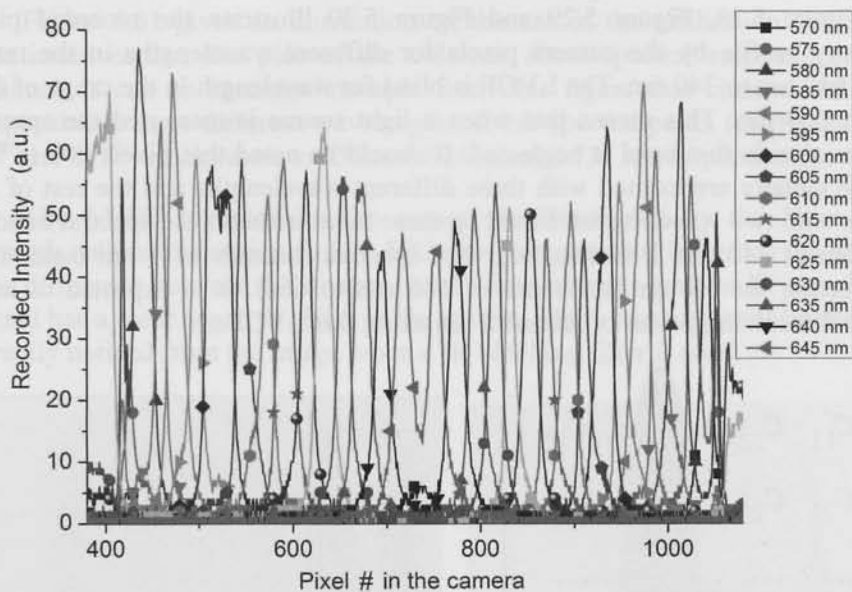

Figure 5.29. *Recorded intensity profile by the camera at wavelengths 570nm - 645nm.*

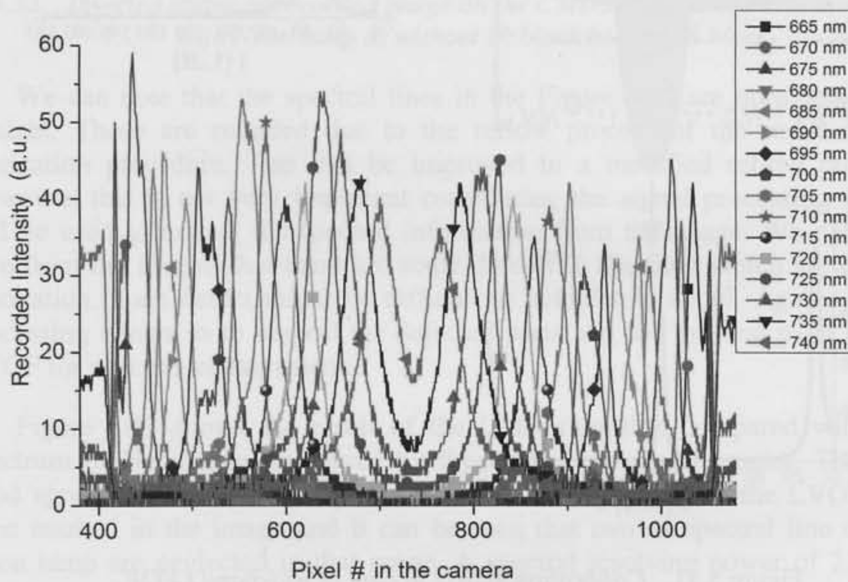

Figure 5.30. *Recorded intensity profile by the camera at wavelengths 665nm - 740nm.*

Figure 5.28, Figure 5.29 and Figure 5.30 illustrate the recorded pixel intensity profile by the camera pixels for different wavelengths in the range from 540 nm to 740 nm. The LVOF is blind for wavelength in the range of 646 nm to 664 nm. This means that when a light source is measured the spectral information in that band is neglected. It should be noted that pixels 600 to 900 on the camera are excited with three different wavelengths and the rest of the pixels with two wavelengths. Based on these measurements the spectral band of 540 nm to 740 nm is divided into 183 spectral channels of 1 nm bandwidth (neglecting the 18 nm bandwidth of 646 nm to 664). It is expected to have spectral resolving power of around 2 nm using this LVOF.

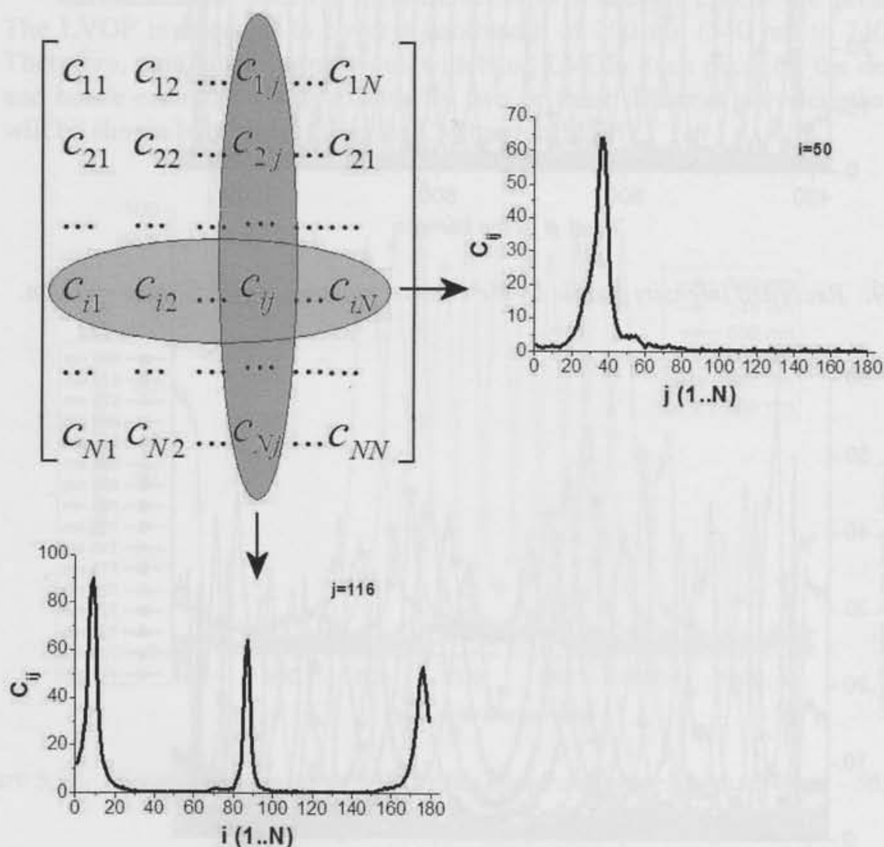

Figure 5.31. *Calibration matrix in case of wideband LVOF.*

Figure 5.31 gives an illustration on the use of the calibration matrix. As mentioned earlier, the plot of the columns show spectral response of each channel. It can be seen for example from this figure that channel 116-th is responsive to three different wavelengths. It has spectral peaks for channels 10th, 84th and 175th which relate to 550 nm, 624 nm and 731 nm respectively.

The LVOF mounted on the camera is illuminated by the Neon lamp through collimating optics. Figure 5.32 show the recorded image on the camera. The difference between the images clearly demonstrates that the IR out of band signal has a clear negative effect in the system. Many more spectral lines can be directly noticed from the image when a IR blocking filter is used.

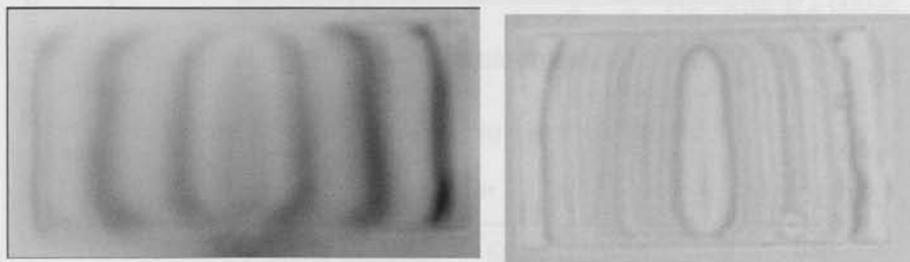

Figure 5.32. *Inverted image of recorded image on the CMOS camera when illuminated with Neon lamp a) without IR block b) with IR block.*

We can note that the spectral lines in the Figure 5.32 are not completely straight. These are rounded due to the reflow process of the resist in the fabrication procedure. This can be improved in a modified reflow process. However, this is not very important considering the signal processing which will be used to extract the spectral information from the image. We can also note from the images that there are some defects in the filter which are due to fabrication. Such defect might be difficult to completely avoid. Again, signal processing allows us to neglect the defected parts and use the best parts of the LVOF for spectral measurement.

Figure 5.33 shows the result of the LMS algorithm compared with the spectrum of Neon lamp measured by the commercial spectrometer. There is good agreement between the spectrums. The blind spectrum of the LVOF has been marked in the image and it can be seen that two of spectral line of the Neon lamp are neglected in that range. A spectral resolving power of 2.2 nm can be extracted from the measurement. Better agreement between the calculated spectrum and measured spectrum for this LVOF relates to better

quality of the LVOF and its smoother profile. This can be understood by comparing the result in Figure 5.21 to that in Figure 5.29 or Figure 5.30.

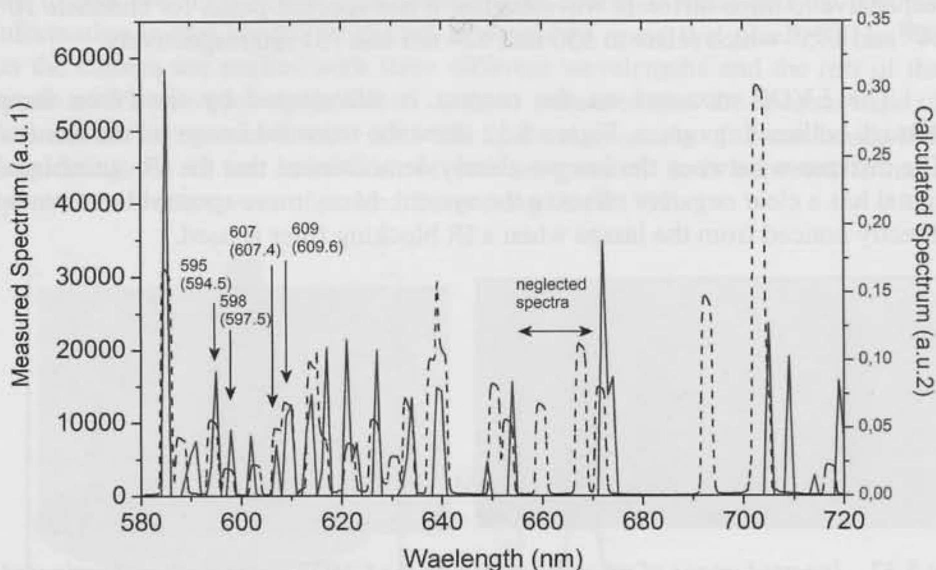

Figure 5.33. *Comparison between calculated spectra and spectrum of Neon lamp measured by the commercial spectrometer.*

5.8 Visible LVOF with Silver as metallic mirrors

In this paper we present fabrication of a Linear Variable Optical Filter with Silver mirrors. The advantage of using silver as a reflector for the Fabry-Perot Linear Variable Filter is the wide spectral bandwidth. A Linear Variable Filter has been designed and fabricated to cover the visible spectral range of 400 nm – 700 nm. Such a filter can be used if wide spectral wavelength range is more important than spectral resolution.

Figure 5.34 shows reflection from different metallic layers [5.7]-[5.8]. From the Figure can be noted that Ag has over 90 % reflection in the visible spectral range of 400 nm – 700 nm.

Table 5.2 shows the optimized thicknesses of the layers for the LVOF.

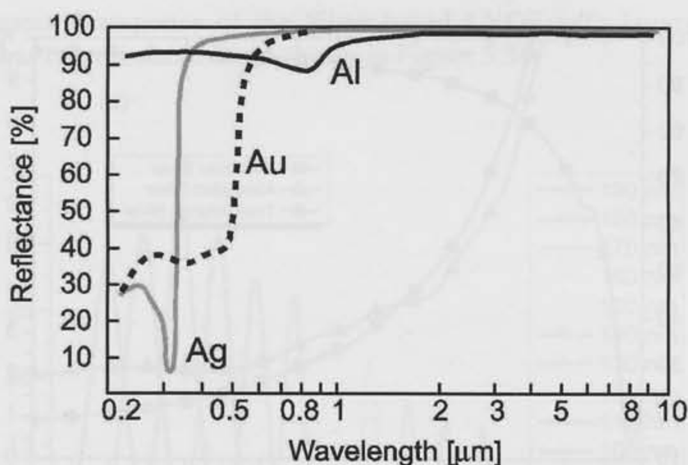

Figure 5.34. *Optical reflectance of Au, Ag and Al.*

Table 5.2.*Layer structure of the Linear Variable Filter with Silver mirrors*

Layer Material	Layer thickness
Silver	45 nm
SiO_2	90 nm – 190 nm
Silver	45 nm
SiO_2	220 nm

The LVOF has two 45 nm Silver reflectors. The reflection, absorption and transmittance of a 45 nm Silver layer has been shown in Figure 5.35a. As it can be seen from the figure a 45 nm silver layer results in over 90 % reflection in visible range while absorption and transmission are in the same order of magnitude. In order to show the advantage of Silver to Aluminum a comparison between the two metals needs to made. 35 nm is the minimum thickness for an Aluminum layer that gives the same reflectance as a 45 nm Silver layer. Figure 5.35b shows in turn reflection, absorption and transmittance for a 35 nm Aluminum layer.

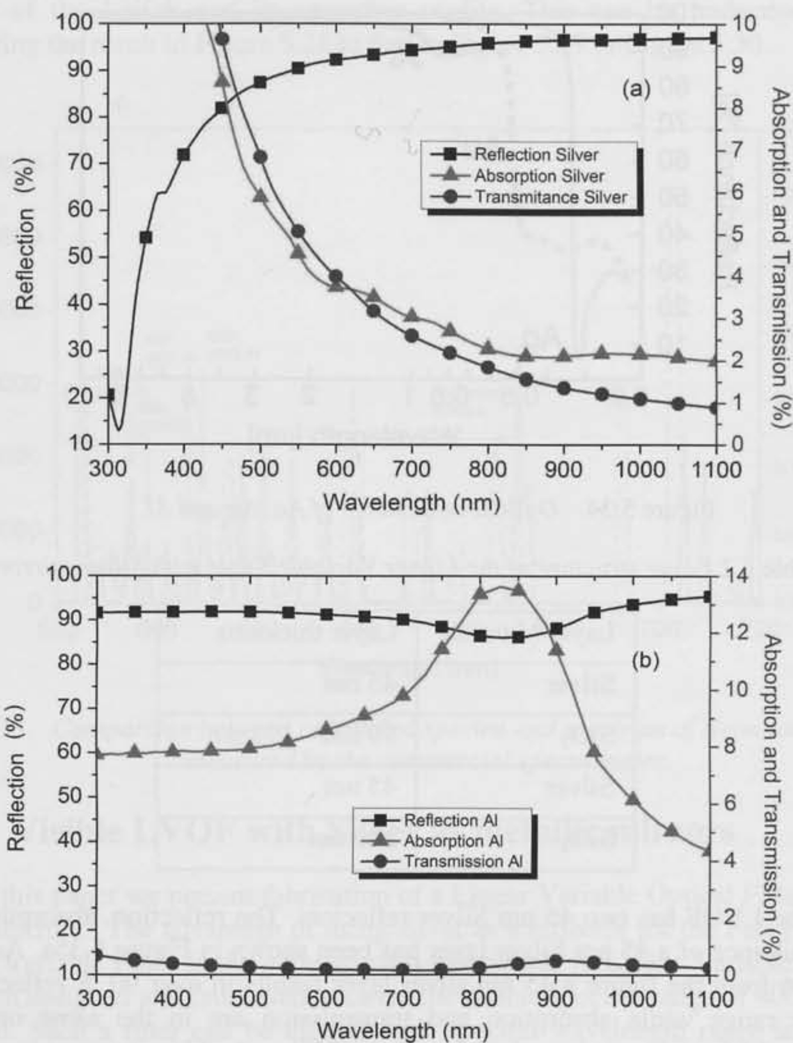

Figure 5.35. *Reflectance, transmission and absorption of a) 45 nm Silver and b) 35 nm Aluminum.*

It can be seen that in case of Aluminum most of the light which is not reflected is absorbed and not much is transmitted through the layer. Hence, a resonance filter with Aluminum has a very low throughput and not practical. A more detailed theoretical explanation can be given, however the basic idea can be directly seen by comparing the two figures.

The spectral response of the Silver-based LVOF with layers defined in Table 5.2 has been simulated and shown in Figure 5.36.

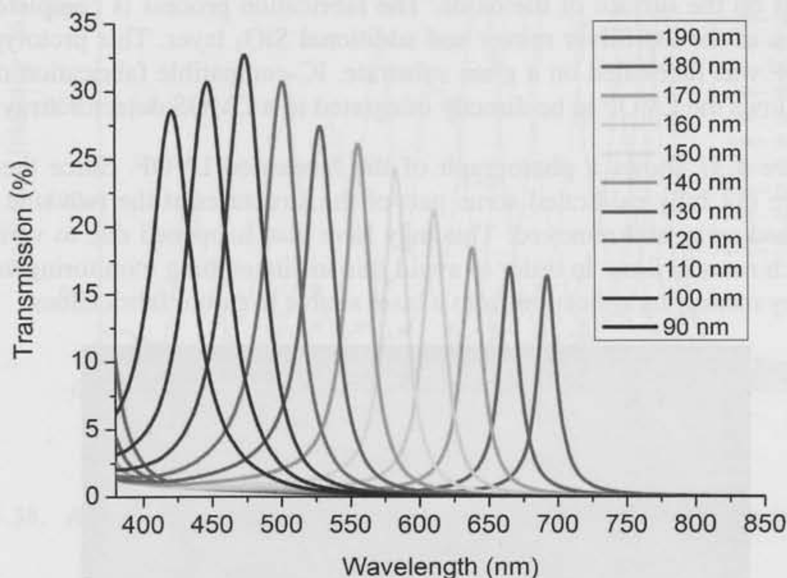

Figure 5.36. *Transmission through the LVOF at different thicknesses of the cavity.*

The LVOF has a throughput of 15 % - 30 % covering the whole visible range and blocking the infrared. The cavity layer thickness should vary from 90 nm to 190 nm along. Producing such a small variation in thickness is the challenging part of the fabrication. The top 220 nm SiO_2 layer will increase the reflection at the top mirror and further protects the underlying Silver layer from oxidation.

Silver-based LVOF fabrication is similar to previous LVOFs. It starts by deposition of 45 nm of Silver and 350 nm of SiO_2 on a glass substrate. Both depositions are done in a Leybold L560 evaporation deposition tool without breaking the vacuum to avoid Silver being exposed to air. Tapered layer fabrication is based on reflow of a specially patterned layer of resist as explained in chapter 4. A series of trenches of constant width and with variable spatial frequency or trenches of variable width and constant pitch are etched over the length of the strip of resist to vary the effective amount of resist per

unit area. The subsequent reflow transfers this gradient volume of resist into a smooth tapered resist layer. The topography of the tapered resist layer is transformed into the thick oxide cavity layer by an appropriate plasma etching process. The dry etching process has to be optimized to result in minimum roughness on the surface of the oxide. The fabrication process is completed by deposition of the top Silver mirror and additional SiO_2 layer. This prototype of the LVOF was fabricated on a glass substrate. IC-compatible fabrication of the LVOF allows the LVOF to be directly integrated to a CMOS detector array.

Figure 5.37 shows a photograph of the fabricated LVOF. Since the etch rates were not fully calibrated some part of the structures at the two side have been etched away and removed. This may have also happened due to variation of the etch rates in time. In order to avoid this in-situ etching monitoring can be applied by measuring reflection from a laser source in future fabrications.

Figure 5.37. *Photograph of a Linear Variable Optical Filter (LVOF).*

The LVOF is placed in front of a CMOS camera and collimated monochromatic light is projected on the Camera. The wavelength is swept from 400 nm to 740 nm with 5 nm step. At each wavelength only a part of the Camera which the LVOF passes is illuminated. Figure 8 shows the plot of recorded intensity of pixels at 500 nm – 695 nm wavelength range with 15 nm steps. Due to over etching of the structure one third of the structure is removed and thus the LVOF does not operate in 400 – 500 nm wavelength range.

The peak of the recorded intensity changes 1.5 - 2.5 pixels/nm, therefore it is expected that using such a filter can provide 5 nm spectral resolution when signal processing is applied.

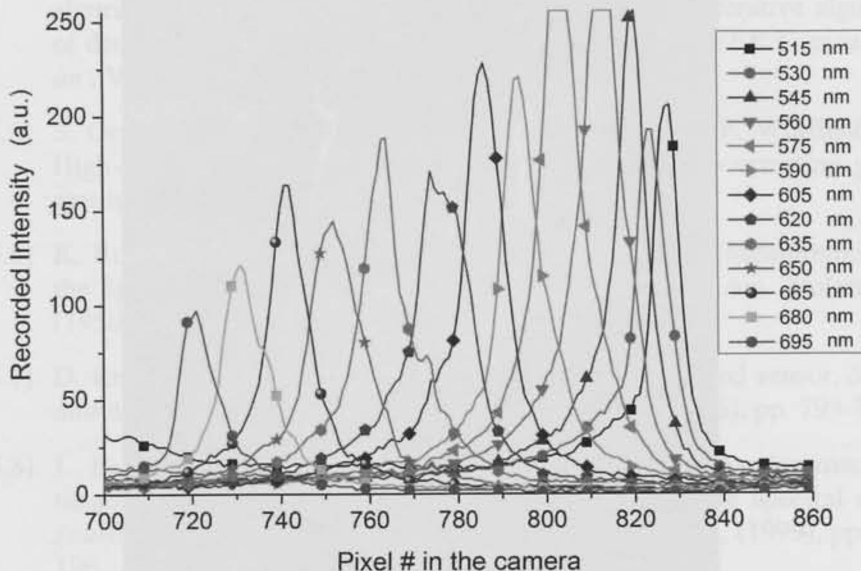

Figure 5.38. *Recorded intensity in the camera pixels at 500 nm – 695 nm with 15 nm wavelength steps.*

Figure 5.39 shows the images recorded on the camera at 600 nm and 650 nm wavelengths. The two outer lines in each image show the area of the LVOF structure and the two illuminated lines in the middle move along the structure as the wavelength is changed. The image shows that the lines are not perfectly parallel which is due to thickness irregularities. This problem can be solved in the future fabrications.

Figure 5.39. *Image recorded on the CMOS camera at 600 nm and 650 nm.*

5.9 References

[5.1] Paul L. Kebabian, Arnold F. Theisen, Spiros Kallelis, and Andrew Freedman, A passive two-band sensor of sunlight-excited plant fluorescence, *Rev. Sci. Instrum*, Volume. **70**, Number 11, (1999), pp. 4386-4393.

[5.2] M. Meroni, M. Rossini, L. Guanter, L. Alonso, U. Rascher, R. Colombo, J. Moreno, Remote sensing of solar-induced chlorophyll fluorescence: Review of methods and applications, *Remote Sensing of Environment*, Volume **113**, Issue 10, (2009), pp. 2037-2051.

[5.3] M.P. Wisniewski, R.Z. Morawski, A. barwicz, Algorithms for interpretation of spectrometric data-a comparative study, *Instrumentation and Measurement Technology Conference, 2000. IMTC 2000. Proceedings of the 17th IEEE*, Volume **2**, (2000), pp.703-706.

[5.4] D. Massicotte, R.Z. Morawski, A. Barwicz, Kalman-filter-based algorithms of spectrometric data correction-Part I: an iterative algorithm of deconvolution, *Instrumentation and Measurement, IEEE Transactions on* , Volume **46**, Number 3, (1997), pp. 678-684.

[5.5] S. Grabarnik, A. Emadi, H. Wu, G. de Graaf, and R. F. Wolffenbuttel, High-resolution microspectrometer with an aberration-correcting planar grating, *Appl. Opt.*, Volume **47**, (2008), pp. 6442-6447.

[5.6] K. Burns, K. B. Adams, and J. Longwell, Interference Measurements in the Spectra of Neon and Natural Mercury, *J. Opt. Soc. Am.*, Volume **40**, (1950), pp. 339-344.

[5.7] D. Rossberg, Optical properties of the integrated infrared sensor, *Sensor and Actuators A: Physical*, Volume **54**, Issues 1-3, (1996), pp. 793-797.

[5.8] J. H. Correia, M. Bartek, R. F. Wolffenbuttel, Bulk-micromachined tunable Fabry-Perot microinterferometer for the visible spectral range, *Journal Sensors and Actuators A: Physical*, Volume **76**, (1999), pp. 191-196.

6 *LVOF microspectrometer for the UV spectral range*

6.1 Introduction

Many biological molecules are fluorescent. The excitation wavelengths are usually in the UV part of the optical spectrum. MEMS-based microspectrometers operating in the UV spectral range (e.g. 230-280 nm) require either a small feature size in grating design or a cavity width less than 140 nm in optical resonator design. Fabrication and electronic modulation of a resonator with such a narrow air-gap between the two mirrors is severely hindered by capillary forces inside of the cavity. Also, electrostatic pull-in and subsequent sticking of the two mirrors limits the operating range of the device to one third of the initial air gap [6.1]-[6.2].

These problems are avoided in UV Linear Variable Optical Filters (LVOF) fabricated in post-processing steps after completion of UV photodetector and circuit in a standard IC technology.

6.2 Design and fabrication of UV LVOF

The LVOF is intended to operate in the wavelength range in between 315 nm and 400 nm. Table 6.1 shows the designed thickness of the layers used for the multilayered LVOF. HfO_2 and SiO_2 have been used as high-n and low-n materials. The optical properties and characteristics of these materials have been discussed in 3.4 The thickness of the tapered cavity layer changes linearly from 440 nm to 600 nm to cover the spectral range of interest. The spectral response of the filter is simulated using TFCalc® 3.3 and is shown in Figure 6.1. FSR has been marked in Figure 6.1.

It should be noted that based on the simulations of the designed values of the layers, for any value of the cavity thickness (any position along the LVOF) two different wavelengths are transmitted through the filter. These two wavelengths are from different resonance orders and their wavelength separation equals to Free Spectral Range (FSR).

Table 6.1.*Layers thicknesses of multilayered UV Linear Variable Filter.*

Material	Thickness (nm)
HfO2	43.5
HfO2/ SiO2	43.5/59
HfO2/ SiO2	43.5/59
HfO2/ SiO2	43.5/59
HfO2/ SiO2	43.5/59
SiO2	440 - 600
HfO2/ SiO2	43.5/59
HfO2/ SiO2	43.5/59
HfO2/ SiO2	43.5/59
HfO2/ SiO2	43.5/59
HfO2/ SiO2	43.5/59
HfO2	43.5

Increasing the thickness of the cavity from 440 nm to 600 nm (Looking from bottom to top in Figure 6.1) one resonance order covers the spectral range of 315 nm to 350 nm, while the other covers 350 nm to 400 nm. Since From

(2.6) FSR depends on the optical properties of the dielectric materials used in the filter structure.

For HfO_2 and SiO_2 and a reference wavelength of λ_0 = 350 nm the maximum stopband of the dielectric mirrors results from (2.6) as $\Delta\lambda$ = 84 nm. Consequently, FSR=42 nm. Since two different wavelengths are transmitted at each position along the LVOF, there is no simple one to one correlation between the pixels on the detector array (placed under the LVOF) and the spectral bands. Thus signal processing needs to be applied to determine the spectral bands. In other words, signal processing is required to enable us to use the entire $\Delta\lambda$ (84 nm) bandwidth instead of smaller bandwidth of FSR (42 nm).

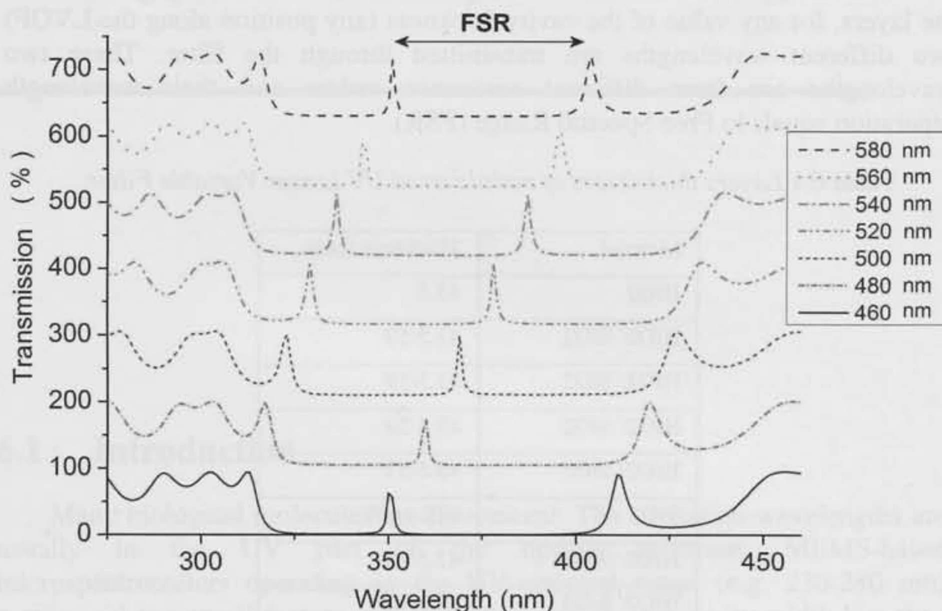

Figure 6.1. *Simulated spectrum of the LVOF for different values of cavity thickness.*

Fabrication involves the IC-Compatible process discussed earlier in section 5.3 . Initially, layers 1-10 were sputtered on the substrate. Sputtering of the dielectric layers has been done in the FHR MS 150 sputtering machine. It is possible to achieve a 2 % optical thickness variation control of the layers with this tool. Photoresist was spin-coated and patterned by a special pattern optimized to produce a linear slope after reflow. The tapered resist pattern was

transferred into a SiO_2 cavity layer by a dry-etching process that was optimized for minimum surface roughness.

Figure 6.2 shows a photograph of fabricated UV LVOFs. The rainbow pattern on the LVOFs is the result of the slope of the structures. The IC-compatible process for fabrication of the tapered layers allows the possibility to fabricated different slopes with one lithography step. Figure 6.3 shows a LVOF deposited on glass substrate and mounted on a CMOS camera for characterization and spectral measurement.

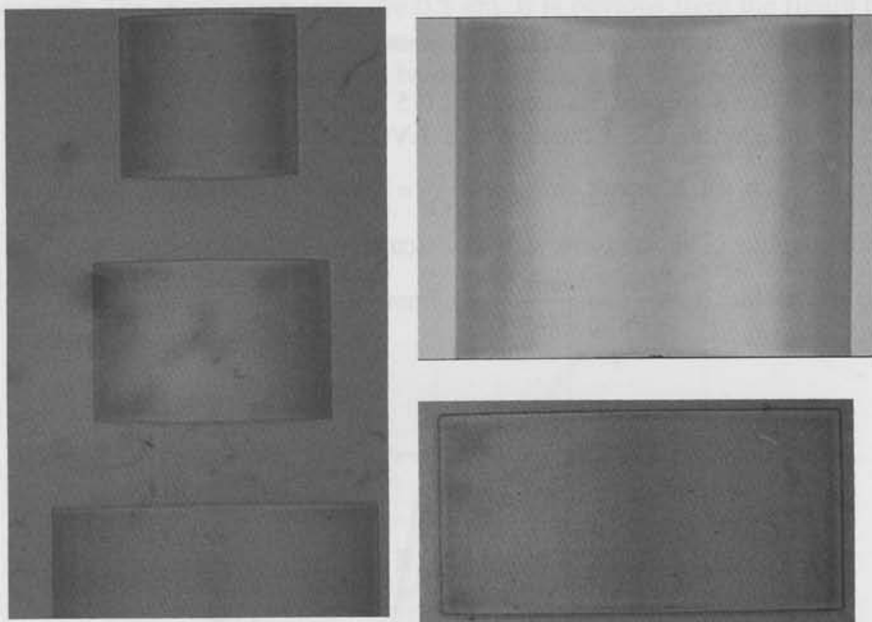

Figure 6.2. *Photograph of UV LVOFs fabricated on glass substrates.*

Figure 6.4 shows simulation results of the transmission through UV LVOF at different angles. We can note that in case of a 5° deviation from the normal incident the spectral peak of transmission shifts around 0.4 nm.

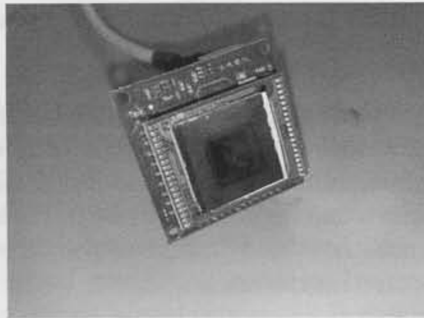

Figure 6.3. *UV LVOF on glass substrate mounted on a CMOS camera.*

Therefore, for a spectral inaccuracy of 0.5 nm, the value of φ=5° is chosen and fed to equation (2.15). Considering a LVOF with a length of 5 mm and assuming NA = 0.25 result in $f = \frac{D}{2\mathrm{NA}} = 10\mathrm{mm}$ for the focal length of collimating optics. The aperture size is calculated from (2.15) and with the given values yields: $d = \frac{D\varphi}{\mathrm{NA}} = \frac{5\mathrm{mm} \times 5^{\circ}}{0.25\mathrm{rad}} \approx 1.7\mathrm{mm}$.

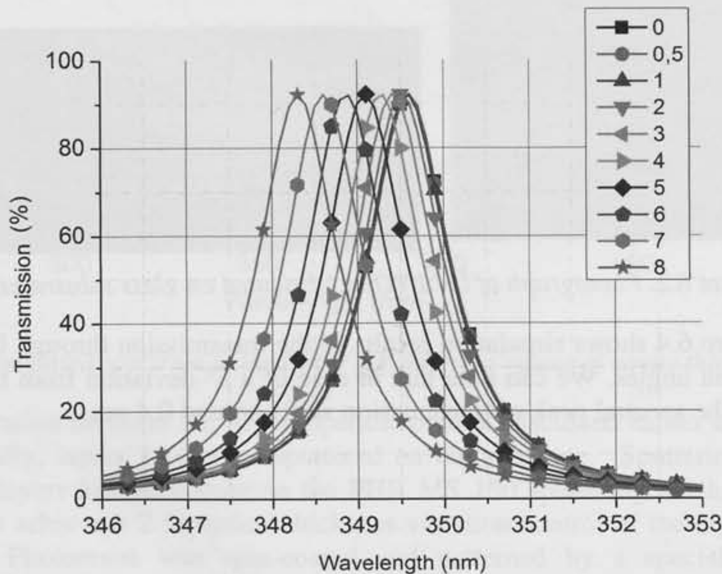

Figure 6.4. *Transmission through Fabry-Perot at different angles in degrees.*

6.3 Characterization and calibration of UV LVOF

Since a conventional CMOS camera, which is not optimized for wavelengths below 400 nm, is used for measurements, the wavelength dependent responsivity of the pixels has to be taken into account. The CMOS camera has 8-bit output and thus the output of each pixel is a value between 0 and 255. Figure 6.5 shows recorded output of the pixels of the camera at different wavelengths for the relatively uniform spectrum of a Xenon lamp. The wavelength has been selected using a monochromator between the lamp and the camera. The wavelength steps are 0.5 nm. It is obvious from the figure that the responsivity of the CMOS camera is strongly reduced in the UV spectrum and it is not practical to use the camera below 325 nm.

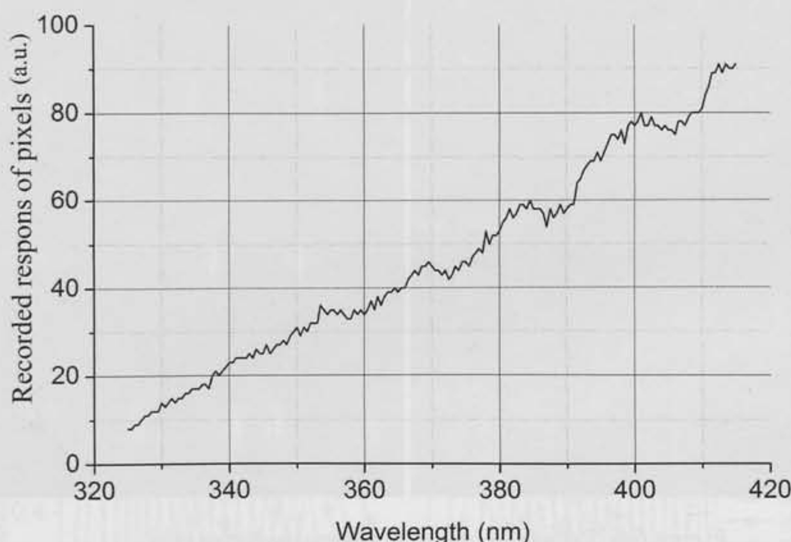

Figure 6.5. *Recorded output of camera pixels vs. wavelength.*

Monochromatic light has been projected on the LVOF mounted on the CMOS camera. The wavelength of the projected light changes from 315 nm to 400 nm with 0.5 nm steps resulting in 171 spectral channels. Figure 6.6 shows recorded image on the LVOF spectrometer for different wavelengths in the range from 315 nm to 400 nm. We can see the reoccurrence of illuminated regions on the images at around 40 nm steps. This is due to 42 nm Free Spectral

Range (FSR) as explained previously. The recorded intensity profile on the camera pixels is normalized at each wavelength by dividing it to the measured camera responsivity of Figure 6.5. Figure 6.7 shows the normalized intensity profile of the CMOS camera pixels at different wavelengths.

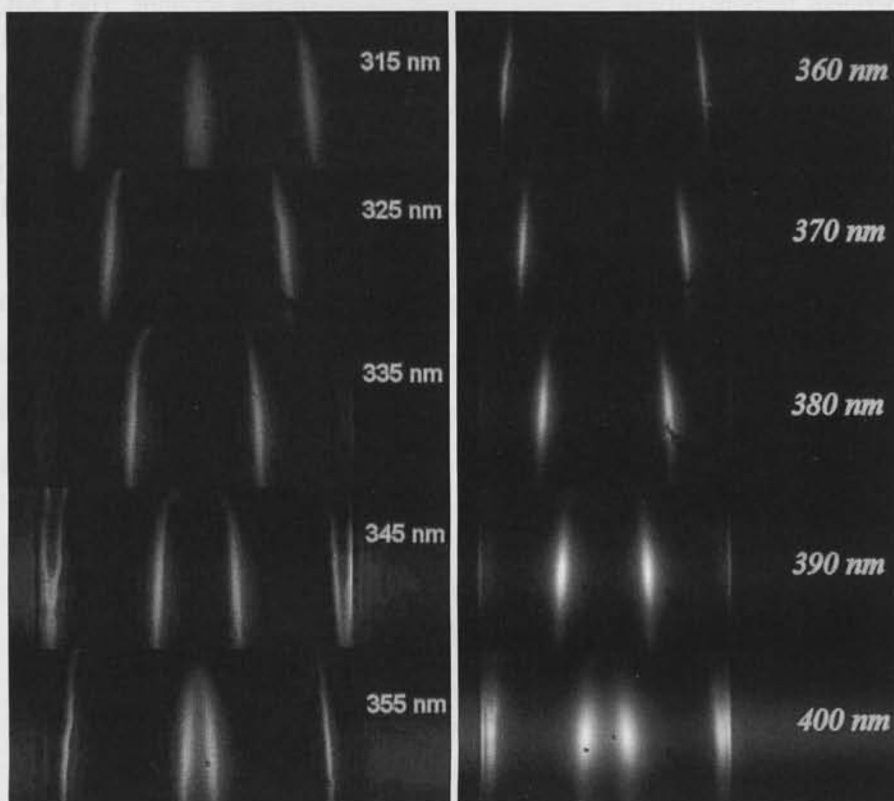

Figure 6.6. *Recorded image at several wavelengths.*

Once again due to 42 nm FSR of the LVOF and the occurrence of illuminated regions on the camera with 42 nm steps, two separate set of curves are plotted each covering 40 nm bandwidth. The curves are plotted with 2 nm wavelength steps. The measured (without normalization) intensity profile on the camera at each wavelength is imported into signal processing algorithm to result in the LVOF microspectrometer calibration matrix, introduced in 5.5

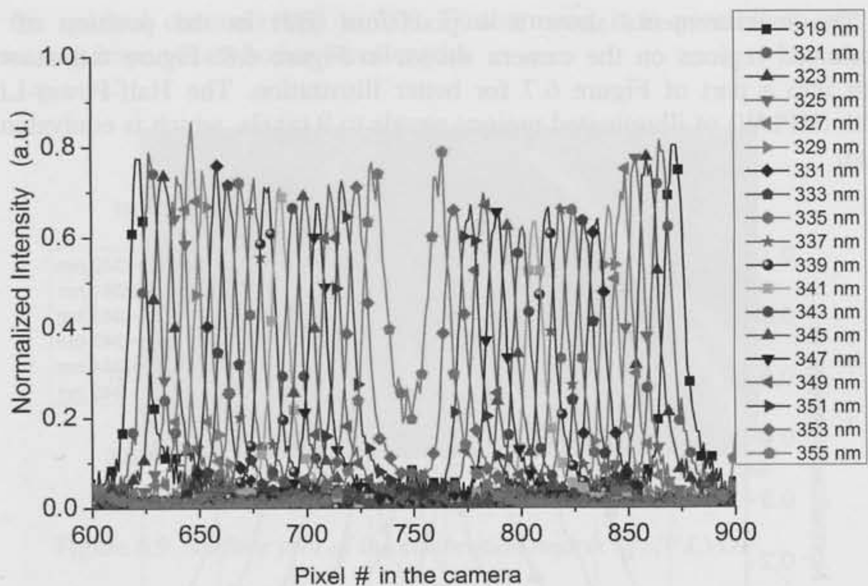

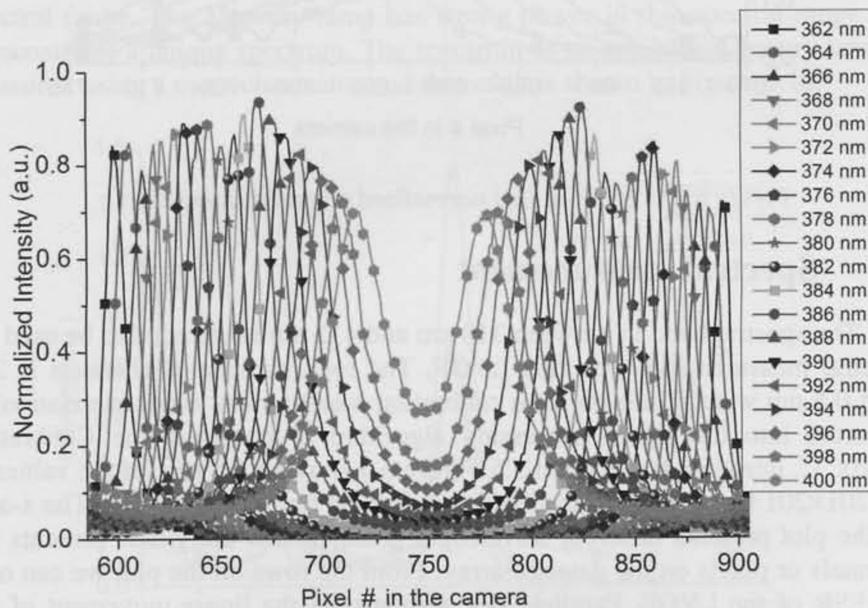

Figure 6.7. *Normalized recorded intensity on the LVOF spectrometer for the 315 nm to 400 nm wavelength region.*

The measurements show a 4 pixels/nm shift in the position of the illuminated regions on the camera shown in Figure 6.8. Figure 6.8 shows a zoom into a part of Figure 6.7 for better illustration. The Half-Power-Line-Width (HPLW) of illuminated regions equals to 9 pixels, which is equivalent to 54 μm.

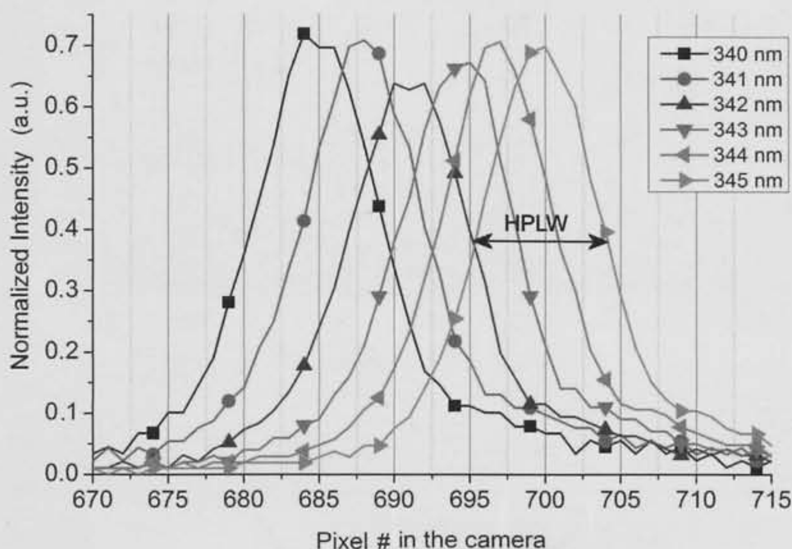

Figure 6.8. *A zoom-in into normalized recorded intensity.*

6.4 Spectral measurement

The spectral band in between 310 nm and 415 nm is intended to be used for spectral measurements with this LVOF. The total number of channels is 201 each 0.5 nm wide. The data from calibration measurement (characterization) is imported into the signal processing algorithm to construct the Calibration matrix, C, introduced in section 5.5 Figure 6.9 shows a 2D plot of the values in the 201×201 Calibration matrix, which is formed for the UV LVOF. The x-axis on the plot presents different wavelength channels and the y-axis presents the channels or pixels on the detector array. From the rows on the plot we can note the FSR of the LVOF. Parallel lines demonstrate the linear movement of the illuminated regions on the LVOF for linearly increased wavelength in the operation bandwidth. We can also see the widening of the illuminated regions (due to widening of the spectral peaks) when the wavelength gets closer to 400

nm for spectral channels 160 to 200. Furthermore, it is possible to see the decreasing response at shorter wavelengths.

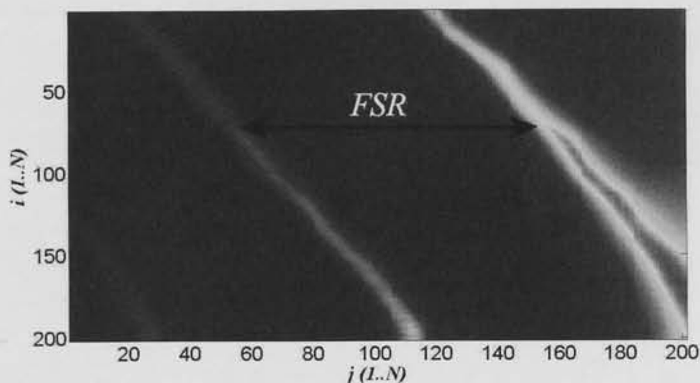

Figure 6.9. *Surface plot of the calibration matrix of UV LVOF.*

The objective is to measure the spectrum of a Mercury lamp in the UV spectral range. The Mercury lamp has strong power in this spectral range and demonstrates a unique spectrum. The spectrum of an available Mercury lamp is measured using a monochromator and the result is shown in Figure 6.10.

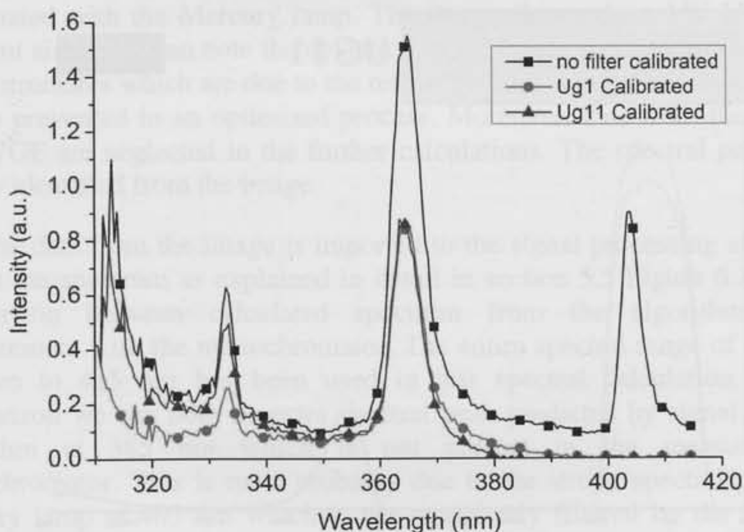

Figure 6.10. *Spectrum of Mercury lamp, including the effect of UG1 and UG11 filters.*

The spectrum of Mercury lamp has been measured with the effect of commercial UG1 and UG11 filters. UG1 or UG11 need to be applied in the spectral measurement with the UV LVOF to limit the light bandwidth to the spectral bandwidth of LVOF. Figure 6.11 shows the transmission spectra of these two filters.

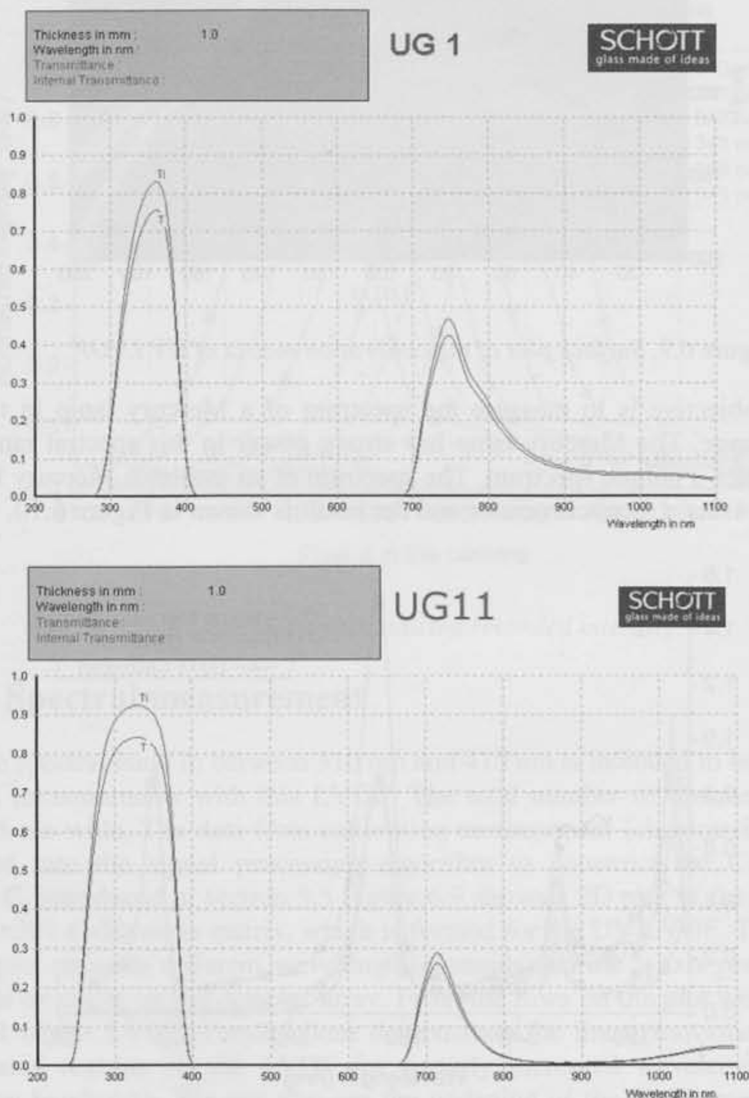

Figure 6.11. *Transmission spectral response of Schott filters, UG1 and UG11.*

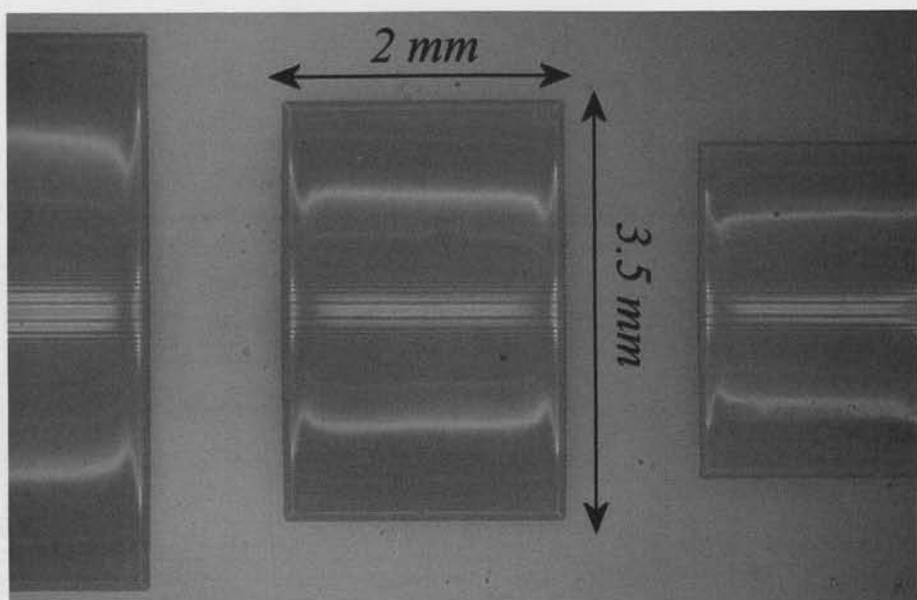

Figure 6.12. *Image recorded on the UV LVOF microspectrometer when illuminated by Mercury lamp.*

Figure 6.12 shows the recorded image on the LVOF camera when it is illuminated with the Mercury lamp. The image shows three UV LVOFs with different sizes. We can note the deviation of the bright spectral lines at the sides of the structures which are due to the reflow process step in the fabrication. This can be prevented in an optimized process. Moreover, data from these parts of the LVOF are neglected in the further calculations. The spectral peaks can be readily identified from the image.

The data from the image is imported to the signal processing algorithm to extract the spectrum as explained in detail in section 5.5 Figure 6.13 shows a comparison between calculated spectrum from the algorithm and the measurement with the monochromator. The entire spectral range of the LVOF, 320 nm to 415 nm has been used in this spectral calculation. From the comparison we can note an extra spectral peak predicted by signal processing algorithm at 385 nm which is not present in the measurement by monochromator. This is most probably due to the strong spectral peak of the mercury lamp at 405 nm which is not completely filtered by the UG1 filter. Considering the much higher sensitivity of the CMOS camera at 405 nm, we can expect that any out of band light at higher wavelengths can have a strong

negative effect on the performance of the system. The other characteristic difference is the lower calculated baseline of spectral power in the calculated spectrum.

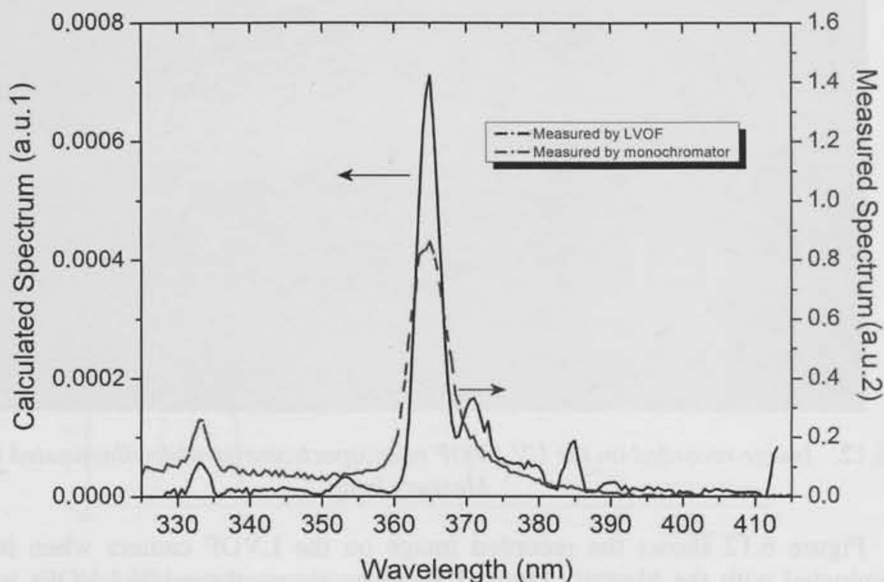

Figure 6.13. *Calculated spectrum from LVOF compared with measurement by monochromator.*

In a second attempt the spectral band in the signal processing algorithm is limited to 325 nm to 380 nm. Figure 6.14 shows the result. In both calculations the spectral response of CMOS pixels as shown in Figure 6.5 has been taken into account. The spectrum calculated for the narrower bandwidth has better agreement with the measurement with the monochromator. In both cases the low sensitivity of the CMOS camera in the UV leads to noise. To improve the calculations detector arrays with high sensitivity in the UV spectral range need to be applied.

The result proves that the LMS signal processing technique presented in 5.5 is suitable for measurements in the case of continuous spectrums (Mercury lamp) as well as spectrums with sharp spectral peaks (such as Neon lamp).

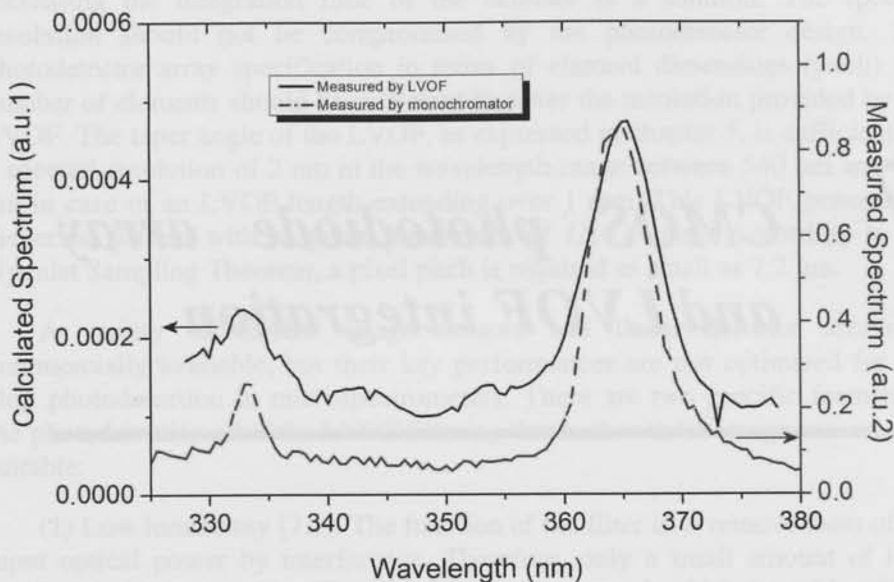

Figure 6.14. *Result of spectral calculation for 325 nm to 380 nm spectral range.*

6.5 References

[6.1] J. H. Correia, M. Bartek, R. F. Wolffenbuttel, Bulk-micromachined tunable Fabry-Perot microinterferometer for the visible spectral range, *Journal Sensors and Actuators A, Elsevier Science*, Volume **76**, (1999), pp. 191-196.

[6.2] A. T. T. D. Tran, Y. H. Lo, Z. H. Zhu, D. Haronian, E. Mozdy, Surface micromachined Fabry-Perot tunable filter, *IEEE Photonics Technology Letters*, Volume **8**, (1996), pp. 393-395.

7 CMOS photodiode array and LVOF integration

7.1 Introduction

A high-quality LVOF-based microspectrometer requires a custom-designed imaging system covered by the LVOF. The combined limitations of the LVOF design and the imaging system determine the performance of the microspectrometer in terms of spectral resolving power and light detection limit due to optical throughput (etendue). The spectral resolution of the microspectrometer is primarily determined by the LVOF design, whereas the etendue is limited by the optical design and imposes a detection limit requirement on the detector in terms of minimum optical intensity. These parameters determine the quality of this microspectrometer.

Unfortunately, reduced spectrometer dimensions are difficult to combine with high resolving power and etendue [7.1]. A reduced optical throughput can

be compensated for in a special mode of operation of the photodetector. Increasing the integration time of the detector is a solution. The spectral resolution should not be compromised by the photodetector design. The photodetector array specification in terms of element dimensions (pitch) and number of elements should be sufficient to cover the resolution provided by the LVOF. The taper angle of the LVOF, as expressed in chapter 5, is sufficient for a spectral resolution of 2 nm in the wavelength range between 540 nm and 720 nm in case of an LVOF length extending over 1 mm. This LVOF generates a dispersed pattern with a spatial bandwidth of 1/14.4 μm^{-1}. According to the Nyquist Sampling Theorem, a pixel pitch is required as small as 7.2 μm.

A variety of CMOS image sensors and linear detector arrays is commercially available, but their key performances are not optimized for on-chip photodetection in microspectrometers. There are two specific features in the photodetection after the LVOF filtering that makes those image sensors less suitable:

(1) Low luminosity [7.1]. The function of the filter is to remove most of the input optical power by interference. Therefore, only a small amount of light reaches the detector array. Thus the imaging system should be capable of low illumination detection. This does not necessarily exclude image sensors, since very low noise detectors are available. However, these sensors are intended for video applications whereas an image sensor for a LVOF-based microspectrometer can operate at much lower frame-rate. The pixel sizes required for a LVOF microspectrometer application can have a larger area than normally commercial sensors. High spectral resolution requires the pixels to have a small pitch in the direction of the LVOF. However, the size of the pixels in the other direction can be larger which results in higher sensitivity at low luminosity conditions.

(2) CMOS-compatibility. The smallest overall system dimensions are obtained when fabricating a LVOF directly on top of the imaging system. This is an essential feature in applications such as lab-on-a-chip [7.2]. Thus a photodetection system with standard CMOS process is preferred for its low cost and high compatibility. This does not exclude commercially available CMOS detectors.

7.2 Smart CTIA-APS

A CTIA-APS linear array with 128 elements has been designed and fabricated within this framework, where CTIA is short for Capacitive Transimpedance Amplifier and APS is short for Active Pixel Sensor. This detector array design is based on the LVOF developed in chapter 5. The idea is to take advantage of the special optical pattern generated by the LVOF and to implement an IC-compatible photodetection module suitable for operation at low illumination intensities.

7.2.1 Detector array

As discussed, the detector should satisfy three requirements:

(1) Small pitch along the LVOF length for high spatial sampling frequency;

(2) Large light-sensitive area, for ensuring maximum sensitivity and SNR;

(3) IC compatibility.

The first two problems can be solved by applying a linear array of strip-like pixels. The extension of pixel length should compensate for the narrow pixel width. The nwell-psubstrate junction is selected for photodetection for an optimized responsivity in the visible spectral range. Considering all the specifications, the pixel size was selected at 7.2 μm × 300 μm.

7.2.2 Active pixel sensor with CTIA

Image sensors usually apply a junction capacitor as the charge-to-voltage convertor, which is not good for linearity; the popular 3T-APS has its light sensitive areas in proportional with its junction capacitance, which resulted in a limited sensitivity [7.3]-[7.4]. A capacitive transimpedance amplifier is included in each pixel to avoid this problem, as shown in Figure 7.1.

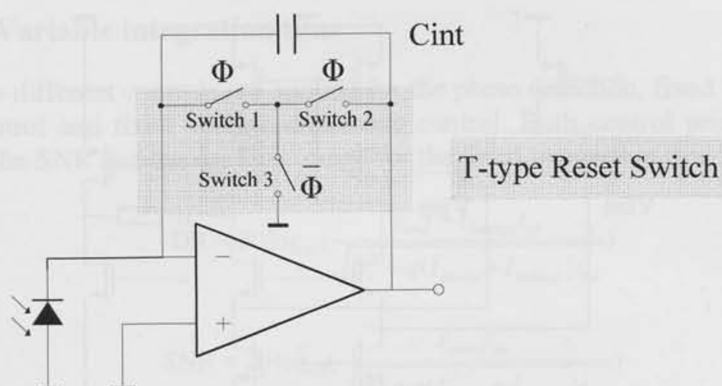

Figure 7.1. *Capacitive Transimpedance Amplifier (CTIA) with a T-type switch.*

The introduction of the CTIA brings several benefits:

(1) The dependence between the light sensitive area and the charge-to-voltage conversion is avoided. The sensitivity can be improved by enlarging the pixel length and by decreasing the integration capacitor;

(2) The dependence between the accumulated charge and the integration capacitor is avoided. The linearity can be improved by implementing the integration capacitor as a poly-to-poly structure;

(3) The amplifier enables the implementation of T-type switches with large off-resistance [7.5], and thus long integration time. The readout time can then be traded for higher signal-to-noise ratio.

(4) By means of the virtual ground, the photodiode can be biased with a constant biasing voltage, which reduces the charge modulation effect dramatically and leads to higher accuracy. The amplifier schematic is shown in Figure 7.2. A two-stage circuit is chosen for large output swing. The T-type switch that is across the input and output of the amplifier results in an off-resistance much larger than feasible with a single pass switch.

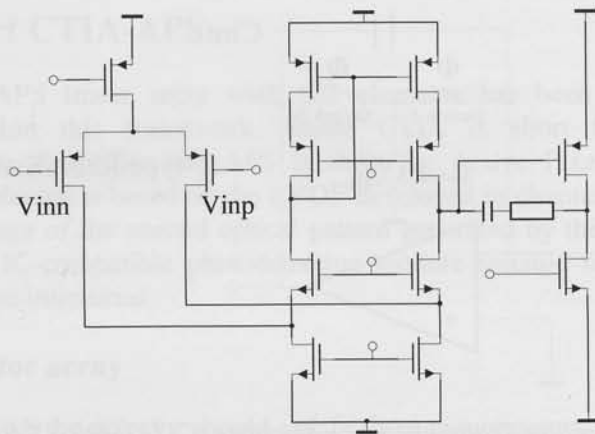

Figure 7.2. *Schematic of the in-pixel amplifier.*

7.2.3 In-pixel CDS

Correlated Double Sampling (CDS) as the traditional technique for reducing low-frequency noise is also applied here. The schematic [7.3] and the timing chart are shown in Figure 7.3.

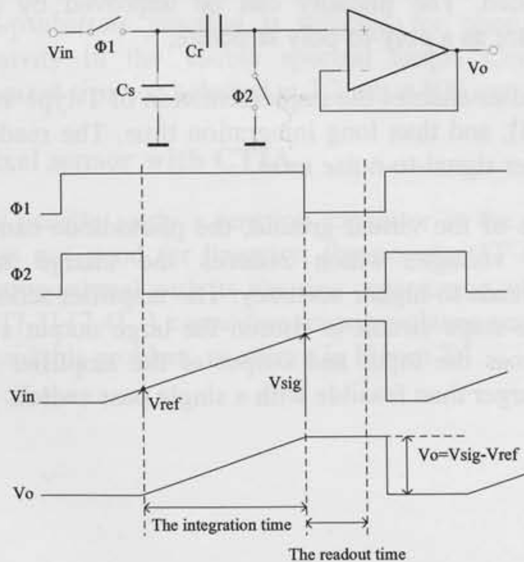

Figure 7.3. *Schematic and timing chart for the buffered CDS.*

7.2.4 Variable integration time

Two different controls are applied for the photo detection, fixed integration time control and fixed voltage difference control. Both control principles are tested. The SNR and the dynamic range for the fixed integration time are:

$$\mathrm{DR} = 20\log_{10}\left(\frac{q_{\max} - I_{\mathrm{leakage}} t_{\mathrm{int}}}{\sqrt{\sigma_r^2 + q(I_{\mathrm{photo}} + I_{\mathrm{leakage}}) t_{\mathrm{int}}}}\right) \tag{7.1}$$

$$\mathrm{SNR} = 20\log_{10}\left(\frac{I_{\mathrm{photo}} t_{\mathrm{int}}}{\sqrt{\sigma_r^2 + q(I_{\mathrm{photo}} + I_{\mathrm{leakage}}) t_{\mathrm{int}}}}\right) \tag{7.2}$$

These expressions demonstrate that the SNR increases with integration time while the dynamic range decreases. Therefore, besides the fixed integration time control, the fixed voltage difference control is also introduced to boost both the dynamic range and the signal-to-noise ratio. In the fixed voltage difference control, the time consumed by the CTIA-APS output to increase from V1 to V2 is recorded, with the assistance of a reference clock [7.8]. This control principle brings three benefits:

(1) There is always a large amount of photons captured, even for low illumination levels. The photon shot noise will be the dominant noise source, which means a high SNR detection;

(2) The control principles can be implemented with digital logic circuits and integrated into each pixel simply. Each pixel can then work independently, needing no other control signals;

(3) The A/D conversion can be finished in the time recording by clock counters;

(4) The dynamic range can be improved by designing the clock and the counter appropriately, unlike in the fixed integration time control where it is jeopardized by the increasing of integration time. The working principle is shown in Figure 7.4.

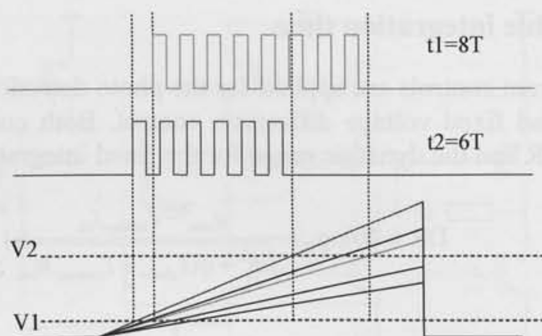

Figure 7.4. *Operating principle for fixed voltage difference control.*

7.2.5 Circuit diagram

The circuit diagram of the readout is shown in Figure 7.5 (for simplicity the readout of only four pixels is shown). The standard timing chart of the pixel operation over one cycle is also presented in Figure 7.6.

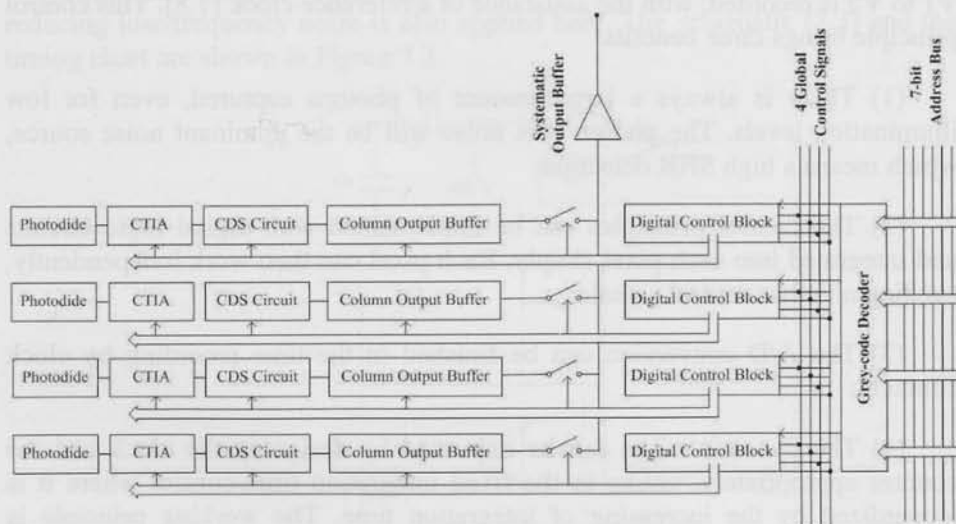

Figure 7.5. *Complete system diagram.*

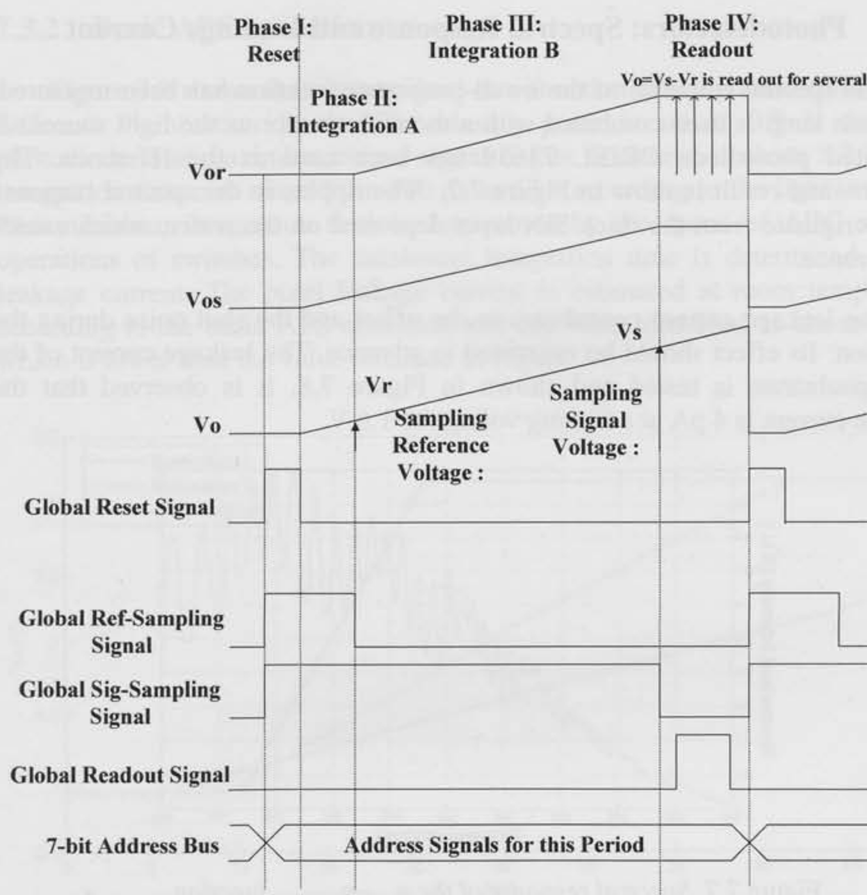

Figure 7.6. *Standard timing chart for one pixel operation in one cycle.*

7.3 Device performance

The prototype of this CTIA-APS array is designed and fabricated in standard CMOS technology, AMIS A/D 0.35µm. The initial tests used a halogen light source. A DAQ board controlled by a Lab View program is used for data acquisition, signal processing and generating control signals. The experimental results are to be discussed so as to demonstrate the performance of the device, including photodetectors' responsivity, leakage current, linearity, temporal noise and the APS operations under both control principles.

7.3.1 Photodetectors: Spectral Response and Leakage Current

The spectral response of the nwell-psubstrate junction has been measured. A Xenon lamp is used combined with a monochromator as the light source. A calibrated photodiode ORIEL 71638 has been used as the reference. The experimental result is show in Figure 7.7. The ripples in the spectral response curve originate from the thick SiN layer deposited on the wafer, which causes interference.

The leakage current contributes to the offset and the shot noise during the detection. Its effect should be estimated in advance. The leakage current of the nwell-psubstrate is tested and shown in Figure 7.8. It is observed that the leakage current is 4 pA at a biasing voltage of 1.6 V.

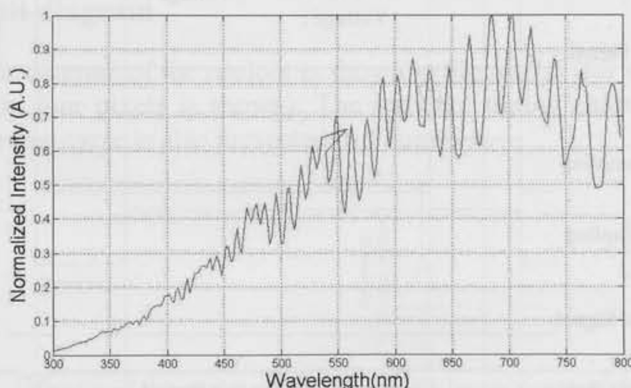

Figure 7.7. *Spectral response of the* n_{well}-$p_{substrate}$ *junction.*

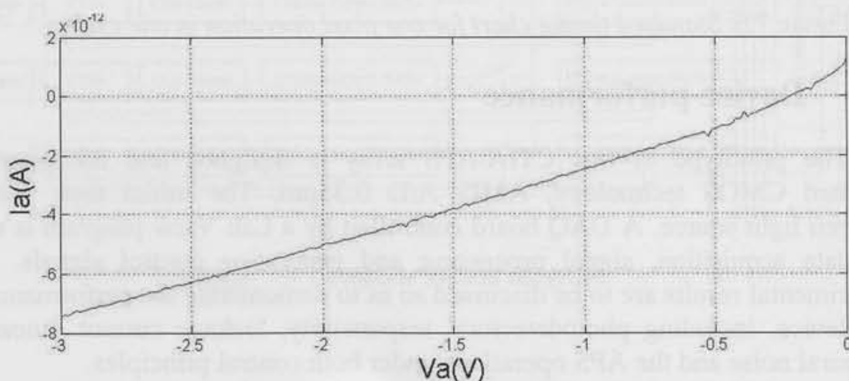

Figure 7.8. *Leakage current of the* n_{well}-$p_{substrate}$ *junction.*

7.3.2 Basic APS operation

Figure 7.9 shows the output signal as a function of integration time at four different illumination levels. The biasing point is set at 0.9 V for each photodiode. The maximum output signal before saturation is about 3.2 V. The integration time can range from 100 µs to 63 s according to the light intensity. The minimum integration time is determined by the speed of ADC and the operations of switches. The maximum integration time is determined by the leakage current. The pixel leakage current is estimated at room temperature according to the basic APS operation and has been measured as about 30 fA, which is lower than the value obtained in Figure 7.8.

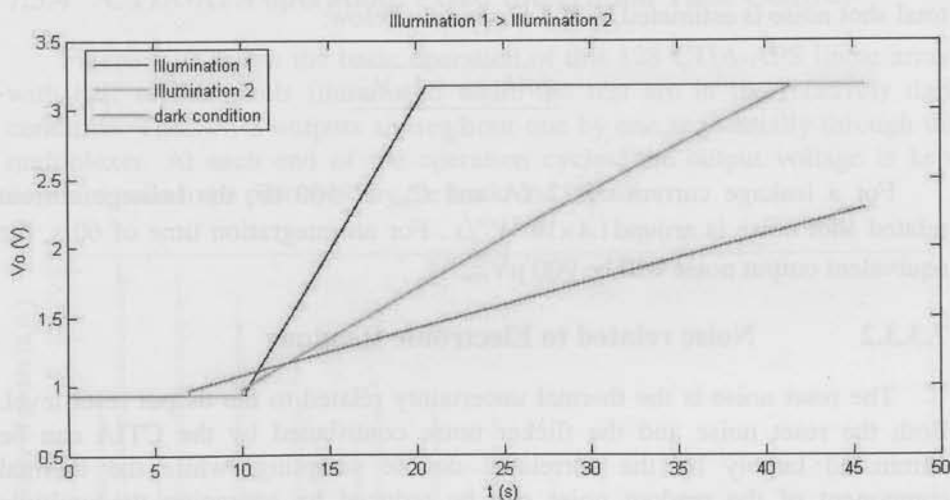

Figure 7.9. *Output signal versus integration time.*

7.3.3 Temporal noise

The temporal noise determines the minimum detectable signal. It is contributed by every stage along the in-pixel signal chain:

(1) The photodiode contributes shot noises related to photocurrent and leakage current.

(2) The CTIA contributes a readout MOS device noise as well as a reset noise.

(3) The CDS circuit contributes a kT/C noise.

(4) The in-pixel buffer contributes another component of circuit noise.

(5) the DAQ board contributes the sampling noise. The temporal noise is first observed for all the stages of the test pixel. The measurement results are listed and discussed below.

7.3.3.1 Noise related to Photodetectors

The optical power is taken full advantage of in the photodetection only when the photocurrent-related shot noise dominates in the temporal noise. The total shot noise is estimated by the expression below:

$$\frac{\sqrt{q(I_{leakage}+I_{ph})t_{\text{int}}}}{C_{\text{int}}} \quad (7.3)$$

For a leakage current of 22 fA and C_{int} of 500 fF, the leakage current related shot noise is around $1.4\times10^{-8}\,V^2/s$. For an integration time of 60 s, the equivalent output noise will be 900 μV_{rms}.

7.3.3.2 Noise related to Electronic Readout

The reset noise is the thermal uncertainty related to the output reset level. Both the reset noise and the flicker noise contributed by the CTIA can be eliminated largely by the correlated double sampling, while the thermal component of the readout noise can be reduced by averaging the multiple readout results. The CTIA readout noise is quantified at the output of the Capacitive Transimpedance Amplifier while the reset switch is kept on and in the dark condition. The noise of around 220 μV_{rms} is observed. The readout noise contributed by the output buffer is tested similarly, as around 300 μV_{rms}.

The kT/C noise of CDS is another major noise source at the APS output. It is a low frequency noise related to the two un-correlated sampling operations. This noise is quantified at the output of the CDS circuit in the dark condition, while the reset switch is kept on and the two CDS switches operate according to the standard timing chart for several cycles. The CTIA readout noise, which would otherwise appear at the CDS output, is removed by averaging the samples obtained within one cycle. The kT/C noise of CDS is observed as around 240 μV_{rms}.

7.3.3.3 Overall Temporal Noise

The overall temporal noise is tested at the output of the test pixel in the dark condition, with all the switches operates according to the standard timing chart. An integration time of 5 ms is applied in this case. A noise floor of 700 μV_{rms} is observed, which is higher than the summing of the estimated noise contributions. On one hand, the DAQ board contributes part of the noise; on the other hand, the reset noise and the readout flicker noise can not be removed fully at the same time. According to the applied timing chart and the given integration time, the flicker noise higher than 200 Hz remains at the output.

7.3.4 CTIA-APS operation: Fixed Integration Time Control

Figure 7.10 shows the basic operation of this 128 CTIA-APS linear array, with half of the pixels illuminated while the rest are in the relatively dark condition. Their APS outputs are read out one by one sequentially through the multiplexer. At each end of the operation cycles, the output voltage is kept constant so as to be processed by the back-end circuit.

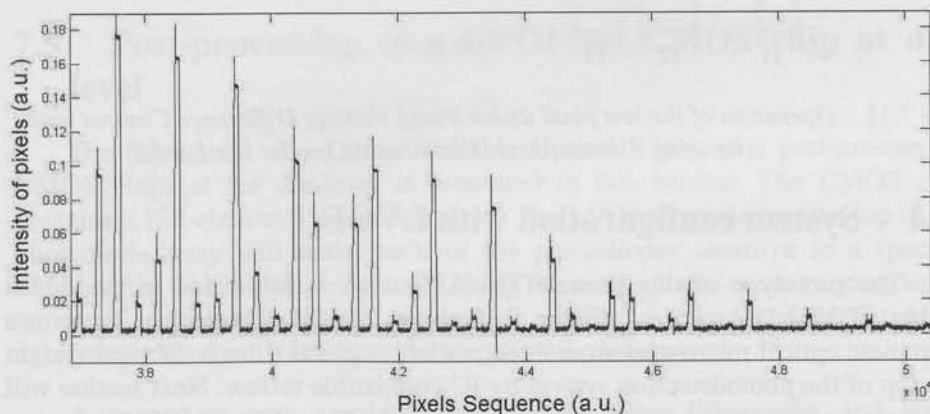

Figure 7.10. *Operation of pixels under Fixed Integration Time Control.*

7.3.5 CTIA-APS operation: Fixed Voltage Difference

For the low illumination detection, a long integration time can be applied to ensure enough signal energy. Under the fixed voltage difference control, the pixel adapts its integration time according to the sensed illumination. Figure 7.11 shows how the tested pixel responds to the change of light intensity.

In this control, the noise level is constant for all illumination levels, allowing a sensitive detection even for small optical power. For a further on-chip integration of this self-adapting functionality, two problems should be noticed: a limit on the maximum detectable signal is introduced by the speed of sampling and related logic control circuits; a limit on the minimum detectable signal may be introduced by the implementation for the in-pixel counter which is necessary for the time recording and the A/D conversion.

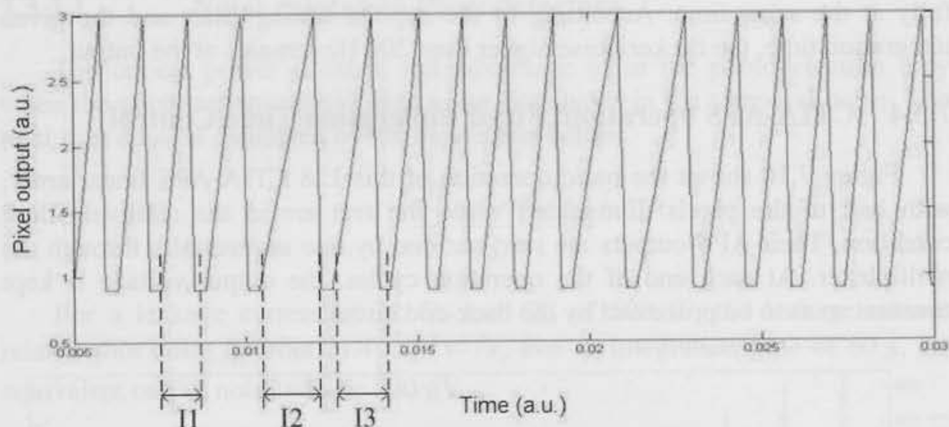

Figure 7.11. *Operation of the test pixel under Fixed Voltage Difference Control with changing illuminations (Illumination levels: $I_1 > I_3 > I_2$).*

7.4 System configuration with LVOF

The prototype of this linear CTIA-APS array is fabricated in the AMIS 0.35μ C035M-D/A process. Figure 7.12 shows the die photograph. To form a complete optical micro-system, a linear variable optical filter is fabricated right on top of the photodetection system by IC-compatible reflow. Next section will discuss the integration process of depositing LVOF on this CMOS chip at the die level. In such a combination, each pixel is supposed to detect a unique wavelength of light. Thus, by multiplexing the APS in this linear array, the interested spectrum can be scanned.

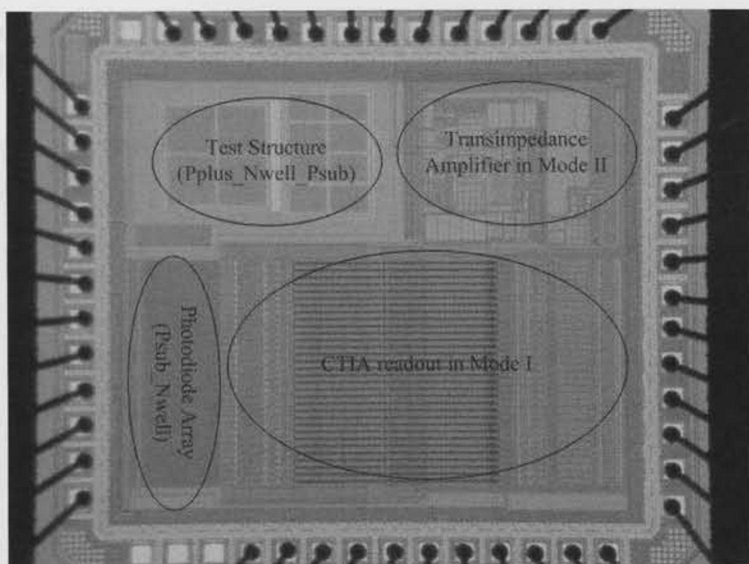

Figure 7.12. *The die photo of the 128 CTIA-APS linear array.*

7.5 Post-processing of a LVOF on CMOS chip at die-level

The fabrication of a Linear Variable Optical Filters as a post-process on CMOS chips at the die-level is presented in this section. The CMOS chip contains a 128-element Photodiode array. The LVOF deposited on the top of the photodiode array will make each of the photodiodes sensitive to a specific wavelength, which changes linearly along the array. A one-mask process based on trench etching in resist and subsequent reflow is used to fabricate a tapered cavity layer for the LVOF on top of the photodiode array.

A special process has been designed to allow lithography and wafer processing on pre-fabricated CMOS dies, based on die bonding to a carrier wafer and a reflow planarization. The result is an on-chip spectrometer. The technique can be generally applied to chips from a multi-chip design processed at an external foundry service that supplies chips only.

Since the 2×2 mm^2 CMOS chips are too small for handling in process, they have to be initially mounted on a substrate. Using SU-8 as an adhesive material the chips are glued to 1×1 cm^2 Silicon or Glass substrates. The SU-8 is heated to reflow and planarize the sharp edges on the chip. This is necessary

to enable subsequent spin coating of photoresist and processing. Figure 7.13 shows a photograph of a chip after bonding to the substrate by SU-8 and planarization.

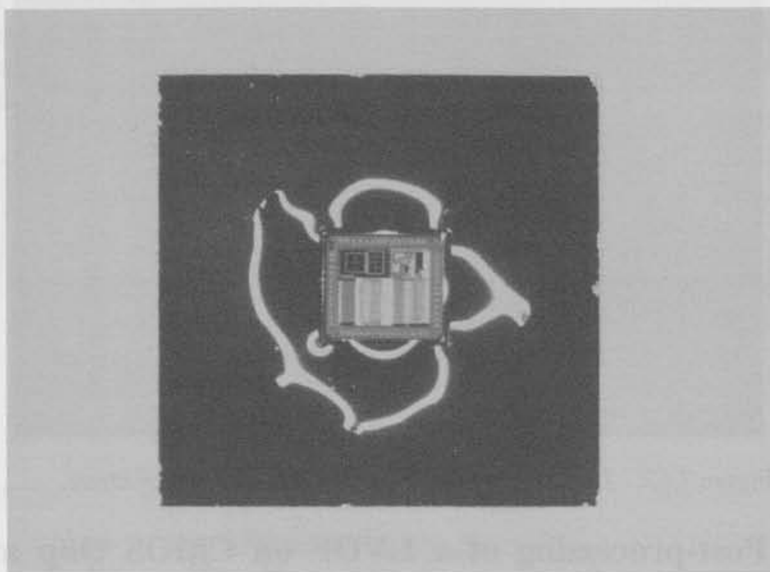

Figure 7.13. *Chip die bonded to substrate with SU-8.*

The benefit of using SU-8 is that it is not removed by the AZ resist developer during subsequent lithography steps. The lithography step is required for covering the bonding pads with photoresist before deposition of dielectric layers. Lift-off processing has been applied with image reversal photoresist, AZ 5214E. Planarization of the die sharp edges makes it possible to spin coat photoresist on the die. Figure 7.14 shows the photoresist mask opening on the photodiodes array part of the CMOS chip, while covering the bonding pads. The thickness of the resist layer is 5.5 μm.

The LVOF consist of 15 alternating layers of TiO_2 and SiO_2 shown in Table 7.1. The layers are sputter deposited using a FHR MS150. The 2 % precession control of the thicknesses and optical properties are essential for a reliable interference-based optical filter.

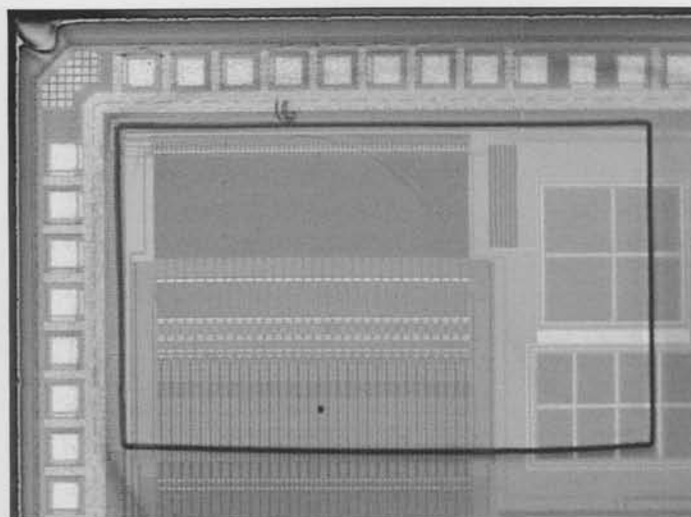

Figure 7.14. *Photoresist lift-off mask opening on the photodiode array, the mask covers the bonding pads.*

Table 7.1.*Layer structure of the Linear Variable Optical Filter*

Layer Material	Thickness (nm)
TiO_2	67
SiO_2/TiO_2	112 / 67
SiO_2/TiO_2	112 / 67
SiO_2/TiO_2	112 / 67
SiO_2	**850 - 1000**
TiO_2/SiO_2	67 / 112
TiO_2/SiO_2	67 / 112
TiO_2/SiO_2	67 / 112
TiO_2	67

The obvious disadvantage of sputtering is a difficult lift-off process due to the non-directional deposition, which causes coating of the sidewalls of the patterned photoresist and reduced access of the Acetone. Figure 7.15 shows a photograph of CMOS die chip after deposition of the first stack of dielectric layers.

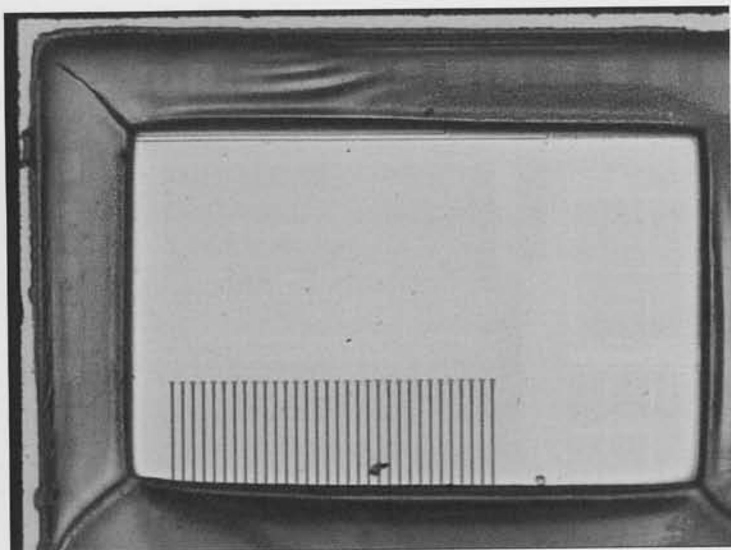

Figure 7.15. *Dielectric layers deposited on the CMOS die through photoresist lift-off.*

The lift-off is done in an ultrasonic bath with Acetone heated to 50° C. The complete lift-off takes about 3 hours. The use of Shipley remover 1165, which can potentially help in an easier lift-off, was avoided due to the fact that it can etch the Aluminum bonding pads. Figure 7.16 shows the photograph of a die after the lift-off process.

As it can be seen, the dielectric layers are covering all the photodiode pixels on the chip and bonding pads, while the remainder of the chip is kept clear. In the next step, lithography is applied for the fabrication of the tapered cavity layer. Initially, a lithography step is done on the chip using low viscosity SU-8 2002 to cover the bonding pads. Subsequently, lithography is done using S1813 photoresist to result in a tapered photoresist layer as described in chapter 4.

As mentioned before, the exposed SU-8 is not removed in the Shipley MF 322 which is used for development of AZ5214E and S1813. This allows us to implement two subsequent lithography steps: the first with SU-8 2002 used for protection of the bonding pads and the second with S1813 to form the tapered resist layer. After completion of the lithography and reflow processing, the tapered resist layer is transferred into the underlying SiO_2 layer as described in section 4.6 .

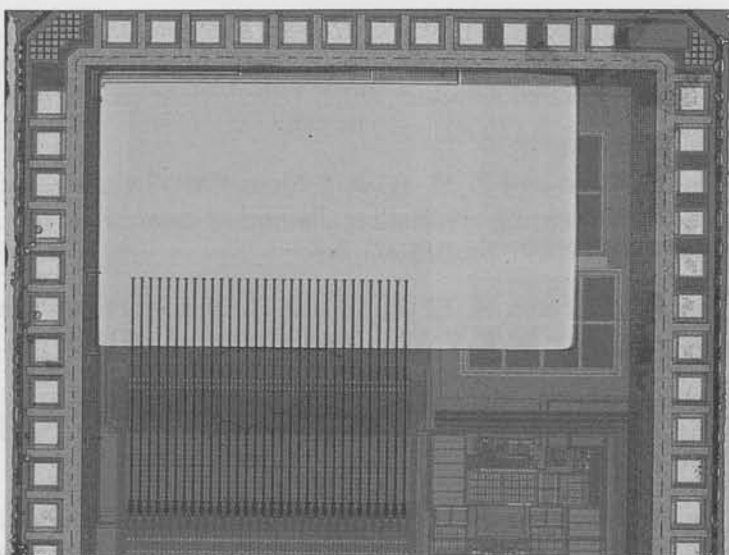

Figure 7.16. *The die photo with the LVOF on top of the 128CTIA-APS linear array.*

Samples are cleaned in Acetone after dry etching step to remove photoresist residuals. Exposed SU-8 is removed in Acetone provided that it is not hard-baked. This also causes the die to detach from the substrate and the SU-8 covering the bonding pads is also cleaned. The die chips are bonded to a substrate again and a lift-off mask using AZ 5214E is made with the same procedure for the deposition of the second stack of dielectric layers, layers 9-15 in Table 7.1. The process is completed after the lift-off.

7.6 References

[7.1] S. Grabarnik, Optical microspectrometers using imaging diffraction gratings, *PhD thesis*, Delft University of Technology, (2010), ISBN: 978-90r-r9025048-9.

[7.2] O. Schmidt, M. Bassler, P. Kiesel, C. Knollenberg and N. Johnson, Fluorescence spectrometer-on-a-fluidic-chip, *Lab Chip*, Volume **7**, (2007), pp. 626-629.

[7.3] L. Hannati, P. Pittet, G.N. Lu and G. Carrillo, CMOS 32-APS linear array for high-sensitivity, low-resolution spectrophotometry, *Sensors and Actuators B: Chemical*, Volume **120**, (2006), pp. 142-149.

[7.4] H. Nagata, H. Shibai, T. Hirao, T. Watabe, M. Noda, Y. Hibi, M. Kawada and T. Nakagawa, Cryogenic capacitive transimpedance amplifier for astronomical infrared detectors, *IEEE Transactions on Electron Devices,* Volume **51**, Issue 2, (2004), pp. 270-278.

[7.5] N. Liu, G. Chen and Z. Hong, A 0.18μm CMOS fluorescent detector system for bio-sensing application, *Journal of Semiconductors*, Volume **30**, Number 1, (2009), pp. 015002, 1-6.

[7.6] T. Chen, P. Catrysse, A. El Gamal and B. Wandell, How small should pixel size be, *Proc SPIE,* Volume **3965**, (2000), pp. 451-459.

[7.7] P.B. Catrysse, A.B. Wandell and A. El Gamal, Comparative analysis of color architectures for image sensors, *Proc SPIE,* Volume **3650**, (1999), pp. 26-35.

[7.8] C. Xu, S. Chao and M. Chan, A New Correlated Double Sampling Technique for Low Voltage Design Environment in Advanced CMOS Technology, *ESSDERC*, (2002), pp. 117-120.

8 *Conclusions*

This final chapter will combine the conclusion of the previous chapters and gives suggestions for future works.

8.1 UV to IR Linear Variable Optical Filter microspectrometers

Single-chip optical microspectrometers have huge potential in many applications, such as identification of bio-molecules, gas detection and in chemical analysis, because of their properties such as low-cost and low sample volume [8.1]-[8.5]. A small Linear Variable Optical Filter (LVOF) integrated with an array of optical detectors is a very suitable candidate for a microspectrometer that should feature both low unit cost and high resolving power [8.6]-[8.7]. Although grating-based microspectrometers generally outperform optical resonance based systems, such as the Fabry–Perot etalon or the LVOF-based microspectrometer, in case of operation over a wide spectral bandwidth, LVOF-based microspectrometers are more suitable for operation with high resolving power over a narrow spectral band, as is required in spectral analysis around an absorption line [8.8]. IC-Compatible fabrication enables the fabrication of LVOFs as a post-process in CMOS. Having the detector array and

electronic circuits realized in CMOS prior to application of the post-process offers opportunities for low unit costs in case of a high production volume.

The LVOF is basically a one-dimensional array of many Fabry–Perot (FP)-type of optical resonators. Rather than a huge number of discrete devices [8.9], the LVOF has a center layer (the resonator cavity) in the shape of a strip and a thickness that changes linearly over its length. Dielectric mirrors are on either side. The spectral resolution of a Fabry–Perot interferometer is determined by surface flatness, parallelism between the two mirror surfaces and mirror reflectivity. The possibility to have high number of spectral channels in an LVOF spectrometer theoretically makes it possible to have spectral resolution better than 0.2 nm in the visible spectrum range using signal processing techniques. For a Fabry–Perot type of LVOF, the thickness variation of the cavity layer has to be in order of quarter of the wavelength and very well controlled, which makes fabrication of miniature LVOFs a technological challenge. The theoretical limit for the spectral resolving power of the LVOF-based spectrometer is the spectral bandwidth divided by the number of channels in the detector array. However, this is difficult to achieve when considering the signal to noise ratio. This simple geometric optimum is only approached in case of a high SNR.

An IC-Compatible fabrication process for the realization of the tapered dielectric layer results in the possibility for integration of LVOF with CMOS detector arrays which leads to on-chip μ-spectrometers. The thickness of the cavity layer of a LVOF typically varies only around quarter of the reference wavelength (center wavelength) that it is designed to operate. This means around 100 nm for UV spectral range and around 1 μm for IR spectral range. Considering a typical length of 2.5 mm for the detector array, this is equivalent to 0.002° to 0.020° angles of the tapered cavity.

There are several techniques for fabrication of tapered layers such as gray-tone lithography, shadow masking, etc [4.1]-[4.3]. However, these processes are not suitable for IC-compatibly issues. A process based on resist reflow is presented in Chapter 4. A pattern of trenches is made on a photoresist layer. The pattern is designed by a geometrical model and optimized by Finite Element Modeling of resist reflow process. The reflow of the patterned resist structures result in smooth tapered resist layers. The reflow is done by exposing the resist to its solvent during heating in order to avoid cross-linking and hardening of the resist. The reflow process is optimized for various desired values of tapered angle. This approach is very suitable for the IC-compatible batch fabrication of

LVOFs of different slopes on one single chip. The resist structures are transferred into silicon and silicon dioxide by plasma etching to result in the cavity layers of LVOFs. Different slopes and thicknesses can be fabricated and control is done by a single lithography step.

The same principle of design can be applied for realization of LVOF in wavelength ranges of visible, Infrared and UV. The difference would be the choice of dielectric materials for the LVOF filter and suitable detector array. For near-infrared region, for example Poly-Silicon and SiO_2 are to be used as dielectric materials and MEMS fabricated thermopile arrays as detectors.

Filter banks have been designed, fabricated and measured for spectral ranges of UV, visible and Infra-red. The measured results have been compared with initial simulations. The realization of the filter banks which are based multilayered Fabry-Perot filters is an initial step for the fabrication of the final LVOFs. Moreover, the filters can also be used in spectroscopic application such as Non-Dispersive-Infra-red sensors [8.5] and [8.9]. Ellipsometery technique has been used as a powerful tool for characterization and calibration of thin films fabrication. Practical issues such as tolerances in thickness control have been discussed in section 2.3 It has been noted that the realization of a multilayered Fabry-Perot at an exact desired peak transmission wavelength is very challenging due to thickness variations. However, the thickness of the cavity is linearly varied along the length of the tapered strip in case of an LVOF, which allows the channel with a certain peak transmission to be fond as the position of one of the detectors underneath the filter using an initial calibration.

Theory of Fabry-Perot has been discussed in section 2.3.3 It has been noted that number of spectral channels and hence spectral resolving power which is possible to achieve by a Fabry-Perot interferometer depends on the finesse. High resolving power requires extremely reflective mirrors which might not be practical due to limitations in fabrication. An algorithmic solution is proposed in 5.5 to achieve higher resolving powers in case of a Linear Variable Optical Filter. Theoretically the number of spectral channels is determined by the number of pixels in the detector the array.

The operating spectral bandwidth of the LVOF is divided into N channels, and the maximum value for N is number of available pixels in the detector array. N pixels on the detector array are selected. The spectral response of all the N pixels in the detector is measured in an N step calibration process. The obtained data is imported into a Least Mean Square algorithm for calculation of the spectrum of the incident light on the Linear Variable Filter microspectrometer.

In principle the algorithm finds coefficients for the N recorded values of the detector array in monochromatic calibration such a way that their superposition equals the recorded values in the detector array in case of a multi-spectral spectrum.

The algorithm is applied for spectral measurements for fabricated visible and UV LVOFs. In our case we have been limited by the spectral bandwidth and accuracy of the monochromator used for calibration process. The monochromator demonstrates a minimum bandwidth of 0.5 nm. Therefore in the realization the algorithm in the UV and visible LVOFs minimum spectral channels of 0.5 nm are imposed. The number of the spectral channels, N, is thus the operating bandwidth of the LVOF divided by 0.5 nm. Spectral channels of 0.5 nm means a spectral resolving power of better than 1 nm can be expected.

The spectrum of Neon lamp shows distinctive peaks in the 580 nm – 720 nm. The algorithm has been applied for a narrowband LVOF covering 615 nm – 675 nm spectral range. The results show good agreement with measurements done by a commercial spectrometer and a high-resolution grating-based microspectrometer. A spectral resolving power of at least 1.1 nm can be concluded from the measurements. The results are discussed in section 5.6

The algorithm has also been applied to another visible LVOF covering a wider spectral range of 580 nm – 720 nm. The basic difference in the operation between the two LVOF is that for the narrowband LVOF each detector pixel (or channel) is excited by a single wavelength whereas in the wideband LVOF each pixel (or channel) is excited by two or even three wavelength. The distinction between the wavelengths which illuminate each pixel is done in the signal processing algorithm. The result for the wideband visible LVOF presented in 5.7 shows a spectral resolving power of at least 2.2 nm.

A LVOF based on silver mirrors has also been proposed and implemented to cover entire visible spectral range of 400 nm – 700 nm. The difference between silver and Aluminum as metallic reflector has been discussed. It is concluded that to achieve acceptable light throughput in the LVOF, silver is a much more appropriate choice. The characterization and simulations show 15 % - 30 % light throughput in the filter. It is expected to achieve around 5 nm spectral resolution from such a LVOF when signal processing is applied. The simplicity and wide spectral range of this LVOF makes is a good candidate for applications where high spectral resolving power is not required.

A linear array of 128 Active Pixel Sensors has been developed in standard CMOS technology and a Linear Variable Optical Filter (LVOF) is added using CMOS-compatible post-process described in 7.5 , resulting in a single chip highly-integrated high-resolution microspectrometer. The optical requirements imposed by the LVOF result in photodetectors with small pitch and large length in the direction normal to the dispersed spectrum (7.2μm×300μm). The specific characteristics of the readout are the small pitch, low optical signals (typically a photocurrent of 100fA~1pA) and a much longer integration time as compared to regular video (typically 100μs~63s). These characteristics enable a very different trade-off between SNR and integration time and IC-compatibility. The prototype is fabricated in the AMIS 0.35μm A/D CMOS technology and the LVOF is integrated on the top of the photodetector array in at the small chip die level.

8.2 Suggestions for future work

The process for fabrication of tapered resist layers can be further developed for faster and more reproducible result. The process can be based on imprinting of the currently optimized patterns on special nano-impriting thermoplastic polymers. The reflow is done at low temperatures slightly higher than the glass-temperature of the polymer. Reflow properties of nano-impriting polymers has been vastly studied experimentally for imprinting applications and the information can be used in our application.

The current signal processing algorithm is based on the initial calibration process to form the calibration matrix. The spectral limitation imposed in the calibration process limits the spectral resolution of the LVOF microspectrometer to that of the calibrating monochromator. However, since the structure of the LVOF is always known from the initial design simulations can readily provide a good initial guess for the Calibration matrix used in the LMS algorithm. Having a good initial guess for the values of the calibration matrix, a similar LMS algorithm can be used to find the real values by fitting the measurement of a single step calibrating source. The algorithm has to be further developed and tested for such an application. The spectral resolving power can be improved considerably and the limiting factor would be the number of pixels in the detector array and their electronic noise.

The chip with LVOF integrated with photodetector array can be further developed to include all the necessary digital controlling signals. The result is an easy-to-use single chip microspectrometer. A simple RF transmitter can be

also included in the chip to have a wireless microspectrometer. This has potential for applications that contact with the sensor is difficult such as biomedical implantation or in case of harsh environments.

8.3 References

[8.1] G. Minas, R.F. Wolffenbuttel, J.H. Correia, An array of highly selective Fabry–Perot optical channels for biological fluid analysis by optical absorption using a white light source for illumination, *J. Opt. A: Pure Appl. Opt.*, Volume **8**, (2006), pp. 272–278.

[8.2] J.C. Ribeiro, G. Minas, P. Turmezei, R.F. Wolffenbuttel and J.H. Correia, A SU-8 fluidic microsystem for biological fluids analysis, *Sens. Actuators A,*Volumes **123–124**, (2005), pp. 77–81.

[8.3] G. Minas, R.F. Wolffenbuttel, J.H. Correia, A lab-on-a-chip for spectrophotometric analysis of biological fluids, *RSC Lab Chip*, Volume **5**, (2005), pp. 1303–1309.

[8.4] S. Grabarnik, R.F. Wolffenbuttel, A. Emadi, M. Loktev, E. Sokolova and G. Vdovin, Planar double-grating micro-spectrometer, *Opt. Express*, Volume **15** , (2007), pp. 3581–3588.

[8.5] L. Fonseca, R. Rubio, J. Santander, C. Calaza, N. Sabate, P. Ivanov, E. Figueras, I.Gracia, C. Cane, S. Udina, M. Moreno, S. Marco, Qualitative and quantitative substance discrimination using a CMOS compatible non-specific NDIR microarray, *Sens. Actuators B: Chem.*, Volume **141**, (2009), pp. 396-403.

[8.6] R. McLeod and T. Honda, Improving the spectral resolution of wedged etalons and linear variable filters with incidence angle, *Opt. Lett.*, Volume **30**, Issue 19, (2005), pp. 2647–2649.

[8.7] S.F. Pellicori, Wedge-filter spectrometer, *US Patent* 4,957,371, (1990).

[8.8] S. Grabarnik, Optical microspectrometers using imaging diffraction gratings, *PhD thesis*, (2010), Delft University of Technology.

[8.9] R. Rubio, J. Santander, L. Fonseca, N. Sabate, I. Gracia, C. Cane, S. Udina, S. Marco, Non-selective NDIR array for gas detection, *Sens. Actuators B: Chem.*, (Special Issue: Eurosensors XX),Volume **127**, (2007), pp. 69–73.

Summary

On-chip optical microspectrometers have huge potential for implementation in applications that cannot be served with conventional bulky and expensive spectroscopic instruments. For instance, optical analysis of the blood of a patient for hemoglobin, glucose, toxin etc. could be considered, which would allow a rapid diagnosis at the point-of-care or even at home.

Microspectrometers are classified in this thesis according to the dispersion element used, which can be grating(s) or optical filter(s). Microspectrometers based on gratings typically feature a very good spectral resolution (0.5 nm) over a wide (400 – 700 nm) spectral operating range. However, optimizing the design of such a microspectrometer for spectral resolution results in very low values for its numerical aperture. This implies low throughput (low efficiency), which makes the system unsuitable in case of measurement on low-intensity light sources, such as in fluorescent spectroscopy. The alternative category of microspectrometers can be realized by integration of different optical filters on an array of photodetectors in a CMOS-compatible fashion in a post-process, which is the topic of this thesis work.

The benefits of the filter approach are: Firstly, a strongly reduced dependence of the spectral resolution on the numerical aperture of the optical system. This implies that a design would become possible in which a higher numerical aperture is achieved at a specified resolving power. Secondly, the possibility to deposit the optical filters as a post-process results in a fully IC-compatible process for fabrication of single-chip microspectrometers. The main weakness of this approach is that the benefits are significant only when the spectrometer is designed for operation over a relatively narrow spectral band. This feature does limit the scope of application, however makes the microspectrometer particularly suitable in applications that require the spectral analysis around an absorption line.

The spectral resolving power of such a microspectrometer is mainly limited by the number of different optical filters that can be realized. A higher resolving power requires a larger number of different optical filters. In previously reported research a discrete number of Fabry-Perot types of optical filters were integrated with an array of CMOS photodiodes. The minimum number of required lithography steps to result in *N* optical resonators of different thickness

(which is required for N different spectral channels) is $^{2}\log N$. This approach becomes impractical for a large value of N, especially when considering the thickness tolerances in the deposited or back-etched layers. The solution is application of a Linear-Variable Optical Filter (LVOF).

A LVOF is in principle a Fabry-Perot type of filter in which the thickness of the resonance cavity changes linearly along its length, resulting in principle in an infinite number of different Fabry-Perot filters. Hence, the number of separate spectral channels depends solely on the number of the elements in the photodetector array. Integration of a LVOF with a detector array can result in a robust, high-resolution on-chip microspectrometer.

The operating spectral bandwidth of such a microspectrometer is typically less than that of a grating based microspectrometer. This limited is due to the small bandwidth over which the dielectric multilayered structure of the Fabry-Perot mirrors can be designed to be highly reflective. This bandwidth is solely depending on the optical properties of the dielectric materials.

The linear thickness variation of the cavity layer of the LVOF is in the order of quarter of the central wavelength of the LVOF spectral bandwidth. Since the length of the LVOF strip typically extends over several mm, a very small taper angle, ranging from 0.2° to 0.002°, need to be realized in an IC-compatible process. This is the main technical challenge in the fabrication of IC-compatible Linear-Variable Optical Filters. A process based on reflow of a patterned layer of photoresist has been developed for the fabrication of such tapered layers and is presented in this thesis.

The process is based on the use of only one masked lithography step. A pattern of trenches is formed in a photoresist layer. The trench density is defined by the local amount of material to be removed. The following reflow step on this patterned photoresist locally planarizes the remaining strips of the material. The result is an effective local reduction of the resist layer thickness by a value defined by localized trench density and hence a smooth tapered resist layer is realized. The pattern is designed by a geometrical model and optimized by FEM simulations.

The process flow for fabrication of a LVOF is as follows: Initially the first stack of dielectric materials for the first dielectric mirror plus a thick oxide layer is deposited on a detector array chip (or in a substrate to be subsequently mounted on top of a detector array). In the next step, photoresist is spin-coated

and pattered. In the following reflow step the patterned structures in the resist layer of constant thickness are transformed into smooth linear tapered layers. Subsequently, the topography of the tapered resist layer has to be transferred into the thick oxide layer to be used as the actual optical resonator by plasma etching. A carefully designed etching recipe is required to avoid the introduction of surface roughness. Finally, a second stack of dielectric materials is deposited for the realization of the second mirror on the tapered oxide cavity layer completes the Linear-Variable Optical Filter.

This fabrication principle can be applied for the realization of Linear-Variable Optical Filters irrespective of the spectral operating range from UV (300 nm) up to IR (5 μm). The specific operating spectral range merely determines: the dielectric materials that need to be used, the slope of the taper and the type of the photodetector.

Although the number of spectral channels can be huge when using a LVOF-based microspectrometer, a dedicated signal processing algorithm is required to achieve the highest possible spectral resolution. This is inherent to the small Half-Power BandWidth (HPBW) at each location along the LVOF. The HPBW is translated into Half-Power Line Width (HPLW) on the photodetector array. Without implementation of a signal processing, the maximum possible spectral resolving power is determined by the finesse of the Fabry-Perot structure of the LVOF. A signal processing algorithm based on the Least Mean Square (LMS) error has been developed and implemented to improve spectral resolution of the fabricated LVOF microspectrometer.

A LVOF has been designed, fabricated and characterized for the UV spectral range of 300 – 400 nm, which is based on HfO_2 and SiO_2 as the optical materials. A total number of 21 HfO_2 and SiO_2 layers are used in stack for the UV LVOF. The spectrum of a Mercury lamp has been measured with 0.5 nm spectral channels and has been compared with measurement using a monochromator.

Two different types of LVOFs have been realized for operation in the spectral range between 580 nm and 720 nm. The first LVOF realization was designed to cover the entire spectral range, whereas the other one had been designed for narrowband operation and covers the spectral range from 615 nm to 680 nm. The spectrum of a Neon lamp has been measured with both types of LVOF and the results are compared with the spectral measurements that were carried out using a commercially available spectrometer. The results confirm that the best results can be achieved when using a LVOF in a narrowband

application. A spectral resolution of 1.2 nm can be achieved in case of narrowband LVOF and for the wideband LVOF a spectral resolution of 2.2 nm can be expected.

A wideband LVOF based on Siler metallic layer was also designed, fabricated and characterized in this thesis. The choice of silver over other metallic mirrors is due to its lower absorption of light. Such a LVOF can cover the entire visible spectral range. However, due to absorption in the metallic mirror the light throughput is around 15 % to 30 %. The realized LVOF can be used in spectral measurements where light intensity is not limited. The spectral resolution of the realized Silver-based LVOF is 5 nm.

The IC-compatibility of the fabrication process was demonstrated by actual implementation of the post-processing of the LVOF on a CMOS chip at the die-level. A special process based on positioning of the chip on a wafer and reflow of a deposited layer has been designed to enable the post-processing on a die. This is a very relevant result, because most foundry services supply multi-user CMOS processes where the users receive only dies of the processed design. The process presented in this thesis provides the possibility to do post-processing on a single chip. The CMOS chip, realized in a 0.35 μm CMOS process, contains a 128-element photodiode array together with readout circuitry that was designed for operation at low light illumination conditions and long integration times. The integration of the LVOF and the photodiode array with readout in CMOS results in a complete single-chip microspectrometer.

Samenvatting

Optische microspectrometers op een chip maken vele nieuwe toepassingen, die niet haalbaar zijn met de gebruikelijke omvangrijke en dure spectroscopie instrumenten, mogelijk. Toepassingen, zoals het bepalen van bloedwaarden (hemoglobine, glucose, toxine etc.) bijvoorbeeld, kunnen hiermee ter plaatse uitgevoerd worden. Een snelle diagnose ter plaatse van de behandeling, of zelfs thuis, is hiermee in de toekomst mogelijk.

Microspectrometers zijn in deze dissertatie geclassificeerd op basis van het dispersieve element, namelijk door tralie(s) dan wel optische filter(s). Microspectrometers gebaseerd op tralies kunnen een zeer goede spectrale resolutie (0.5 nm) vertonen over een brede (400 nm -700 nm) spectrale band. Echter, het optimaal ontwerpen van een dergelijke spectrometer met een hoge spectrale resolutie resulteert veelal in zeer lage waarden voor de numerieke apertuur. Dit betekent een lage efficiëncy wanneer wordt gemeten met een lage lichtintensiteit, zoals bij toepassingen in fluorescentie spectroscopie. Een alternatief voor tralies is na de fabricage van grote series identieke foto detectoren in CMOS technologie op een enkele chip deze te integreren met optische filters met verschillende optische eigenschappen. Deze benadering wordt beschreven in dit proefschrift.

De voordelen van deze benadering zijn: Ten eerste is men minder afhankelijk van de spectrale resolutie ten opzichte van de numerieke apertuur van het optisch systeem. Dit betekent dat een hogere numerieke apertuur voor een gewenst oplossend vermogen mogelijk is. Ten tweede maakt de mogelijkheid om de optische filters als laatste ('post') fabricage stap te fabriceren, een volledig 'IC'-compatibel proces voor de fabricatie van microspectrometers op een chip mogelijk. Voor een aantal toepassingen zal de inflexibiliteit van het optisch ontwerp beperkingen opleveren, echter niet in de vaak voorkomende toepassingen die een spectrale analyse rond een absorptielijn vereisen.

Het spectraal oplossend vermogen van een dergelijke microspectrometer is vooral beperkt door het aantal verschillende optische filters dat gerealiseerd kan worden. Hogere spectrale resoluties vereisen een groter aantal verschillende optische filters. In eerdere projecten zijn verschillende Fabry-Pérot type optische filters via meerdere lithografische stappen geïntegreerd met CMOS

fotodiodes. Het minimale aantal benodigde lithografische stappen dat resulteert in N spectrale kanalen is $\log_2 N$. Als echter het aantal lithografische stappen toeneemt, dan staan de toleranties in het proces veelal niet toe dat het gewenste resultaat bereikt wordt. De oplossing hiervoor is de toepassing van een Lineair Variabel Optisch Filter (LVOF).

Een Lineair Variabel Optisch Filter (LVOF) is in principe een Fabry-Pérot type filter waarin de optische weglengte van de resonantieholte lineair verandert met de lengte van het filter. Dit resulteert in principe in een oneindig aantal verschillende Fabry-Pérot filters. Hierdoor hangt het aantal onderscheidbare spectrale kanalen af van het aantal elementen in de rij fotodetectoren. Integratie van een LVOF met een dergelijke reeks detectoren kan resulteren in een robuuste, hoge resolutie microspectrometer op een chip.

De bruikbare spectrale bandbreedte van een dergelijke microspectrometer is in het algemeen kleiner dan die van een microspectrometer op basis van tralies. Dit wordt veroorzaakt door de beperkingen in de reflectieve bandbreedte van de dïelectrische meerlaags structuur van de spiegels die het Fabry- Pérot filter vormen. Deze bandbreedte is alleen afhankelijk van de optische eigenschappen van de dïelectrische materialen.

De lineaire variatie in dikte van de optische resonantieruimte van de LVOF is in de orde van grootte van een kwart van de centrale golflengte van de LVOF. Daarom moet een zeer kleine hellingshoek, varïerend van 0,2 tot 0.002 graden, worden gerealiseerd in een IC-compatibel proces. Dit is de belangrijkste technologische uitdaging in de fabricatie van IC-compatibele Lineair-Variabele Optische Filters. In deze dissertatie wordt een proces beschreven en gepresenteerd voor de fabricatie van deze zeer kleine hellingshoek in de diverse lagen, gebaseerd op selectief etsen en planarisatie (reflow) van fotoresist.

Dit proces is gebaseerd op slechts één lithografische stap met een masker. Een patroon van rechthoekige groeven wordt gemaakt in een fotoresist laag. De dichtheid van de groeven bepaalt de hoeveelheid van een materiaal die ter plekke weggehaald moet worden. De daaropvolgende planarisatie stap egaliseert dit patroon in de fotoresist. Het resultaat is een effectieve vermindering van de laagdikte met een waarde gedefinieerd door de lokale dichtheid van de groeven. Hierdoor wordt een lokaal zeer vlakke fotoresist laag gerealiseerd met geleidelijk toenemende dikte. Het patroon is ontworpen met behulp van een geometrisch model en geoptimaliseerd met behulp van FEM simulaties.

Het proces schema voor de fabricatie van een LVOF is als volgt: Als eerste wordt de eerste lagenstructuur van de diëlectrische spiegel inclusief een dikke oxidelaag aangebracht op een serie detectoren (de 'detector array chip') of op een substraat, dat later gemonteerd wordt op de 'detector array'. Bij de volgende stap wordt de fotoresist aangebracht door middel van "spin-coating" en door middel van een lithografische stap en etsen wordt het patroon van groeven hierin aangebracht. De hierop volgende planarisatie stap verandert de groeven structuur in een vloeiende, langzaam en lineair in dikte toenemende laag fotoresist. Daarna, wordt de topografie van de lineair in dikte toenemende laag fotoresist overgezet in de onderliggende oxidelaag door middel van plasma-etsen, waarbij de helling van LVOF resonantieruimte zijn definitieve vorm krijgt. Tenslotte wordt de LVOF compleet door het aanbrengen van de tweede lagenstructuur van de diëlectrische spiegel.

Hetzelfde principe kan worden toegepast bij de realisatie van LVOF voor spectrale afstanden welke varieren van UV (300 nm) tot IR (5 μm). De gewenste werkzame golflengte bepaalt de diëlectrisch materialen die gebruikt moeten worden, de hoek van de helling en het type detector.

Hoewel het aantal spectrale kanalen van een LVOF microspectrometer zeer groot kan zijn, is een toegepast signaal processing algoritme nodig om de hoogst mogelijke spectrale reolutie te bereiken. Dit wordt veroorzaakt door de inherente 'half-power' bandbreedte (HPBW) van ieder punt langs de LVOF. Deze HPBW wordt vertaald naar een 'Half-Power Line Width' (HPLW) op de reeks fotodetectoren. Zonder implementatie van signaalbewerking algorithmes wordt de maximaal mogelijke spectrale resolutie bepaald door de fijnheid van de Fabry-Perot structuur van de LVOF. Een signaalbewerkings algoritme gebaseerd op Least Mean Square (LMS) is ontwikkeld en geïmplementeerd om de spectrale resolutie van de gefabriceerde LVOF microspectrometer te verbeteren.

Er is een LVOF is ontworpen, gefabriceerd en gekarakteriseerd voor het spectrale bereik van 300-400 nm (UV). De diëlectrische materialen die zijn gebruikt, zijn HfO_2 and SiO_2. Een totaal aantal van 21 HfO_2 en SiO_2 lagen zijn wisselend gebruikt in de opbouw van de UV LVOF. Het spectrum van een kwikdamplamp is gemeten met 0.5 nm brede spectrale kanalen en vergeleken met een meting met behulp van een monochromator.

Er zijn twee typen LVOF's gerealiseerd in het spectrale bereik van 580–720 nm. De eerste LVOF is ontworpen voor het gehele spectrum en de andere is ontwerpen voor de smallere spectrale band van 615–680 nm. Het spectrum van een neonlamp is gemeten met beide LVOF's en vergeleken met spectrale metingen met behulp van een commerciële spectrometer. Uit de resultaten blijkt dat de beste resultaten worden bereikt wanneer men gebruik maakt van de smalbandige LVOF. Een spectraal oplossend vermogen van 1.2 nm kon worden bereikt met de 'narrow-band' LVOF en voor de 'wide-band' LVOF kon een oplossend vermogen 2.2 nm gehaald worden. In deze dissertatie wordt ook een 'wide-band' LVOF gebaseerd op spiegels bestaande uit een zilveren metaallaag ontworpen, gefabriceerd en omschreven. De keus voor zilver is het gevolg van de lagere absorptie van licht door zilver, ten opzichte van andere metalen. Een dergelijke LVOF kan het gehele zichtbare spectrum omvatten. Echter door absorptie in de metalen spiegel is slechts 15% tot 30% lichtdoorlaat mogelijk. De gerealiseerde LVOF kan worden gebruikt in spectrale metingen als de lichtsterkte voldoende hoog is. De spectrale resolutie van de op zilveren spiegels gebaseerde LVOF is 5 nm.

De IC- compatibiliteit van het fabricageproces is aangetoond door na de fabricage van de CMOS detector chips de LVOF op de detectoren van de afzonderlijke chips aan te brengen ('die-level post-processing'). Er is een speciaal proces ontwikkeld waarbij de individuele chips op een wafer worden geplaatst en ook een reflow van de gedeponeerde lagen mogelijk is. Dit is een belangrijke stap daar in de meeste multi-user CMOS processen losse chips worden geleverd. Het proces dat gepresenteerd wordt in deze dissertatie geeft de mogelijkheid om de 'post'-processing te doen op individuele chips ('die-level'). De CMOS chip, gemaakt in een 0.35 CMOS proces, bevat een reeks van 128 fotodiodes die samen met de uitleeselectronica speciaal zijn ontworpen voor lage verlichtingcondities en lange integratie tijden. De integratie van de LVOF met de lineaire serie fotodiodes resulteert in een complete microspectrometer op een chip.

Acknowledgements

This thesis work has been supported by the Dutch technology Foundation STW under grant DET.6667.

This work would have not been possible without the help of many people to whom I am indebted. It is my pleasure to heartily thank all those who helped me during these years. In particular, I would like to express my deepest gratitude to:

Dr. Reinoud Wollffenbuttel, my supervisor, for his support and guidance during this project. I would like to thank him for all the encouragement and belief. I am deeply grateful for all the discussions, help and support and patience during hard times. I have certainly learnt many things from him.

Prof. Gerard Meijer, my promoter, to whom I am very thankful for his valuable advices on my work and preparation of this thesis.

All the committee members for their valuable remarks, which improved the quality of this thesis.

My closest collogues; Ger de Graaf, Semen Grabarnik, Huaiwen Wu and Chi Liu. I am very happy that I have had the pleasure to use their discussion in various phases of the project. Ger de Graaf has always been there for any practical problems in the lab, helping with the instruments and software's and many other things which would have taken me much longer to solve alone. Semen Grabarnik has always helped me in any optical problem. I would like to especially thank Huaiwen Wu for all the help in the clean room in the early phases of developing the reflow process. I would also like to thank Chi Liu for her work on the design of photodiode array chip.

Rob Vink (TNO) and other members of the STW user committee, for their input at different stages of the project.

All the members at the Electronic Instrumentation Laboratory and the head of the Laboratory Prof. Paddy French, for the friendly and warm research environment. I am thankful to Willem van der Sluys for his constant help in any financial and administration issue. I am grateful to Joyce Siemers, Ilse van der

Kraaij, Trudie Houweling and Inge Egmond for all their administration support. I would like to thank Antoon Frehe, Maureen Meekel, Jeff Mollinger and Piet Trimp for their help with technical, instruments and IT problems. Special thanks to Zuyao Chang for his help with the first measurements on the LVOF filters. I would also like to thank my fellow PhD students, especially Sarma Mokkapati, Mehdi Kashmiri, Eduardo Margallo, Vijay Rajaraman and Hamed Sadeghian for their collaboration and friendliness.

All the members of the nanofabrication laboratory at Chalmers University, MC2. It has been a great honor for me to use the facility and expertise in the nanofabrication laboratory of MC2 during my Ph.D work. Especially I would like to thank Ulf Södervall for all the arrangement he did for my visits to MC2. I would like to thank Karin Hedsten for the arrangements and discussions. I am indebted to Henrik Frederiksen for all the help and support for the sputtering of the materials. I am thankful to Mats Hagberg for the valuable discussions and help with dry etching processes. I would like to thank Örjan Arthursson for training and help with ellipsometry for material characterization. Most of the work done in MC2 was supported by the EU-funded project of MC2ACCESS.

Prof. Vladmir Krasnov, my supervisor for my master thesis. It was a great honor for me to learn so much about micro and nano-fabrication techniques from him.

Kasper Zwetsloot and Solomon Agbo for their great help in the measurements of the filter banks.

To my parents and brother and sister *Arman and Azadeh*, for their continuous support, encouragement and love over all these years. *To you I dedicate this thesis.*

my friends in Delft, *Shahin, Pegah, Rouzbeh, Lucka, Lida, Pourya, Gilda, Maurits, Yasmin, Wijbrand, Hooman, Human, Amir, Roham, Jafar, Alireza, Safa, Kamran, Arman, Shadi* and others for all the pleasant time we have spent together during my stay in Delft. And my family and friends in Gothenburg, *Parvin, Ali, Simin, Neda, Mehdi, Abdi, Behrokh, Parham, Poria, Shahnaz, Alireza, Ali, Hamid, Romina, Rojano, Iman, Bahar, Farzan, Pirooz* and many others for their hospitality and great times during my visits to Gothenburg.

Finally, I would like to express my profound appreciation for my girlfriend Jorien (and her family) for emotional support during the long months of writing and correction of this thesis.

List of Publications

In Scientific Journals

A. Emadi, H. Wu, S. Grabarnik, G. de Graaf, K. Hedsten, P. Enoksson, J.H.G. Correia, R.F. Wolffenbuttel, Fabrication and characterization of IC-compatible linear variable optical filters with application in a micro-spectrometer, *Sensors and Actuators A: Physical*, Volume **162**, Issue 2, (2010), pp. 400-405.

A. Emadi, H. Wu, S. Grabarnik, G. de Graaf and R. F. Wolffenbuttel, Vertically tapered layers for optical applications fabricated using resist reflow, *J. Micromech. Microeng.*, Volume **19,** (2009), pp. 074014/1-9.

H. Wu, S. Grabarnik, A. Emadi, G. de Graaf and R. F. Wolffenbuttel, Characterization of thermal cross-talk in a MEMS-based thermopile detector array, *J. Micromech. Microeng.*, Volume **19**, (2009), pp. 074022/1-7.

S. Grabarnik, A. Emadi, E. Sokolova and G. Vdovin and R.F. Wolffenbuttel, Optimal implementation of a microspectrometer based on a single flat diffraction grating, *Journal of Applied Optics*, Vol. **47**, Issue 12, pp. 2082-2090.

S. Grabarnik, A. Emadi, H. Wu, G. de Graaf, G. Vdovin and R.F. Wolffenbuttel, Fabrication of an imaging diffraction grating for use in a MEMS-based optical microspectrograph, *J. Micromech. Microeng.*, Volume **18**, Number 6, (2008), pp. 064006/1-6.

H. Wu, S. Grabarnik, A. Emadi, G. de Graaf and R.F. Wolffenbuttel, A thermopile detector array with scaled TE elements for use in an integrated IR microspectrometer, *J. Micromech. Microeng.*, Volume **18**, (2008), pp. 064017/1-7.

S. Grabarnik, A. Emadi, H. Wu, G. de Graaf and R.F. Wolffenbuttel, High-resolution microspectrometer with an aberration-correcting planar grating, *Journal of Applied Optics*, Volume **47**, Number 34, (2008), pp. 6442-6447.

J. H. Correia, A. Emadi and R. F. Wolffenbuttel, UV Bandpass optical filter for microspectrometers, *ECS transactions*, Electro Chemical Society, Volume **4**, Number 1, (2006), pp.141-147.

S. Grabarnik, R.F. Wolffenbuttel, A. Emadi, M. Loktev, E. Sokolova, and G. Vdovin, Planar double-grating microspectrometer, *Optics Express*, Volume **15**, Issue 6, (2007), pp. 3581-3588

In conference proceedings

A. Emadi, H. Wu, S. Grabarnik, G. de Graaf, K. Hedsten, P. Enoksson, J.H.G. Correia, R.F. Wolffenbuttel, An UV Linear Variable Optical Filter-Based Micro-Spectrometer, *Procedia Engineering*, Volume **5**, Eurosensor XXIV, (2010), pp. 416-419.

A. Emadi, S. Grabarnik, H. Wu, G. De Graaf and R. F. Wolffenbuttel, Spectral Measurement with a Linear Variable Filter Using a LMS Algorithm, *Procedia Engineering*, Volume **5**, Eurosensor XXIV, (2010), pp. 504-507.

A.Emadi, V.R.S.S. Mokkapati, H. Wu, G. de Graaf and R. F. Wolffenbuttel, Linear Variable Optical Filter with Silver metallic layers, Proc. MME, September 26-29, 2010, Enschede, The Netherlands, 4pp

H. Wu, A. Emadi, G de Graaf and R. Wolffenbuttel, Inerference filter based absorber for thermopile detector array by surface micromachining, Proc. MME, September 26-29, 2010, Enschede, The Netherlands, 4pp

A. Emadi, H. Wu, G. de Graaf and R. F. Wolffenbuttel, Post-Processing of Linear Variable Optical Filter on CMOS chip at die-level, Proc. MME, September 26-29, 2010, Enschede, The Netherlands, 4pp

A. Emadi, H. Wu, S. Grabarnik, G. de Graaf, R. F. Wolffenbuttel, CMOS-compatible LVOF-based visible microspectrometer, *Proc. SPIE*, Volume **7680**, (2010), pp. 76800W/1-6.

H. Wu, A. Emadi, G. de Graaf, R.F. Wolffenbuttel, Encapsulated thermopile detector array for IR microspectrometer, *Proc. SPIE*, Volume **7680**, (2010), pp. 76800Z/1-6.

H. Wu, A. Emadi, G. de Graaf, R.F. Wolffenbuttel, Thin film encapsulated 1D thermoelectric detector in an IR microspectrometer, *Proc. SPIE*, Volume **7726**, (2010), pp. 772612/1-7.

C. Liu, A. Emadi, H. Wu, G. de Graaf, R.F. Wolffenbuttel, A CMOS 128-APS linear array integrated with a LVOF for high sensitivity and high-resolution micro-spectrophotometry, *Proc. SPIE*, Volume **7726**, (2010), pp. 772616/1-8.

A. Emadi, H. Wu, S. Grabarnik, G. de Graaf, K. Hedsten, P. Enoksson, J.HG. Correia, R.F. Wolffenbuttel, Spectral measurement using IC-compatible linear vairable optical filter, *Proc. SPIE*, Volume **7716**, (2010), pp. 77162G.

H. Wu, S. Grabarnik, A. Emadi, G. de Graaf and R. F. Wolffenbuttel, Study of Thermal Cross-Talk in Micromachined Thermopile based infrared detector arrays, *Proc. Sense of Contact*, (2009), Zeist, the Netherlands, 4 pp.

A. Emadi, S.Grabarnik, H. Wu, G. de Graaf and R F Wolffenbuttel, IC-compatible fabrication of linear variable optical filter for micro-spectrometer, *Proc. Sense of Contact*, (2009), Zeist, the Netherlands, 4 pp.

G. de Graaf, A. Emadi and R. F. Wolffenbuttel, Fabrication and characterization of IC-compatible multi-layer interference filters, *Proc. IRS^2 SENSOR+TEST Conference,* (2009), Nurnberg, Germany, pp. 313 – 318.

H. Wu, S. Grabarnik, G. de Graaf, A. Emadi and R. F. Wolffenbuttel, Thermal cross-talk in IC-compatible micromachined infrared thermopile detector arrays, *Proc. IRS^2 SENSOR+TEST*, (2009), Nurnberg, Germany, pp. 319 – 323.

H. Wu, A. Emadi, G. de Graaf, J. Leijtens and R. F. Wolffenbuttel, Self-powered optical sensor systems, *Proc. Transducers*, June 21 - 25, (2009), Denver, Colorado, USA, pp. 1373-1376.

S. Grabarnik, A. Emadi, H. Wu, G. de Graaf and R. F. Wolffenbuttel, Microspectrometer with a concave grating fabricated in a MEMS technology, *Procedia Chemistry*, Volume **1**, Issue 1, Proceedings of the Eurosensors XXIII conference, (September 2009), pp. 401-404.

H. Wu, A. Emadi, S. Grabarnik, G. de Graaf and R. F. Wolffenbuttel, Static and dynamic analysis of thermal cross-talk in an thermopile detector array for

use in a microspectrometer, *Procedia Chemistry*, Volume **1**, Issue 1, Proceedings of the Eurosensors XXIII, (September 2009), pp. 1139-1142.

A. Emadi, H. Wu, S. Grabarnik, G. De Graaf and R. F. Wolffenbuttel, IC-compatible fabrication of linear variable optical filters for micro-spectrometer, *Procedia Chemistry*, Volume **1**, Issue 1, Proceedings of the Eurosensors XXIII conference, (September 2009), pp. 1143-1146.

A. Emadi, H. Wu, S. Grabarnik, G de Graaf and R. F. Wolffenbuttel, Interference filter based IR absorber for MEMS thermopile array, *Proc. MME*, September 20-22, (2009), Toulouse, France, 217/D21, 4 pp.

S. Grabarnik, A. Emadi, H. Wu, G. de Graaf and R.F. Wolffenbuttel, Concave diffraction gratings fabricated with planar lithography, *Proc. of SPIE*, Vol. **6992**, (2008), pp. 699214/1-8.

S. Grabarnik, A. Emadi, H. Wu, G. de Graaf, G. Vdovin and R.F. Wolffenbuttel, IC-compatible microspectrometer using a planar imaging diffraction grating, *Proc. of SPIE*, Vol. **6992**, (2008), pp. 699215/1-10.

S. Grabarnik, A. Emadi, H. Wu, G. de Graaf, G. Vdovin and R.F. Wolffenbuttel, Planar MEMS-compatible microspectrograph, *Proc. APCOT*, (2008), Tainan, Taiwan, June 22-25, pp. 53-56.

H. Wu, A. Emadi, W. van der Vlist, S. Grabarnik, G. de Graaf, and R.F. Wolffenbuttel, Design and fabrication of a thermopile detector array with scaled elements for an integrated IR microspectrometer, *Proc. APCOT*, (2008), Tainan, Taiwan, June 22-25, pp. 213-216.

S. Grabarnik, A. Emadi, H. Wu, G. de Graaf and R.F. Wolffenbuttel, Optical microspectrometer with planar grating and external spherical lens, *Proc. Eurosensors 2008*, Dresden Germany, September 7-10, (2008), pp. 350-353.

H. Wu, S. Grabarnik, A. Emadi, G. de Graaf and R.F. Wolffenbuttel, Cross-talk characterisation of a thermal detector array, *Proc. Eurosensors 2008*, Dresden Germany, September 7-10, (2008), pp. 366-369.

A. Emadi, H.Wu, S. Grabarnik, G. de Graaf and R.F. Wolffenbuttel, Fabrication of tapered optical structures using resist reflow, *Proc. MME'2008 (19th MicroMechanics Europe)*, Aachen, Germany, 28-30 September, (2008), pp. 113-116.

A. Emadi, H.Wu, S. Grabarnik, G. de Graaf and R.F. Wolffenbuttel, Simulation and analytical calculation of reflowed resist structures, *Proc. MME'2008 (19th MicroMechanics Europe)*, Aachen, Germany, 28-30 September, (2008), pp. 347-350.

H.Wu, S. Grabarnik, G. de Graaf, A. Emadi and R.F. Wolffenbuttel, Characterization of thermal cross-talk in thermopile detector array used in a MEMS-based IR microspectrometer, *Proc. MME'2008 (19th MicroMechanics Europe)*, Aachen, Germany, 28-30 September, (2008), pp. 415-418.

H.Wu, A. Emadi, G. de Graaf, S. Grabarnik and R. F. Wolffenbuttel, Design and fabrication of thermopile detector array for micro spectrometer application, *Proceedings of MME*, Guimaraes, Portugal, 16-18 September, (2007), pp. 103-106.

A. Emadi, S. Grabarnik, H.Wu, G de. Graaf, R.F. Wolffenbuttel, Fabrication and characterization of infra-red multi-layered interference filter, *Proceedings of MME*, Guimaraes, Portugal, 16-18 September, (2007), pp. 249-252.

A. Emadi, H. Wu, S. Grabarnik, G. de Graaf, R. F. Wolffenbuttel, Infrared thermopile detector array for the integrated micro spectrometer, *IEEE Sensors*, Atlanta, USA, 28-31 October 28-31, (2007), pp. 435-438.

S. Grabarnik, A. Emadi, H.Wu, G de. Graaf, G. Vdovin, R.F. Wolffenbuttel, Spectral sensor based on an imaging diffraction grating and fabricated with MEMS technologies, *Proceedings of MME*, Guimaraes, Portugal, 16-18 September, (2007), pp. 175-178.

J. H. Correia, A. Emadi and R. F. Wolffenbuttel, UV Bandpass optical filter for microspectrometers, *Proc. of SBMICRO 2006*, Ouro Preto, Brazil, 28 August - 1 September, (2006), pp.1-7.

A. Emadi, J.H. Correia, G. de Graaf, R.F. Wolffenbuttel, Silicon compatible Fabry-Perot optical filter for mid-IR microspectrometer applications, *Proc. Eurosensors XX*, 17-20 September 2006, Gothenburg, Sweden, pp.1-3.

About the Author

Arvin Emadi was born in Tehran, Iran, on 17th February 1982. He graduated from Alborz high school in 1998 when he was awarded Silver medal in national student's mathematics Olympiad. He got Bachelor degrees in Telecommunications and Electronics from Amirkabir University of Technology (Polytechnic of Tehran) in 2003. His bachelor graduation project was about Active Noise Cancellation.

He graduated with distinction from his master in Hardware for Wireless Communication from Chalmers University of Technology, Sweden in 2005. He has worked with electromagnetic wave simulations, high frequency circuit designing and has experience with micro and nano fabrication techniques. He joined the Electronic Instrumentation Laboratory from Feb 2006 and he has worked on a microspectrometer project. His research interests are micro and nano fabrication techniques, IR to UV filters and photodetectors, spectroscopy applications, IC designing and high-Tc superconductors.

Propositions accompanying the thesis

Linear-Variable Optical Filters for microspectrometer application

1- Inexpensive, chip-size microspectrometers are optical systems of high potential, since these can bring about applications which are not feasible with bulky, expensive spectral instruments.
2- On-chip microspectrometers can be realized by integration of an IC-compatible Linear-Variable Optical Filter (LVOF) with a CMOS photodiode array.
3- The crucial step in the fabrication of an IC-compatible Linear-Variable Optical Filter is the realization of the tapered layer, which is intended to be used as the optical resonator.
4- In order to get a smooth surface, the patterned resist should be exposed to its solvent vapor during reflow.
5- To avoid a rough surface, the required plasma etching for the fabrication of a tapered oxide layer should be carried out at a rate not exceeding 10 nm/min and a pressure less than 4 mTorr.
6- Without signal processing, the resolution of an LVOF microspectrometer is determined by the finesse of the applied Fabry-Perot structure.
7- Before applying new processes in the clean-room, it is important to talk with people who have experience with similar processes, since many important details have not been written down.
8- Innovations have the same function in new technology as the small step-by-step mutations have in the evolution.
9- Although modern society puts emphasis on specialization, a broader view helps us to recognize patterns that could be essential for successfully dealing with a specific problem.
10- History should only be studied to learn lessons for a better future. Using history to justify revenge or punishment can easily result in an endless cycle of hostilities.
11- Democracy, even in its simplest form, is put under a strain when the country is threatened by foreign forces.
12- For a peaceful solution to political disputes between Western and Eastern countries, the differences in culture and mentality need to be considered.
13- Economic sanctions have a time-dependent effect; first these bring poverty to the people and only much later affect the ruling class. In a time-constrained conflict it may be better to open the doors for trades and dialogue.
14- A wish is born and an endeavor has begun to reach it. After the wish has come true it soon gets forgotten and another newly born wish leads to another cycle, like traveling through a spiral with nothing in the middle except the passage of life (Inspired by an Iranian saying).

Arvin Emadi, 17th November 2010

These propositions are regarded as opposable and defendable, and have been approved as such by the supervisor, Prof. dr. ir. G.C.M. Meijer.

Stellingen behorende bij het proefschrift

Linear-Variable Optical Filters for microspectrometer application

1- Goedkope microspectrometers met de afmetingen van een chip zijn optische systemen met een hoog groeipotentieel, aangezien deze toepassingen mogelijk maken die niet haalbaar zijn met omvangrijke, dure spectrale instrumenten.
2- On-chip microspectrometers kunnen worden gerealiseerd door de integratie van een IC-compatibel Lineair Variabel Optisch Filter (LVOF) met een rij van CMOS fotodiodes.
3- De cruciale stap in de fabricage van een IC-compatibel Lineair Variabel Optisch Filter is de realisatie van de taps toelopende laag, welke wordt gebruikt als de optische resonator.
4- Teneinde een glad oppervlak te verkrijgen dient de fotoresist tijdens reflow te worden blootgesteld aan dampen van het oplosmiddel.
5- Teneinde een ruw oppervlak te voorkomen dient bij de vervaardiging van een taps toelopende oxidelaag de benodigde plasma-etshandeling te worden uitgevoerd bij etssnelheiden van niet meer dan 10 nm / min en bij een druk van minder dan 4 mTorr.
6- Indien er geen signaalverwerking plaatsvindt, wordt de resolutie van een LVOF microspectrometer bepaald door de finesse van de gebruikte Fabry-Perot structuur.
7- Bij het gebruik van een nieuw proces in de clean-room is het van belang om te praten met de mensen die ervaring hebben met dit soort processen, omdat veel belangrijke details niet zijn opgeschreven.
8- Innovaties hebben dezelfde functie met betrekking tot het genereren van nieuwe technologie als de kleine stap-voor-stap mutaties in de evolutie.
9- Hoewel de moderne samenleving de nadruk legt op specialisatie, is een bredere kijk noodzakelijk om patronen te herkennen die essentieel kunnen zijn voor een succesvolle aanpak van een specifiek probleem.
10- Geschiedenis mag alleen worden bestudeerd om lessen te leren voor een betere toekomst. Het met behulp van de geschiedenis rechtvaardigen van wraak of straf kan gemakkelijk resulteren in een eindeloze cyclus van vijandigheden.
11- Democratie, zelfs in zijn meest eenvoudig vorm, komt onder druk te staan indien het land wordt bedreigd door buitenlandse troepen.
12- Voor een vreedzame oplossing voor de politieke twisten tussen Westerse en Oosterse landen, moeten verschillen in cultuur en mentaliteit worden meegewogen.
13- Economische sancties hebben een tijdsafhankelijk effect; eerst brengen deze armoede bij de mensen en pas veel later zijn ze van invloed op de heersende klasse. In tijdkritische conflicten kan het beter zijn om de deuren te openen voor handel en dialoog.
14- Een wens is geboren en een poging is begonnen om die te realiseren. Nadat de wens is uitgekomen is deze al snel vergeten en een andere pasgeboren wens leidt tot een nieuwe cyclus, vergelijkbaar met het reizen door een spiraal met niets in het midden, behalve de loop van het leven (geïnspireerd door een Iraanse zegswijze).

Arvin Emadi, 17th November 2010

Deze stellingen worden opponeerbaar en verdedigbaar geacht en zijn als zodanig goedgekeurd door de promotor, Prof. dr. ir. G.C.M. Meijer.

Uitnodiging

Hierbij nodig ik U van harte uit
voor het bijwonen
van de verdediging van mijn
proefschrift getiteld

Linear-Variable Optical Filters for microspectrometer application

op woensdag 8 december 2010
van 10:00 tot 11:00 uur
in de Senaatzaal van de Aula
van de Technische Universiteit
Mekelweg 5 te Delft

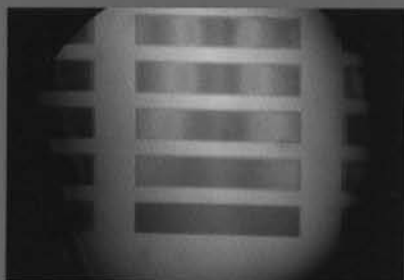

Voorafgaand aan de
verdediging om 9:30 uur,
zal ik een korte uitleg geven
over mijn werk.

Na afloop bent U van harte
welkom op de receptie in de
Frans van Hasseltzaal in de Aula.

Arvin Emadi
Email:: A.Emadi@TUDelft.NL
Tel: 015-2786285

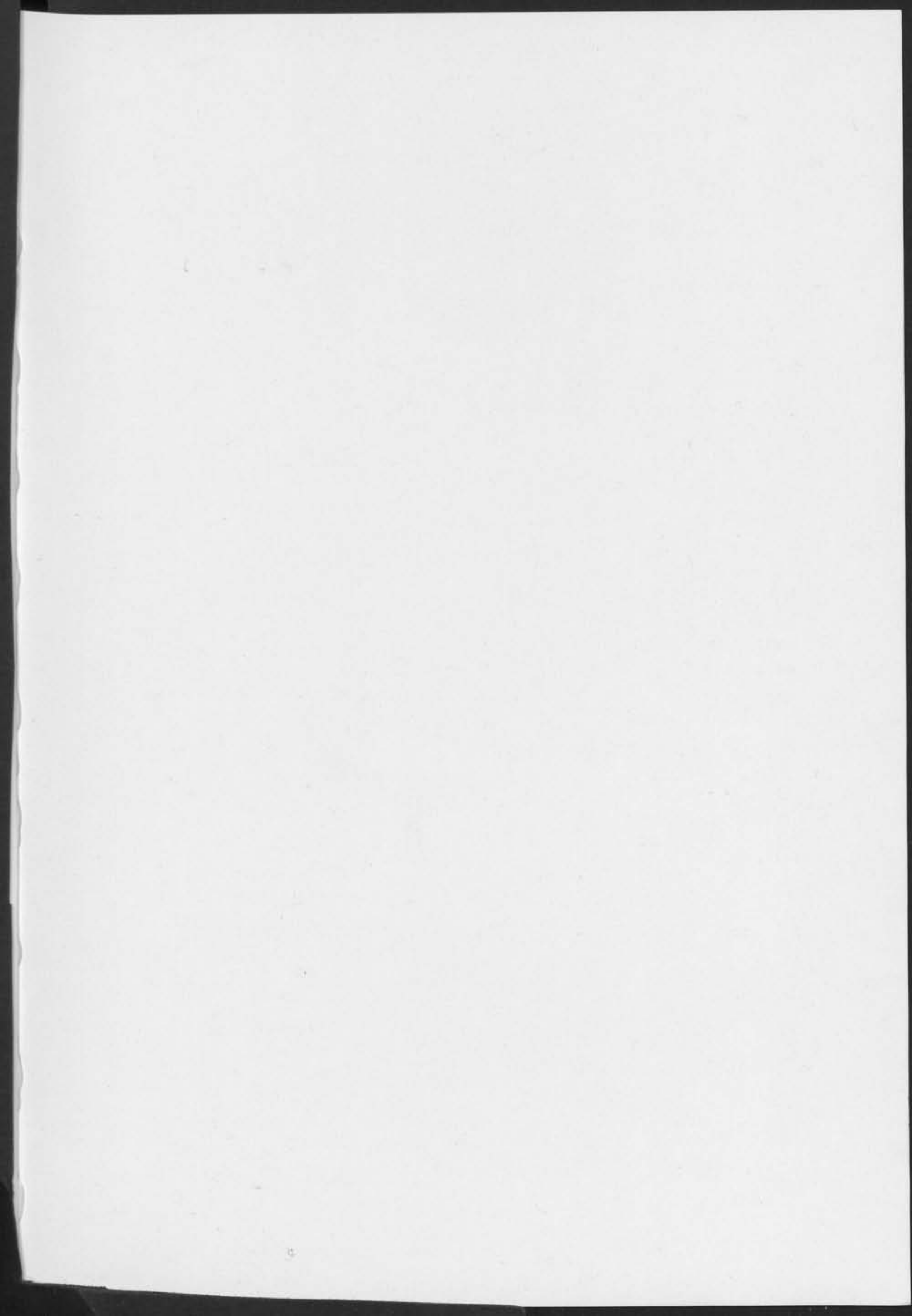

DIMES
Delft Institute of Microelectronics
and Submicron Technology

ISBN: 978-90-813316-8-5